Thermal X-ray Emission From Young Type Ia Supernova Remnants

Carles Badenes Montoliu

Memòria presentada per optar al grau de Doctor

Director: Eduard Bravo Guil

Departament de Física i Enginyeria Nuclear
Universitat Politècnica de Catalunya

Institut d'Estudis Espacials de Catalunya

Barcelona, Maig 2004

A la Núria,

per fer possibles tantes coses...

Was ich weiss, kann jeder wissen,

mein Herz habe ich allein.

El que jo sé, ho pot saber qualsevol,

el meu cor només el tinc jo.

Johann Wolfgang von Goethe (1749-1832). *Werther.*

Thermal X-ray Emission From Young Type Ia Supernova Remnants

Carles Badenes

Abstract

The relationship between Type Ia supernovae and the thermal X-ray emission from their young supernova remnants is explored using one dimensional hydrodynamics and self-consistent ionization and electron heating calculations coupled to a spectral code. The interaction with the ambient medium is simulated for a grid of supernova explosion models which includes all the physical mechanisms currently under debate. The differences in density profile and chemical composition of the ejecta for each supernova explosion model have a profound impact on the hydrodynamic evolution, plasma ionization and emitted thermal X-ray spectra of the supernova remnant, even several thousand years after the explosion. This has two important consequences. First, new possibilities are opened for the use of the high quality X-ray observations of Type Ia supernova remnants as a tool to study supernova explosions. Second, it follows immediately that an accurate analysis of such observations is not possible unless the characteristics of the supernova explosion are considered in some detail. These results are applied to the remnant of the Tycho supernova (SN1572), which appears to be the result of a delayed detonation explosion based on a comparison between its X-ray spectrum and the synthetic model spectra. The imprint of the presupernova evolution predicted by current Type Ia progenitor models on the dynamics of the supernova remnants is also explored, and found to be important. The observations, however, do not show hints of any such imprint.

Acknowledgments/Agraïments

Aquesta tesi ha estat possible gràcies a dues institucions: la Generalitat de Catalunya, que em va concedir una beca FI (2000FI 00376) i l'Institut d'Estudis Espacials de Catalunya, a través del seu director, Jordi Isern, qui em va proporcionar una segona beca que ha permés enllestir la feina.

La meva gratitud, però, va dirigida sobretot a les persones que m'han ajudat al llarg de tot aquest temps. Vull deixar ben clar que és del tot impossible mencionar a tothom, així que si em descuido algú, espero que em perdoni. Potser sembla estrany que escrigui alguns agraïments en anglés, però em sembla just que cadascú pugui entendre la part que li pertoca.

En primer lloc, vull donar les gràcies a les dues persones que han fet una contribució més important a aquesta tesi: el meu director, Eduard Bravo, i el professor Kazik Borkowski.

Al llarg dels anys que porto treballant amb l'Eduard (comencen a ser uns quants!), he aprés moltíssim, i he arribat a apreciar sincerament la seva manera clara i concisa d'explicar les coses. Li he d'agraïr el fet que sempre hagi mantingut la calma, fins i tot (i especialment) quan jo no ho feia; realment ha estat una sort per mi poder comptar amb ell.

I have benefited many times from both the vast knowledge and endless patience of Kazik Borkowski. There's simply no way I could have done this without his help. Working with him has been a pleasure, and I hope that I will have the chance to keep on learning from him. I am also looking forward to more trips to the mountains!

I have been very lucky to meet a number of people in the US who showed an interest in my work, and with whom I have shared interesting discussions, and also a laugh or two. Una Hwang was a charming host at GSFC, and made a very significant contribution to the chapter devoted to Tycho. Martin Laming has been an unquenchable source of encouragement, and he also provided help with radiative losses and a quote by Tolstoy. It has been wonderful to talk about SNRs, astrophysics and life in general, over e-mail, over coffee and sometimes even over a beer with Jack Hughes, Steve Reynolds, Dan Dewey, Cara Rakowski, Parviz Ghavamian, Jessica Warren, John Blondin, Dick McCray, Vikram Dwarkadas and many, many more. Hello to Keith, Fatima and the Ridge Road Zoo at Greenbelt, and to Lisa and Ivan at Raleigh. Thanks also to the CESR gang at Toulouse.

Tornem al català. Aquesta secció no estaria completa sense una menció a tota la gent de l'IEEC. He d'agrair molt sincerament els ànims i els consells de moltes persones, entre els quals vull destacar a Margarida Hernanz, Enrique García-Berro, Jordi Isern, Jordi José, Chema Torrelles i Gabriel Martínez-Pinedo. Una abraçada per les noies d'administració i pel grup del cafè matiner: Alina, Jose, Pep i Sílvia (el nucli dur), i també al Fermí i la resta dels becaris. L'Alina, a més a més, ha llegit gran part del text i ha intentat corregir la meva gramàtica anglesa creativa. Pel final em reservo dues persones que es mereixen un agraïment especial. Gràcies, Josep, pel suport informàtic, per les converses surrealistes i per fer-me riure gairebé sempre (aquest cop no és un comentari sarcàstic). Segueixo

buscant xiclets de garrofa. Gràcies, Glòria, per tots aquests anys de doctorat a l'IEEC. Ha estat molt agradable compartir-los amb tu. Us trobaré molt a faltar.

Gràcies també als meus amics: Pere, Marta, Miquel, Carles, Liberto, Blanca i tots els que en algun moment heu hagut d'aguantar les meves paranoies. Una salutació al Lluís i la Cèlia pels dissabtes al Tiju, a la Milena i al Paolo a Toulouse i a tota la gent d'Atzeneta, en especial Mª Tere, Mª José i Sònia. També als incombustibles Aitor, Toni i Àngel, amb els que he compartit moltes tardes de rol i moltes nits de festa. Finalment, una abraçada ben forta per la Maria, que m'ha ajudat a tirar això endavant, ingerint heròicament litres i litres de cafeïna més enllà del deure de l'amistat.

Moltes gràcies a tota la meva família: avis, tiets i cosins, en especial al Tico i la Raquel, a la Tere i a la Marta.

Moltes gràcies a la Núria, a qui dedico aquesta tesi. En la immensitat del temps i l'espai, la meva sort és compartir un planeta i una època amb ella.

El lloc d'honor en aquesta secció correspon sens dubte als meus pares, que sempre m'han fet costat i m'han animat. Ells comparteixen, i sempre compartiran, una part del mèrit en tot el que jo pugui fer.

A tots vosaltres, moltes gràcies.

Barcelona, 19 de Maig de 2004

Foreword

Even in a relatively homogeneous scientific community like that of astrophysics, there is an enormous range of criteria about what a Ph D thesis dissertation should and should not be. In order to avoid confusion, I will state here explicitly that I have not intended to produce a compilation of published or soon to be published results in more or less the same form that they could be found in a refereed journal. Rather, my aim has been to give a global vision of the subject in all its aspects, from the initial statement of the problem to the techniques that have been developed for its solution, and the limitations of these techniques in the context of the current state-of-the-art. With that goal in mind, I have included some material in each chapter that would be superfluous in a specialized scientific paper, but that I think plays an important role in the shaping of that global vision. It is up to the reader to judge what degree of success, if any, has been attained in the achievement of these objectives.

A word about the use of personal pronouns. Throughout the text, I will make free use of 'we', meaning 'I', for a purely aesthetic reason. All the work presented here is my own, with the exception of the supernova explosion models detailed in chapter 2, which were calculated by Eduard Bravo. Other punctual but important contributions are explicitly acknowledged in the text.

> *First my fear; then my courtesy; last my speech.*
>
> *My fear is, your displeasure; my courtesy, my duty;*
>
> *and my speech, to beg your pardons. If you look*
>
> *for a good speech now, you undo me: for what I have*
>
> *to say is of mine own making; and what indeed I*
>
> *should say will, I doubt, prove mine own marring.*
>
> *But to the purpose, and so to the venture.*

William Shakespeare (1564-1616). *Henry IV, Part 2; Epilogue.*

Contents

List of Acronyms and Abbreviations

ACIS   AXAF CCD Imaging Spectrometer (*Chandra* instrument)

AGB   Asymptotic Giant Branch

AIC   Accretion-Induced Collapse

AM   Ambient Medium

AMU   Atomic Mass Unit

ASCA   Advanced Satellite for Cosmology and Astrophysics (also known as *Astro-D*)

AXAF   Advanced X-ray Astrophysics Facility (former name of *Chandra*)

CCD   Charge Coupled Device

CD   Contact Discontinuity

CFL   Courant-Friedrichs-Lewy

Ch   Chandrasekhar

CIE   Collisional Ionization Equilibrium

CO   Carbon and Oxygen

CR   Cosmic Rays

CSD   Charge State Distribution

CSM   Circumstellar Medium

DD   Double Degenerate

DDT   Delayed Detonation

DEF   Deflagration

DET   Detonation

DOF   Degrees Of Freedom

EPIC   European Photon Imaging Camera (*XMM-Newton* instrument)

ESU	ElectroStatic Unit
EXOSAT	European X-ray Observatory SATellite
GROSS	Get Rid Of Slimy girlS (Calvin and Hobbes club)
HD	HydroDynamic
HS	Hamilton & Sarazin (spectral code)
IME	Intermediate Mass Element
IDL	Interactive Data Language
IR	InfraRed
MOS	Metal Oxide Semiconductor
NEI	Non-Equilibrium Ionization
NSE	Nuclear Statistic Equilibrium
PDD	Pulsating Delayed Detonation
R-T	Rayleigh-Taylor
RGS	Reflection Grating Spectrometer (*XMM-Newton* instrument)
ROSAT	ROentgen SATellite
S-Ch	Sub-Chandrasekhar
SCH	Sub-Chandrasekhar
SD	Single Degenerate
SN	SuperNova
SNR	SuperNova Remnant
SPH	Smooth Particle Hydrodynamics
UV	UltraViolet
VLA	Very Large Array
WD	White Dwarf
XMM	X-ray Multi Mirror
XSPEC	X-ray SPECtral fitting program

Chapter 1

Introduction

'I shall make my report as if I told a story, for I was taught as a child on my home world that Truth is a matter of the imagination. The soundest fact may fail or prevail in the style of its telling.'

Ursula K. Le Guin, *The Left Hand of Darkness*

1.1   A flash of light in the dark

On the night of November 11, 1572, the Danish astronomer Tycho Brahe was going home from his laboratory, where he had been conducting alchemical experiments. As was his wont, he paused for a while to look at the stars, and there, next to the familiar shape of Cassiopeia, he saw something unexpected. A bright, white star flashed where no star had ever been before. Tycho started to record his observations of the new star immediately, and published them in a short book called *De Stella Nova*, which appeared in 1574. He calculated the parallax of the star and came to the conclusion that it was beyond the Moon, among the fixed stars. The Aristotelian doctrine then en vogue considered this region of the sky to be immutable, so the discovery of the *stella nova* of 1572 had an enormous philosophical significance in its time. The ensuing scientific debate contributed to shape the conception of the Universe in the turmoil of the Renaissance (see Clark and Stephenson, 1977, chapter 10). Unfortunately, we shall have to leave that engaging topic in more able hands and concentrate on the astrophysical implications of the event.

During the following years, the title of Tycho's book gave its name to a whole class of astronomical objects, the *novae*: stars which appear suddenly, shine for a few weeks or months, and then fade and disappear completely. Johannes Kepler, who was Tycho's assistant some years later, observed another *nova* in 1604, in the constellation of Ophiuchus. As the use of telescopes and accurate star catalogs became commonplace among scientists, the list of these objects grew steadily. It was not until Edwin Hubble made the first realistic measurements of extragalactic distances in the early twentieth century that astronomers came to realize that there were two distinct classes of *novae*. The vast majority of them had only moderate brightness, and were relatively common in the vicinity of the of the Sun, but others were seen over distances so large that they had to be several orders of magnitude brighter. This was first noted by Knut Lundmark in 1920, who obtained an astonishing $\mathcal{M}_v = -15$ for the *nova* that had been observed in 1885 in the Andromeda Nebula. The term *supernova* was coined to describe these objects by Walter Baade and Fritz Zwicky in 1934. The *novae* observed by Tycho and Kepler four centuries ago, so bright that they could be seen with the naked eye, were in reality supernovae located within our own Galaxy.

Our understanding of the nature of supernovae (SNe) has improved greatly over the last decades. We know that they are violent, explosive events that mark the death of certain stars, making them shine more brightly than their host galaxies for a few months. Supernovae have an enormous importance in what is sometimes called the 'ecology of galaxies', because they are the sites where most of the elements heavier than oxygen are produced. These elements are ejected to the interstellar medium by the explosion, where they are mixed with the gas that will give birth to the next generation of stars. Life as we know it would not be possible if the material that formed the solar system had not been enriched with the heavy elements synthesized in supernovae that exploded billions and billions of years ago. Little did Tycho know, on that cold November night in 1572, that he was witnessing the transmutation of the elements that he had been trying to achieve in his laboratory. The philosopher's stone of the alchemists was beyond his grasp, thousands of light years away, among the stars in the sky.

1.2   Type Ia supernovae: the cosmic yardstick

More recently, a special property of a subclass of supernovae has put these objects at the heart of one of the most important scientific breakthroughs of the past decade. The so called Type Ia supernovae have remarkably uniform peak magnitudes and light curves that enable, after some manipulation, to calculate the distance to the supernova from its apparent brightness. Since supernovae are bright enough to be observed at enormous distances, this means that they can be used as 'standard candles' to measure cosmic length scales. The further away in space an object is, the further back in time it is seen due to the finite speed of light, so these distant supernovae bear the imprint of how the expansion of our universe has evolved from the Big Bang to the present epoch. The shocking result that this expansion is being *accelerated* was published almost simultaneously by two groups in 1998 (Riess et al., 1998; Perlmutter et al., 1999). This discovery has revolutionized our understanding of the basic interactions of nature and the structure of the universe. In order to reconcile an accelerated cosmic expansion with the theory of general relativity, a 'cosmological constant' has to be introduced in Einstein's equations. This 'constant' represents a mysterious repulsive force that acts alongside the familiar force of gravity, and counteracts the tendency of the matter in the universe to slow down its expansion. The implications of this discovery are still being debated, but no physical cause has been found yet that can explain this hitherto unknown force.

It is precisely because of the spectacular conclusions that have been drawn from the properties of Type Ia supernovae that our failure to understand the details of the process which originates them is so disturbing. It has been known for some time that these supernovae are the result of the explosion of white dwarfs formed mainly of carbon and oxygen, which are destabilized somehow by accreting material from a companion star. Once it becomes unstable, the carbon inside the white dwarf ignites and burns, liberating enough energy to unbind the star and produce the supernova explosion. Thus, thermonuclear combustion is the source of energy for Type Ia SNe, in contrast with Type II, Ib and Ic SNe, which are produced by the gravitational collapse of the cores of massive stars. Even though this picture for the origin of Type Ia SNe is almost certainly correct, at least for a majority of them, fundamental issues such as the mass of the white dwarf at the moment of the explosion, the location of the ignition and the propagation mode of the burning front have not been established yet. A number of theoretical models or paradigms are capable of reproducing with reasonable accuracy the most fundamental physical properties of Type Ia SNe. However, the details of the composition and structure of the ejected material are

different for each of these paradigms, and there is an active debate about which of them is ultimately responsible for the explosion of Type Ia supernovae. Until this controversy is closed and these objects are understood completely, the use of their peak magnitudes and light curves as distance indicators will lack a solid theoretical foundation.

In this context, it is specially important to look for ways to constrain the structure and composition of the ejecta in order to discriminate between the contending explosion paradigms for Type Ia SNe. Light curves and optical spectra have usually been the primary source of these constraints, and considerable effort has been made to establish connections between the spectral evolution of the supernovae and the chemical composition profile of the ejecta. Even though much has been learned from the modeling of optical spectra, this technique has limitations that do not allow to reach a definitive conclusion as to what mechanism or mechanisms operate in the explosion. An alternative method, the study of the γ-ray emission from Type Ia SNe, has been much less successful, mostly due to the difficulty in performing the required observations. As a result, our knowledge of these objects is still far from being complete, and it has become imperative to search for new sources of information that can shed some light on the detailed workings of thermonuclear supernovae.

1.3 Raising the dead

If a telescope is pointed to the location in Cassiopeia that Tycho Brahe recorded so carefully with his naked eye, there is not much to see, other than a few very faint filaments of red light from hydrogen. However, the extraordinary development of astronomy in the last half of the twentieth century has opened new windows to the universe that allow to go beyond these disappointing optical filaments. At radio and X-ray wavelengths, a bright, bubble-shaped nebula can be seen at the location of the supernova of 1572. This nebula is known as the supernova remnant (SNR) of Tycho.

Supernova remnants are the aftermath of supernova explosions. Due to the titanic energies liberated in the explosion, the material ejected by supernovae moves at very high velocities. As the ejecta encounter the ambient medium (AM) surrounding the supernova progenitor system, they are slowed down, and supersonic shock waves are formed which heat the gas to temperatures of several millions of degrees. This hot plasma is a bright source of thermal X-rays, with a spectrum that often displays strong emission lines from the heavy elements present in the shocked material. In this way, hundreds of years after the death of the progenitor star, the chemical composition of the ejecta is revealed once again by the shock waves in the supernova remnant. The present generation of X-ray astronomical satellites, led by *Chandra* and *XMM-Newton*, has performed a large number of observations of SNRs with an unprecedented level of spatial and spectral resolution. In many cases, the signature of the supernova ejecta can be seen clearly in the X-ray spectrum of the SNR. Given the excellent quality of these observations, it is rather surprising that they have not been applied extensively to constrain the theoretical ejecta models for either core collapse or thermonuclear supernovae.

The main reason for this is that the X-ray spectra of SNRs are very difficult to analyze. The interaction with the AM that heats the ejecta to X-ray emitting temperatures also results in a complex physical state of the plasma, which is usually out of thermal and ionization equilibrium. In order to model the emitted spectrum, this physical state of the shocked plasma must be known with some accuracy, and this requires a careful study of the ejecta-AM interactions that lead to it. In other words, the information about the ejecta is encoded somehow in the X-ray spectrum of the SNR, but the tools to interpret this

spectrum do not exist, and without them, quantitative estimations about the structure of the ejecta cannot be made. The lack of adequate spectral models for the shocked ejecta in SNRs has become a serious problem in X-ray astronomy, to the point that, in many of the excellent available observations, the ejecta emission has not been analyzed with detail. This should be seen as an opportunity, rather than a problem, because much is to be gained by the development of such models.

1.4   Outline of the dissertation

The purpose of this dissertation is to explore the connection between thermonuclear supernovae and the thermal X-ray spectrum from the shocked ejecta in their supernova remnants. By developing the techniques to interpret this spectrum in terms of the structure and composition of the material synthesized in the supernova explosion, we hope to open new possibilities for the use of SNRs as constraints for theoretical supernova models. In this context, we aim to make valuable contributions to the fields of supernovae and supernova remnants, and to increase the relationship between them. In addition to the specific results that can be obtained from this effort, we expect to provide the community of X-ray astronomy with a set of useful tools for the spectral analysis of the ejecta in Type Ia SNRs.

Abundant introductory material about Type Ia supernovae, supernova remnants, X-ray spectra, spectral analysis and other relevant topics is provided in each chapter as it becomes necessary. Helpful reviews and books are referenced in the text, in case the reader's curiosity should extend beyond the issues directly connected with the present work. The stage is set in chapter 2 with a discussion of the state of the art in models for Type Ia SNe. A model grid representative of all the explosion mechanisms currently under debate is introduced and compared with other models for thermonuclear supernovae, including some of the most cited in the literature and a few examples of very recent 3D calculations. In chapter 3, the process of formation of supernova remnants is reviewed, together with the most important characteristics of their multi-wavelength emission, with an emphasis on the X-ray spectrum. The specific problems relevant to the connection between this X-ray spectrum and the structure of the ejecta in thermonuclear supernovae are outlined, and a modeling strategy is proposed. This strategy is based on following the ejecta-AM interaction with a hydrodynamic code coupled with simulations of the nonequilibrium ionization and heating processes in the shocked plasma. In order to ensure the maximum level of consistency, a considerable effort has been made to include all the relevant physics in these calculations. Significant differences are discovered in the plasma state of the shocked ejecta depending on the supernova explosion model and the density of the AM that it interacts with. In chapter 4, these simulations are taken one step further with the calculation of synthetic X-ray spectra that can be compared with the observations. The properties of these synthetic spectra are discussed, and it is found that the differences in the state of the shocked plasma lead to dramatically different emitted X-ray spectra, confirming the usefulness of SNRs as tools to discriminate between supernova explosion models. Several important issues are raised regarding the role that can be played by these synthetic spectra in the framework of the analysis techniques currently used in X-ray astronomy. In chapter 5, the spectral models are applied to the Tycho SNR, and some of the difficulties that are encountered in their use for the analysis of real X-ray data are pointed out. The imprint that the presupernova evolution of the progenitor systems has on the formation of Type Ia SNRs is discussed in chapter 6, and comparisons are made with the models that do not take this effect into account. The conclusions of this

dissertation and the possible lines for future work are presented in chapter 7. Finally, some important technical information concerning the tools and techniques that have been developed for or used in this work is provided in appendixes A, B and C.

Chapter 2

A model grid for thermonuclear SNe

'Yes, it will be a long time before people know what I know. How much of iron and other metal there is in the sun and the stars is easy to find out, but anything which exposes our swinishness is difficult, terribly difficult.'
Liev Nikolaievich Tolstoy (1828-1910), *The Kreutzer Sonata.*

2.1 Introduction: An overview of Type Ia SNe

2.1.1 Observations

Supernovae are classified on the basis of distinguishing features in their optical spectra. Formally, a supernova is Type Ia if its early spectrum lacks conspicuous lines of H but contains a prominent Si II absorption feature at about 6100 Å, blueshifted from 6355 Å (for the origins of the current classification scheme see Minkowski, 1941; Elias et al., 1985; and Branch, 1986). A striking feature of these objects is that most of them are quite homogeneous in terms of their spectra, light curve shapes and peak absolute magnitudes. These 'normal' events, sometimes referred to as 'Branch normal', undergo a characteristic spectral evolution, showing P Cygni-like lines of some ions of intermediate mass elements (IMEs) like Si II, Ca II, S II, O I and Mg II prior to and near maximum light, developing blends of P Cygni permitted Fe II lines shortly thereafter, and finally blends of forbidden emission lines of Fe and Co ions. The spectral evolution is so uniform, in fact, that the use of template spectra to determine the age of Type Ia SNe with respect to maximum light has become a common practice. The events that do not fit this description are classified as 'peculiar', and are a more heterogeneous group; the latest studies find an intrinsic peculiarity rate of $36\% \pm 9\%$, much larger than older estimates (Li et al., 2001[1]). Among the peculiar events, roughly 20% of all Type Ia SNe are brighter than usual, with weaker IME lines and prominent Fe III excitation features, while 16% are dimmer than usual and have stronger IME lines and a broad Ti II absorption trough around 4100 Å. These subclasses are known as '1991T-like' and '1991bg-like' objects, but given the heterogeneity of the samples it is hard to say how meaningful this classification is.

The Doppler broadening of the lines that appear in Type Ia SN spectra imply velocities of up to $30,000 \, \mathrm{km \cdot s^{-1}}$ for the fastest ejecta and a total kinetic energy of roughly

---

[1] This work is based on a volume-limited survey with a sample of only 45 SNe. See Branch, 2001, for a discussion.

10^{51}erg. The characteristic light curve of normal events has a rise time of about 20 days, a first epoch of fast decline after the maximum that lasts 50 days, and finally an exponential phase during which the decline rate matches very well the rate of the decay chain ^{56}Ni $\rightarrow^{56}$ Co $\rightarrow^{56}$ Fe. The fact that these nuclei are indeed responsible for the exponential decline of the light curve has been verified by direct observation of the decay process (Kuchner et al., 1994). There is also a well defined color evolution, with $B - V$ reddening from near 0.0 at maximum light to 1.0 about a month later. A significant correlation exists between luminosity and light curve shape: the slower, broader, light curves are intrinsically brighter at peak than the faster, narrower light curves (Barbon et al., 1973; Pskovskii, 1977; Branch, 1981; Branch, 1982; Phillips, 1993). This crucial property allows to re-normalize the luminosity of a given object using the shape of its light curve. Doing so yields a corrected peak absolute magnitude of

$$\mathcal{M}_B \approx \mathcal{M}_V \approx -19.30 \pm 0.03 + 5log(H_0/60) \tag{2.1}$$

with a dispersion of $\sigma_{\mathcal{M}} \leq 0.3$ (Hamuy et al., 1996). This low dispersion of the corrected value is what makes possible the use of Type Ia SNe as standard candles, but it is important to emphasize that it is based on the luminosity - light curve correlation, an observational property whose physical cause has not been identified yet (see the following section).

Type Ia SNe are the only supernovae that are found in all galactic types, including elliptical galaxies with no recent history of star formation. Statistical studies have found a correlation between the host galaxy and the photometric properties of the supernovae, with more luminous objects related to younger parent populations (Schmidt et al., 1998). In our own Galaxy, the estimated rate of Type Ia SNe is $4 \cdot 10^{-3}\,\mathrm{yr}^{-1}$ (Tammann et al., 1993).

For reviews of the observational properties of Type Ia SNe and their applications, see Branch and Khokhlov, 1995; Branch, 1998; and Leibundgut, 2000. A more complete vision, if somewhat outdated, of Type Ia SN research can be found in Ruiz-Lapuente et al., 1997.

2.1.2   Models: setting the scenarios

The considerable efforts made to identify the physical mechanism or mechanisms responsible for Type Ia SNe have only been partially successful so far. Theoretical scenarios should be able to reproduce both the homogeneity of these objects and the diversity within their homogeneity. A fully satisfactory model has not been found yet, but there is a general agreement that Type Ia SNe are the result of the thermonuclear explosions of carbon and oxygen white dwarfs (CO WDs; Hoyle and Fowler, 1960). The chain of events leading to the supernova starts when a CO WD in a close binary system is destabilized due to accretion from its companion. As a result of the destabilization, the temperature of the degenerate material rises to a critical value and ignites, creating a nuclear burning front that propagates through the star. Enough energy is released by the nuclear burning to both unbind the WD and deposit roughly 10^{51} erg of kinetic energy in the ejecta (see Branch and Khokhlov, 1995, and references therein). Such explosions would produce mostly ^{56}Ni and, depending on the conditions, varying amounts of intermediate mass elements (Si, S, Ca), but no H, in agreement with the features present in the optical spectra. The light curve decline rate, required energy budget and minimum inferred progenitor age are also consistent with the observational constraints, but this picture poses several problems:

Progenitor systems. The immediate binary progenitors of Type Ia SNe have not been identified yet. There are two possible ways for the WD to accrete material: from a companion WD (double-degenerate scenario, DD) or from a non-degenerate star (single-degenerate scenario, SD). For SD systems, the companion could be either a slightly evolved main sequence or subgiant star (supersoft systems, Hachisu et al., 1999b) or a low mass red giant (symbiotic systems, Hachisu et al., 1999a). The nature of the companion is particularly important because it determines the rate of accretion and composition of the material that falls on top of the WD, and might have an impact on the shaping of the circumstellar medium (CSM) around the progenitor (see chapter 6 for a more detailed discussion on progenitor systems)

Ignition conditions. For a long time, it was thought that the only way to destabilize a WD was to drive it very close to the Chandrasekhar mass ($M_{Ch} \simeq 1.4\,M_\odot$), the limit over which the pressure of the degenerate electron gas is unable to support the star. In Iben and Tutukov, 1984, an alternative was suggested: the ignition of an accreted He layer on top of a sub-Chandrasekhar WD. In the so called sub-Chandrasekhar scenario (sub-Ch), a shock wave propagates inward from the burnt He layer, heats the material at the WD core and triggers a secondary ignition that unbinds the star. Thus, the primary ignition may happen at the core of a Ch WD or at the accreted He layer of a sub-Ch WD, and these two kinds of models are sometimes known as Carbon ignitors and He ignitors, respectively. In either case the transition from the hydrostatic to the hydrodynamic phase is poorly understood, but it seems clear that the number and location of hot spots which trigger the runaway is important for the outcome of the explosion (Höflich and Stein, 2002; García-Senz et al., 1999; García-Senz and Bravo, 2004).

Burning front propagation. Following the ignition of one or many hot spots, the propagation of the burning front can either be driven by heat diffusion at subsonic speeds (deflagration) or by a strong shock at supersonic speeds (detonation). This is a crucial issue, because the elements synthesized in the nuclear burning depend on the density at which the reactions take place and hence on whether the fuel has been able to expand before being reached by the burning front. Burning at high densities usually allows for nuclear statistic equilibrium (NSE) to set in, the main product of which is ^{56}Ni, while burning at lower densities produces more intermediate mass elements. The prompt detonation of the whole WD would burn most of its mass to ^{56}Ni, but this possibility can be discarded as an explosion mechanism due to the lack of intermediate mass elements in the ejecta (Arnett, 1969). Only two options remain: either the burning front propagates as a deflagration through the whole star (Nomoto et al., 1984) or the flame undergoes a transition to a detonation at some point, in what is known as the delayed detonation scenario (Khokhlov, 1991). There is a variation of the delayed detonation scenario, the pulsating delayed detonation, in which the detonation is originated only after the WD has pulsated, following a deflagration phase that fails to unbind it (see section 2.3 for details and examples).

In Branch et al., 1995, it is argued that certain types of SD-Ch systems are the 'best bets' for Type Ia SN progenitors, a point of view that is shared by a majority of the SN community at the time of writing this work (2004). Double degenerate models are discarded on the grounds that they seem to lead to accretion-induced collapse (AIC) rather than to Type Ia SN (Segretain et al., 1997; Guerrero, 2001). Of the SD systems, it has been shown that Sub-Ch explosion models produce light curves and spectra that do not agree with observations of normal Type Ia SNe (Höflich and Khokhlov, 1996). Still, some researchers claim that the white dwarf in a SD-Ch system would be unable to grow

quietly to attain the Chandrasekhar mass by accretion from a non-degenerate companion (Cassisi et al., 1998). Until a fully self-consistent evolutionary path is found for the WD in SD systems to grow to the Chandrasekhar mass, this will remain an open issue.

Even if it is assumed that SD-Ch systems are indeed the progenitors of Type Ia SNe, the outcome of the thermonuclear burning of a Chandrasekhar mass CO WD is still uncertain. A key issue is that deflagrations in a gravitational field are inherently turbulent, and they can only be studied properly with 3D simulations. But the need to couple 3D hydrodynamics, energy transport, a degenerate equation of state and explosive nucleosynthesis poses one of the most formidable computational problems in modern physics (see section 2.4). The length scales of the burning front structure differ by many orders of magnitude from those of the WD, whose temperature and density gradients regulate the front propagation, and the need for subgrid-scale models arises to deal with important microphysical processes. The vast majority of the theoretical models available today are still 1D calculations where the nucleosynthetic output depends on parametrized schemes to resolve the flame propagation.

In order to constrain explosion models, many attempts have been made to correlate Type Ia SN spectra to the detailed ejecta structure obtained in theoretical calculations. The observed spectral evolution implies that O, Si, S and Ca are present in the outer, high velocity layers of ejecta (from $8,000$ to $30,000\,\mathrm{km\,s^{-1}}$) and that the inner parts of the ejecta are rich in Fe-group elements, but more detailed information is difficult to extract from the spectra. This is mainly due to the complexity of the radiation transport calculations under nonlocal thermodynamic equilibrium conditions and the poor quality of the available opacities. An ejecta model can always be discarded if a particular element is absent in the model in a velocity range where it is detected in the observations. The inverse, however, is not true: an element that is present in the ejecta in a given velocity range might not be revealed in the observations due to the physical processes involved in spectra formation (Baron et al., 2003). Many synthetic spectra calculations seem to favor delayed detonation models (Fisher et al., 1997; Höflich et al., 1998; Wheeler et al., 1998), and some authors claim that these models provide a natural explanation for the luminosity - light curve correlation (Mazzali et al., 2001), but the debate is still open.

A complete review of Type Ia SN explosion models can be found in Hillebrandt and Niemeyer, 2000; see also sections VII and VIII in Ruiz-Lapuente et al., 1997, and chapters 9, 11 and 13 in Arnett, 1996.

2.2 A grid of one dimensional Type Ia SN explosion models

For an unbiased and meaningful comparison between different explosion mechanisms it is desirable that all the models be calculated consistently, i.e. with the same physics included in the same hydrodynamic and nucleosynthetic codes. Even though such model grids exist in the literature (Höflich and Khokhlov, 1996; Iwamoto et al., 1999), it is impossible to have an adequate control over the physical aspects of the problem by using published models as 'black boxes'. With this requirement in mind, a grid of thermonuclear supernova explosion models has been computed in one dimension, assuming spherical symmetry. The hydrocode, the nucleosynthesis and the physics included (equation of state, nuclear reaction rates, etc) are described in Bravo et al., 1996. For each model, the explosion has been followed until 10^6 s after the ignition, when the expansion has reached a nearly homologous ($v \propto r$ everywhere) stage. The energy released in the radioactive decay of ^{56}Ni is taken into account in the supernova code by assuming that the gamma photons deposit their energy locally, which is a good approximation up to ~ 100 days (Basko,

1994). After 10^6 s, ^{56}Ni disintegration becomes dynamically irrelevant because: 1) most of it has already decayed to ^{56}Co, and 2) an increasing fraction of the energy of the photons escapes the supernova due to the drop in opacity caused by the expansion.

The parameters of all the models in the grid are given in Table 2.1, together with the calculated values for the bolometric magnitude at light curve maximum, $\mathcal{M}_{max}$, and the drop in bolometric magnitude 15 days after maximum, $\Delta\mathcal{M}_{15}$. The light curves were computed by I. Domínguez, who kindly provided the results shown in Table 2.1 (private communication, 2003). The density and chemical composition profiles as a function of Lagrangian mass coordinate can be found in Figures 2.1 and 2.2 for a sample subgrid. The composition is given after the decay of the isotopes whose half-life is shorter than one year, like ^{56}Ni. The density profiles as a function of radius and velocity are also provided in Figure 2.3. The different categories of SN Ia explosion models included in the grid are:

Pure detonation model (DET): In this class of models, the flame starts close to the center of the WD, and propagates supersonically nearly through the whole star, incinerating most of it to Fe-group elements (Fig. 2.1). As explained in section 2.1.2, this kind of models is ruled out by observations, and is merely included for comparison purposes. The model was obtained from a $\sim 1.38\,\mathrm{M}_\odot$ WD in hydrostatic equilibrium, composed of equal masses of ^{12}C and ^{16}O plus a 1% by mass of ^{22}Ne, whose internal energy structure was adjusted to an adiabatic thermal gradient. The central density ρ_c was $2 \cdot 10^9\,\mathrm{g} \cdot \mathrm{cm}^{-3}$.The ignition was initiated by incinerating the mass in the central layer, and afterwards the detonation propagation was obtained consistently by solving the hydrodynamic and nuclear evolutionary equations. Details of a similar model can be found in Bravo et al., 1996.

Sub-Chandrasekhar mass model (SCH): In this explosion paradigm, a He detonation is started at the edge of a helium envelope, which feeds a converging shock wave into the C-O core. Close to the center, the shock wave transforms into a C-O detonation which propagates outwards and processes the rest of the core. The example presented here was obtained from a WD formed by a C-O core of $\sim 0.8\,\mathrm{M}_\odot$ surrounded by a He envelope of $\sim 0.2\,\mathrm{M}_\odot$. This envelope was the result of He accretion over the C-O core at a steady rate of $3.5 \cdot 10^{-8}\mathrm{M}_\odot \cdot \mathrm{yr}^{-1}$. The hydrostatic evolution of the white dwarf subject to accretion was computed by J. José, who kindly provided the initial model for the SN explosion calculation (private communication, 2002). In this initial model, the temperature at the base of the He envelope was high enough to induce a spontaneous He detonation. The evolution past this point was followed with the supernova hydrocode. The explosion produces a sandwiched structure, rich in Fe-group elements both in the inner and in the outer parts of the ejecta (below a Lagrangian mass of $\sim 0.4\,\mathrm{M}_\odot$ and above $\sim 0.8\,\mathrm{M}_\odot$, in what was the He envelope), and rich in intermediate-mass elements plus C-O in between. In Figure 2.1, the 0.7-0.8 deficit in normalized abundance of the outer Fe-rich region is made up of leftover He from the He detonation, which is not shown on the plot.

Pure deflagration models (DEF): In these models the deflagration propagates at the laminar flame velocity (a small fraction of the sound velocity) close to the center, until the Rayleigh-Taylor instability develops, deforms the flame surface, and increases the flame mass consumption rate. The flame remains subsonic all the way and is quenched by expansion when its velocity becomes comparable to that of the material. The flame propagation velocity was obtained as the maximum between the laminar flame velocity (as

Model	Para-meter	ρ_{tr} $[\text{g}\cdot\text{cm}^{-3}]$	M_{ej} $[\text{M}_\odot]$	E_k $[10^{51}\text{erg}]$	$\mathcal{M}_{max}$ [mag]	$\Delta\mathcal{M}_{15}$ [mag]	M_{Fe} $[\text{M}_\odot]$	M_{C+O} $[\text{M}_\odot]$	M_{Si} $[\text{M}_\odot]$	M_S $[\text{M}_\odot]$	M_{Ar} $[\text{M}_\odot]$	M_{Ca} $[\text{M}_\odot]$
DET			1.38	1.59	-19.87	1.01	1.22	0.0003	0.008	0.0007	0.002	0.0002
SCH			0.97	1.01	-17.53	1.03	0.50	0.09	0.14	0.10	0.024	0.026
DEFa	0.06		1.37	0.51	-18.97	0.85	0.55	0.69	0.025	0.017	0.0038	0.0040
DEFb	0.08		1.37	0.64	-19.14	0.94	0.61	0.61	0.025	0.017	0.0040	0.0043
DEFc	0.10		1.37	0.74	-19.29	0.99	0.68	0.55	0.021	0.014	0.0032	0.0032
DEFd	0.12		1.37	0.80	-19.34	1.02	0.71	0.52	0.021	0.014	0.0032	0.0034
DEFe	0.14		1.37	0.81	-19.29	0.98	0.73	0.49	0.021	0.013	0.0029	0.0028
DEFf	0.16		1.37	0.84	-19.43	1.04	0.75	0.48	0.017	0.012	0.0028	0.0029
DDTa	0.03	$3.9\cdot10^7$	1.37	1.40	-19.73	1.11	1.03	0.04	0.087	0.071	0.019	0.022
DDTb	0.03	$2.6\cdot10^7$	1.37	1.36	-19.67	1.11	0.98	0.05	0.10	0.084	0.022	0.027
DDTbb	0.01	$2.5\cdot10^7$	1.37	1.31	-19.66	1.12	0.99	0.05	0.10	0.084	0.022	0.027
DDTc	0.03	$2.2\cdot10^7$	1.37	1.16	-19.51	1.11	0.80	0.12	0.17	0.13	0.033	0.038
DDTd	0.03	$1.5\cdot10^7$	1.37	1.08	-19.30	0.94	0.72	0.14	0.20	0.15	0.037	0.043
DDTe	0.03	$1.3\cdot10^7$	1.37	1.02	-19.00	0.94	0.56	0.19	0.25	0.19	0.046	0.054
PDDa	0.03	$4.4\cdot10^7$	1.37	1.45	-19.79	1.10	1.11	0.02	0.055	0.045	0.012	0.015
PDDb	0.03	$2.2\cdot10^7$	1.37	1.36	-19.72	1.14	1.04	0.03	0.085	0.070	0.018	0.022
PDDc	0.03	$1.5\cdot10^7$	1.37	1.25	-19.64	1.11	0.98	0.04	0.11	0.093	0.024	0.029
PDDd	0.03	$1.2\cdot10^7$	1.37	1.24	-19.53	1.04	0.89	0.05	0.15	0.13	0.034	0.041
PDDe	0.03	$7.7\cdot10^6$	1.37	1.12	-19.02	0.95	0.58	0.10	0.27	0.22	0.057	0.067

Table 2.1: Characteristics of the grid of explosion models. The parameter given in the first column is κ for the DEF models and ι for the DDT and PDD models.
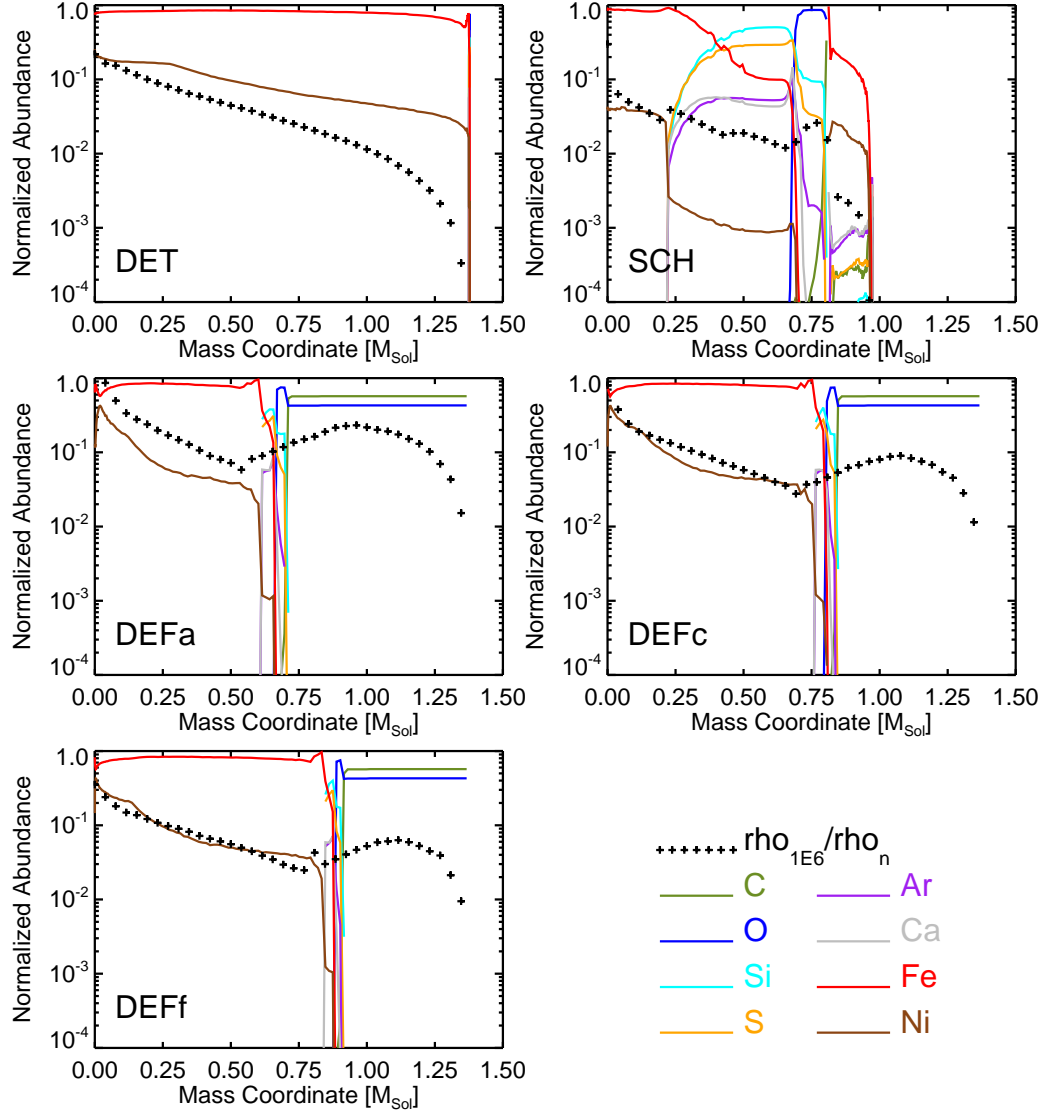
Figure 2.1: Density and chemical composition profiles for the sample DET, SCH and DEF models as a function of Lagrangian mass coordinate. The abundances are represented as number abundances after decay of all short lifetime isotopes. The density profiles at $t = 10^6$ s after the explosion have been normalized by $\rho_n = 10^{-11}\,\mathrm{g \cdot cm^{-3}}$ for visualization purposes.

given by Timmes and Woosley, 1992, and updated by Bravo and García-Senz, 1999) and the turbulent velocity, v_{RT}. The turbulent velocity was calculated as $v_{RT} = \kappa r_{fl}/\tau_{RT}$, where r_{fl} is the flame radius, τ_{RT} is the local Rayleigh-Taylor time scale at the flame location, and κ is a parameter given in Table 2.1 (see Bravo et al., 1996, for details). Furthermore, the mixing of matter and energy across the flame front was limited as proposed by Wheeler et al., 1987. In this formulation, the mixing is not allowed until the Rayleigh-Taylor front has propagated to a prescribed fraction, θ, of the mass of the shell (in all the deflagration models presented here, $\theta = 0.5$). Thus, the mixing was started when $\int_{t_0}^{t}(dM_{RT}/dt)dt = \theta\Delta M$, with ΔM the mass of the shell ahead of the flame front, t_0 the time of incineration of the last incinerated shell, and $dM_{RT}/dt = 4\pi r_{fl}^2\rho_{fl}v_{RT}$. Once this condition was fulfilled, the transfer of internal energy between the Rayleigh-Taylor unstable shells was allowed. Afterwards, the flame propagation was obtained consistently by the consequent increase in the nuclear energy generation rate and its feedback on temperature. At densities below a few times $10^7 \text{g} \cdot \text{cm}^{-3}$ the energy generated goes predominantly to create and maintain an electron-positron pair gas rather than to increase the temperature, which is the ultimate cause of the quenching of the flame. The initial configuration was an isothermal WD in hydrostatic equilibrium, with the same chemical composition and central density as that used in the DET model. The differences in the thermal structures of both configurations account for the small difference in total mass that can be seen in Table 2.1. Explosion models starting from different central densities (i.e. WD masses) do not produce substantially different energies or light curves (with the exception of a slight decrease of ^{56}Ni yield with increasing central density due to a larger electron capture rate, Bravo et al., 1993), so variations in ρ_c were not considered.

Six pure deflagration models were calculated with different values of κ. In each case, the flame quenches at different Lagrangian coordinates, ranging from $\sim 0.7\,\text{M}_\odot$ for model DEFa (the slowest flame and hence the earliest quench) to $\sim 0.9\,\text{M}_\odot$ for model DEFf (the fastest flame). A narrow ($\sim 0.1\,\text{M}_\odot$ wide) region rich in intermediate mass elements is formed at the quenching flame front in all the models, followed by a bump in the density profile due to the sudden termination of nuclear energy generation. A large mass of unburnt C-O is ejected in the outer layers. Note that these models do not present intermediate mass elements at high velocities, and therefore are not in agreement with optical spectra from Type Ia SNe.

Delayed detonation models (DDT): In these models the flame was propagated initially as a deflagration. In that phase, the flame velocity was taken as a constant fraction, ι, of the local sound velocity (see Table 2.1). As the flame traveled through lower densities, the sound velocity and hence the deflagration speed decreased, and the flame was eventually quenched. Afterwards, the flame front was artificially accelerated to a large fraction of the sound speed. Following this fast propagation through a few mass shells (typically 2-3 shells were enough) a detonation formed and burned the rest of the star. The location of the transition is determined by the parameter ρ_{tr}(Tab. 2.1), the density ahead of the flame at which the sudden acceleration is imposed.

Six DDT models were calculated, five of them with $\iota = 0.03$ and different values of ρ_{tr} and one, DDTbb, with a lower value of ι (see Tab. 2.1). The differences produced by the change of ι were minor. The transition from deflagration to detonation happens around a Lagrangian mass of $0.2\,\text{M}_\odot$ in all cases, where its imprint on the density profile can be seen (Fig. 2.2). For the model with the highest ρ_{tr}, DDTa, the chemical structure is dominated by Fe-group elements up to $\sim 1.0\,\text{M}_\odot$. At that point the flame density was too low to incinerate matter to NSE, and a buffer of intermediate mass elements was created, with

a thin region at the top dominated by oxygen. For DDTc and DDTe, which have lower values of ρ_{tr}, the regions dominated by intermediate elements and O are much larger.

Pulsating delayed detonation models (PDD): These models differ conceptually from delayed detonation models in that the transition to detonation is induced only after the white dwarf has pulsed. The pulsation is due to the inefficient burning produced by a slow deflagration, which is unable to rise the whole energy of the white dwarf (gravitational + internal + kinetic) above zero. The deflagration is propagated initially as in the DDT models, but once the flame quenches, the rate of energy generation drops to zero and the WD recollapses. The shock wave driven by this recollapse triggers the detonation that eventually unbinds the star.

Five PDD models were calculated with different values of ρ_{tr}. The chemical composition profiles obtained are very similar to those of the DDT models, but the different hydrodynamical histories of the models are reflected in their density profiles (see Fig 2.3). At the time of the transition, the density of the external layers of the PDD models was on average about two orders of magnitude lower than in the DDT models. As a result, the PDD models display low density tail in the outer parts of the ejecta, but the density profile gradient is steeper at lower radii.

As a concluding remark on the model grid, it is appropriate to emphasize the tight correlation that exists between chemical composition, density profiles, and kinetic energy of the ejecta in all models. This is an important feature of self-consistently calculated models for thermonuclear supernovae, and arises naturally as a consequence of the same process being responsible for all these characteristics: the propagation of the combustion front. In this respect, thermonuclear supernovae are clearly different from core-collapse supernovae, in which the composition is not correlated with the dynamic output of the explosion. A partial description of this model grid was published in Badenes et al., 2003.

2.3 One dimensional models outside the grid

The model grid presented in the previous section carries out a thorough exploration of the parameter space for theoretical Type Ia explosion calculations, with consistency between different models guaranteed by the fact that all of them have been calculated with the same code. Given the diversity of codes used by the community, however, it is advisable to include models from other sources, both for comparison purposes and as a means to verify the results that can be obtained by the grid. Two 1D models calculated by other groups have been incorporated (see Figures 2.4 and 2.5, and Table 2.2 for their characteristics):

The W7 model: This classic pure deflagration model is described in Nomoto et al., 1984, and it is arguably the most popular Type Ia SN model ever published. Synthetic spectrum calculations of various levels of complexity have shown that model W7 or slightly modified versions of it can reproduce with a reasonable degree of accuracy the optical spectra of normal Type Ia SNe (see Lentz et al., 2001, for a recent work with a discussion of the limitations of W7). The model was constructed by varying the speed of the burning front until the desired nucleosynthetic output was obtained, and in that sense it is different from the DEF models of the grid, whose burning front speeds are calculated using a more physical scheme. The chemical composition profile after short half-life decays is in fact more similar to that of the DDT and PDD models in the grid than to the DEF models, because this parametrized burning front speed turns out to be quite large (W7 is sometimes
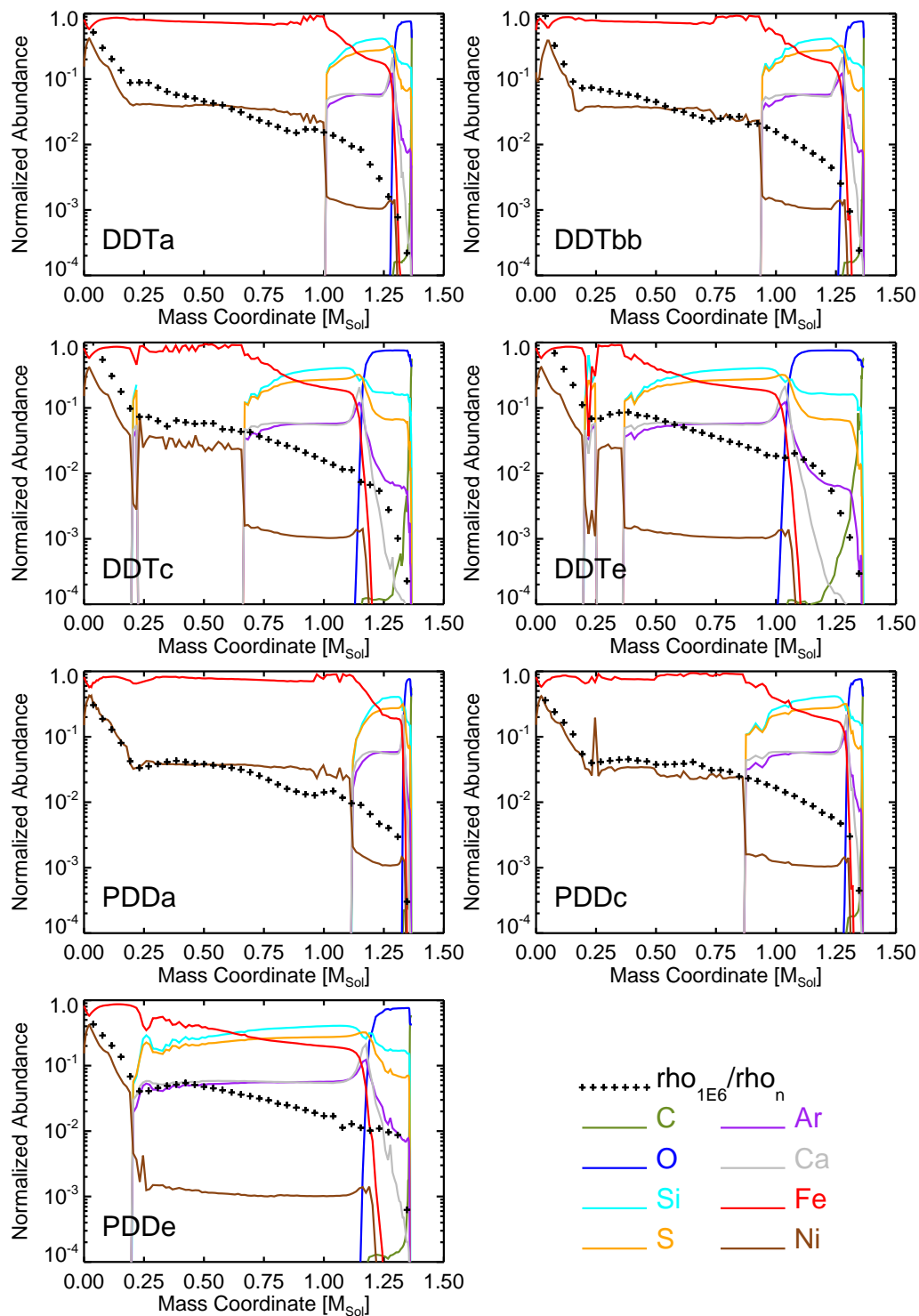
Figure 2.2: Density and chemical composition profiles for the sample DDT and PDD models as a function of Lagrangian mass coordinate. Magnitudes and normalization are as in Figure 2.1.
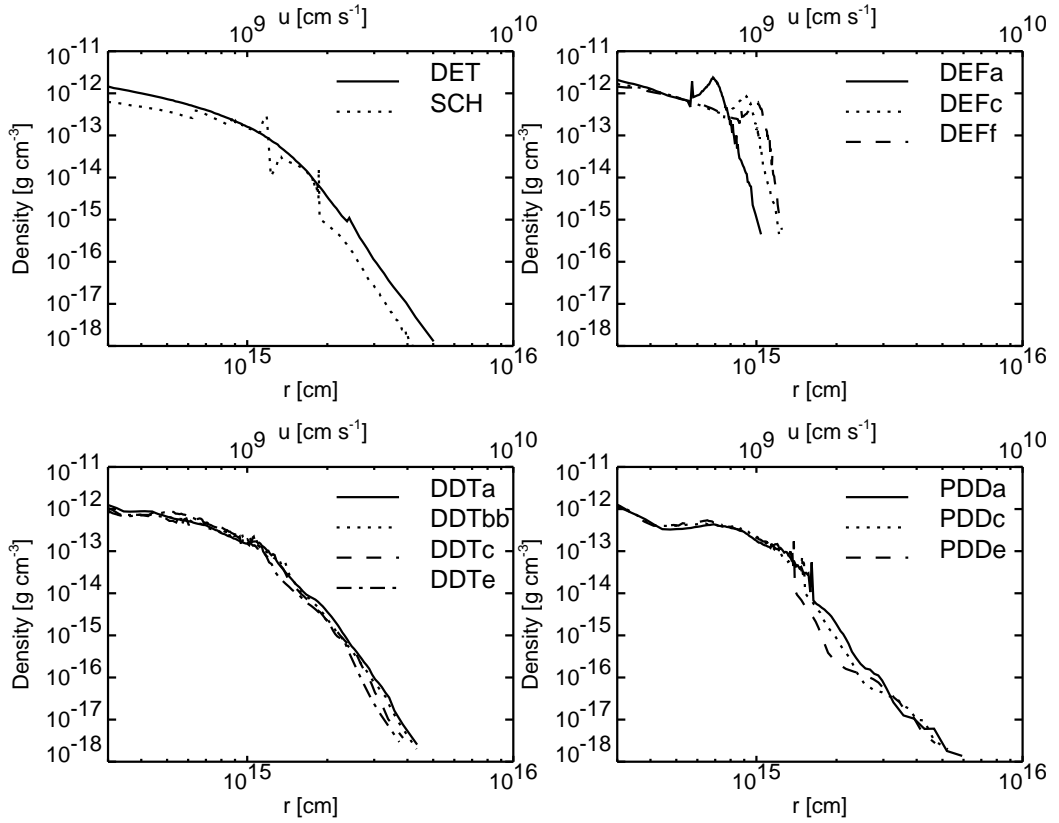
Figure 2.3: Density profiles at $t = 10^6$ s after the explosion for the sample models as a function of radius and velocity.

known as a 'fast' deflagration). The density profile presented in Figures 2.4 and 2.5 was produced by homologous expansion to $t = 10^6$ s of the profile at $t = 20$ s after the explosion. Note that by doing this, the effect of the energy deposition due to the decay of ^{56}Ni on the density profile is neglected, a detail that has to be taken into account when comparing it to other models. The W7 model was kindly provided by K. Nomoto (private communication, may 2003).

The 5p0z22.25 model: This delayed detonation model is described in Höflich et al., 2002. It is calculated with a resolution about four times greater than that of the grid models, and assuming a different initial configuration for the WD. The model was provided at $t = 10^6$ s after the explosion, so the density profile includes most of the effect of ^{56}Ni decay. The main difference with the other DDT models of the grid is the presence of a substantial amount of Mg in the outer ejecta layers of ejecta dominated by O (Mg is not not shown in Figure 2.4). The 5p0z22.25 model was kindly provided by P. Höflich (private communication, October 2003).

Model	M_{ej} $[M_\odot]$	E_k $[10^{51}erg]$	M_{Fe} $[M_\odot]$	M_{C+O} $[M_\odot]$	M_{Si} $[M_\odot]$	M_S $[M_\odot]$	M_{Ar} $[M_\odot]$	M_{Ca} $[M_\odot]$
W7	1.38	1.17	0.73	0.19	0.15	0.087	0.016	0.012
5p0z22.25	1.38	1.20	0.74	0.07	0.22	0.12	0.025	0.025
DEF3D30b	1.37	0.42	0.53	0.66	0.045	0.011	0.0019	0.0017
DDT3Da	1.37	0.78	0.76	0.38	0.063	0.027	0.0066	0.0072
SCH3DOP	1.02	1.14	0.58	0.23	0.064	0.035	0.0093	0.0077
SCH3DMP	1.02	1.19	0.67	0.07	0.081	0.054	0.019	0.017
b30_3d_768	1.39	0.54	0.50	0.65	0.05	0.02	0.005	0.004

Table 2.2: Characteristics of the explosion models outside of the grid.

2.4   Three dimensional models

The first three dimensional calculations of Type Ia SN explosions have just begun to appear in the literature (Reinecke et al., 2002; Gamezo et al., 2003; García-Senz and Bravo, 2004). Even though it is clear that the future of Type Ia SN models lies in 3D calculations, these new results need to be considered carefully. A common feature of all the published 3D models, and the most remarkable difference with respect to 1D models, is the uniform mixing of unburnt C and O material with ^{56}Ni and the other products of nuclear burning throughout the ejecta. In Gamezo et al., 2003, it was pointed out that the lack of evidence for low-velocity C and O in the optical spectra of Type Ia SNe was in apparent contradiction with the nucleosynthetic output of 3D deflagration models. This argument is being revised (Baron et al., 2003), but there are many other clues from SN and SNR observations that favor a stratified ejecta composition for Type Ia SNe. Until these issues are clarified, a shade of doubt is cast on the validity of 3D models.

Another important question has been brought up by the recent detection of polarization in the spectra of two Type Ia SN. A normal Type Ia SN, SN2001el, presented an intrinsic polarization level of $\sim 0.3\%$ (Wang et al., 2003; Kasen et al., 2003), while a subluminous one, SN1999by, had an intrinsic polarization level of $\sim 0.7\%$ (Howell et al., 2001). These polarimetric observations can only be explained if there is some degree of asphericity in the supernova ejecta, but it is not clear whether this asphericity is related to the dynamics of the explosion itself or to the interaction of the ejecta with the binary companion of the WD in the progenitor system (see Kasen et al., 2004, for a discussion). So far, no hint of a significant asphericity in the ejecta has appeared in any of the published 3D explosion calculations.

Five one-dimensional mappings of 3D models have been incorporated to the grid. Given the current status of this kind of models, they are merely presented for comparison purposes, and no attempt will be made to explain the technical details involved in their calculation. Four of the models (DEF3D30b, DDT3Da, SCH3DOP and SCH3DMP) have been obtained with the SPH nucleosynthetic code described in García-Senz et al., 1998. Model DEF3D30b is a 3D deflagration initiated by the ignition of 30 hot bubbles at the core of the WD. Model DDT3Da is a 3D version of the delayed detonation scenario, with an artificial induction of the deflagration-detonation transition. In those regions where the turbulent flame resulting from the deflagration phase is well described by a fractal surface of dimension larger than 2.5, a detonation is induced. Models SCH3DOP and SCH3DMP are sub-Chandrasekhar explosions in which the He layer on top of the WD is ignited at

Figure 2.4: Density and chemical composition profiles for the models outside the grid as a function of Lagrangian mass co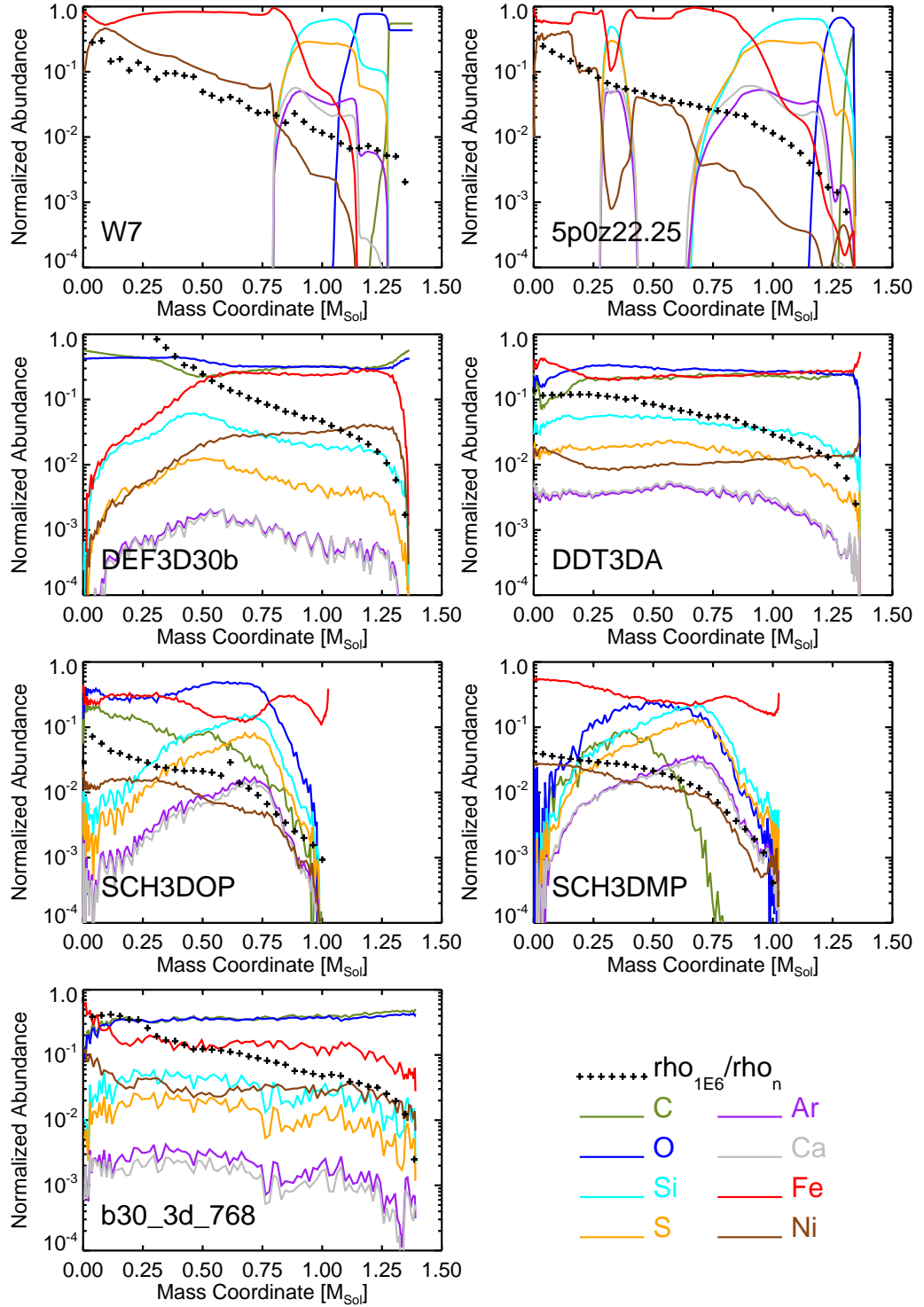ordinate. Magnitudes and normalization are as in figure 2.1. Except in the case of model 5p0z22.25, the density profiles have been obtained by homologous expansion from a few seconds after the explosion.
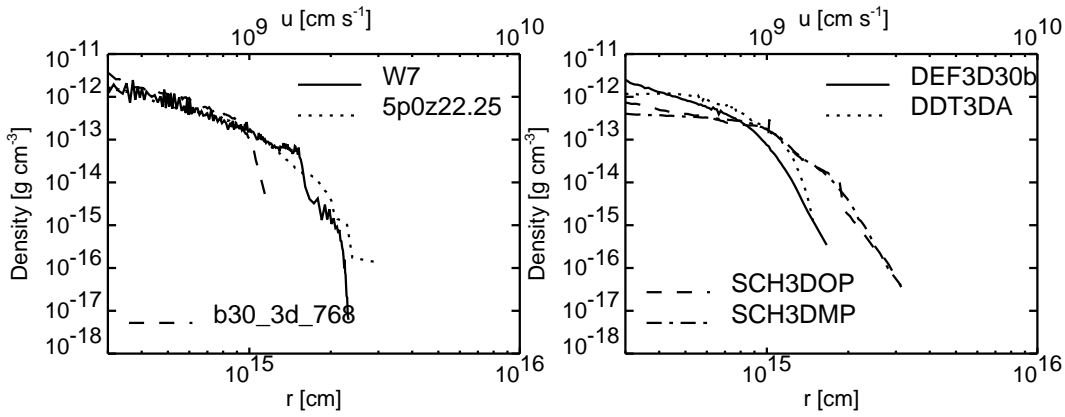
Figure 2.5: Density profiles at $t = 10^6 s$ after the explosion for the models outside the grid as a function of radius and velocity. Except in the case of model 5p0z22.25, the profiles have been obtained by homologous expansion from a few seconds after the explosion.

one and five points, respectively (García-Senz et al., 1999). The fifth model, b30_3d_768, is a deflagration that has been obtained with the code described in Reinecke et al., 2002, and has been kindly provided by C. Travaglio and W. Hillebrandt (private communication, November 2003).

The characteristics of the 3D models are presented in Table 2.2, and their composition and density profiles in Figures 2.4 and 2.5. The SCH models still retain a certain degree of stratification, but for the others, it is easy to appreciate the high degree of mixing in the ejecta. There is a considerable amount of material that remains unburnt, resulting in kinetic energies generally lower than those of 1D models. Model DEF3D30b has the peculiarity that in the inner $\sim 0.2\,M_\odot$ of the WD very little fuel is burnt, and therefore the amount of nuclear energy liberated is very small. As a consequence, this region is not ejected and remains behind at the center of the SNR (this is due to the buoyancy of the hot burnt bubbles, which are lit near the center but migrate very rapidly towards more external regions of the WD, see García-Senz and Bravo, 2004). None of the 3D models has been followed for a sufficient time to account for the effects of ^{56}Ni decay in the density profiles.

Chapter 3

From SN to SNR: dynamics and ionization structure

The motion of nature

is cyclic and returning.

Its way is to yield,

for to yield is to become.

Lao Tzu (ca. 600 BC), *Tao Te Ching.*

3.1 Introduction: An overview of SNRs

3.1.1 The life cycle of SNRs.

Supernova remnants are the result of the interaction of the material ejected in a supernova with the ambient medium (AM) that surrounds the supernova progenitor at the moment of the explosion. The release of roughly 10^{51} erg of kinetic energy into the AM has dramatic effects: the supersonic shock waves that are formed heat the progenitor's neighborhood, warp the galactic magnetic fields, accelerate particles to relativistic velocities and trigger star formation in dense gas clouds. Supernova remnants last for several tens of thousands of years, and emit radiation across virtually the entire electromagnetic spectrum. They play a central role in the dynamic and chemical evolution of galaxies, being responsible for distributing throughout the interstellar medium the heavy elements synthesized in SN explosions.

The simplified picture of the stages in the life of a SNR drawn by L. Woltjer more than 30 years ago (Woltjer, 1972), can still be used to set a framework for a more in-depth study:

Phase 0: Free expansion. From the point of view of fluid dynamics, the sudden irruption of the ejecta into the AM can be assimilated to the problem of a piston moving at constant velocity into a volume of gas initially at rest. This leads to the formation of a discontinuity, or shock wave, that propagates supersonically into the gas (see Zel'dovich and Razier, 1966, section I.2). At first, the expansion of the shock wave and the ejecta is not affected by the rarefied AM but eventually, as the shock sweeps a significant amount of mass, it begins to slow down and the likeness with the piston problem is lost. The duration of this phase depends on the amount of mass swept by the shock at any given

time, and hence on density structure of the AM. It can last anywhere from a few weeks to several years.

Phase I: Self-similar driven wave (reverse shock). As soon as the shock begins to slow down, the still freely expanding ejecta collide with the swept-up AM and a reverse shock is formed that starts traveling inward in a Lagrangian sense (McKee, 1974). The SNR develops a characteristic nested structure from the center outwards: freely expanding ejecta, reverse shock, shocked ejecta, contact discontinuity (CD) between ejecta and AM, shocked AM and forward shock expanding into the undisturbed AM. During this stage, both shock waves move at speeds of several thousand kilometers per second. The bulk kinetic energy is transformed into thermal energy and the plasma is heated to temperatures of several million degrees Kelvin, becoming a bright source of X-rays. Under these conditions, the shock waves are usually adiabatic, meaning that the energy radiated away by the shocked material has no impact on the dynamics of the SNR. If the density profiles of the ejecta and AM are approximated with a power law, the evolution during this stage can be analytically described by a self-similar driven wave solution (SSDW; Chevalier, 1982). This phase lasts up to a few thousand years after the explosion.

Phase II: Sedov-Taylor. Eventually, the reverse shock disappears after all the ejecta have been heated, and the motion of the forward shock tends to follow the law $R_{fwd} \propto t^{2/5}$. This is known as the Sedov-Taylor solution for a point explosion in a uniform medium (Sedov, 1959), and is characteristic of adiabatic structures whose total energy (kinetic + thermal) is constant. The mass swept up by the forward shock becomes much larger than the mass of the ejecta, the blast wave keeps slowing down and the signature of the explosion that gave birth to the SNR fades away and is lost. The forward shock can linger in this state for several thousands of years.

Phase III: Radiative snow-plow. When the speed of the forward shock drops below a few hundred kilometers per second, the temperature of the newly shocked material also becomes lower, shifting the peak emission from the X-rays to the ultra violet (UV) and even to the visible. At these wavelengths, energy is radiated away at a much more efficient rate, and the impact on the dynamics of the SNR becomes important. The shock wave is significantly decelerated and a thin, dense shell of radiatively cooled material forms behind it. The SNR is no longer expanding because of its kinetic energy, but rather driven by the pressure of the shocked gas in its interior, a mechanism referred to as pressure driven snow-plow.

Phase IV: Merging with the ISM. Finally, the shock wave becomes subsonic, most of the energy is radiated away and the SNR blends with the surrounding interstellar medium.

Despite being instructive, this picture is an oversimplification inadequate as a model for SNR dynamics. In a real case, neither the SN ejecta nor the AM are smooth, and the details of their structure can modify substantially the evolution of a given object. Any particular phase in Woltjer's scheme may be very brief or not happen at all, and objects that seem to be in the same phase might actually have very different ages. SNRs evolving in an AM modified by presupernova stellar winds, for instance, can become radiative at an early age. Local deviations from spherical symmetry are intrinsic to the dynamic evolution of SNRs, because the CD, where the flow of a fluid (the shocked ejecta) is slowed

by another fluid of lower density (the shocked AM), is subject to the Rayleigh-Taylor and other hydrodynamical instabilities. On a larger scale, the spherical symmetry can be broken by the structure of the ejecta or the AM, leading to different dynamic behaviors in different regions of the same SNR. A further complication arises in the case of some core collapse supernovae, which leave behind rapidly rotating neutron stars (pulsars) as stellar remnants. These pulsars modify the surrounding unshocked ejecta, creating the so-called 'pulsar wind nebulae' that can become more conspicuous than the SNR itself. In view of all these considerations, it is important to approach the study of SNRs with an open mind, and consider each object separately. The understandable tendency to classify individual SNRs according to common features in their morphology or emitted spectra can be misleading if individual characteristics are overlooked for the sake of generalization.

The number of known SNRs is uncertain, because faint or heavily obscured objects are sometimes difficult to identify as such. The standard reference for Galactic SNRs is the catalogue maintained by D. Green ; its most recent version (Green, 2004) contains 231 objects. Of these, at least 7 can be confidently associated with supernovae through historical records (see Table 3.1). There is also a small group of Galactic SNRs that are known to have ages of a few hundred years but have not been associated with any historical SN, like Cas A (G111.7-2.1). As of 1999, 38 supernova remnants were identified in the Large Magellanic Cloud (Williams, 1999), including the youngest known SNR, SN 1987A. Several surveys have identified a total of 16 SNRs in the Small Magellanic Cloud (see van der Heyden et al., 2003, and references therein). Many other objects have been identified in nearby galaxies, such as M31, NGC 7793, NGC 2403 and NGC 6946.

SNR Position [G.C.]	Alternative Name	SN [A.D.]	Observations
G315.4-2.3	RCW 86	185	China
G348.5+0.1 or G348.7+0.3	CTB 37 A or CTB 37 B	393	China
G327.6+14.6	SN1006	1006	Europe (at St.Gallen, Beneveto and other places), China, Japan, Korea, Arabs
G184.6-5.8	Crab Nebula	1054	China, Japan, Arabs
G130.7+3.1	3C58	1181	China, Japan
G120.1+1.4	Tycho	1572	Europe (by Tycho Brahe, Jerónimo Muñoz and others), China, Korea
G4.5+6.8	Kepler	1604	Europe (by Johannes Kepler and others), China, Korea

Table 3.1: Confirmed associations between Galactic SNRs and historical SNe. Data from Clark and Stephenson, 1977; and Green, 2004.

Supernova remnants are often classified according to their morphology at radio and X-ray wavelengths. Shell type remnants are essentially spherical, and they appear as ring-like structures due to limb brightening (examples: Tycho, SN1006). Objects that are dominated by pulsar wind nebulae and have a center-filled morphology are called plerionic SNRs (example: the Crab Nebula). Those that show a plerion in the X-rays and a shell at radio wavelengths are called composite remnants (example: G11.2-0.3). Finally, the remnants that appear as shells in the radio but are center-filled in the X-rays, without evidence for a pulsar wind nebula, are called mixed-morphology SNRs (example: IC443;

Rho and Petre, 1998). A more elaborate classification, with many examples is presented in Weiler and Sramek, 1988.

For an overview of SNR evolution, with interesting discussions of many relevant problems, see Jones et al., 1998. A complete review of the state of the art in SNR research, with a focus on young objects, can be found in Holt and Hwang, 2001.

3.1.2 Emission from SNRs as a tool for the study of Type Ia SN ejecta

Supernova remnants emit at radio, infrared (IR), optical, ultraviolet (UV), X-ray and gamma-ray wavelengths. The physical processes that give rise to this multi-wavelength spectrum can be divided in two categories: those that involve exclusively the interactions among the ions and electrons in the hot plasma between the forward and reverse shocks, and those that involve other types of interactions. The first group includes processes like bremsstrahlung, radiative recombination and collisional excitation. The second group includes synchrotron emission, inverse Compton scattering, nuclear decay lines from unstable isotopes and warm dust emission. A detailed review of all these emission processes is outside the scope of this work; the interested reader is referred to the standard textbook of Rybicki and Lightman (Rybicki and Lightman, 1985). For more specific discussions on SNR multi-wavelength spectra, see chapter 2 of Dyer, 2001; also selected papers in Holt and Hwang, 2001, specially Raymond, 2001; Arendt, 2001; Blair, 2001; Hwang, 2001; and Milne, 2001. As outlined in the introduction, our goal is to use Type Ia SNRs as tools to learn more about the structure and composition of the ejecta from thermonuclear SNe. This goal effectively constrains which among the possible observation targets and wavelengths offer the best prospects for success.

Regarding the targets, it is evident that the focus should be placed on young supernova remnants. In more evolved SNRs, the ejecta density keeps decreasing after the reverse shock disappears, and eventually the ejecta emission becomes too faint to be detected. But exactly how young is a young SNR? To some extent, it is a matter of personal choice when to classify a particular SNR as 'young', because, as noted in section 3.1.1, objects with similar ages might be in different evolutionary stages. In fact, there is no accurate way to determine the age of a SNR from its morphology or spectra, and the only SNRs with well known ages are those associated with historical SNe. For practical purposes, then, a young SNR is a SNR where it is possible to study the supernova ejecta, no matter what its actual age may be.

The wavelength to observe is also an easy choice. In young remnants, the shock waves usually move at several thousand kilometers per second and heat the material to X-ray emitting temperatures. Adiabatic expansion and radiative cooling will eventually lower this temperature, shifting the emission peak to UV or even optical wavelengths, but by the time this happens the SNR has usually evolved beyond the 'young' stage as defined above. In addition to being produced by virtually all of the shocked ejecta, X-ray emission is interesting because there are several prominent emission lines in the X-ray energy range which can reveal the presence of specific elements or ions in the emitting material. Present day X-ray observatories, like *Chandra* and *XMM-Newton*, provide excellent observing opportunities for SNRs, with ample capabilities for spatially resolved spectroscopy of extended objects. High quality observations of several young SNRs with distinct line emission from the shocked ejecta have been produced using these instruments (see Hwang, 2001; Ballet and Decourchelle, 2002; and Vink, 2004, for reviews, and Seward et al., 2004, for an on-line catalog of observations).

The X-ray spectrum of SNRs

The X-ray band extends from photon energies of 0.1 to beyond 10 keV. A complete description of all the processes that contribute to the formation of the X-ray spectrum of SNRs can be found in Longair, 1998; Mewe, 1998; and Raymond, 2001; here we will provide just a brief outline of the most relevant ones. Before that, however, a few words about the characterization of the ion and electron populations in the shocked plasma are in order. Diffusive acceleration mechanisms at the shocks can modify the thermal ion and electron energy distributions by contributing a high velocity tail to the Maxwellian cores, usually modeled with a power law. Another important characteristic of the shocked plasma in SNRs is the absence of thermal equilibrium between the Maxwellian cores of the ion and electron distributions. The dynamic adjustment of these temperatures over the lifetime of the SNR results in significant departures from ionization equilibrium and a generally underionized plasma. Nonthermal particle distributions, electron-ion thermal equilibration and nonequilibrium ionization are mentioned here because they are important for the following discussion, but they will be revisited with greater detail in section 3.4.

Bremsstrahlung Also known as free-free radiation, it is produced when an electron collides with an ion and is deflected from its path. The emitted spectrum has constant intensity up to a cutoff that depends on the electron velocity, and therefore on the electron velocity distribution. Bremsstrahlung from thermal electron distributions is usually the dominant contribution to the soft X-ray continua, and has a characteristic spectral shape $\propto T^{-1/2} \exp\left(-E/kT\right)$. When the electrons responsible for the emission come from the nonthermal tail of the energy distribution, the process is known as nonthermal bremsstrahlung, and it contributes to harder X-rays.

Collisional excitation Also known as bound-bound emission, it is produced when an interaction with another particle, usually an electron, excites an ion that then reverts to the ground state by emitting a photon of the appropriate energy. Since the final and initial energy levels are quantized, the emitted photons have discrete energies, and this emission mechanism generates lines instead of a continuum. As a consequence, it is possible to know the charge state and atomic number of the emitting ion from the photon energy. The brightest lines in the X-ray band involve the ions of elements with $Z \geq 6$ (C and beyond), which are excited by electrons with temperatures in excess of 10^6 K. At such high temperatures, most ions are stripped of all but one or two of their electrons, leading to H-like or He-like ions. X-ray lines are associated in line complexes when they become blended due to the limited spectral resolution of the instruments used to observe them. A list of selected lines and line blends at X-ray energies is given in Table 3.2, together with a short description of the usual spectroscopic notation.

Radiative recombination Also known as free-bound radiation: a free electron is captured into the bound state of an ion. This produces a continuum with emission edges, and recombination to excited states can result in emission lines. Its overall contribution to the spectrum is modest, specially in underionized plasmas like those in SNRs, but recombination emission can be important for the lines of He-like ions.

	Lines from H-like ions			Other lines		
Element	Ion	Notation	Energy [keV]	Ion	Notation	Energy [keV]
C	C^{+5}	C Lyβ	0.44	C^{+4}	C Heα	$0.30 - 0.31$
N	N^{+6}	N Lyα N Lyβ	0.50 0.59	N^{+5}	N Heα	$0.42 - 0.43$
O	O^{+7}	O Lyα O Lyβ	0.65 0.77	O^{+6}	O Heα	$0.56 - 0.57$
Ne	Ne^{+9}	Ne Lyα Ne Lyβ	1.0 1.2	Ne^{+8}	Ne Heα	$0.91 - 0.92$
Mg	Mg^{+11}	Mg Lyβ	1.7	Mg^{+10}	Mg Heα	$1.33 - 1.35$
Si	Si^{+13}	Si Lyα	2.0	Si^{+12}	Si Heα Si Heβ Si Heγ	$1.84 - 1.86$ 2.18 2.29
S	S^{+15}	S Lyα	2.6	S^{+14}	S Heα S Heβ S Heγ	2.43-2.46 2.87 3.03
Ar	Ar^{+17}	Ar Ly α	3.3	Ar^{+16}	Ar Heα Ar Heβ Ar Heγ	3.11-3.14 3.69 3.88
Ca	Ca^{+19}	Ca Ly α	4.1	several Ca^{+18}	Ca Kα Ca Heα Ca Heβ	3.69 3.86-3.90 4.59
Fe	Fe^{+25}	Fe Ly α	7.0	several Fe^{+24}	Fe Kα Fe Heα	6.40 6.63-6.70
Ni	Ni^{+27}	Ni Ly α	8.1	several Ni^{+26}	Ni Kα Ni Heα	7.48 7.75-7.80

Table 3.2: Selected X-ray lines common in SNRs. Lines for transitions in H-like ions to the $n = 1$ level are called Lyman lines (Lyα if the transition is from level $n = 2$, Lyβ if it is from $n = 3$, Lyγ if it is from $n = 4$). In He-like ions, the α, β and γ notation is retained for $n = 2$ to $n = 1$, $n = 3$ to $n = 1$, and $n = 4$ to $n = 1$ transitions, but Heα is actually a blend of four lines (one resonance, two intercombination and one forbidden). Formally, the notation Kα refers to all lines related to $n = 2$ to $n = 1$ transitions in multielectron ions, including He-like ions. The Kα lines listed here correspond to the $n = 2$ to $n = 1$ transitions in neutral atoms, which often have associated lines from several other ions. In the remainder of the text, the Kα notation will be used to refer to lines from all $n = 2$ to $n = 1$ transitions *excluding* those from He-like ions. Data from Kaastra, 1998.

Dielectronic recombination   This is the capture of a free electron into a doubly excited ion state through simultaneous excitation of a bound electron. It is primarily important for determining the plasma ionization state, but it also produces satellites to resonance lines of some ions (He-like ions in particular). As with radiative recombination, its contribution is diminished in underionized plasmas.

Synchrotron emission.   Charged particles in a magnetic field move in curved trajectories, circling the field lines due to the Lorentz force. If the particles are relativistic electrons, the radiation emitted due to the charge acceleration is called synchrotron radiation. In SNRs, the electrons can be accelerated to relativistic energies at the shocks,

which also compress the ambient magnetic field, providing an ideal setting for the production of synchrotron radiation. The pulsar wind nebulae in the interior of some core collapse SNRs are also sources of synchrotron radiation. The emitted spectrum depends on the strength of the magnetic field and the properties of the particle energy distribution, and spans over a wide range of wavelengths. In SNRs, synchrotron emission is important at radio wavelengths and in the hard X-rays, extending to TeV gamma-rays. The radio emission is produced by the relativistic electrons from the nonthermal power law of the velocity distribution, while the X-ray emission comes from much more energetic (ultrarelativistic) electrons, where the power law begins to roll off. A detailed discussion of models for synchrotron emission in SNRs is given in Reynolds, 1998, and Dyer, 2001.

For our goal of learning about the ejecta structure and composition, the most interesting contribution to the X-ray spectrum of a SNR is obviously the line emission produced by collisional excitation. Careful analysis of the X-ray lines should provide valuable information about the elements present in the ejecta and their spatial distribution. Nevertheless, it would be a mistake to focus on the lines of the thermal X-ray spectrum from the shocked ejecta, consider them the 'signal' and treat the rest of the emission from the SNR as 'noise', a nuisance to be discarded. In order to study any part or aspect of an object as complex as a SNR, it is important to have a general picture that is as accurate as possible, a picture that has to be pieced together from all the wavelengths where the SNR emits appreciably. This issue shall be revisited in chapter 4.

The integrated X-ray spectrum obtained by *XMM-Newton* from the Tycho SNR (Figure 3.1) will serve as an illustrative example. This is the remnant of SN1572 (Table 3.1), and it is considered the prototypical Type Ia SNR. A discussion of this integrated spectrum and other details of the observation can be found in Decourchelle et al., 2001. Apart from minor features from Mg and O, the prominent emission lines are probably associated with ejecta emission from several ions of Si, S, Ar, Ca and Fe, all of which are common products of the models for Type Ia SNe (see chapter 2). The continuum that underlies the lines is a mixture of thermal emission (bremsstrahlung and radiative recombination) and nonthermal emission (probably synchrotron). Even though a spectrum like this contains a lot of information about the present state of the SNR, its relationship with the structure of the material ejected by the supernova that Tycho Brahe observed in 1572 is very complex, as we shall see. Tycho's SNR will be analyzed with some depth in chapter 5.

3.2 The SN - SNR connection challenge for thermonuclear supernovae

In astronomy, the methods and techniques used to analyze observational data are often as important as the data themselves. The standard analysis procedure in X-ray spectroscopy involves the fitting of parametric analytical models to the data sets. A maximum likelihood fit is produced by varying the model parameters to minimize the χ^2 function that serves as a statistical measure of the difference between model and data. The result is an estimate for the values of the model parameters, which should provide information about the physical conditions of the object under study. As a consequence of the systematic use of this technique, the spectral models have become filters through which all X-ray observations are analyzed. These filters are necessary to establish a relationship between the observed spectra and the physical properties of the emitting plasma, but great care must be taken not to confuse the actual data with the abstractions that are used to analyze them.
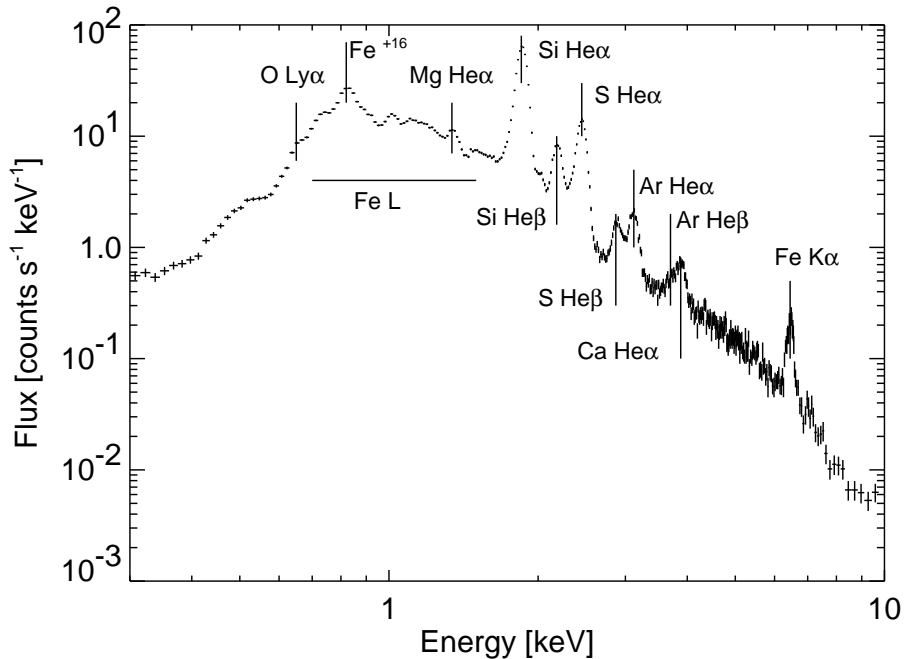
Figure 3.1: Integrated X-ray spectrum of a region of the Tycho SNR obtained by the *XMM-Newton* satellite. See Table 3.2 for details on the emission lines and section 5.3.1 for a discussion on how the spectrum was produced.

The analysis of SNR observations, and particularly the analysis of the ejecta emission in X-ray spectra like the one in Figure 3.1, poses many technical difficulties. Separating the contributions of the different emission mechanisms, for instance, is not an easy task. But the most important problem is that the properties of the shocked plasma in SNRs make the production of adequate spectral models specially difficult. These properties are related to the fact that the plasma has a very low density and is heated impulsively by the passage of the shock waves. This implies that the characteristic relaxation timescales for collisional processes are long compared to the age of the SNR, and the plasma is in a transient state, out of thermal and ionization equilibrium. In the case of the ejecta, this is further complicated by the chemical inhomogeneity and the dominant presence of heavy elements.

Unfortunately, the analysis tools presently available to SNR observers often make an inadequate treatment of these important issues. In order to produce useful spectral models, approximations have to be made; it is merely a question of whether the approximations still allow for a physically meaningful description of the plasma. Nowadays, even the most sophisticated models for the ejecta emission from SNRs that can be found in standard analysis packages like XSPEC (Arnaud, 1996) make fundamental oversimplifications that compromise their validity. The simplifications vary for each model, and range from planar shock geometry to self-similar dynamics and homogeneous composition profiles for the ejecta. These models generally fail to provide good fits to high resolution X-ray spectra of SNRs like Tycho.

The following sections will be devoted to study the physical processes involved in the generation of the thermal X-ray spectra from the ejecta through simulations of the hydrodynamic evolution (section 3.3) and the related nonequilibrium ionization and heating processes (section 3.4). These simulations will be used in chapter 4 to compute predicted spectra that can be compared with observations. A detailed discussion of the application

of these synthetic spectra to the quantitative analysis of X-ray observations of Type Ia SNRs and the prospects for the production of useful spectral models will be addressed in section 4.4.

3.3   Dynamic evolution of Type Ia SNRs

3.3.1   Simulation of young Type Ia SNRs with a 1D hydrodynamic code

The dynamic interaction between the SN ejecta and the AM surrounding the progenitor system is a complex issue. Some key processes in the evolution of young SNRs, like ejecta clumping or the development of Rayleigh-Taylor instabilities at the contact discontinuity can only be studied using multidimensional hydrodynamics (Chevalier et al., 1992; Wang and Chevalier, 2001). Other complications arise from the fact that, strictly speaking, SNRs do not remain adiabatic up to the radiative snow-plow stage. Deviations from adiabaticity can arise as a result of acceleration processes at the shock fronts that transfer part of the kinetic energy to particles that escape the SNR (Ellison et al., 2004), or due to radiative losses in the plasma before the shocks themselves become radiative. In addition to this, the distribution of internal energy within the remnant could be modified by thermal conduction. Since it is impractical to model every physical process in detail, the assumptions of spherical symmetry, absence of thermal conduction and adiabaticity in the SNRs will be made here as a first approximation. These assumptions have the advantage of simplicity and flexibility, allowing to explore a larger number of cases of interest. The limitations of one dimensional adiabatic dynamics without thermal conduction, however, should always be kept in mind when it comes to analyze results and compare with observations. These limitations will be revisited in section 3.5.

In order to study the interaction between ejecta and AM, a one dimensional hydrodynamic code has been built. This code is very similar to the one described in Truelove and McKee, 1999: explicit and Lagrangian, with an ideal gas equation of state ($\gamma = 5/3$), nonlinear pseudoviscosity and no external energy sources or sinks. More details about the hydrodynamic code are given in appendix A. Under the simplifying assumptions of spherical symmetry, absence of thermal conduction and adiabaticity, the dynamic evolution of the SNR depends only on the structures of the ejecta and the AM. The density profiles of the Type Ia SN models presented in chapter 2 (Figures 2.3 and 2.5) account for the possible variations in the ejecta structure due to the physical mechanisms at play during the explosion. The structure of the AM, on the other hand, is intimately related to the evolution of the progenitor system. Thermonuclear supernovae are not associated with stellar progenitors that undergo significant mass loss episodes during the presupernova phase (see section 2.1.2), so a constant density AM will be assumed to avoid the introduction of an excessive number of parameters in the SNR models. Discussion of the validity of the constant density AM hypothesis is deferred to chapter 6, where the relationship between the evolution of the progenitor systems and the structure of the AM at the moment of the explosion will be studied with detail.

It is important to note that, if the ejected mass M_{ej}, kinetic energy E_k and density profile associated with the ejecta are fixed, the interaction with a constant density AM follows a scaling law for the AM density ρ_{AM} (Gull, 1973). Therefore, it is sufficient to perform the hydrodynamic calculations for each ejecta profile with a certain value of ρ_{AM} and then use the characteristic magnitudes defined in eqs. 3.1, 3.2, and 3.3 to rescale the results to any other ρ_{AM} value that might be of interest (see Dwarkadas and Chevalier, 1998, and Truelove and McKee, 1999, for further comments on these scaling laws).

$$R' = \left(\frac{M_{ej}}{(4\pi/3)\rho_{AM}} \right)^{1/3} \tag{3.1}$$

$$V' = \left(\frac{2E_k}{M_{ej}} \right)^{1/2} \tag{3.2}$$

$$T' = \frac{R'}{V'} = \frac{M_{ej}^{5/6}}{((4\pi/3)\rho_{AM})^{1/3}(2E_K)^{1/2}} \tag{3.3}$$

The dynamic interaction of a grid of thermonuclear supernova explosion models with a constant density AM in one dimension was first explored in Dwarkadas and Chevalier, 1998 (hereafter DC98). In that paper, six ejecta density profiles from Type Ia supernova models were examined and compared with three analytical density functions: an exponential, a power law of index $n = 7$ with a constant density core, and a constant density profile. The model grid in DC98 included two sub-Chandrasekhar models, a delayed detonation, two pulsating delayed detonations and the W7 model. Approximate temperature profiles were also calculated assuming solar abundances for the supernova ejecta. The conclusions of DC98 were:

- In all cases the density of the shocked ejecta increases from the reverse shock towards the contact discontinuity, a feature that is reproduced by the exponential and constant ejecta density profiles, but not by the power law profile. Based on this, DC 98 recommended the exponential profile as an analytical model for the ejecta in Type Ia SNRs.

- The density rise towards the CD is coupled with a drop in temperature.

- The sharp structures in the ejecta profiles, especially in sub-Chandrasekhar models, give rise to secondary waves propagating in the interaction region which could affect the instantaneous X-ray emissivity of the remnants.

These conclusions will be a useful benchmark for the results presented in the next section.

3.3.2   Results

For the present work, the dynamic evolution of the SNRs generated by the 19 Type Ia SN models of the grid has been simulated for an interaction with $\rho_{AM} = 10^{-24}\,\mathrm{g \cdot cm^{-3}}$. The simulations start $10^7\,\mathrm{s}$ after the SN explosion, and the evolution is followed up to an age of $10,000\,\mathrm{yr}$. The 7 models outside the grid have also been included, as well as the exponential ejecta density profile (EXP) recommended by DC98, constructed assuming $E_k = 10^{51}\,\mathrm{erg}$ and $M_{ej} = 1.4\,\mathrm{M_\odot}$ (Fig. 3.2).

It would be impractical (and rather devoid of interest) to analyze extensively the structure of the supernova remnants obtained from all the supernova explosion models as a function of time. Instead, the dynamics of the forward and reverse shocks will be discussed for the sample subgrid of 12 models: SCH, DET, DEFa, DEFc, DEFf, DDTa, DDTbb, DDTc, DDTe, PDDa, PDDc and PDDe. The shocked ejecta structure will be studied with detail for a selection of these models at two representative ages.

The behavior of the forward and reverse shocks can be seen in Figures 3.3, 3.4, and 3.5. The time axis spans between 30 and 10,000 years after the explosion, and the reverse shock parameters have been plotted only up to the time when the shock reaches the center of the simulation space. Afterwards, the reverse shock rebounces and starts propagating
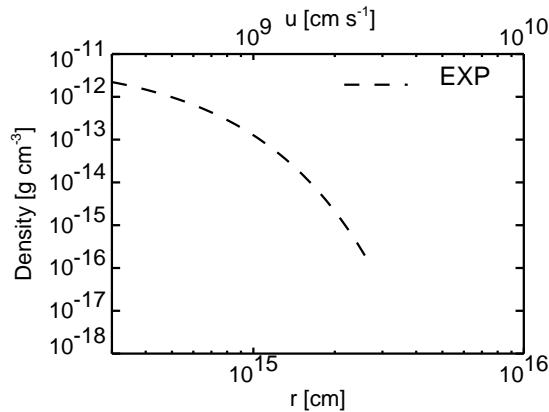
Figure 3.2: The exponential density profile EXP ($E_k = 10^{51}$ erg, $M_{ej} = 1.4\,\mathrm{M}_\odot$). Compare with Figure 2.3.

outwards into the hot, shocked ejecta, albeit with diminished strength. The plots show the time evolution of the forward and reverse shock radii (r_{fwd} and r_{rev}, Fig. 3.3), the velocity of the forward shock and the velocity of the reverse shock in the rest frame of the expanding ejecta (u_{fwd} and $u_{rev} = (r_{rev}/t) - (dr_{rev}/dt)$, Fig. 3.4) and the expansion parameters for both shocks, defined as $\eta_{fwd,rev} = d\ln(r_{fwd,rev})/d\ln(t)$ (Fig. 3.5).

The dynamics of the forward shock is affected by the differences in the density profiles only during the first thousand years. Afterwards, all the models converge towards the Sedov-Taylor solution, $\eta_{fwd} = 0.4$. This transition leads to the change of slope of the forward shock radii in the log-log plots of Fig. 3.3. For the deflagration models, the shock trajectories lag behind those of the other models because their E_k is lower. The deflagrations can also be distinguished by their high η_{fwd} values at early times (Fig. 3.5), about 50% higher than in the other models. Sudden increases in η_{fwd} can be seen in the PDD models around $t = 4 \cdot 10^9$ s, and in the SCH model at $t = 2 \cdot 10^9$ s and $t = 6 \cdot 10^9$ s. In general, high η_{fwd} values are found in models that have high density material in the outermost ejecta, as the DEF models, or a high density region surrounded by lower density material, as the PDD models around $u = 1.5 \cdot 10^9\,\mathrm{cm \cdot s^{-1}}$, and SCH at $u = 1.2 \cdot 10^9\,\mathrm{cm \cdot s^{-1}}$ and $u = 1.8 \cdot 10^9\,\mathrm{cm \cdot s^{-1}}$ (see Fig. 2.3). These high density regions in the outer ejecta transfer their momentum to the shocked material and to the forward shock, leading to the noted increases in η_{fwd}. Note also the deceleration of the reverse shock as it overcomes the steep density gradients in the ejecta. The shocks of the analytic profile EXP have a very smooth evolution, somewhat similar to those of the DET model, whose density profile is the result of the uniform propagation of a detonation burning front (see section 2.2).

The structure of the shocked ejecta for the models DEFc, DDTc, PDDc, DET and SCH is presented in Figures 3.7, 3.8, 3.9, 3.10 and 3.11. The models are plotted 430 and 1000 yr after the explosion, the approximate ages of the prototype Galactic Type Ia SNRs Tycho and SN1006. The choice of ages is rather arbitrary, since in order to compare with a real object the AM density should be chosen accordingly, and $\rho_{AM} = 10^{-24}\,\mathrm{g \cdot cm^{-3}}$ is probably too low for Tycho and too high for SN1006. The output of the hydrodynamic code is shown on panels a and e of the figures; discussion of the other panels, which display the results of the ionization calculations, is deferred to section 3.4.3. In agreement with the results of DC98, the structure of the shocked ejecta is dominated by a density enhancement towards the contact discontinuity for all models at all times. This enhancement is associated with a drop in specific internal energy, and therefore in mean plasma temperature. Model SCH

Figure 3.3: Positions of the forward and reverse shocks as a function of time for the sample grid models. The reverse shock plots are truncated at the time of the rebounce.
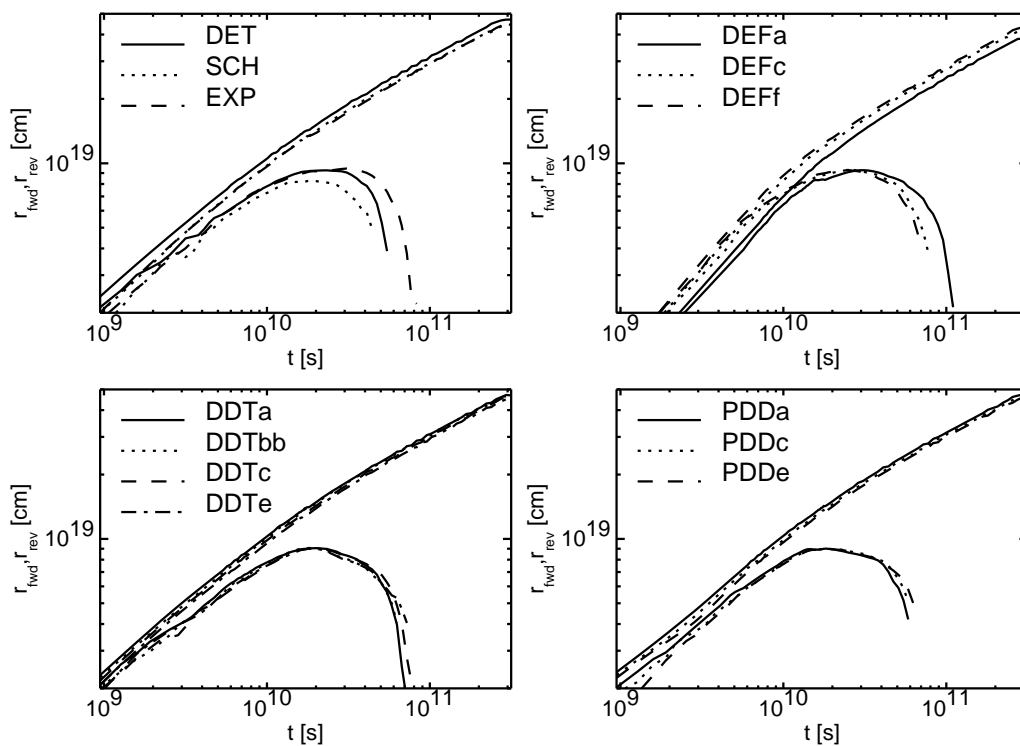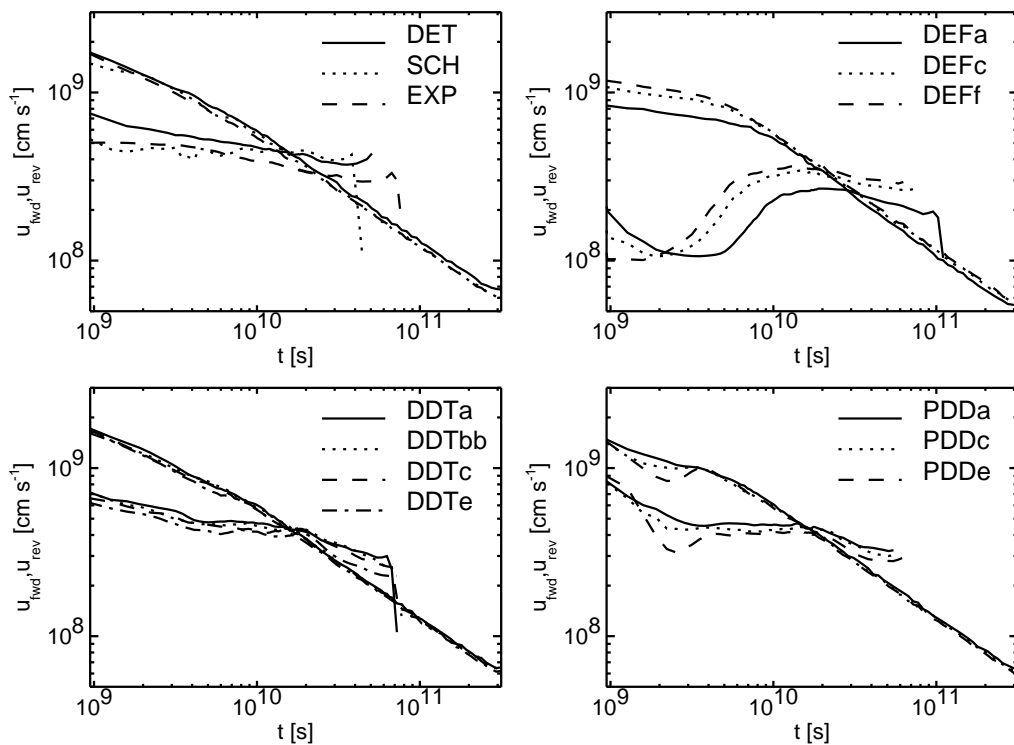

Figure 3.4: Velocities of the forward and reverse shocks as a function of time for the sample grid models. The reverse shock plots are truncated at the time of the rebounce.
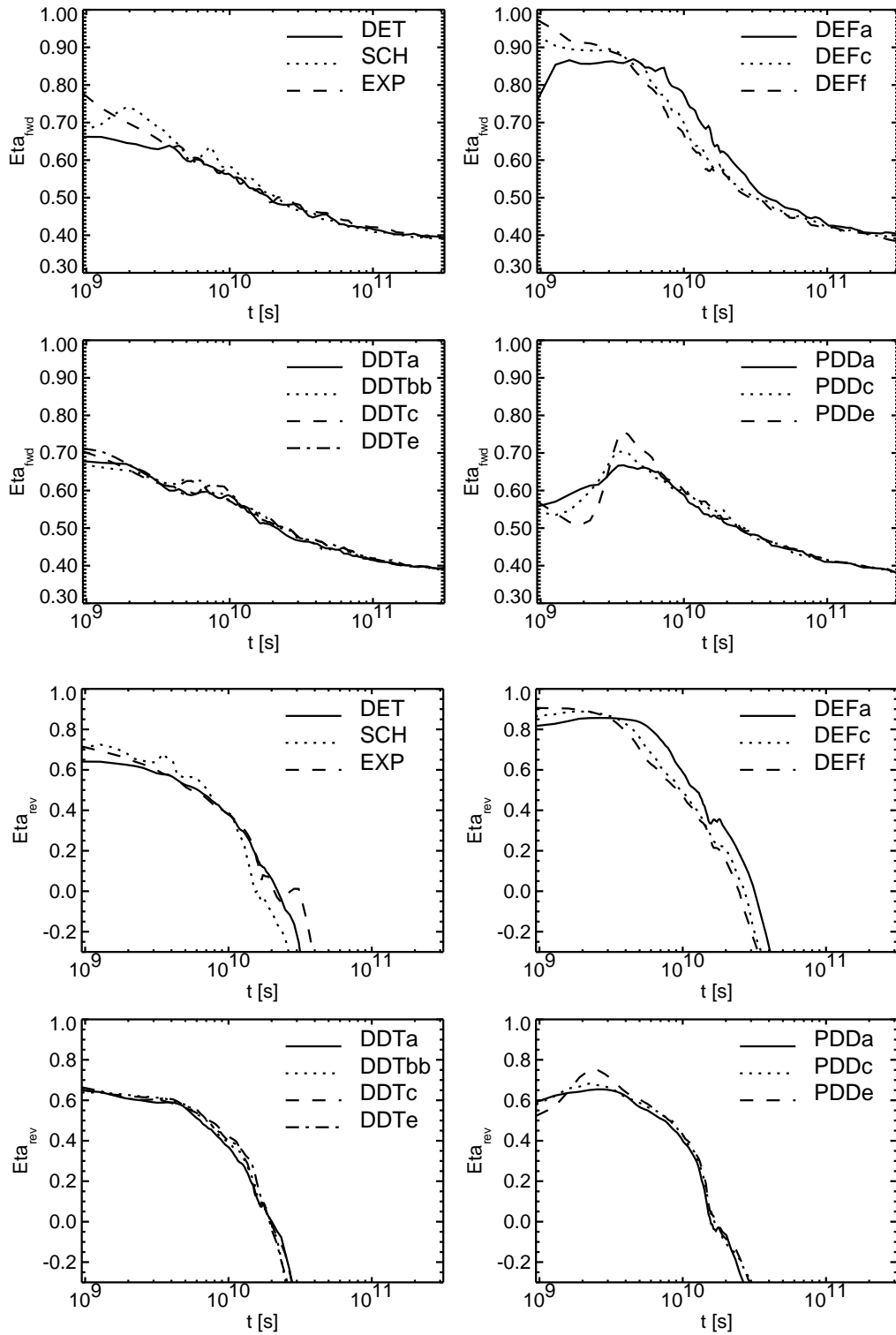
Figure 3.5: Forward shock (top four panels) and reverse shock (bottom four panels) expansion parameters as a function of time for the sample grid models.

also has a prominent secondary density peak associated with the boundary between the He layer and the rest of the WD in the explosion (see Figure 2.1 and section 2.2). The density enhancement effect is stronger for those models that undergo sudden increases in η_{fwd} early in their evolution, like DEFc or PDDc, than for those that do not, like DDTc. The high density material in the outer ejecta, which is responsible for the efficient momentum transfer and the increase in η_{fwd}, is compressed by the reverse shock and stays close to the contact discontinuity. In addition to this, the low density tail that surrounds the high density layers in models like PDDc is recompressed by the reflected shocks that ensue when the high density layers are overcome by the reverse shock. The result is that the density enhancement effect close to the contact discontinuity is stronger for the DEF, PDD and SCH models than for the DDT and DET models, where the evolution of η_{fwd} is smoother. As pointed out by DC98, the rich internal structure of some explosion models produces a series of secondary shock waves that travel along the shocked ejecta and AM, reheating and recompressing the material. In general, the shock behavior and dynamic structure of the models loosely resemble those of the EXP profile (see Figure 3a in DC98), whose density peaks towards the CD, but significant deviations are found in most cases.

3.4 Ionization and heating in the ejecta of Type Ia SNRs

3.4.1 Characterization of the plasma in SNRs.

Setting the stage

In this section, a number of important considerations will be made that are needed to describe accurately the state of the shocked plasma and simulate the heating and ionization processes that lead to the thermal X-ray emission. Since the aim is to model thermonuclear supernova ejecta, special emphasis will be placed on plasmas that are rich in heavy elements. A detailed discussion of many of the issues that will be treated here can be found in Hamilton and Sarazin, 1984 (hereafter HS84).

As a starting point, the following assumptions can be made for a low density plasma which is impulsively heated to high temperatures by the passage of a supersonic shock wave (adapted from Mewe, 1998):

1. The plasma is optically thin. Ion and electron populations are decoupled from the radiation field, so that processes like photoionization, photoexcitation and electron scattering by radiation don't have to be taken into account.

2. The populations of the excited states of all ions are negligible compared to the population of the ground state.

3. Radiative losses are balanced by mechanical heating.

4. All the particles present (ions and electrons) are relaxed to Maxwell-Boltzmann energy distributions, so that each particle population x can be fully described with its temperature T_x.

The first assumption implies that, once the plasma has been shocked, its state will be determined only by collisional interactions among ions and electrons. The inelastic collisions result in ionization and recombination, which affects the charge state distribution of the plasma, while the elastic collisions affect the temperature of the plasma particles. The second assumption makes it possible to represent the population of each ion by a single

number, with no need to take the excited states into account. Both assumptions 1 and 2 are true for the plasma in SNRs under most conditions. The validity of assumptions 3 and 4, however, is not so straightforward. If a given fluid element radiates energy for a long time, or if its density is unusually high at some point during its evolution, radiative losses might become important (see section 3.5). Assumption 4 is not true in a strict sense for SNRs, because, as mentioned previously, the acceleration processes at the shocks contribute a high energy tail to the Maxwellian distributions. This tail is usually approximated by a power law, and is the origin of the so called nonthermal X-ray emission (nonthermal bremsstrahlung and synchrotron emission).

In theory, the presence of nonthermal particle populations, specially nonthermal electrons, should have an impact on the ionization of the plasma. The nonthermal velocity distributions in the shocked plasma would have to be convolved with the cross sections for the elastic and inelastic collision processes to find the collision rates, which would be different from the rates obtained assuming Maxwellian distributions. This problem has already been explored by some authors. In Brinkmann, 1992, it was found that the effect of modified electron distributions on the ionization state of SN ejecta rich in Fe was of the order of a few percent, and could be safely neglected. In a later and more detailed work (Porquet et al., 2001), the conclusion was that only plasmas in ionization equilibrium would be severely affected, and the deviations would be small for transient plasmas. Since the plasma inside young SNRs is generally out of ionization equilibrium, the effect of having nonthermal electron populations should be small. In the remainder of this work, thermal distributions will be assumed for all the particle populations.

Preshock ionization state

Ambient UV starlight and X-ray emission from the shocked material have the capability of photoionizing the cool, unshocked material in the ejecta and AM, which is more vulnerable to this effect than the shocked plasma subject to collisional ionization. This photoionization will determine the charge state of the ions that enter the forward and reverse shocks, and the number of free electrons that accompany them. The details, however, are complex, because the intensity of the UV starlight depends on the location of the SNR, and the bulk X-ray emission from the shocked ejecta and AM evolves with time. In addition to this, the cold ejecta keep expanding freely until they are overrun by the shock, so the efficiency of the photoionization process might be very different for different ejecta layers (see HS84 and Borkowski et al., 1994, for details).

To make observations of the preshock ionization state in SNRs is extremely difficult, because the emission from the cool unshocked material is very weak. In some cases, like the Tycho SNR, a photoionization precursor to the forward shock has been identified (Ghavamian et al., 2000), but the attempts to detect similar emission ahead of the reverse shock have failed. The unshocked ejecta can be observed in absorption, but this technique demands the fortuitous location of a sufficiently known source behind the SNR. So far, only two remnants have been studied in absorption. One of them is SN 1006, where the optical and UV spectrum of an OB subdwarf, known as the Schweizer and Middleditch star (Schweizer and Middleditch, 1980), is modified by absorption features from the shocked and unshocked material in the SNR in front of it. Analysis of *HST* observations of this star has yielded low preshock ionization states, between 1 and 2 times ionized, for Si and Fe (Hamilton et al., 1997). The other case is the remnant of SN 1885, which has been observed against the bulge of its host galaxy M31, revealing neutral and one time ionized unshocked Fe and Ca (Fesen et al., 1989). In any case, unless the preshock ionization state is very high, it is not expected to have a profound impact on the postshock evolution, due

to the properties of the ionization equations (see appendix B). For the present work, all the elements in the unshocked material have been assumed to be in the singly ionized state.

Physics of collisionless shocks

A shock is considered collisionless if the shock transition occurs on a length scale that is much shorter than the particle mean free paths to Coulomb collisions. Instead of direct particle collisions, the mechanisms that produce the shock transition are collective motions of the plasma known as plasma waves, that interact with the ambient magnetic field and scatter the particles that enter the shock. The exact nature of these waves and interactions, and their effect on the shocked particles, however, are not well understood, and this has become a major source of uncertainty in the spectral models for SNRs (see Laming, 2000, and references therein).

For a supersonic shock with a sufficiently high Mach number, the application of the Rankine-Hugoniot relations (conservation of energy, momentum and particle flux at the shock transition) yields the downstream temperature for ions (i) and electrons (e):

$$T_{i,e} = \frac{3}{16} \frac{m_{i,e} v_s^2}{k} \tag{3.4}$$

where v_s is the shock speed, k is Boltzmann's constant and $m_{i,e}$ are the ion and electron masses, respectively. From this expression, the postshock ion temperature is expected to be much higher than the electron temperature. After the shock passage, Coulomb collisions would tend to equilibrate the temperatures of the particle populations, but in SNRs this process is very slow due to the low density of the plasma. In all but the most evolved SNRs, the characteristic equilibration time is much longer than the age of the object.

According to Cargill and Papadopoulos, 1988, the excitation of plasma waves in collisionless shocks can modify this scenario of cold electrons and hot ions behind the shock. The plasma waves can be damped by heating the electrons behind the shock, thus forcing some degree of equilibration between the postshock ion and electron temperatures. Since neither the exact nature of the waves nor the intricacies of the damping mechanism are known, it is difficult to quantify the degree of equilibration that will ensue and the impact on the electron energy distribution. The value of T_e/T_i just after the shock is usually parametrized. For a more detailed discussion of plasma wave generation, plasma wave damping and postshock ion-electron equilibration, see Laming, 2001a.

A considerable effort has been done in recent times to provide observational tests of T_e/T_i behind the shocks of several SNRs in the Galaxy and the Magellanic Clouds. A very successful technique for this is the measurement and modeling of the broad-to-narrow ratio of the faint optical Balmer Hα and Hβ line emission in nonradiative shocks. These lines are produced by the progressive ionization of neutral H behind the shock, and the structure of their broad and narrow components contains information about the ratio of postshock electron to proton temperatures, as pointed out in Chevalier and Raymond, 1978 (see Ghavamian, 1999, and references therein for a detailed discussion). So far, the evidence from this and other techniques suggests a decreasing level of equilibration for increasing shock speeds or Mach numbers (Ghavamian et al., 2001; Rakowski et al., 2003). Thus, one would expect small values of T_e/T_i for young SNRs, whose shocks have not been substantially decelerated yet, and indeed the most recent measurements give $T_e/T_i \lesssim 0.1$ for the forward shocks of Tycho (Ghavamian et al., 2001) and SN1006 (Vink et al., 2003). Unfortunately, Balmer line spectroscopy cannot be applied to reverse shocks

propagating into Type Ia SN ejecta, for obvious reasons (lack of neutral H). Analysis of the absorption features in the spectrum of the Schweizer and Middleditch star has provided a measurement of this quantity for the remnant of SN1006: the amount of thermal energy in the shocked electrons was found to be negligible, implying a low value of T_e/T_i for the reverse shock as well (Hamilton et al., 1997).

Plasma model

In view of the considerations made up to now, the simplest reasonable model that can be adopted for the shocked plasma is the so called two-fluid model (Itoh, 1978), where two Maxwellian populations are used to characterize ions and electrons. Just behind the shock, the properties of the plasma are determined by the preshock ionization state, the shock velocity and the amount of collisionless electron heating. From this initial state, ionizations, recombinations and Coulomb collisions drive the temporal evolution of the charge state distribution and the ion and electron temperatures in the plasma.

An alternative, three-fluid, approach was also proposed in the 1980s (Itoh, 1984; HS84). In this model, the electron population is split in two, a 'hot' component, comprising the electrons that are initially heated at the collisionless shock, and a 'cold' component, formed by the electrons ejected in the subsequent plasma ionization. The temperature of the 'cold' electrons is lower because their energies are of the order of the ionization potentials, in contrast to the 'hot' electrons, whose energies are determined by the shock velocity. The electron populations will eventually merge with a time scale shorter than that of the Coulomb ion-electron interactions. The hot electron component was thought necessary because, prior to the detection of nonthermal X-rays from SNRs (Koyama et al., 1995), the observed X-ray spectra could not be explained with thermal models alone. Nowadays it is clear that thermal electrons are not the sole contributors to X-ray spectra, but the rationale behind the three fluid model is not invalidated by this fact. The relative importance of the hot electron population depends on the efficiency of the collisionless heating at the shock, on the preshock ionization state of the ejecta and on the composition of each layer. In general, this relative importance will decrease with time as more 'cold' electrons are produced by postshock ionization, especially if collisionless electron heating is not efficient, the preshock ionization state is low and the plasma is rich in heavy elements. Since these are precisely the conditions relevant to thermonuclear SN ejecta in SNRs, the use of three particle populations is not justified, and a two fluid plasma model is considered a reasonable approximation to the problem at hand.

3.4.2 Ionization and electron heating processes

Definitions and notation

The dynamic state of a given fluid element is determined by its density ρ and specific internal energy per unit mass ε, which are calculated with the hydrodynamic code (section 3.3). In the context of the two fluid model, the electron and ion populations are described by their temperatures T_e and T_i (in K) and their number densities n_e and n_i (in cm^{-3}). The mean plasma temperature is defined as $T \equiv \frac{n_e T_e + n_i T_i}{n}$, with $n = n_e + n_i$. At any given time, the total internal energy is distributed among ions and electrons so that $\varepsilon = \varepsilon_i + \varepsilon_e$, and the respective temperatures and number densities are related to the specific internal energies per unit mass in each population by $\varepsilon_{e,i} = (3kT_{e,i}n_{e,i})/2\rho$.

The chemical composition of the fluid element can be represented with the normalized number abundances or molar fractions for each element X, $f_X \equiv \frac{n_X}{n_i}$, where n_X is the total number density of all the ions of element X (these are the quantities represented

in Figures 2.1, 2.2 and 2.4). Using the same notation, the ionization structure or charge state distribution (CSD) of the fluid element can be represented by the normalized ion fractions, $f_{X^q} \equiv \frac{n_{X^q}}{n_X}$, with n_{X^q} the number density of the ion of X that has a charge of q (0 for neutral ions, $Z_X + 1$ for bare ions). The element abundances and ion fractions must verify $\sum_X f_X = 1$ and $\sum_q f_{X^q} = 1$ at all times. Two interesting average quantities are the mean mass per ion in AMU, $\overline{A} \equiv \sum_X A_X f_X$, with A_X the element mass number[1], and the mean number of electrons per ion or mean ion charge in units of e, $\overline{Z} \equiv \sum_X f_X \sum_q q.f_{X^q}$.

A little algebra yields the following useful expressions:

$$n_i = \frac{\rho}{\overline{A}m_u}, \; n_e = \overline{Z}n_i = \frac{\overline{Z}\rho}{\overline{A}m_u} \tag{3.5}$$

$$\varepsilon_i = \frac{\frac{3}{2}kT_i}{\overline{A}m_u}, \; \varepsilon_e = \frac{\frac{3}{2}kT_e\overline{Z}}{\overline{A}m_u} \tag{3.6}$$

$$T_i = \frac{\overline{A}m_u\varepsilon_i}{\frac{3}{2}k}, \; T_e = \frac{\overline{A}m_u\varepsilon_e}{\frac{3}{2}k\overline{Z}} \tag{3.7}$$

where m_u is the value of an AMU ($1.66 \cdot 10^{-24}$ g).

The ionization equations

As we have seen, the initial state of the shocked plasma is determined by its preshock ionization state, the shock velocity and the efficiency of the collisionless electron heating. The value of the postshock ion temperature $T_{i,s}$ is related to the shock velocity (see eqn. 3.4), while the postshock electron temperature $T_{e,s}$ is determined by the efficiency of the collisionless electron heating, which can be parametrized as

$$\beta \equiv \frac{T_{e,s}}{T_{i,s}} \tag{3.8}$$

where β can range from $\beta_{min} = \frac{m_e}{m_i} = \frac{m_e}{\overline{A}m_u} = \frac{5.49 \cdot 10^{-4}}{A}$, corresponding to the limit of no collisionless electron heating (from eqn. 3.4), to $\beta_{max} = 1$, corresponding to full electron-ion temperature equilibration.

From the initial postshock state, the charge state distribution of the fluid element evolves due to the inelastic collisions between ions and electrons, according to the ionization equations:

$$\frac{df_{X^q}}{dt} = \frac{\overline{Z}\rho}{\overline{A}m_u} \left[I_{X^{q-1}}f_{X^{q-1}} + R_{X^{q+1}}f_{X^{q+1}} - (I_{X^q} + R_{X^q})f_{X^q} \right] \tag{3.9}$$

Here, I_{X^q} and R_{X^q} are the ionization and recombination rates *from* ion X^q (that is, into ions X^{q+1} and X^{q-1}), and the time derivative is Lagrangian. The values of I_{X^q} and R_{X^q} are functions of the electron temperature alone. To illustrate the typical behavior of the rates, the ionization and recombination rates for C are plotted in Fig. 3.6.

At the same time, elastic collisions between ions and electrons tend to equilibrate the temperatures of the Maxwellian populations, at a rate proportional to the temperature difference (Spitzer, 1962). Adopting the notation from HS84, the internal energy transfer can be expressed as

---

[1] Note that for SN ejecta the mean mass of each element might be different from the solar value due to the isotopic composition resulting from explosive nucleosynthesis.
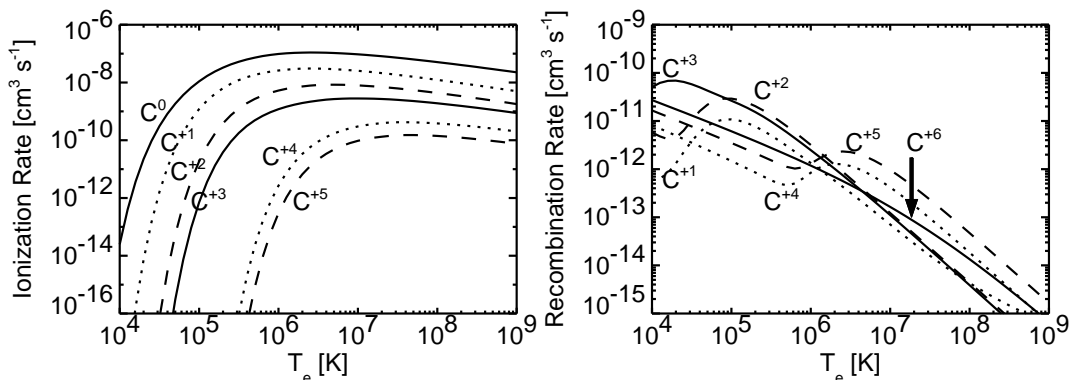
Figure 3.6: Ionization and recombination rates for C, I_{C^q} (left) and R_{C^q} (right), as a function of T_e. Note the different scale of the y-axis. Data from Mazzotta et al., 1998.

$$-\frac{d\varepsilon_i/\varepsilon}{dt} = \frac{d\varepsilon_e/\varepsilon}{dt} = \frac{1}{\rho\varepsilon}\frac{2^{5/2}\pi^{1/2}e^4 n_e n_i \overline{Z}^2 \ln\Lambda}{m_e \overline{A} m_u k^{1/2}}\frac{(T_i - T_e)}{(\frac{T_i}{\overline{A}m_u} + \frac{T_e}{m_e})^{3/2}} \quad (3.10)$$

with e the electron charge in ESU, $\ln\Lambda$ the Coulomb logarithm and k the Boltzmann constant. The expression for the Coulomb logarithm is (Spitzer, 1962)

$$\ln\Lambda = \ln\left(\frac{3}{2\overline{Z}e^3}\left[\frac{k^3 T_e^3}{\pi n_e}\right]^{1/2}\right) \quad (3.11)$$

The integration of equations 3.9 and 3.10 merits a few comments. In plasmas with solar composition, H and He dominate the electron pool, and as soon as these elements are completely ionized, $\overline{Z}$ can be assumed to be constant and the ionization and internal energy transfer equations can be integrated separately. In plasmas rich in heavy elements, however, this is not possible, because $\overline{Z}$ is a function of the charge state distribution, and the equations are coupled. As noted in section 3.2, this is one of the reasons why spectral models for the thermal X-ray emission from the ejecta in SNRs are difficult to produce. In order to follow the evolution of the charge state distribution and heating processes in the SNR ejecta, an implicit Lagrangian ionization code has been built. The code inputs are the dynamic evolution $\rho(t)$, $\varepsilon(t)$ of each fluid element as calculated by the hydrodynamic code (section 3.3) and its chemical composition as computed in the explosion models (chapter 2). The code integrates equations 3.9 and 3.10 to produce $T_e(t)$, $T_i(t)$ and $f_{X^q}(t)$ for all the ions of the elements with $f_X \geq 10^{-3}$. The global evolution of the shocked ejecta is obtained by putting together the outputs for all the fluid elements. The ionization code, along with the numerical techniques it uses and some specific examples, is described in appendix B.

Some reflections on the quality of the atomic data

While the internal energy transfer rate in eq. 3.10 is easily derived from basic considerations in the theory of ionized gases (Spitzer, 1962), the physics involved in the calculation of the ionization and recombination rates that appear in eq. 3.9 is complicated by the details of the atomic structure of each ion. The ionization and recombination rates for the present work have been taken from the recent compilation in Mazzotta et al., 1998. This is the most complete and updated set of rates presently available, and features the

ionization and recombination rates for all the ions from He to Ni as a function of electron temperature, with a resolution of 0.1 in $logT_e$ for the range $4.0 \leq logT_e \leq 9.0$.

Even these state-of-the-art rates have shortcomings, however. They are derived from theoretical calculations of the inelastic collisions between ions and electrons, calculations that rely on atomic data which are known only incompletely, and with an enormous range in accuracy. Indeed, the quality of the atomic data has become a major source of uncertainty in the spectral models for thermal, optically thin plasmas. The rate calculations include contributions from direct ionization by electron collisions, autoionization from excited ion states, radiative recombination and dielectronic recombination (details can be found in Arnaud and Rothenflug, 1985, and Mazzotta et al., 1998). Processes like resonance excitation, double autoionization and direct multiple ionization are not included, but their importance is expected to be minor. The inaccuracies in the included processes are of more concern, and in some cases (notably the dielectronic recombination rates) they might be as large as a factor two. Some authors have explored the impact that these uncertainties would have on the ionization balance under CIE conditions (Mewe, 1990; Masai, 1997), but their effect on the time-dependent charge state distribution for NEI plasmas is more difficult to estimate, and no systematic studies can be found in the literature. The shocked ejecta plasma in young Type Ia SNRs is always evolving towards higher ionization states, so the most critical atomic data are expected to be the ionization rates of the most abundant elements, Fe, S, Si, O and C. For these rates, the uncertainties are typically around 20% for the lower ions (Arnaud and Rothenflug, 1985; Mewe, 1998), and even better in some cases, so the results presented in the following section should not be severely affected by the quality of the atomic data.

3.4.3   Results

Under the assumptions detailed in sections 3.3.1 and 3.4.1, the only free parameters in the interaction of a SN explosion model with the AM are the AM density ρ_{AM} and the amount of collisionless electron heating at the shocks β. From the discussion in page 36, the value of β at the reverse shock is not expected to be much larger than 0.1 for young SNRs. The value of ρ_{AM} is harder to constrain, because there is a large range of different environments where Type Ia SNRs are found in the Galaxy and the Magellanic Clouds. In many cases of interest, however, ρ_{AM} does not deviate much from $\rho_{AM} = 10^{-24}\,\mathrm{g \cdot cm^{-3}}$.

The ionization and electron heating processes have been simulated for the sample subgrid of 12 models whose dynamics were studied in the previous section: SCH, DET, DEFa, DEFc, DEFf, DDTa, DDTbb, DDTc, DDTe, PDDa, PDDc and PDDe, up to a time of 5000 yr. after the explosion. The β, ρ_{AM} parameter space was explored in the calculations. Three values for the amount of collisionless heating at the reverse shock were considered: $\beta = \beta_{min}$, or absence of collisionless heating; $\beta = 0.01$, a small amount of heating; and $\beta = 0.1$, a moderate amount of heating, and the largest compatible with the observations. The value of ρ_{AM} was set either to $10^{-24}\,\mathrm{g \cdot cm^{-3}}$, $2 \cdot 10^{-25}\,\mathrm{g \cdot cm^{-3}}$ or $5 \cdot 10^{-24}\,\mathrm{g \cdot cm^{-3}}$, that is, a factor of 5 up and down of the canonical value. The results will be examined first for fixed values of the free parameters in order to compare a sample of the SN explosion models. Then, a specific model will be chosen to exemplify the exploration of the parameter space.

Fixed β and ρ_{AM}

The dynamic structure of models DEFc, DDTc, PDDc, DET and SCH at a time of 430 and 1000 yr after the explosion was discussed in section 3.3.2 for the interaction with an

AM of $\rho_{AM} = 10^{-24} \, \mathrm{g \cdot cm^{-3}}$, and is shown in panels a and e of Figures 3.7, 3.8, 3.9, 3.10 and 3.11, respectively. A representation of the output from the ionization code can be seen in the rest of the panels of those figures, assuming that there is no collisionless electron heating at the reverse shock ($\beta = \beta_{min}$).

The single most important factor that determines the evolution of the ionization state and electron temperatures in the shocked ejecta is the density structure. Both ionization and electron heating are collisional processes, and they proceed much faster in the high density regions than in low density ones. Examined under this light, the density enhancement effect towards the contact discontinuity that was pointed out in section 3.3.2 acquires a new relevance. The ionization state and electron heating in the outermost ejecta layers will evolve more rapidly than in the innermost layers, and especially so in those models whose ejecta density profiles tend to favor higher densities towards the CD (specifically, the DEF, PDD and SCH models). It is worth noting that it is precisely in the outermost ejecta layers where the chemical composition of the ejecta shows the strongest differences between the models (see Figs. 2.1 and 2.2).

One way to quantify and compare the different states of the fluid elements in the shocked ejecta is the ionization timescale, τ, defined as the time integral of the electron density in a fluid element from the moment when it was overrun by the shock wave until the present time t:

$$\tau(t) = \int_{t_{shock}}^{t} n_e dt \tag{3.12}$$

The ionization timescale is widely used in X-ray astronomy to characterize NEI plasmas, and it provides a measure of how far the plasma is from collisional ionization equilibrium. The final onset of CIE depends on several factors, but it is commonly assumed to happen at $\tau \sim 10^{12} - 10^{13} \, \mathrm{cm^{-3} \cdot s}$ (Mewe, 1998). The dynamic range of τ will give an idea of the difference between the outer ejecta layers, which are shocked before they can expand to low densities, and hence will have a more advanced ionization state, and the inner ejecta layers, which are shocked at a later time and will have a less advanced ionization state.

Model DEFc (Fig. 3.7) has the highest density towards the CD, almost $10^{-22} \mathrm{g \cdot cm^{-3}}$ at $t = 430 \, \mathrm{yr}$, and its outer ejecta layers are completely dominated by C and O, as in all the 1D deflagration models. The value of $\overline{Z}$ in this region (panels b and f in Fig. 3.7) is very close to 7, implying that C and O have been fully ionized, even 430 yr after the explosion. The density decreases rapidly towards the regions dominated by Si and Fe, and it is plain to see how the narrow Si-S buffer is still in a transient state ($\overline{Z} \simeq 12$) at $t = 430 \, \mathrm{yr}$, but has been fully ionized ($\overline{Z} \simeq 15$) at $t = 1000 \, \mathrm{yr}$. In the Fe-rich regions, the average charge state of the ions is lower. The temperature profiles (3.7 c and g) also show the impact of the density enhancement effect: while the ion temperature T_i follows more or less the specific internal energy profile (3.7 a and e), the electron temperature T_e always rises towards the CD, coming close to thermal equilibrium with T_i only in the few outermost layers. The ionization timescale in this model has an enormous dynamic range of six orders of magnitude, which remains more or less constant through time.

Models DDTc (Fig. 3.8) and PDDc (Fig. 3.9) have similar chemical composition profiles, but the ejecta density profile of PDDc is steeper in the outer layers, leading to a more pronounced density enhancement towards the CD (see section 3.3.2). Even though the difference in density is not large (it averages to less than a factor 2), it has quite noticeable effects. The values of T_e, $\overline{Z}$ and τ are generally higher for the outer layers of PDDc, suggesting that the ionization states of elements like O, Si and S will be higher at any given time for this model than for DDTc. The ionization state of Fe close to the
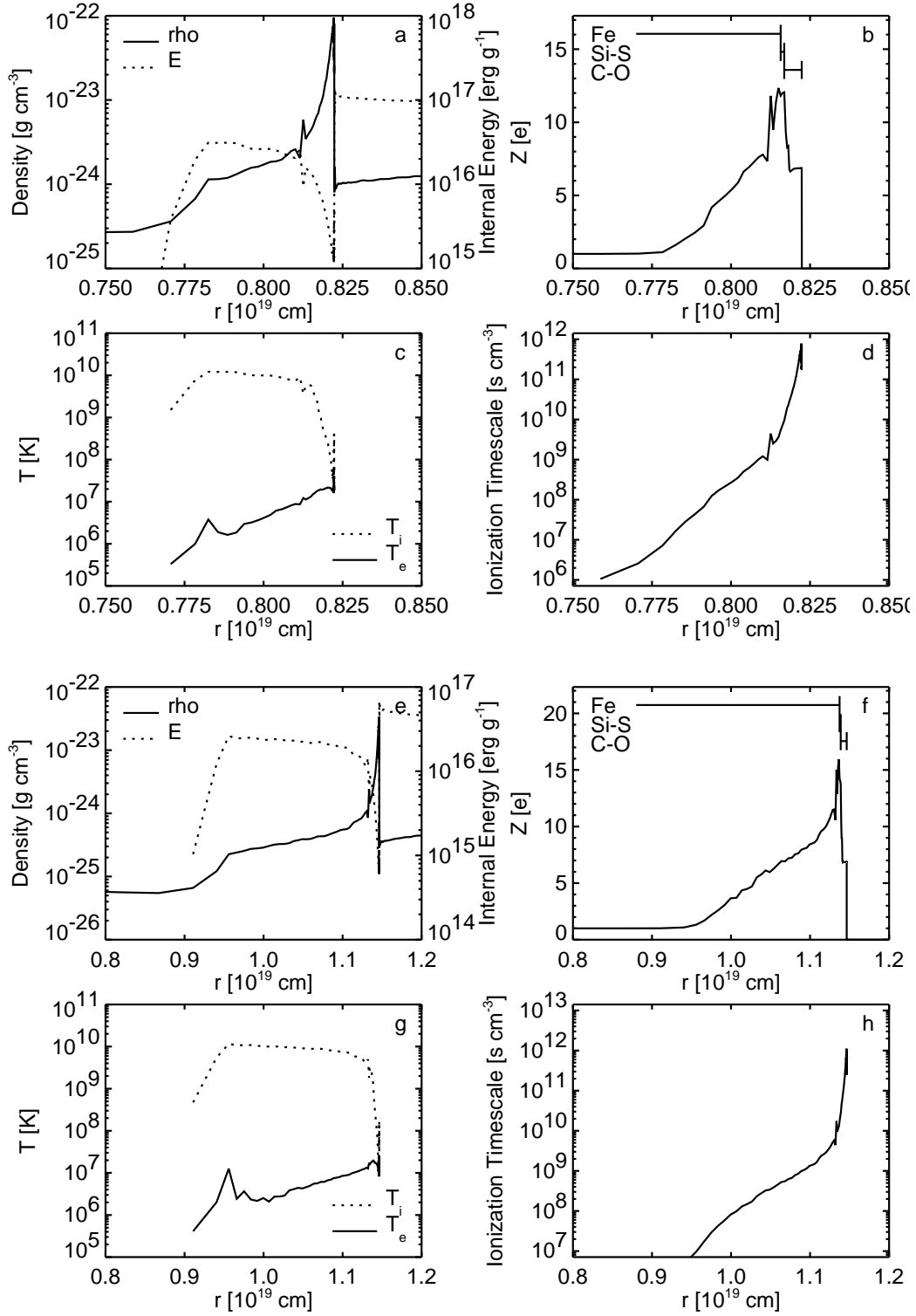
Figure 3.7: Shocked ejecta structure vs. radius for model DEFc, with $\rho_{AM} = 10^{-24}\,\mathrm{g\cdot cm^{-3}}$ and $\beta = \beta_{min}$. Panels a-d correspond to 430 years after the explosion, and show density and specific internal energy (a), mean number of electrons per ion, $\overline{Z}$, with an indication of the ejecta layers dominated by Fe, Si-S and C-O (b), electron and ion temperatures (c) and ionization timescale (d). Panels e-h correspond to 1000 yr after the explosion. The positions of the reverse shock and contact discontinuity are outlined by the limits of the temperature plots in panels c and g.

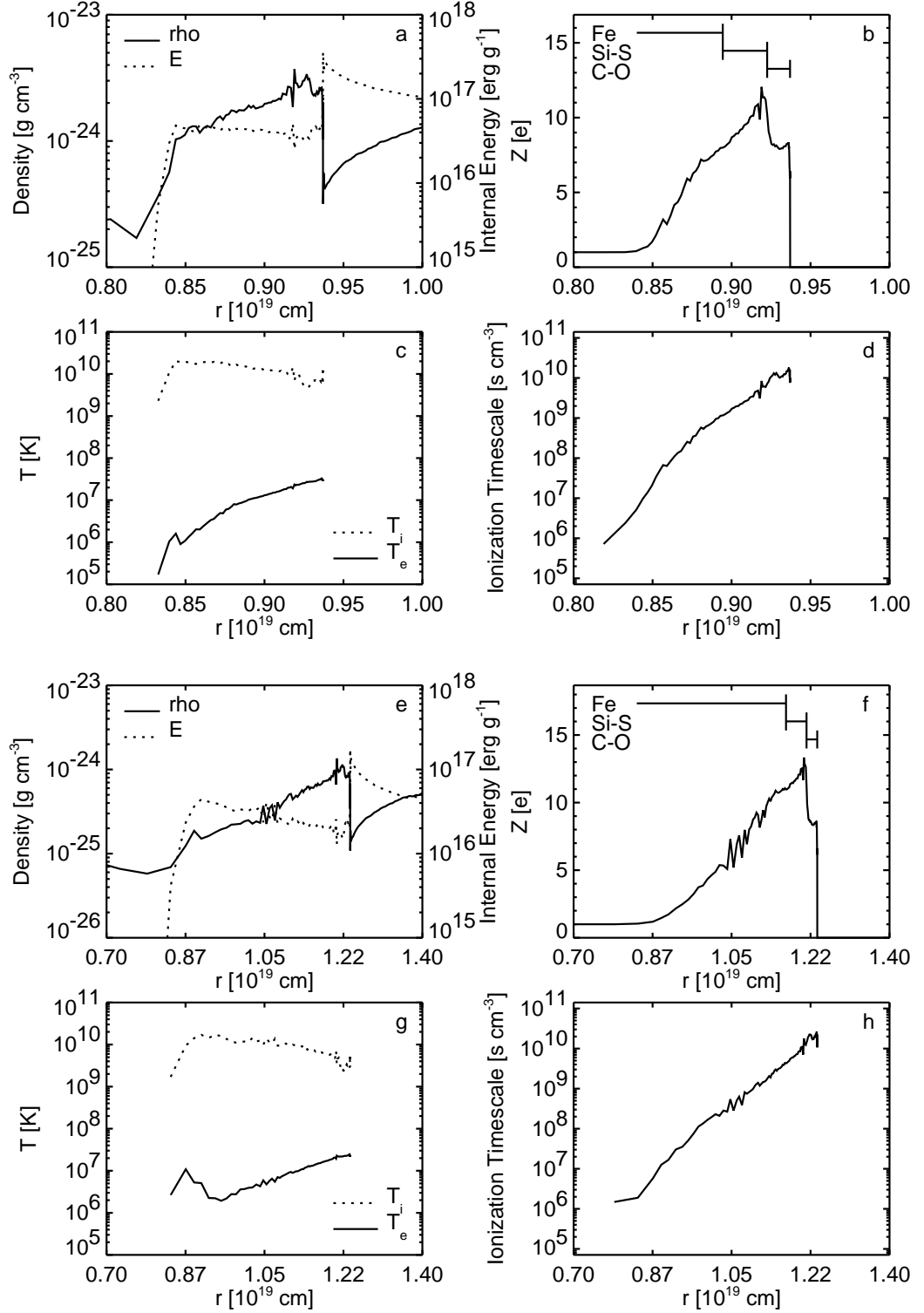Figure 3.8: Shocked ejecta structure vs. radius for model DDTc, with $\rho_{AM} = 10^{-24}\,\mathrm{g}\cdot\mathrm{cm}^{-3}$ and $\beta = \beta_{min}$. Panels a-d correspond to 430 yr after the explosion, and panels e-h to 1000 yr. All magnitudes as in Figure 3.7

Figure 3.9: Shocked ejecta structure vs. radius for model PDDc, with $\rho_{AM} = 10^{-24}\,\mathrm{g \cdot cm^{-3}}$ and $\beta = \beta_{min}$. Panels a-d correspond to 430 yr after the explosion, and panels e-h to 1000 yr. All magnitudes as in Figure 3.7.

Figure 3.10: Shocked ejecta structure vs. radius for model DET with $\rho_{AM} = 10^{-24}\,\mathrm{g \cdot cm^{-3}}$ and $\beta = \beta_{min}$. Panels a-d correspond to 430 yr after the explosion, and panels e-h to 1000 yr. All magnitudes as in Figure 3.7.

Figure 3.11: Shocked ejecta structure vs. radius for model SCH with $\rho_{AM} = 10^{-24} \, \text{g} \cdot \text{cm}^{-3}$ and $\beta = \beta_{min}$. Panels a-d correspond to 430 yr after the explosion, and panels e-h to 1000 yr. All magnitudes as in Figure 3.7.
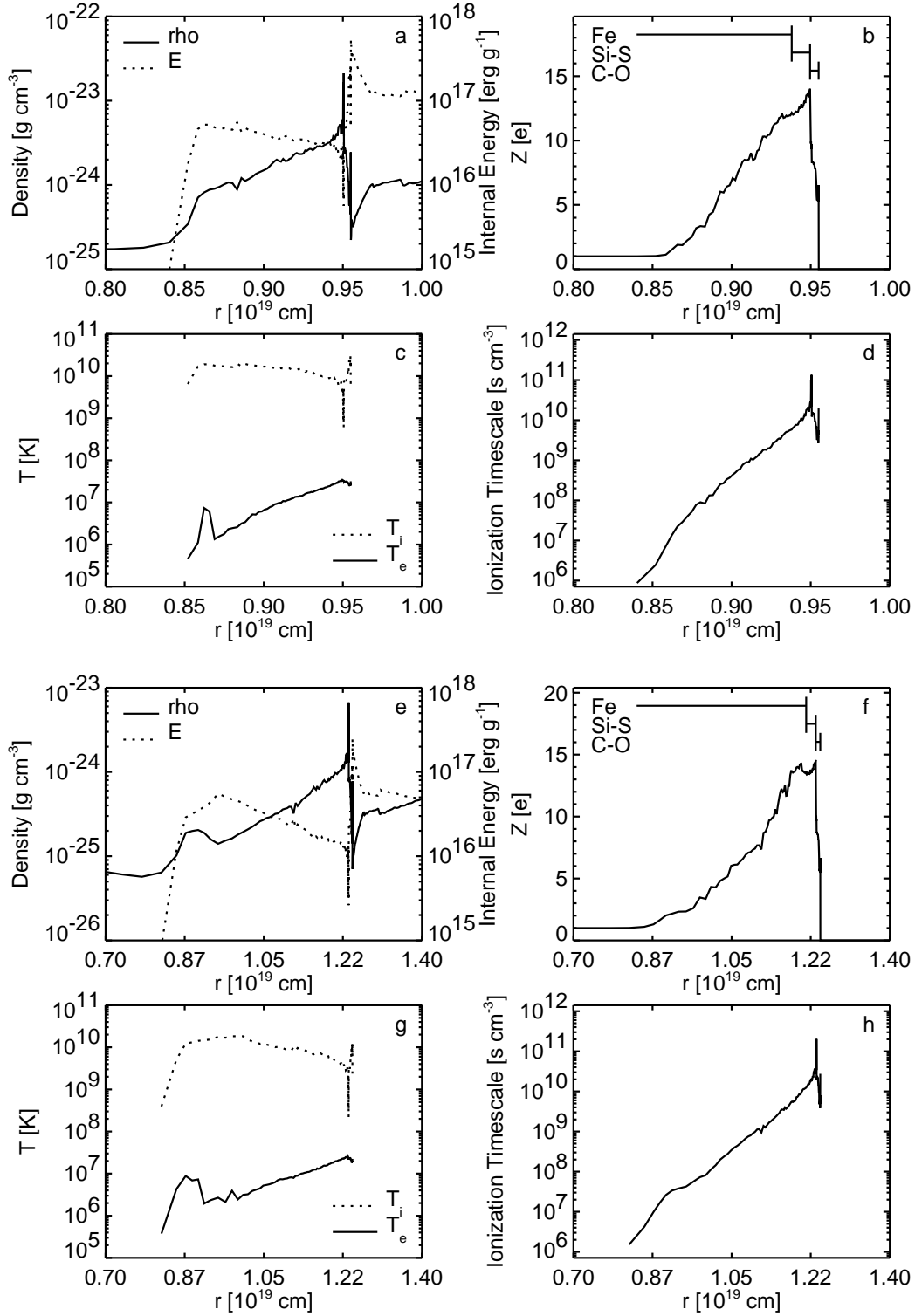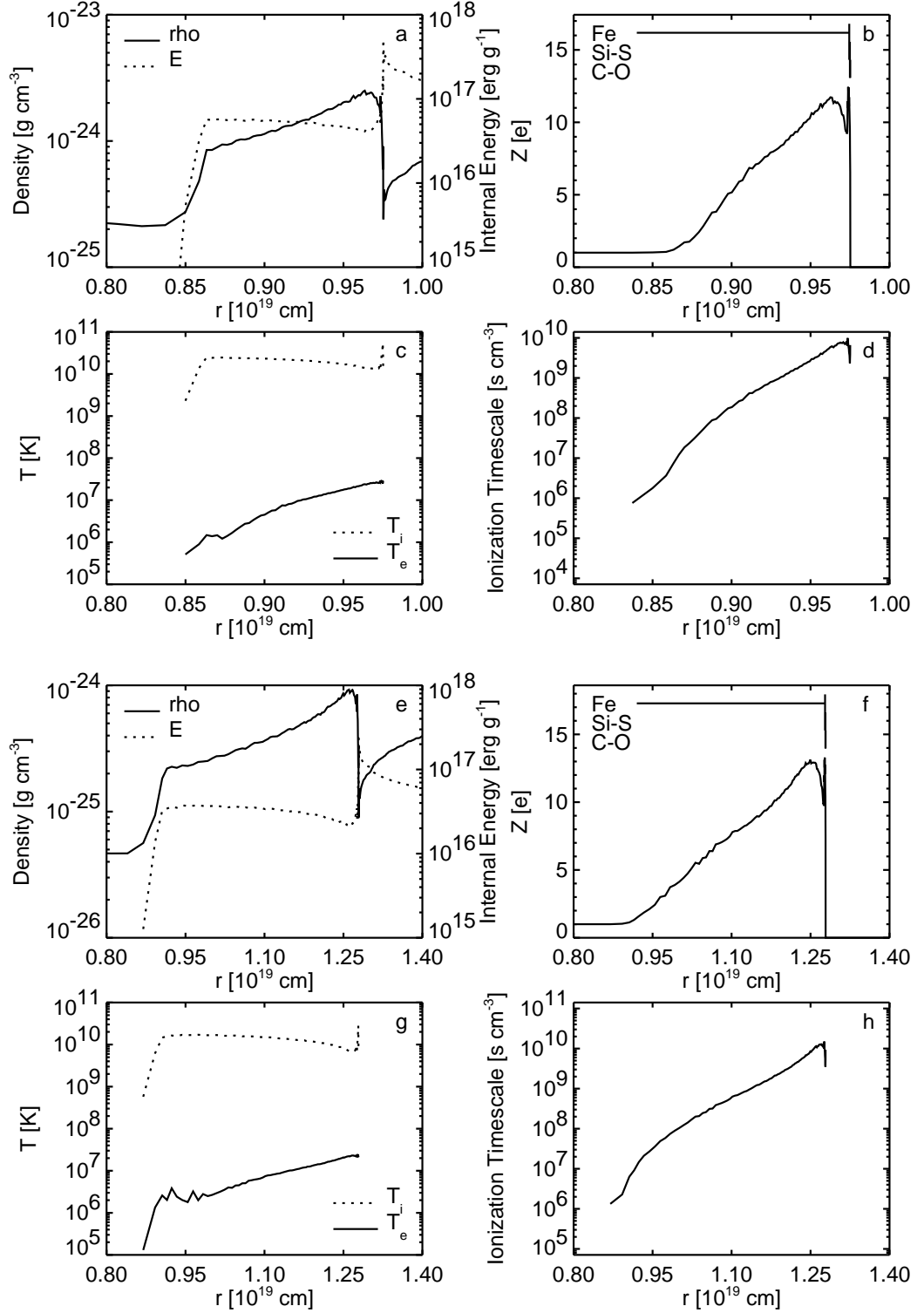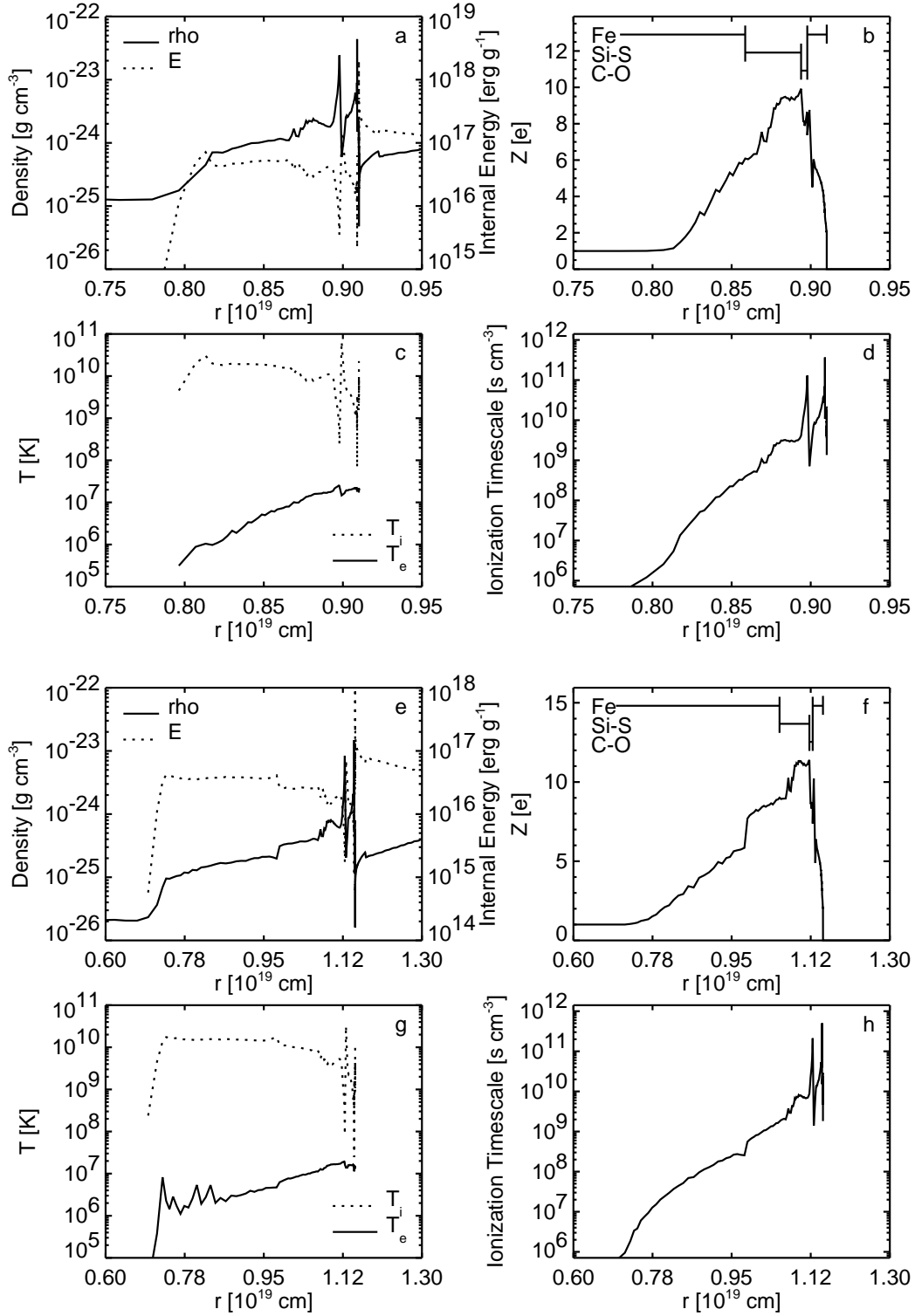
reverse shock is similar in both models, but it gets higher in PDDc as one draws closer to the outer ejecta due to the higher density in that region. Neither model comes close to thermal or ionization equilibrium in any region, even 1,000 yr after the explosion. The dynamic range for τ is still quite large, about five orders of magnitude.

Model DET (Fig. 3.10) is of special academic interest, because its chemical homogeneity and smooth ejecta density profile reveal the kind of structure that is produced only by 'quasi-analytic' SNR hydrodynamics and the transient properties of the plasma. The radial profiles of $\overline{Z}$, T_e and τ are smooth (panels 3.10 b, c d, f, g and h), and the plasma is very far from thermal or ionization equilibrium. The dynamic range for τ is four orders of magnitude.

Model SCH has a somewhat unique behavior because of its characteristic 'sandwiched' structure (see section 2.2). The shocked ejecta structure below the outer Fe-rich layer is similar to the DDT or PDD models, with the inner regions rich in Fe, Si-S and C-O at progressively higher densities, electron temperatures and ionization timescales. The outer Fe-rich layer has a high density and electron temperature, but the high abundance of He keeps the value of $\overline{Z}$ comparatively low.

The trends that have been observed in these sample models and times can be extrapolated to the rest of the model grid. The structure of the shocked ejecta in the other DEF models is very similar to that of DEFc, with a rapid evolution to CIE in the region dominated by C and O. The PDD models always show more advanced ionization stages for all elements than their DDT counterparts of similar kinetic energy. And all models have substantial electron temperature gradients that increase towards the CD, with a peak electron temperature of a few times 10^7 K. This seems to be in contrast with the drop in mean plasma temperature observed in Dwarkadas and Chevalier, 1998 (see page 30), but it is a logical consequence of the density enhancement effect when self-consistent electron heating is taken into account.

Variations of β and ρ_{AM}

Model DDTe has been chosen to illustrate the effects of the collisionless electron heating at the reverse shock on the structure of the shocked ejecta. The results for the simulated ionization and electron heating processes for the interaction of model DDTe with an AM of $\rho_{AM} = 10^{-24}$ g $\cdot$ cm^{-3} are shown in Figure 3.12, for $\beta = \beta_{min}$, $\beta = 0.01$, and $\beta = 0.1$.

The most striking feature of the models with collisionless electron heating at the reverse shock is the change in the T_e profile. Instead of a monotonic rise from reverse shock to contact discontinuity, the collisionless heating drives T_e to high values just behind the reverse shock, around 10^8 K for $\beta = 0.01$, and 10^9 K for $\beta = 0.1$. The value of T_e then drops towards the CD. The physical reason for this is that, even though the fraction of specific internal energy in the electrons $\varepsilon_e/\varepsilon$ always rises in a fluid element as long as $T_e < T_i$, the ongoing ionization forces this energy to be distributed among an increasingly larger number of electrons, thus lowering the value of T_e (see eqn. 3.7). Eventually, the collisional heating processes might drive $\varepsilon_e/\varepsilon$ to a value high enough for the initial contribution to ε_e from the collisionless heating to be comparatively negligible. In that case, the T_e profile will converge with the profile obtained with $\beta = \beta_{min}$. In model DDTe with $\rho_{AM} = 10^{-24}$ g $\cdot$ cm^{-3} and at such early evolutionary stages, this only happens for small amounts of collisionless electron heating ($\beta = 0.01$), and only in the regions close to the CD. The higher values of T_e in the presence of collisionless electron heating bring about lower values of the mean ionization state (Fig. 3.12 b and f) and ionization timescale (Fig. 3.12 d and h). The lower ionization state is the consequence of the behavior of the ionization rates at high temperatures, which decrease slightly with increasing T_e (see Fig.

Figure 3.12: Shocked ejecta structure vs. radius for model DDTe, with $\rho_{AM} = 10^{-24}\,\mathrm{g \cdot cm^{-3}}$
. Panels a-d correspond to 430 yr after the explosion, and panels e-h to 1000 yr. The three plots for $\overline{Z}$ (panels b, f), T_e (panels c, g) and τ (panels d, h) represent the values obtained with $\beta = \beta_{min}$(solid), $\beta = 0.01$ (dashed) and $\beta = 0.1$ (dash-dotted). All magnitudes as in Figure 3.7.
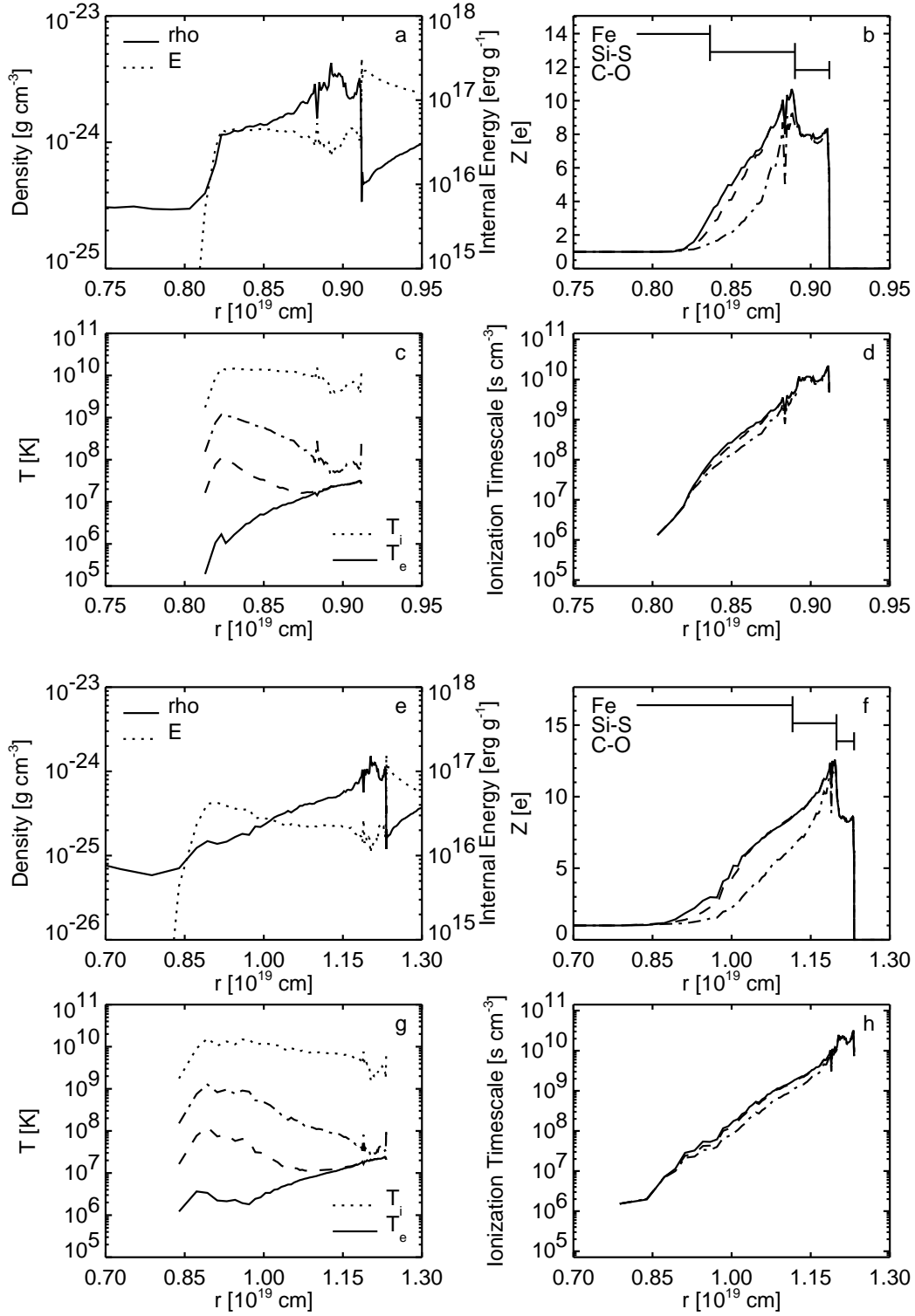
Figure 3.13: Shocked ejecta structure vs. radius for model DDTe, with $\rho_{AM} = 5 \cdot 10^{-24}\,\mathrm{g} \cdot \mathrm{cm}^{-3}$
. Panels a-d correspond to 430 yr after the explosion, and panels e-h to 1000 yr. The three
plots for $\overline{Z}$ (panels b, f), T_e (panels c, g) and τ (panels d, h) represent the values obtained with
$\beta = \beta_{min}$(solid), $\beta = 0.01$ (dashed) and $\beta = 0.1$ (dash-dotted). All magnitudes as in Figure 3.7.

Figure 3.14: Shocked ejecta structure vs. radius for model DDTe, with $\rho_{AM} = 2 \cdot 10^{-25}\,\mathrm{g \cdot cm^{-3}}$. Panels a-d correspond to 430 yr after the explosion, and panels e-h to 1000 yr. The three plots for $\overline{Z}$ (panels b, f), T_e (panels c, g) and τ (panels d, h) represent the values obtained with $\beta = \beta_{min}$(solid), $\beta = 0.01$ (dashed) and $\beta = 0.1$ (dash-dotted). All magnitudes as in Figure 3.7.
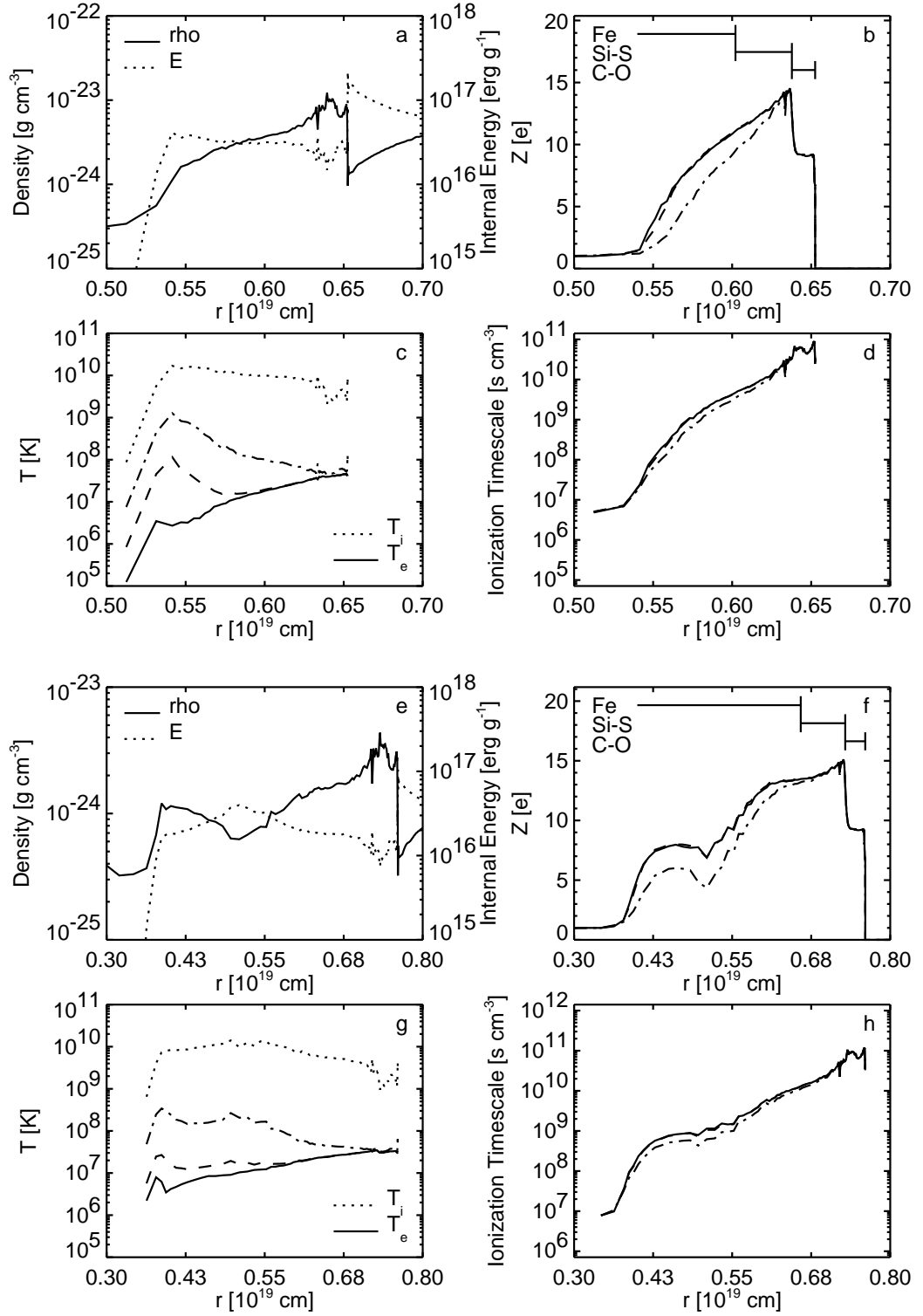
3.6). It takes large deviations in temperature, and therefore large amounts or collisionless electron heating to provoke large deviations in the mean ionization state. The differences in the T_e, $\overline{Z}$ and τ profiles will have a different impact on the models depending on the chemical composition of the affected layers. For model DDTe in particular, note how the ionization state of the C-O buffer is practically the same for all values of β, but varies a lot for the Si-S buffer.

The same model DDTe will be used to illustrate the effects of the variation of the AM density. In Figures 3.13 and 3.14, the result of the interaction of model DDTe with $\rho_{AM} = 5 \cdot 10^{-24}\,\mathrm{g \cdot cm^{-3}}$ and $\rho_{AM} = 2 \cdot 10^{-25}\,\mathrm{g \cdot cm^{-3}}$ is seen for $\beta = \beta_{min}$, $\beta = 0.01$, and $\beta = 0.1$. The hydrodynamics has been scaled following eqns. 3.1, 3.2 and 3.3, and the ionization and heating equations have been integrated as usual. Since M_{ej} and E_k are fixed for each explosion model, the velocities of the fluid elements are unchanged by the scaling, but the times and radii are both affected by a factor $\propto \rho_{AM}^{-1/3}$. This means that a SNR model which evolves in a higher AM density will be in a more advanced dynamic state at any given time, and vice versa for models evolving in lower density AM. Note, for instance, how the reverse shock still has not reached the region dominated by Fe at t=430 yr for $\rho_{AM} = 2 \cdot 10^{-25}\mathrm{g \cdot cm^{-3}}$ (Fig. 3.14 b). For $\rho_{AM} = 5 \cdot 10^{-24}\,\mathrm{g \cdot cm^{-3}}$, on the other hand, the reverse shock has already overtaken the interface between the deflagration and detonation regions in model DDTe at a Lagrangian coordinate of $0.25\,\mathrm{M_\odot}$ (see Fig. 2.2). The higher AM densities also lead to higher densities in the shocked ejecta and an acceleration of the collisional processes of ionization and electron heating. This tends to alleviate the effect of collisionless heating at the reverse shock, speeding up the convergence towards the purely collisional case. For $\rho_{AM} = 5 \cdot 10^{-24}\mathrm{g \cdot cm^{-3}}$, there is very little difference between $\beta = \beta_{min}$ and $\beta = 0.01$, except in the T_e profile in the regions closest to the reverse shock. For lower AM densities, the opposed effect is observed, and the importance of even a small amount of collisionless heating at the reverse shock becomes much greater.

3.5   Discussion of the simulation scheme

3.5.1   Spherical symmetry

The assumption of spherical symmetry in the simulations that have been presented in this chapter is no more than an approximation, and it represents a first step towards the understanding of Type Ia SNRs. In reality, deviations from spherical symmetry are expected to appear in the supernova ejecta, the AM, and the hydrodynamic interaction between both.

Dynamic instabilities

As mentioned in section 3.1.1, the contact discontinuity between shocked ejecta and shocked AM is subject to the Rayleigh-Taylor (R-T) instability. This is crucial to the ionization and heating processes, because it has a direct impact on the density enhancement effect towards the CD, which was found in sections 3.3.2 and 3.4.3 to be determinant for the distribution of electron temperatures and ionization timescales in the shocked ejecta. The development of the R-T instability has been studied extensively with multi-D hydrocodes, first in the framework of self-similar driven waves (Chevalier et al., 1992), and later focusing on Type Ia SNRs by abandoning the power law ejecta profile in favor of an exponential profile (Dwarkadas, 2000; Wang and Chevalier, 2001). The conclusion of these studies is that the R-T instability gives rise to the formation of 'fingers' or 'mushroom caps' of shocked ejecta that penetrate into the shocked AM, grow and then are disrupted by the

shear in the flow (the Kelvin-Helmholtz instability). The instability saturates at an early age, and the result is a region of mixed ejecta and AM around the 'contact discontinuity', which ceases to exist as such, and a mild distortion of the reverse shock. The mixing region has not reached the forward shock for any of the scenarios explored in these works. While the average density profile is significantly smoothed by the instabilities (see Figure 4 in Wang and Chevalier, 2001), the R-T fingers of shocked ejecta still retain a higher density than the shocked AM, so the results from the 1D simulations presented in this chapter might not deviate much from a more realistic case.

Ambient medium

Among the possible inhomogeneities in the AM, it is possible to pinpoint the presence of a density gradient due to a smooth transition in the properties of the ISM, dense clumps of material associated with molecular clouds or star forming regions, and rarefied cavities like the remnants of previous supernova explosions or wind-blown bubbles. These disturbances are of more concern in evolved remnants, as the radius becomes comparable to the mean scales of variation within the ISM, but any particular object might be affected at any evolutionary stage. The impact on the dynamics of the shocked ejecta is not expected to be important unless the disturbance of the AM is very large.

Supernova ejecta

The observational evidence for aspheric Type Ia SN ejecta was discussed in section 2.4, together with the recent 3D explosion models. So far, there are no strong arguments, either observational or theoretical, that suggest an important global asphericity for the majority of Type Ia SNe. The local inhomogeneities in ejecta composition, however, are another issue. Regions of Ni-rich and C-O-rich material are mixed throughout the ejecta in most 3D models, and they might give rise to density inhomogeneities as the ^{56}Ni releases energy in its decay to ^{56}Fe and forces the Ni-rich regions to expand. This is known as the 'Ni bubble effect', and it results in pockets of low density Fe-rich regions surrounded by dense Fe-poor regions in the SN ejecta. This effect was pointed out in Basko, 1994, and its consequences for the dynamics of the ejecta in young Type Ia SNRs were explored in Blondin et al., 2001, using 3D hydrodynamics. According to this work, the presence of two phases (dense, Fe-poor and rarefied, Fe-rich) in the SN ejecta leads to an increase in turbulence and mixing, but the extent of this increase depends on the amount of ^{56}Ni that is initially distributed in the regions that will form the bubbles. Qualitatively, a lower ionization timescale is expected for Fe due to the lower density, and this should have a noticeable impact on the X-ray emission from the shocked ejecta.

The dynamic interaction of over-dense clumps in the ejecta with the structure of a Type Ia SNR was studied in Wang and Chevalier, 2001. Under favorable circumstances, these clumps could survive the passage of the reverse shock and even reach the forward shock. Recent studies have shown that both in Tycho (Hwang et al., 2002) and SN1006 (Long et al., 2003), the ejecta almost reach the forward shock, a fact that cannot be explained by dynamic instabilities in the SNR alone. The presence of clumps in the ejecta may provide an explanation for this, but it is difficult to find a physical mechanism that can form clumps with the required characteristics.

The consequences that all these deviations from spherical symmetry would have on the ionization and heating processes in the shocked ejecta of Type Ia SNRs are very difficult to estimate. An in-depth analysis would require the coupling of an ionization code like that described in appendix B to a multi-D hydrocode. In spite of this, the 1D simulations

Model	$\rho_{AM} = 10^{-24}\,\mathrm{g \cdot cm^{-3}}$	$\rho_{AM} = 5 \cdot 10^{-24}\,\mathrm{g \cdot cm^{-3}}$
DEFa	$3.5 \cdot 10^{10}\,\mathrm{s}$	$2 \cdot 10^{10}\,\mathrm{s}$
DEFc	$2.9 \cdot 10^{10}\,\mathrm{s}$	$1.6 \cdot 10^{10}\,\mathrm{s}$
DEFf	$2.7 \cdot 10^{10}\,\mathrm{s}$	$1.2 \cdot 10^{10}\,\mathrm{s}$
PDDe	-	$1.5 \cdot 10^{11}\,\mathrm{s}$

Table 3.3: Values of t_{rad} for those models with $t_{rad} \leq 5,000\,\mathrm{yr}\,(1.578 \cdot 10^{11}\,\mathrm{s})$.

that have been presented here have the potential to become a useful analysis tool for the interpretation of X-ray spectra, if they are used carefully (see chapter 5).

3.5.2 Adiabaticity

There are two mechanisms capable of breaking down the adiabaticity of the models: radiative losses in the ejecta and nonlinear acceleration processes at the shocks.

Radiative losses in the ejecta

Radiative losses are not important for the solar composition plasma inside SNRs within time scales of a few thousand years. Plasmas rich in heavy elements, however, will radiate at a faster rate, and the losses might have noticeable effects on the dynamics much earlier in the evolution of the SNR. In general, radiative losses are composition and ionization state dependent, so they can only be evaluated if the ionization state of the plasma is known. Within the simulation scheme described in sections 3.3.1 and 3.4.2, it is not possible to include the effect of radiative losses in the hydrodynamics due to the fact that hydrodynamics and ionization calculations are performed in sequence, not in parallel. In spite of this, it is possible to make a rough evaluation of the radiative losses *a posteriori*, that is, once the ionization and heating calculations are done. This is not a self-consistent approach, because radiative cooling is a runaway process: as a fluid element loses energy, it becomes denser and cooler, circumstances that favor an increase in the radiative energy loss rate. In any case, the fluid elements in the shocked ejecta can be monitored for signs of a significant energy loss, and limits of reliability can be set on the simulations.

We have estimated the radiative losses for the shocked ejecta using the atomic data from Summers and McWhirter, 1979, and the procedure described in Laming, 2001b. The necessary routines to adapt the atomic data to the problem at hand were kindly provided by M. Laming (2001, private communication). For evaluation purposes, we define the time scale for the onset of radiative losses, t_{rad}, as the time when the calculated *a posteriori* losses exceed 10% of the specific internal energy ε in a number of layers that amount to at least 5% of the total ejecta mass M_{ej}. The value of t_{rad} increases with increasing values of β, because hotter plasma radiates at a slower rate, and decreases with increasing density, because denser plasma radiates at a faster rate. The models with a value of $t_{rad} \leq 5,000\,\mathrm{yr}$ are listed in table 3.3. Not surprisingly, the models with the strongest density enhancement effect towards the CD are more prone to undergo significant radiative losses. From these, only the DEF models are affected at an early age for moderate values of ρ_{AM}. In all cases where radiative cooling is important, it happens only in the outermost (densest) fluid elements of the ejecta.

The runaway nature of radiative cooling makes the validity of the models beyond t_{rad} difficult to determine. For the DEF models, the material that cools down radiatively and thus no longer contributes to the X-ray spectrum will be mostly C and O, so the line

emission from the rest of the elements should not be severely affected. In the case of model PDDe, the losses will be restricted to the O-rich region in the outer ejecta. In all cases, radiative cooling is confined to a very small volume, and the effect on the overall dynamics of the SNR should not be important (see Hamilton et al., 1986a, and Hamilton et al., 1986b). It is also worth noting that no optical or UV emission from radiatively cooled ejecta has been detected either in Tycho or SN1006 (Smith et al., 1991), in contrast to some Galactic core-collapse SNRs like Cas A, which do display such emission (Fesen et al., 2001). In conclusion, t_{rad} can be taken as a conservative limit on the validity of the Type Ia SNR models that have been presented in this chapter.

Nonlinear acceleration processes at the shock waves

Supernova remnants have been suspected for a long time of being the source of cosmic rays (CRs). The strong, high Mach number shocks are capable, at least in theory, of accelerating charged particles to very high energies through diffusive 2nd order Fermi processes. These accelerated particles will then escape the SNR, becoming cosmic rays and carrying an amount of energy which will depend on the details of the acceleration process. If this amount of energy is a significant fraction of the shock ram energy, compression ratios will be higher and post-shock plasma temperatures will be lower than predicted by the Rankine-Hugoniot relations. The effect of the particle acceleration processes on the dynamics of SNRs is sometimes referred to as cosmic ray pressure.

The impact that this CR-modified dynamics would have on the thermal X-ray emission from SNRs was studied by Decourchelle et al., 2000, in the context of self-similar driven waves. The effect was found to be important for the shocked AM, but small for the shocked ejecta, implying efficient particle acceleration at the forward shock and little or no acceleration at the reverse shock. In later works (Blondin and Ellison, 2001; Ellison et al., 2004), increasingly sophisticated techniques were used to couple the acceleration processes to the hydrodynamics.

As in the case of the deviations from spherical symmetry, the effects that these energy losses would have on the ionization and heating processes in the shocked ejecta are difficult to estimate without performing a full-blown set of self-consistent non-adiabatic calculations. The evidence from previous works, however, suggests that the adiabatic hypothesis might be a good first approximation for the ejecta in Type Ia SNRs under most circumstances.

3.5.3 Absence of thermal conduction

In Bedogni and D'Ercole, 1988, the impact of electron thermal conduction was explored in the context of young SNRs, assuming thermal equilibration between ions and electrons and neglecting the effects of magnetic fields and turbulences in the plasma. Under these assumptions, thermal conduction was found to have a profound impact on the dynamics of SNRs. However, the complex modified structure computed in this work did not compare well with observations, so the existence of some sort of inhibition mechanism was suggested by the authors themselves. Realistic numerical modeling of thermal conduction is difficult, because it involves detailed knowledge of the distribution of the magnetic field inside the remnant, and the process is very sensitive to local density inhomogeneities (see Velázquez et al., 2004, and references therein).

In the case of the ejecta in young Type Ia SNRs, the effects of thermal conduction are not expected to be important, for a number of reasons. First, thermal equilibration between ions and electrons does not happen anywhere in the ejecta, except in some extreme

cases at late stages (see section 3.4.3). The lower electron temperatures in the absence of temperature equilibration will delay the onset of thermal conduction effects, even in the models with a significant amount of collisionless electron heating at the reverse shock. Second, for those young SNRs where detailed radio observations exist, the magnetic field has been found to be turbulent (see Figure 8 in Reynoso et al., 1997, for the Tycho SNR). In such an environment, thermal conduction becomes anisotropic and occurs mainly in the direction parallel to the magnetic field, which should also reduce the effects on the overall SNR structure. And third, some time is required for thermal conduction to modify the SNR structure, so the effect is expected to be more important for old remnants. In fact, most of the recent studies of SNR dynamics including thermal conduction have focused on old SNRs (several tens of thousands of years), and they generally ignore the presence of ejecta, finding that the main effect of thermal conduction is to limit the temperature of the inner shocked AM (Cui and Cox, 1992; Velázquez et al., 2004).

Chapter 4

From SNR to SN: models for the thermal X-ray emission from the shocked ejecta

'Delenda Carthago est!'

Marcus Porcius Cato (234-149 B.C.), in every speech before the Senate.

4.1   Spectral characterization of the shocked ejecta

X-ray spectra of young SNRs are often difficult to analyze and interpret. In the previous chapter, it has been shown that each fluid element in the shocked ejecta has a different density, ionization state, electron temperature and composition. As a consequence of this, each region of the ejecta will have a different contribution to the total spectrum, and so will each chemical element. A convenient way to measure these contributions is the emission measure (EM) for element X, defined as

$$EM_X = \int_{V_{sh}} n_X n_e dV \qquad (4.1)$$

where V_{sh} is the volume of shocked ejecta. For identical physical conditions and a common history, elements with equal emission measures contribute equally to the total spectrum. But the electron temperature T_e and ionization time scale of the plasma τ, which play a key role in the generation of thermal NEI spectra, are different for each fluid element, resulting in different spectra produced by fluid elements with identical emission measures. This problem can be solved in the shocked AM by introducing distribution functions, plots of T_e and τ versus EM (see Borkowski et al., 2001, for an application to SNRs that are in the Sedov expansion phase). The use of this approach for the shocked ejecta, however, would call for an individual distribution function for each chemical element due to the nonuniform chemical composition. An incomplete, yet meaningful, description can be achieved by taking the first moment of the distribution functions and calculating, for each element X, an emission measure averaged electron temperature $\langle T_e \rangle_X$ and ionization timescale $\langle \tau \rangle_X$. (Another quantity, an ionization timescale averaged electron temperature is generally necessary for a reliable modeling of X-ray spectra, but it is less important than $\langle T_e \rangle_X$ and $\langle \tau \rangle_X$). The averaged quantities $\langle T_e \rangle_X$ and $\langle \tau \rangle_X$ will be used here to describe the average physical conditions in the shocked ejecta, and studying their behavior will

help to understand the integrated spectra from the shocked ejecta that will be presented in section 4.2

4.1.1   Grid models

Fixed β and ρ_{AM}

The evolution of the emission measure for the elements C, O, Si, S, Ar, Ca, Fe and Ni is shown in Figures 4.1 and 4.2 for the sample model subgrid (DET, SCH, DEFa, DEFc, DEFf, DDTa, DDTbb, DDTc, DDTe, PDDa, PDDc and PDDe), between 20 and 5000 years after the explosion. The canonical values have been taken for ρ_{AM} ($10^{-24}\,\mathrm{g\cdot cm^{-3}}$) and β (β_{min}). Following a standard procedure in X-ray spectroscopy, the emission measure has been normalized by $4\pi D^2$, taking a fiducial distance to the emitting source of $D = 10\,\mathrm{kpc}$ for these theoretical calculations.

The contributions from the different chemical elements to the ejecta spectra depend strongly on both the composition profile of the models and their dynamic evolution. The density enhancement effect towards the contact discontinuity makes the chemical elements in the outer layers of the ejecta more prominent than those in the inner layers, so the Fe emission measure is generally much less than might be expected on the basis of a Type Ia elemental composition alone.

At this point, it is important to stress that the fitting of model spectra to X-ray observations of SNRs cannot constrain directly the mass of a given element that is present in the shocked ejecta. The quantity that is determined in this way is rather the emission measure of the element. For the chemically inhomogeneous ejecta models of the grid, the ratios of emission measures are time-dependent, and they can differ from the ratios of ejected masses by several orders of magnitude. This relatively low prominence of Fe in spectra of Type Ia SNR candidates might have been noticed on a number of occasions, often accompanied by inordinately high apparent abundances of other elements (see Hendrick et al., 2003, and Lewis et al., 2003). The estimated ejected masses of various elements, which often indirectly rely on the assumption that chemical abundances are proportional to the fitted EM for each element in the spectrum, are difficult to reconcile with the yields of theoretical explosion simulations.

The rise in the emission measure plots of all the models that can be observed around $t = 10^{11}\,\mathrm{s}$ is due to the propagation of the reverse shock after it rebounces at the center, reheating and recompressing the ejecta; this rise happens earlier and is more gradual for the elements in the inner layers than for those in the outer layers.

The detonation model DET is the only one whose spectrum is clearly dominated by Fe at all times, with very minor contributions from all other elements except Ni. As usual, the behavior of model SCH is different from that of the other grid models: the EM plots show an abrupt transition at $t \simeq 100\,\mathrm{yr}$. Before that time, the ejecta emission is in an Fe-dominated phase while the reverse shock is propagating through the He detonation layer. Afterwards, the ejecta enter an O-dominated phase, prompted by the secondary density peak that forms at the interface with the rest of the exploded WD in model SCH (see section 3.3.2). During the first phase, there is an important contribution to the total ejecta EM from shocked He, which is not shown in the plot.

The discrepancy between EM and ejected mass is most dramatic in the deflagration models (Fig. 4.1), whose spectra are completely dominated by C and O, with emission measures of Fe about two orders of magnitude lower at all times, even though the ejected mass of Fe is higher than that of C or O. Note, however, that the peak value of $EM_{Fe}/4\pi D^2$ in the DEF models is about $10^8\,\mathrm{cm^{-5}}$, not very different from other models and only a

factor 5 lower than the most energetic DDT and PDD models. Radiative cooling could reduce considerably the EM of C and O in the deflagration models at late times, as was pointed out in section 3.5.

In the more energetic DDT and PDD models, Fe takes over only after a few hundred years, with important contributions of Si and S throughout the SNR evolution. Less energetic DDT and PDD models have large values of EM_O, and Fe never comes to dominate their ejecta spectrum for $t < 5000\,\mathrm{yr}$.

Since ionization and electron heating proceed faster at higher densities, the corresponding $\langle T_e \rangle_X$ and $\langle \tau \rangle_X$ plots in Figures 4.3, 4.4, 4.5 and 4.6 are also affected by the enhancement towards the contact discontinuity and the reverse shock rebounce. The gradient of the T_e and τ radial profiles that was discussed in section 3.4.3, together with the
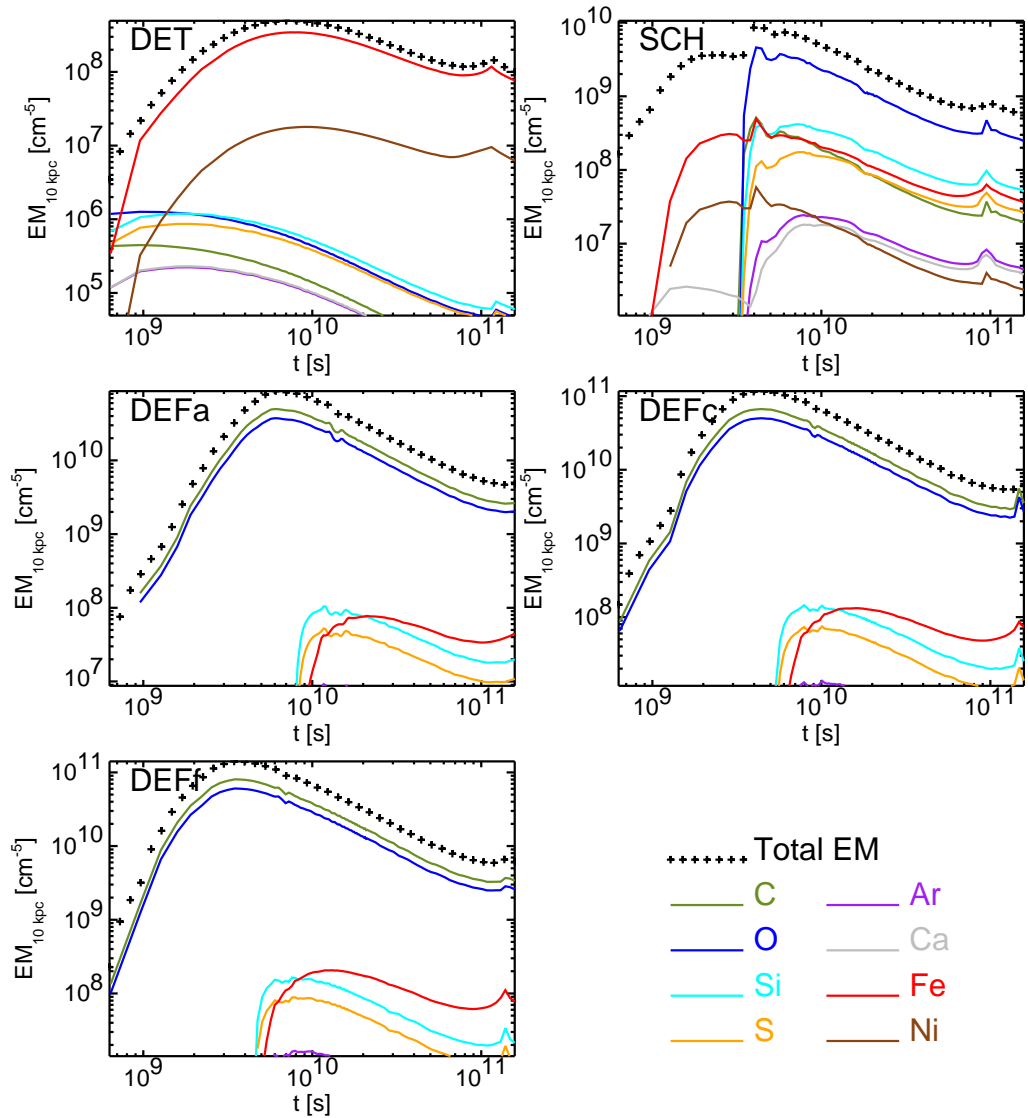

Figure 4.1: Evolution of the emission measure normalized to a fiducial distance of 10 kpc ($EM_{10kpc} = EM/4\pi D^2$, with $D = 10\,\mathrm{kpc}$), for the sample DET, SCH and DEF models. The total emission measure represented in the plots (crosses) corresponds to all the elements present in the ejecta, not just those that are represented here.
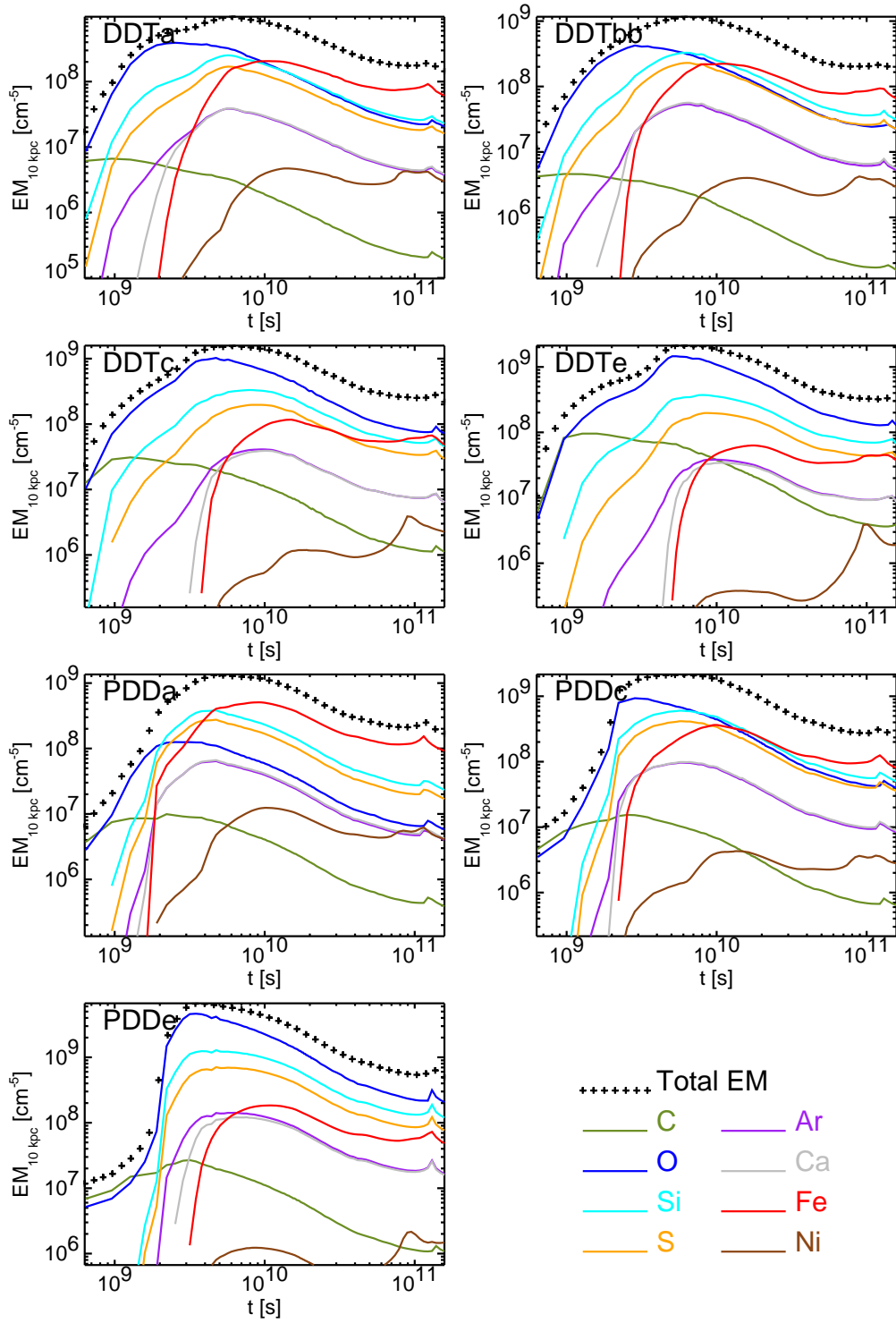
Figure 4.2: Evolution of the ejecta emission measure for the sample DDT and PDD models. Magnitudes and normalization are as in Figure 4.1.

chemical structure of the models, results in a crude ordering of the elements in $\langle T_e \rangle_X$ and $\langle \tau \rangle_X$, with the innermost elements being colder and having lower ionization timescales, and the outermost elements being hotter and having higher ionization timescales. This rough ordering of the elements can be broken in some particular cases. The anomalous behavior of some of the plots (for instance, $\langle T_e \rangle_{Ni}$ and $\langle \tau \rangle_{Ni}$ in the DDT and PDD models or $\langle T_e \rangle_{Ca}$ and $\langle \tau \rangle_{Ca}$ in SCH) is due to the averaging in EM and can be understood by comparing the curves with the chemical composition profiles of Figs. 2.1 and 2.2. As the reverse shock advances into regions with a much higher concentration of a given element, the newly shocked (and therefore cooler and less ionized) layers soon dominate the emission measure, and the averaged quantities shift their values accordingly.

The evolution of $\langle T_e \rangle_X$ and $\langle \tau \rangle_X$ in the DET model is an example of what can be expected for a simple ejecta structure. In this particular case, the plots for C, O, Si, S, Ar and Ca are not very significant quantitatively because of the low emission measure of these elements that can be found in the ejecta of DET (Fig. 4.1), but qualitatively the
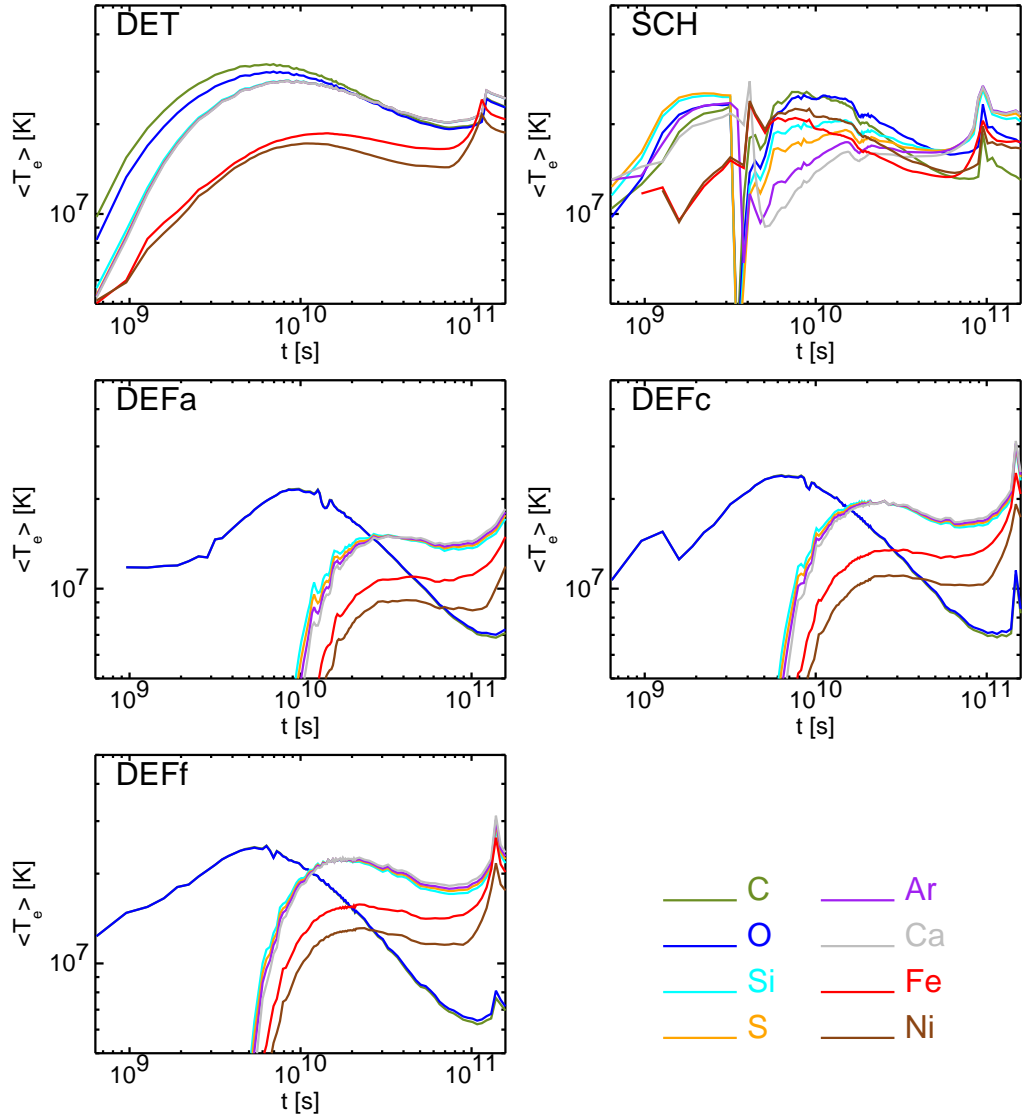

Figure 4.3: Evolution of the emission measure averaged electron temperature, $\langle T_e \rangle$, for the sample DET, SCH and DEF models. The plots for C and O overlap almost completely in the DEF models.
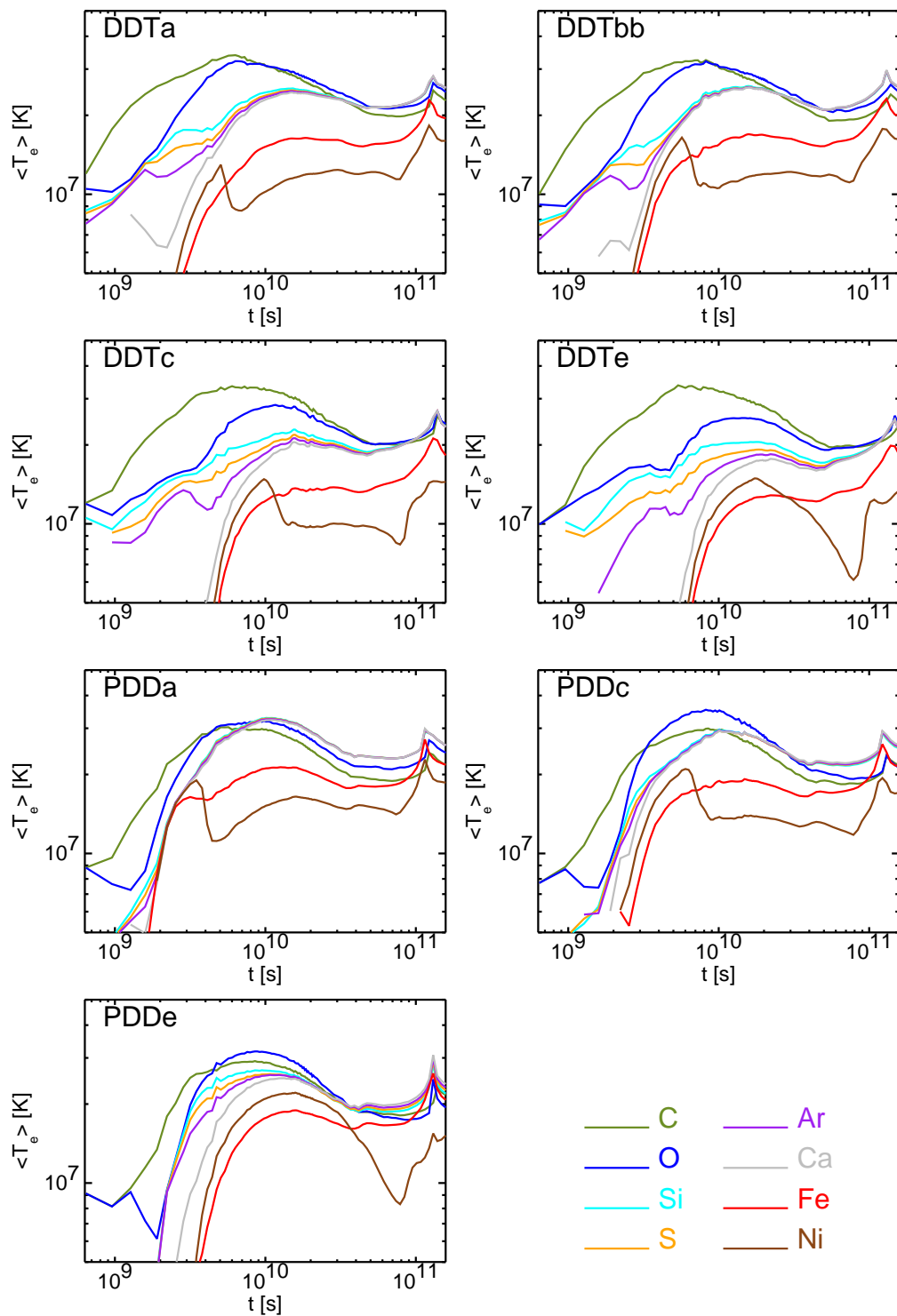
Figure 4.4: Evolution of the emission measure averaged electron temperature, $\langle T_e \rangle$, for the sample DDT and PDD models.

ordering of the elements is plain to see. The SCH model, on the contrary, is an example of what can be expected for a more complicated ejecta structure, with the order of the elements in $\langle T_e \rangle$ and $\langle \tau \rangle$ being altered as the reverse shock enters the inner ejecta.

In the deflagration models, C and O are always at a higher τ and initially hotter than other elements. The values of $\langle T_e \rangle_{C,O}$ have a pronounced drop at later times because in these models the density of the C-O buffer is high enough to bring the electron temperature close to equilibration with the ion temperature (see Fig. 3.8 g). After this partial temperature equilibration, the electrons just cool due to adiabatic expansion of this region of the SNR, while the rest of the elements are still being heated by the reverse shock.

Iron is generally hotter and at a higher τ in the energetic DDT and PDD models than in the DEF models. The stronger density enhancement effect of the PDD models results in higher ionization timescales for all the elements than in the DDT models. This is easy to see for O, Si and S, which are more abundant in the outer ejecta. The averaged electron temperatures are not affected so clearly, even though they are lower in general for most elements in the DDT models.

Variations of β and ρ_{AM}

Increasing the value of β has little influence on EM_X and $\langle \tau \rangle_X$ for the elements in the shocked ejecta, even for the low values of ρ_{AM} which enhance the effect of collisionless heating at the reverse shock. The reason for this was discussed in section 3.4.3, and it has to do with the fact that the ionization rates $I_{X^q}(T_e)$ present a plateau for high values of T_e (see Fig. 3.6 for an example). While significant deviations can be seen in the mean ionization state of some elements at early times in the innermost layers of shocked ejecta, the spatial and temporal integration that is performed to calculate EM_X and $\langle \tau \rangle_X$ minimizes the impact of these deviations. The behavior of $\langle T_e \rangle_X$, however, is an entirely different matter. In Figure 4.7, $\langle T_e \rangle_X (t)$ is plotted for model DDTe, with $\rho_{AM} = 10^{-24}\,\mathrm{g \cdot cm^{-3}}$ and three different values of β. As could be expected from the radial T_e profiles in Figures 3.12, 3.13 and 3.14, the effect of the collisionless heating at the reverse shock on $\langle T_e \rangle_X$ is dramatic, specially for the elements that are more abundant in the innermost layers. For small amounts of collisionless heating ($\beta = 0.01$), the dispersion in averaged electron temperatures for the different elements is significantly reduced, while for large amounts of collisionless heating ($\beta = 0.1$), the ordering of the elements is reversed, resulting in hot Fe and Ni and cooler intermediate mass elements.

Changing the value of ρ_{AM} has a more immediate impact on the emission measures and averaged quantities, mainly through the hydrodynamic scaling laws provided in section 3.3.1. Approximate values for $EM_X(t)$ and $\langle \tau \rangle_X (t)$ at a given ρ_{AM} of interest can be obtained by applying the appropriate scaling factors which result from eqns. 3.1, 3.2 and 3.3. These factors are $\rho_{AM}^{-1/3}$ for the t axis (straight from eqn. 3.3), ρ_{AM} for $EM_X(t)$ ($n_X n_e dV$ goes like $r^{-3-3+3} = r^{-3}$, then apply eqn. 3.1 to scale r) and $\rho_{AM}^{2/3}$ for $\langle \tau \rangle_X (t)$ ($n_e dt$ goes like $r^{-3}t$, then apply eqns. 3.1 and 3.3). These approximate scalings are accurate within a factor 2 for $2 \cdot 10^{-25}\,\mathrm{g \cdot cm^{-3}} \leq \rho_{AM} \leq 5 \cdot 10^{-24}\,\mathrm{g \cdot cm^{-3}}$, but they might break down for values of ρ_{AM} outside this range. A perfect agreement between calculated and scaled quantities is not to be expected, because hydrodynamical scaling does not apply to the ionization and electron heating processes, which are involved in the calculation of $EM_X(t)$ and $\langle \tau \rangle_X (t)$ through the electron density n_e. The effect of a change of ρ_{AM} on the electron temperatures is more complex: some elements keep the shape of the $\langle T_e \rangle_X (t)$ plots, but others suffer minor deviations. Even though these deviations do not alter the ordering of the elements, and an approximate scaling law might also be found for $\langle T_e \rangle_X (t)$, such a law would have little practical use. Whereas an accuracy of a factor

2 is reasonable for magnitudes like EM_X and τ_X, with dynamic ranges that span several orders of magnitude, changes of a factor 2 are too large compared with the dynamic range of T_e, which is about 2 orders of magnitude in the X-ray regime.

4.1.2 Off-grid models

The hydrodynamics, ionization and electron heating processes of the off-grid models follow the same general trends as those of the grid models that have been examined with detail in chapter 3. The density of the shocked ejecta always peaks at the contact discontinuity, and so do the ionization timescales and the electron temperatures, unless there is a significant amount of collisionless electron heating at the reverse shock. In that sense, the temporal evolution of the emission measure and the emission measure averaged quantities for the W7 and 5p0z22.25 models seen in Figs. 4.8, 4.9 and 4.10 is similar to that of the grid models that have been reviewed in section 4.1.1. However, important differences arise
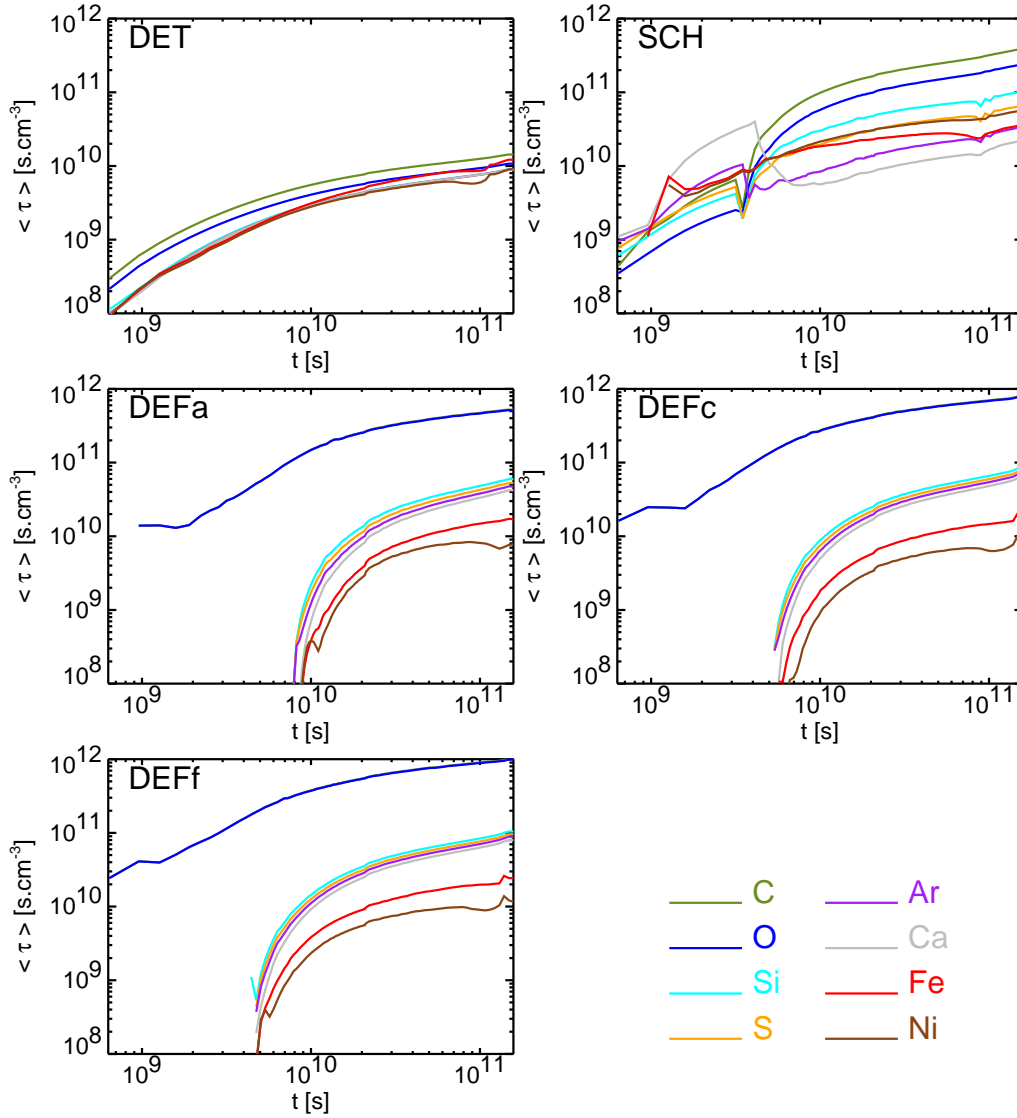

Figure 4.5: Evolution of the emission measure averaged ionization timescale, $\langle\tau\rangle$, for the sample DET, SCH and DEF models. The plots for C and O overlap almost completely in the DEF models.
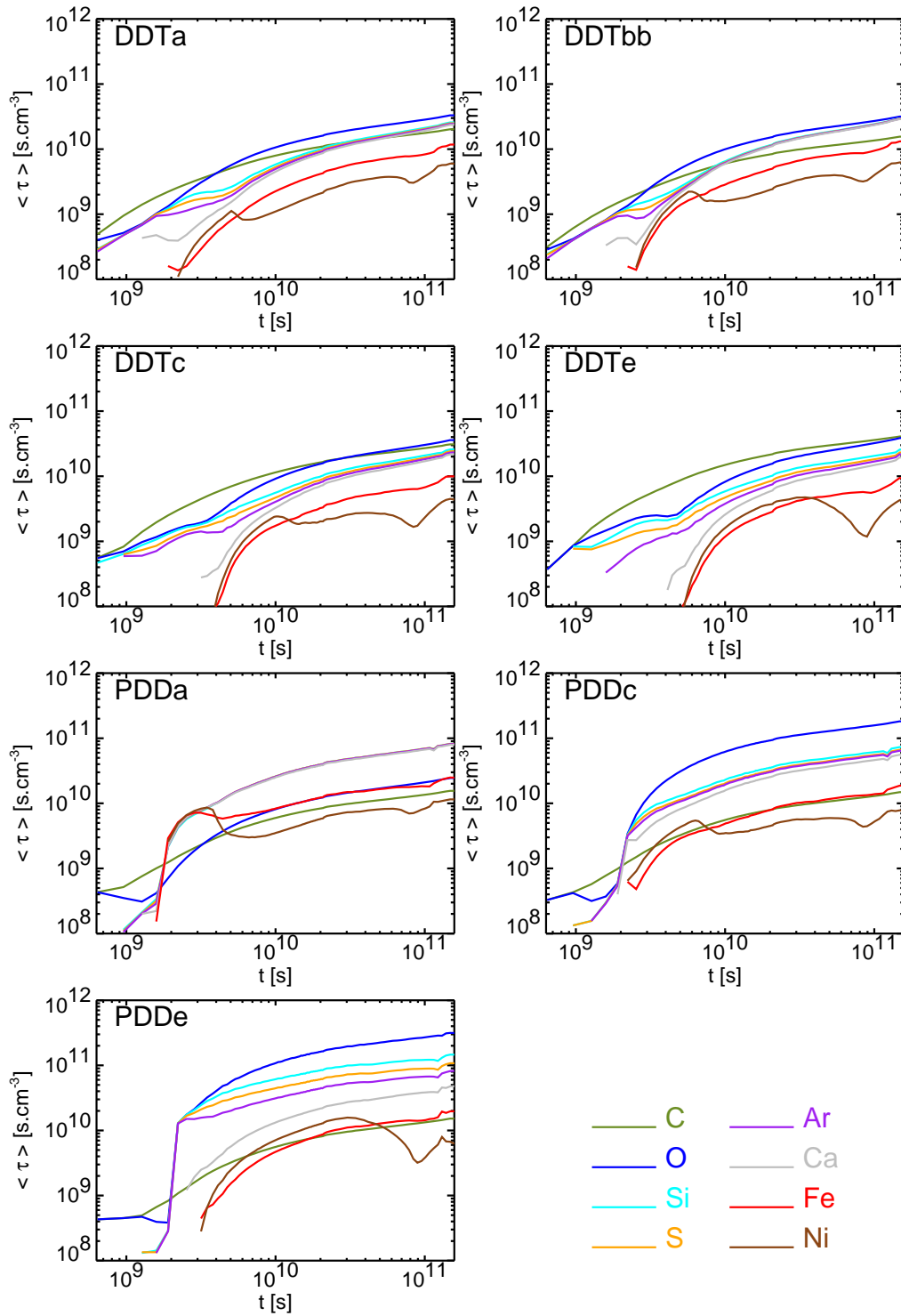
Figure 4.6: Evolution of the emission measure averaged ionization timescale, $\langle \tau \rangle$, for the sample DDT and PDD models.
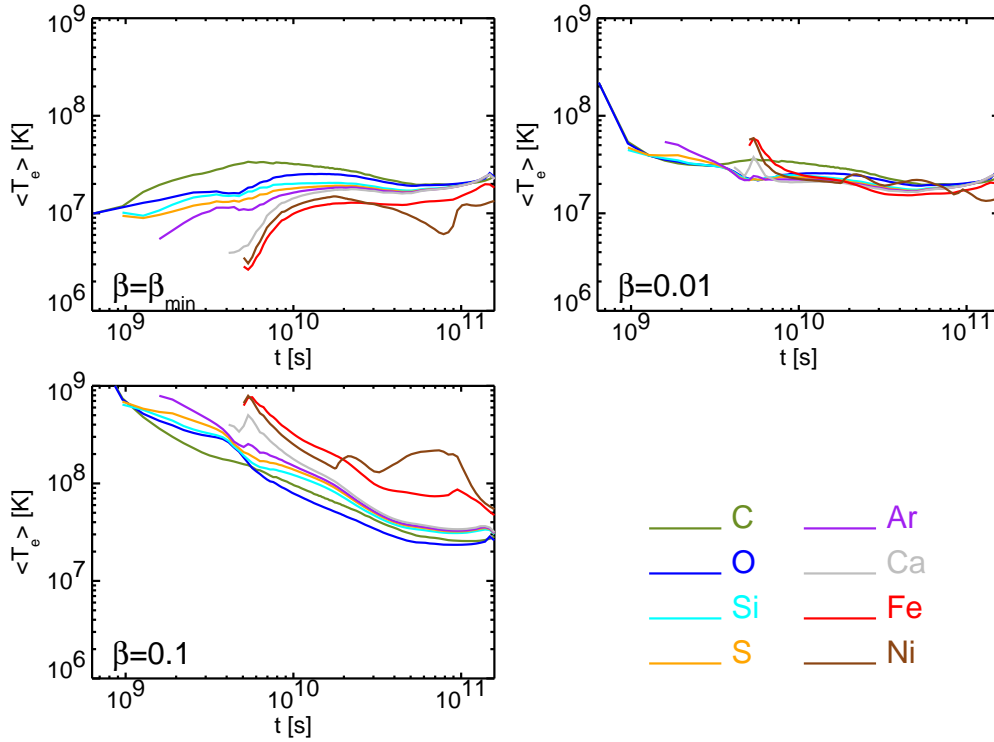
Figure 4.7: Evolution of $\langle T_e \rangle_X$ for model DDTe, with $\rho_{AM} = 10^{-24} \, \mathrm{g} \cdot \mathrm{cm}^{-3}$; $\beta = \beta_{min}$(top left), $\beta = 0.01$ (top right) and $\beta = 0.1$ (bottom left). The top left panel is the same as in figure 4.4.

for those off-grid models that result from 1D mappings of 3D calculations, due to the high degree of mixing between burned and unburned material in 3D calculations, which alleviates the effect of the density enhancement at the contact discontinuity and alters the rough ordering of the chemical elements in $\langle T_e \rangle_X$ and $\langle \tau \rangle_X$.

The best examples of this are models DEF3D30b, DDT3DA and b_30_3d_768, which have a higher degree of mixing than the 3D SCH models. In these models, the ratios of emission measures are much closer to the ratios of ejected masses, with C, O and Fe as the dominant elements and remarkably high emission measures of Ni. The dispersion in the values of $\langle T_e \rangle_X$ and $\langle \tau \rangle_X$ is greatly reduced when compared to 1D models, and, except for Ca and Ar, almost all the elements have similar spectral properties. The strange behavior of model DEF3D30b at $t > 7 \cdot 10^{10} \, \mathrm{s}$ is due to the reverse shock reaching the lump of unejected material at the center of the SNR (see the discussion on section 2.4).

The spectra of the 3D SCH models is strongly dominated by Fe at all times, in contrast to the 1D SCH model, where the contribution of Fe drops below those of O and Si after the initial phase (see Fig 4.1).

4.2 Model spectra

Once the physical properties of the shocked plasma are known, the X-ray spectrum emitted by the shocked ejecta can be calculated with a spectral code. For the present work, an updated and revised version of the code described in Hamilton et al., 1983 (henceforth, the Hamilton & Sarazin code, HS code) has been used. The code inputs are the values of T_e, n_e, n_i, the chemical composition of a fluid element, f_X, and the charge state distribution of each chemical element present, f_{X^q}; the code output is the energy spectrum associated
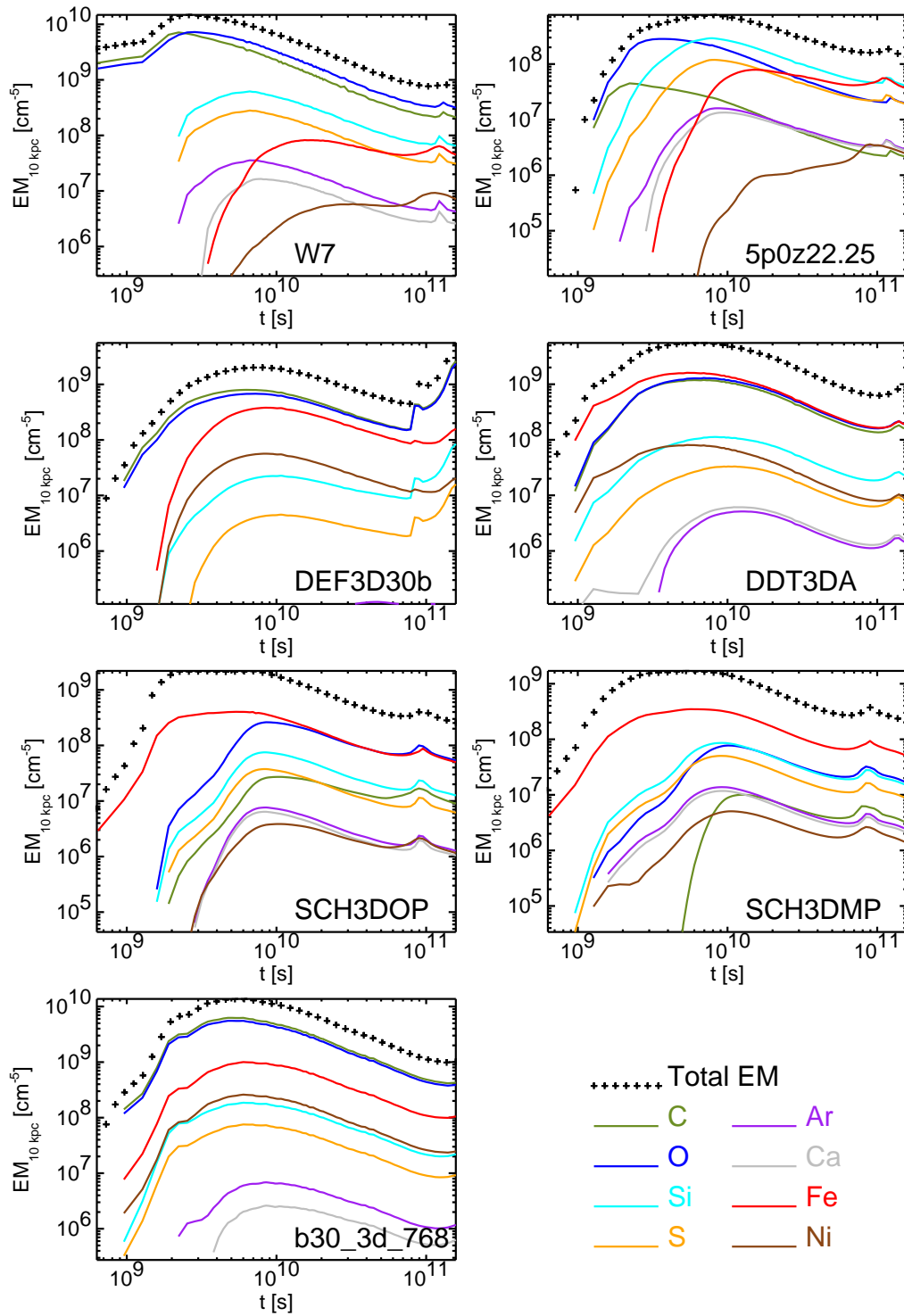
Figure 4.8: Evolution of the ejecta emission measure for the off-grid explosion models. Magnitudes and normalization are as in Figure 4.1.
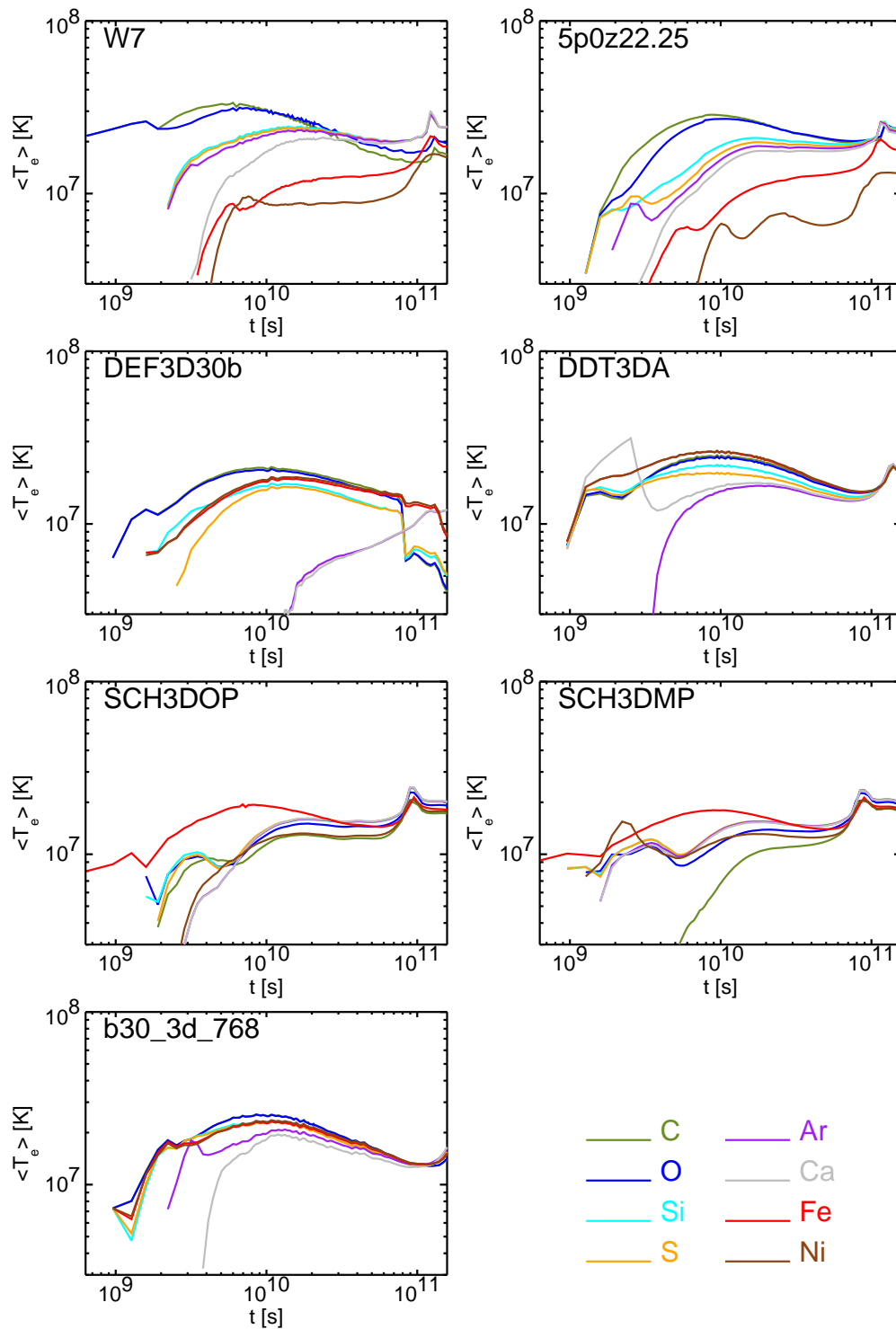
Figure 4.9: Evolution of the emission measure averaged electron temperature, $\langle T_e \rangle$, for the off-grid models.
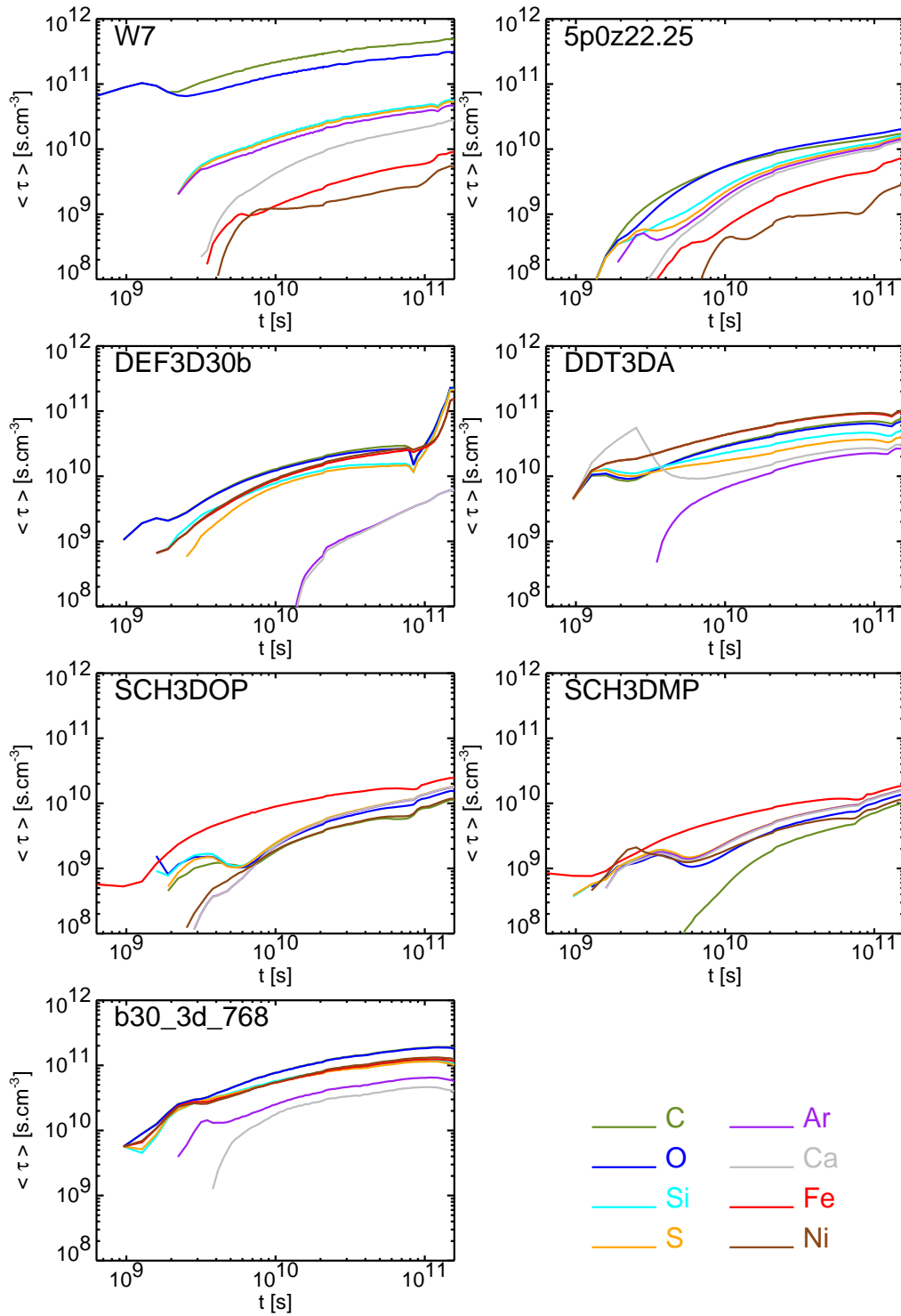
Figure 4.10: Evolution of the emission measure averaged ionization timescale, $\langle\tau\rangle$, for the off-grid models.

with the fluid element. By adding together the output from several fluid elements, the spectrum of a given region of the shocked ejecta can be readily obtained and convolved with the instrumental response of any appropriate instrument.

Some of the comments that were made in section 3.4.2 on the quality of the atomic data for the ionization calculations also apply to spectral codes. The atomic data that are included in each spectral code determine the conditions under which it can be used, an issue that has become a major concern for spectral models in X-ray astronomy. Some codes, for instance, make the implicit assumption that the plasma is at or near collisional ionization equilibrium (CIE), and are therefore inadequate for the study of young SNRs. The HS code has been chosen for the problem at hand because it is the most complete and updated spectral code that is compatible with NEI plasmas. It calculates free-free, free-bound and bound-bound (line) emission at photon energies above 0.1 keV from all ions of the elements H, He, C, N, O, Ne, Mg, Si, S, Ca, Fe and Ni. The processes included in the HS code are collisional excitation of valence or inner shell electrons, radiative and dielectronic recombination, collisional ionization of inner shell electrons, and radiative cascades following any of these processes. No atomic data for Ar emission are available within the code, so the model spectra do not include Ar emission, even though this element is present in the ejecta and has been taken into account in all the ionization and electron heating calculations. A rough estimate for the accuracy of the line emissivities would be around 20%, but there is an enormous range (Raymond, 2001). A more detailed discussion of the HS code, its atomic data and the procedure that is used to calculate the model spectra can be found in appendix C.

4.2.1 Grid models

Fixed β and ρ_{AM}

The integrated synthetic spectra for the sample subgrid models are presented in figures 4.11 and 4.12, for $\rho_{AM} = 10^{-24} \, \mathrm{g \cdot cm^{-3}}$ and $\beta = \beta_{min}$, 430, 1000, 2000, and 5000 years after the explosion. The spectra have been calculated assuming a fiducial distance to the object of $D = 10 \, \mathrm{kpc}$, and they have been convolved with the response matrix of the *XMM-Newton* EPIC-MOS1 camera for visualization purposes. This instrument offers the best spectral resolution currently available for an X-ray CCD camera, and is therefore well suited to study line emission from diffuse objects like SNRs. The spectra do not include any contribution from shocked AM or nonthermal emission, and they are not modified to account for interstellar absorption. The most prominent lines and line complexes have been labeled to facilitate the interpretation of the spectra: O Lyα at 0.65 keV, Si Heα at 1.85 keV, S Heα at 2.45 keV, Ca Heα at 3.88 keV and Fe Kα at 6.4 keV (see Tab. 3.2 for a list of lines and a discussion on notation).

The spectrum of the DET model has only the faintest traces of Si and S emission, the rest being completely dominated by the Fe L complex around 1 keV (individual lines are unresolved by the EPIC-MOS instrument) and the Fe Kα line, with very little continuum. The SCH model, on the other hand, shows line emission from O, Si, S, Ca and Fe at all times, with a higher level of continuum contributed mainly by C, O, Si and S.

The spectra of the deflagration models are always dominated by C and O, to the point that the C and O continua 'veil' the lines of the other elements at early times. This effect is more important for the less energetic model DEFa, which has more C and O and less Fe and intermediate mass elements. Initially, the O Lyα line is prominent in all the DEF models, but as T_e in the external ejecta layers drops (see section 4.1.1), it becomes less conspicuous. This temperature drop also results in a lower level of continuum from C and
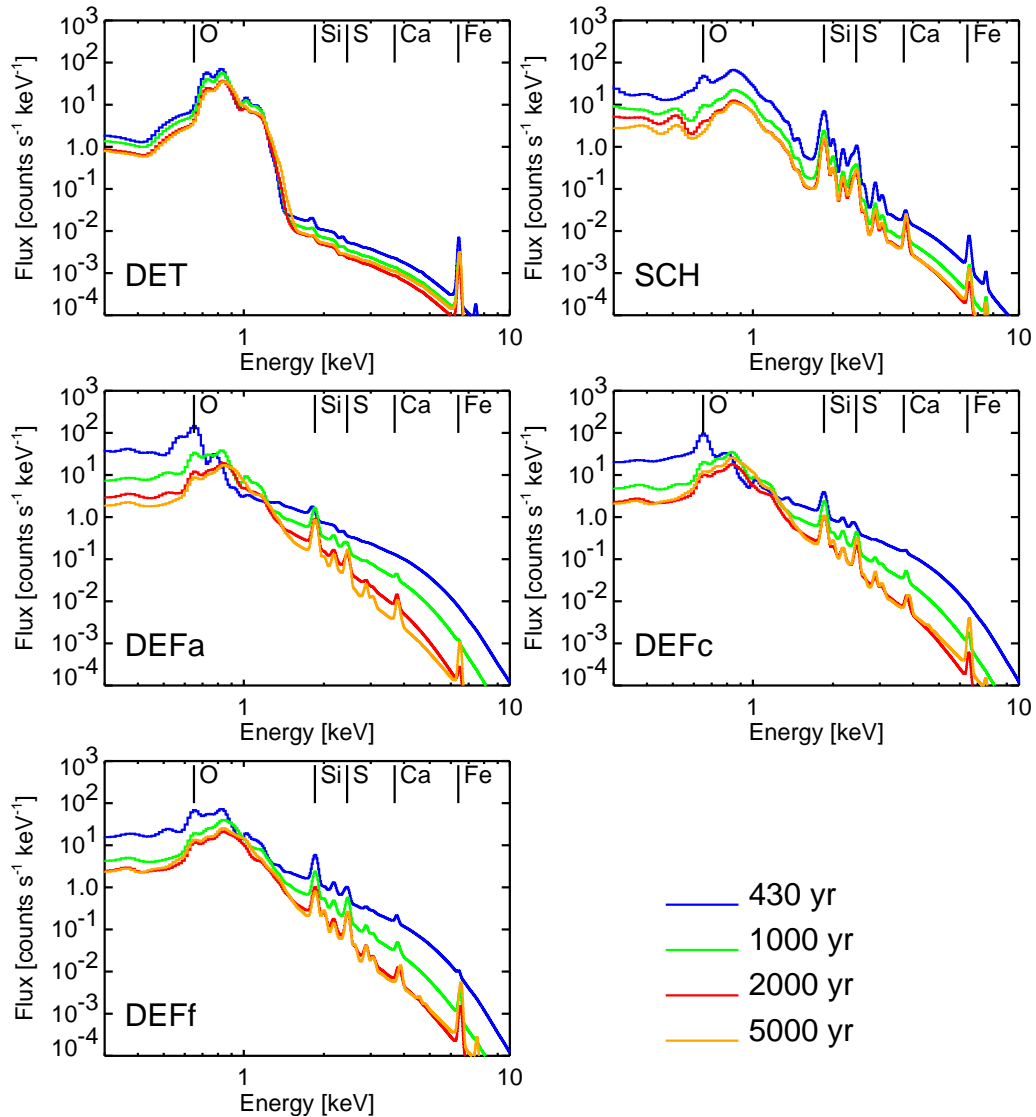
Figure 4.11: X-ray spectra from the shocked ejecta of the sample DET, SCH and DEF models, 430, 1000, 2000 and 5000 yr after the SN explosion.

O, which allows line emission from Si and S to come through, and makes the spectra softer at later times. In the more energetic DEFc and DEFf models, the Fe Kα line also becomes important at later times.

The PDD models have richer line spectra than the DDT models, due to the more advanced ionization state of the elements that are close to the contact discontinuity (see discussion in section 3.4.3). The Lyα lines from H-like ions of Si and S are clearly seen at 2.0 and 2.6 keV in all the PDD models, with S Lyα becoming fainter in the less energetic PDDe model. These lines are absent from the DDT models. The O Lyα line, on the other hand, is more prominent in the DDTc and DDTe models, which have more H-like O in the outer ejecta than their low-energy PDD counterparts. DDTe and DDTc are the only grid models where the Mg Heα line at 1.34 keV can be clearly seen. Even though the amount of Mg in the ejecta is low for these models (of the order of $10^{-4}\,\mathrm{M_\odot}$), its location in the outermost ejecta results in significant Mg Heα emission at early times. The strength of the Fe Kα line depends on the location of Fe within the ejecta. For the most energetic DDT
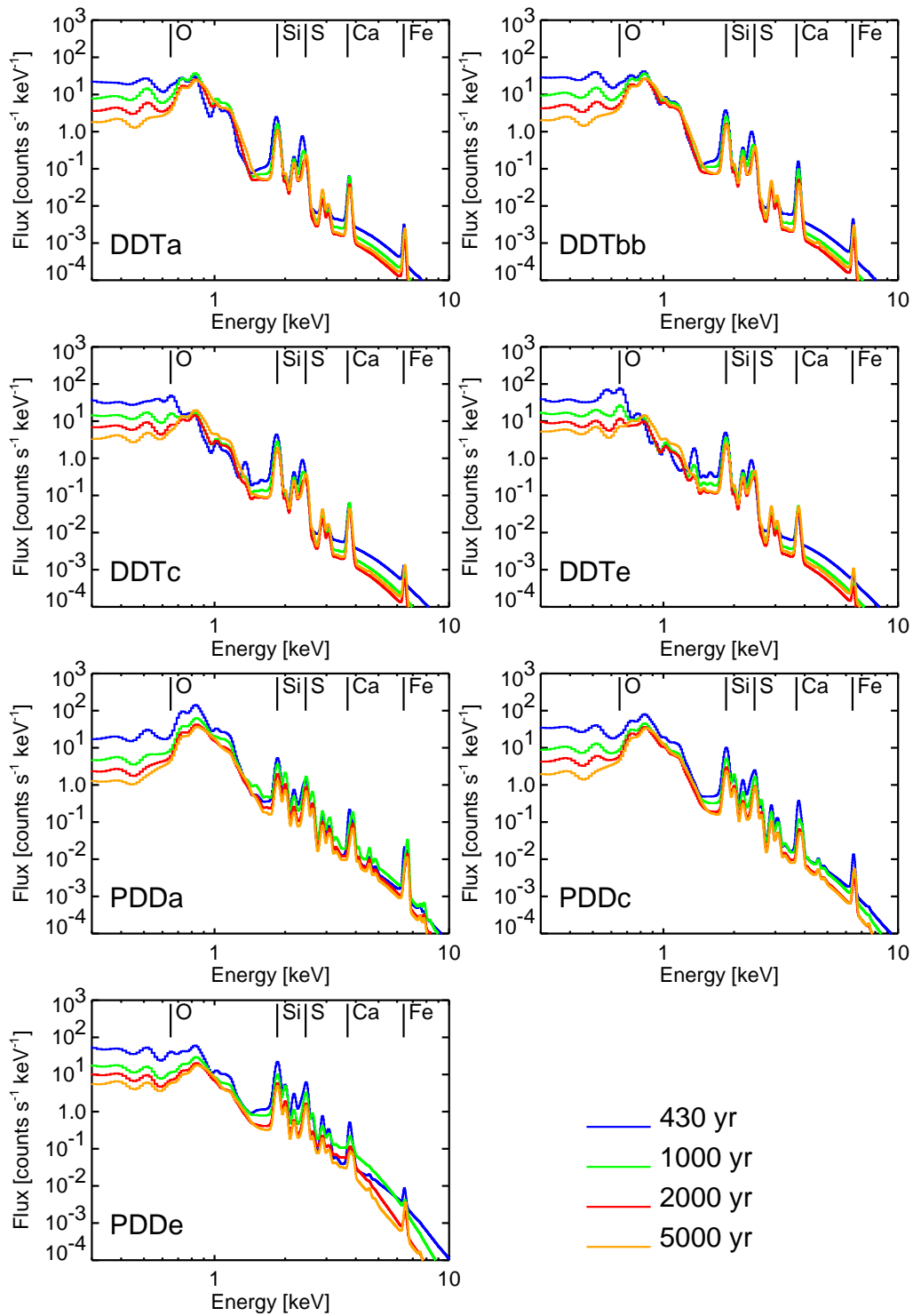
Figure 4.12: X-ray spectra from the shocked ejecta of the sample DET, SCH and DEF models, 430, 1000, 2000 and 5000 yr after the SN explosion.

and PDD models, Fe Kα is conspicuous at all times, while in the less energetic models it rises above the continuum only after a few thousand years, when the Fe-rich regions in the inner ejecta have attained a sufficiently high electron temperature.

The observation made in section 4.1.1 that several models have lower emission measures of Fe than might be expected for the ejecta of a Type Ia SN explosion acquires a new relevance when it is viewed in the light of the emitted spectra. Those models with high EM_O and low EM_{Fe} in particular, like DDTe, PDDe, SCH and the DEF models, show a conspicuous O emission together with weak Fe L and Fe Kα emission at early times. These spectra defy the standard procedure for typing supernovae from their remnants (Hughes et al., 1995), and could be easily mistaken for core-collapse SNRs.

Figure 4.13: X-ray spectra from the shocked ejecta of the DDTe model, 430, 1000, 2000 and 5000 yr after the SN explosion, for the values of $\rho_{AM} = 10^{-24}\,\mathrm{g \cdot cm^{-3}}$ (top panels), $5 \cdot 10^{-24}\,\mathrm{g \cdot cm^{-3}}$ (middle panels) and $2 \cdot 10^{-25}\,\mathrm{g \cdot cm^{-3}}$ (bottom panels); with $\beta = \beta_{min}$ (left panels) and $\beta = 0.1$ (right panels). Note the different flux scale for the bottom panels.

Variations of β and ρ_{AM}

In Fig. 4.13, the spectra of model DDTe are presented for three values of ρ_{AM} (10^{-24}, $5 \cdot 10^{-24}$ and $2 \cdot 10^{-25}\,\mathrm{g \cdot cm^{-3}}$) and two values of β (β_{min} and 0.1). A preliminary inspection reveals that changing the value of ρ_{AM} has profound effects on the calculated spectra. Higher or lower densities in the shocked ejecta lead to more or less advanced ionization states for all the elements, and even if the values of EM_X and $\langle\tau\rangle_X$ can be obtained by an approximate scaling (see section 4.1.1), the spectra look very different, because the presence of different ions excites the emission of different lines. At $\rho_{AM} = 5 \cdot 10^{-24}\,\mathrm{g \cdot cm^{-3}}$, for instance, the more advanced ionization state of Fe leads to a higher flux in the Fe L complex, which interferes with the O Ly α and Mg Heα emission. The increase in the Fe Kα line, on the other hand, is due to the higher temperatures in the ejecta (compare Figs. 3.12 and 3.13). The flux in the O Heα line at 0.56 keV that can be seen at early times for $\rho_{AM} = 10^{-24}\,\mathrm{g \cdot cm^{-3}}$ disappears at higher values of ρ_{AM}, because He-like O is ionized more rapidly. The rise of the Lyα lines of Si and S is also plain to see, as well as a shift in the centroid of the Ca Kα line due to a smaller contribution from the neighboring Ca Heα . The shape and flux of the continuum emission also change. At lower densities, these effects are reversed. The Fe Kα and Fe L complex emission virtually disappears, revealing the Ne Heα and Ne Lyα lines at 0.9 and 1.0 keV. The O Heα line becomes more important than O Lyα, and the Lyα and Heβ lines of Si and S vanish almost completely, as well as the Ca Kα line. The continuum is flattened and the emitted flux is generally lower at all energies.

In contrast with the global effects of a variation of ρ_{AM}, changes in the amount of collisionless heating at the reverse shock have a different impact on different elements, as expected in a model with stratified ejecta. For $\rho_{AM} = 10^{-24}\,\mathrm{g \cdot cm^{-3}}$, the flux in the Fe K$\alpha$ line, which probes material of higher T_e and lower τ than the Fe L complex, is increased by almost two orders of magnitude by setting β to 0.1. None of the other elements seems to be affected at this density, even though model DDTe has a significant amount of S, Si and Ca in the inner ejecta. This increase in the Fe Kα flux becomes less pronounced with time, and is accompanied by a slight change in the shape of the continuum. For $\rho_{AM} = 5 \cdot 10^{-24}\,\mathrm{g \cdot cm^{-3}}$, the continuum is unaffected and the increase of the Fe Kα line flux is reduced to less than an order of magnitude at early times, disappearing completely at late times. At $\rho_{AM} = 2 \cdot 10^{-25}\,\mathrm{g \cdot cm^{-3}}$, however, the collisionless electron heating has a more noticeable effect. The shape of the spectrum is not changed at low energies, but the flux is somewhat lower at early times for $\beta = 0.1$. At high energies, the continuum increases and the Fe Kα line has a spectacular increase.

4.2.2　Off-grid models

The spectra emitted by the shocked ejecta from the off-grid models are presented in Fig. 4.14 for $\rho_{AM} = 10^{-24}\,\mathrm{g \cdot cm^{-3}}$ and $\beta = \beta_{min}$, 430, 1000, 2000, and 5000 years after the explosion.

The spectra of the 1D off-grid models W7 and 5p0z22.25 are qualitatively similar to those of the low energy DDT and PDD models from the grid. Being a deflagration, W7 has a higher continuum level from the dense buffer of unburned C and O in the outer ejecta, as well as a prominent O Lyα line at early times, but its line emission from Si and S is closer to that of PDDc or PDDe than to the DEF models of the grid. The ionization state of Si and S in model 5p0z22.25 is comparable to that of the DDT models. A common feature of these models is that their Fe Kα and Fe L emission is low compared to the DDT or PDD models of similar kinetic energy. This is due to a more abrupt drop of the Fe
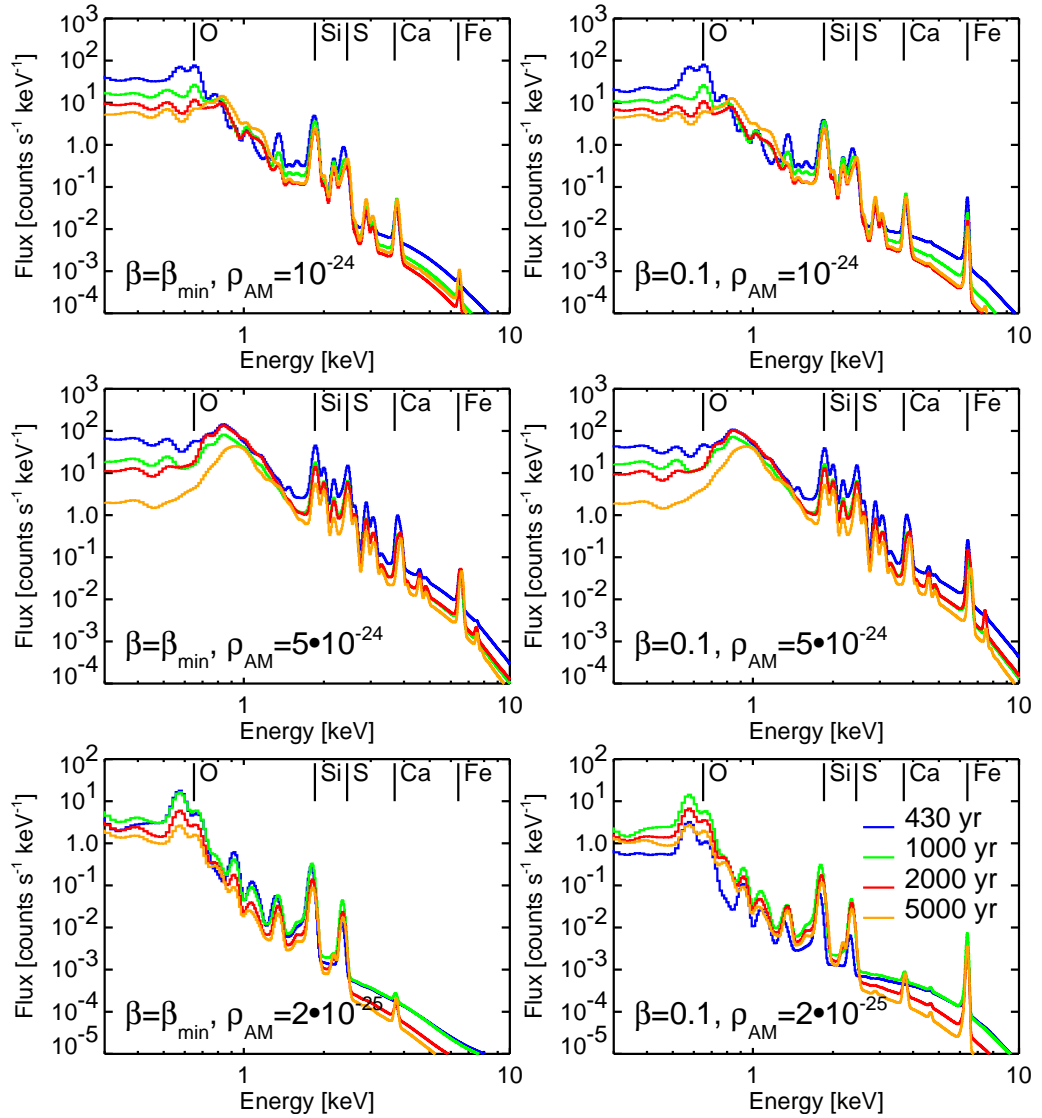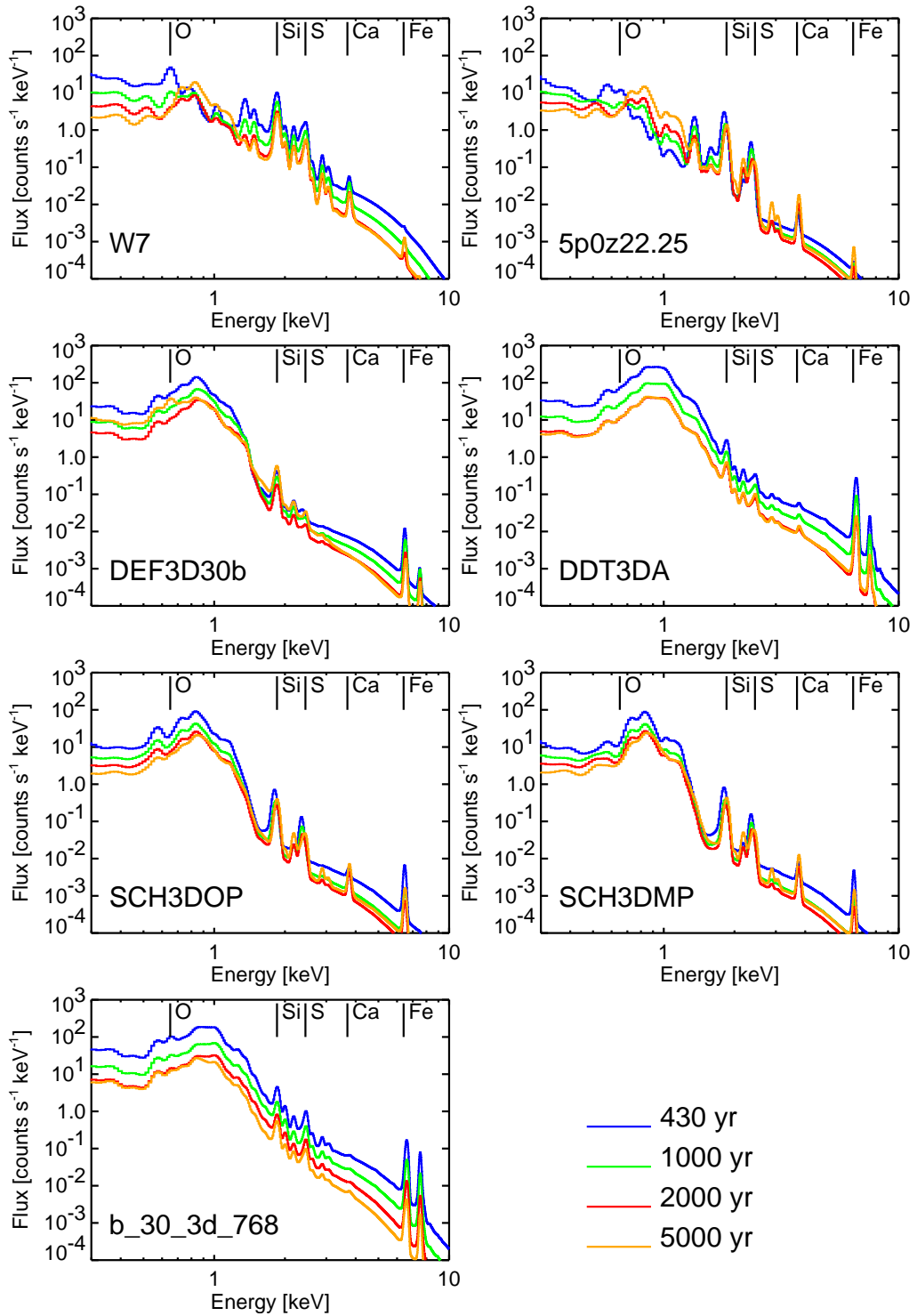
Figure 4.14: X-ray spectra from the shocked ejecta of the off-grid models, 430, 1000, 2000 and 5000 yr after the SN explosion.

abundance in the region dominated by Si and S (compare Figures 2.2 and 2.4). The Fe Kα flux could increase in the presence of collisionless electron heating at the reverse shock. The Mg Heα line is prominent in both models, specially at early times, in part because of the low Fe L flux.

The 3D Chandrasekhar models, on the other hand, have spectra that are very different from all the cases that have been reviewed up to now. They are characterized by a very high flux in the Fe L complex and Fe Kα line, a bright Ni Kα line at 7.48 keV and a high level of continuum, mostly from C, O, Fe and Ni. Line emission from Si and S is comparatively weak, and Ca is almost completely veiled by the continuum. It is remarkable that these characteristics are shared by models calculated using completely different techniques, like DDT3DA and b_30_3d_768. For these models, the effect of a change of β is hardly noticeable, except at very low values of ρ_{AM}, because the chemical composition profile is quite homogeneous, and the spectrum is dominated at all times by the dense outer ejecta.

The 3D sub-Chandrasekhar models also have inordinately high fluxes in the Fe L complex, but Si and S line emission is much stronger, and Ca rises above the continuum at late times.

4.3   Ejecta emission vs. total spectrum: a piece in the jigsaw

It has to be stressed that the discussion of the previous section is merely a comparison among theoretical model spectra under ideal circumstances. In reality, the integrated X-ray spectrum of a Type Ia SNR is the sum of, at least, three distinct contributions: thermal emission from the shocked ejecta, thermal emission from the shocked AM and nonthermal emission from the particles accelerated at the shocks (see section 3.1.2). All the components are in their own turn modified by interstellar absorption, which reduces the flux at low energies, specially below 1keV. Separating the different contributions to the total spectrum is far from being trivial, and it requires a detailed knowledge of the characteristics of each component and the relationship they have with each other. The degree of success that is achieved in the separation of the components will determine the amount of information that can be learned about the shocked ejecta emission.

Shocked AM emission

The spectrum emitted by the shocked AM is generated in the same way as the spectrum emitted by the shocked ejecta: bremsstrahlung, recombination and collisional excitation in a low-density plasma out of thermal and ionization equilibrium. If the assumptions of adiabaticity and spherical symmetry hold, the spectrum can be calculated using the same procedure. In the case of the shocked AM, all the fluid elements have the same chemical composition, that is, solar abundances or those appropriate to describe the AM of the SN progenitor system. For a solar composition AM, the electron pool will be dominated at all times by H and He, meaning that $\overline{Z}$ can be assumed to be 1.08 for the shocked plasma at $T_e \geq 1.6 \cdot 10^5 \, \mathrm{K}$ (Mazzotta et al., 1998) and the ionization and electron heating processes (i.e., eqns. 3.9 and 3.10) are no longer coupled above that temperature.

The thermal X-ray emission from the shocked AM in adiabatic, spherically symmetric SNRs described by the Sedov solution was studied with detail in Borkowski et al., 2001. In that work, shocked AM spectra were calculated as a function of postshock plasma temperature T_s, postshock electron temperature T_{es} and ionization age τ_0, defined as the product of the postshock electron density and the SNR age. These three parameters provide all the information that is necessary to generate model spectra: the postshock

temperatures T_s and T_{es} are related by the amount of collisionless heating at the reverse shock[1], and τ_0 measures the SNR age and the unshocked AM density (for details, see Borkowski et al., 2001). In contrast with the shocked ejecta, the fluid elements of the shocked AM attain the highest density after the passage of the forward shock, then they expand adiabatically. As a result, the ionization timescale peaks behind the forward shock, and, in the absence of collisionless heating, so does the electron temperature (cf. Figs. 2 and 4 in Borkowski et al., 2001). The calculations described in Borkowski et al., 2001, are available as the 'Sedov' spectral model in the XSPEC software package (Arnaud, 1996).
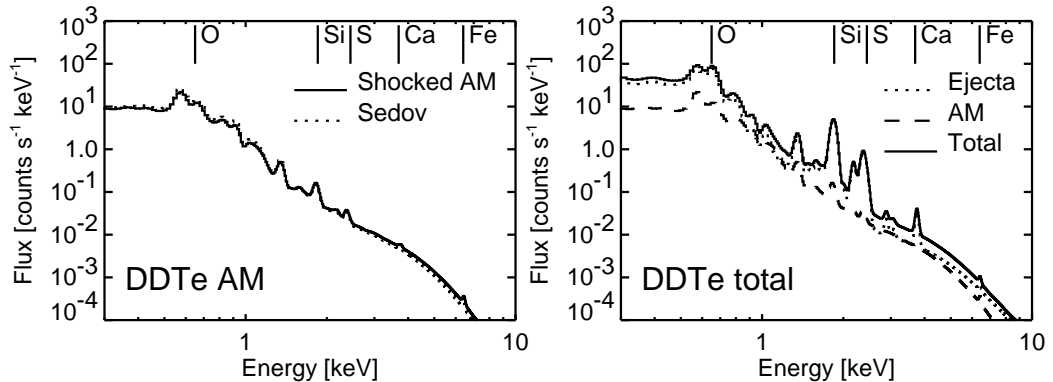

Figure 4.15: Left: spectrum of the shocked AM for the DDTe model at $t = 430\,\mathrm{yr}$, and output of the Sedov model in XSPEC with the parameters calculated from the hydrodynamic simulation of DDTe at $t = 430\,\mathrm{yr}$. Right: total thermal X-ray spectrum of the DDTe model at $t = 430\,\mathrm{yr}$. In all cases, the reference values for ρ_{AM} and β have been used.

In the left panel of Fig. 4.15, a comparison is made between synthetic spectra for the shocked AM calculated using the procedure described in sections 3.3, 3.4 and 4.2 and the spectra obtained from the Sedov model in XSPEC. The spectra are calculated for model DDTe, 430 yr after the explosion. The parameters for the Sedov model can be set from the hydrodynamic calculations alone, assuming $\overline{Z} = 1$ and a solar composition for the unshocked AM. The values of T_s and τ_0 can be readily calculated from eqns. 3.5, 3.6 and 3.7, and $T_{e,s}$ can be set at will depending on the desired amount of collisionless electron heating at the forward shock (in the example, no collisionless heating was assumed). The normalization parameter of the Sedov model spectrum is calculated from the total emission measure of shocked AM, which can also be derived from the hydrodynamic simulations. The agreement between the spectrum from the hydrodynamic, ionization and heating calculations and the output of the Sedov model is remarkable, to the point of suggesting the systematic use of the Sedov model to compute shocked AM emission instead of the cumbersome detailed calculations of our simulation scheme.

The interplay between AM and ejecta spectra merits a few comments. In the course of the evolution of the SNR, the total EM of the shocked AM increases as more and more material enters the forward shock, while the total shocked ejecta EM peaks some time after the explosion and then decreases (see section 4.1). For the spectra, this means that the total emitted flux of the shocked ejecta will drop below that of the shocked AM at some point. When the spectral features of the shocked ejecta emission (continuum shape,

---

[1] Note that the definition of β in eq. 3.8 ($\beta = T_{e,s}/T_{i,s}$) is not equivalent to the definition of β in Borkowski et al., 2001, ($\beta = T_{e,s}/T_s$), though they both represent the amount of collisionless electron heating at a shock wave.

line fluxes and line centroids) become impossible to determine from the total spectrum, the SNR ceases to be 'young', as defined in section 3.1.2. For the case of model DDTe 430 yr after the explosion (right panel of Fig. 4.15), the line emission is contributed almost exclusively by the ejecta, with the AM supplying some of the continuum. With a different value for ρ_{AM}, the relative contributions of ejecta and AM to the spectrum at a given time would change.

It is important to note that, according to Decourchelle et al., 2000, the energy losses due to particle acceleration at the shocks affect the dynamics of the shocked AM, and therefore the shocked AM spectrum, in a profound way (see discussion in section 3.5). Wherever the effect of cosmic ray acceleration is important for the dynamics of the shocked AM, the Sedov model might be a reliable model for the shocked AM emission, but in any case, the parameters for the Sedov model derived from the 1D adiabatic hydrodynamic simulations will not be valid.

Nonthermal emission

Nonthermal emission from the particles accelerated at the shock fronts can take the form of nonthermal bremsstrahlung or synchrotron radiation. In both cases, the emitted spectrum in the X-ray range is a high energy continuum (see section 3.1.2). Nonthermal emission has been identified as a significant contribution to the spectra of some SNRs, first that of SN 1006 (Koyama et al., 1995) and then many more, including Tycho, Kepler, Cas A and RCW 86 (see Petre, 2001, and references therein). In most of these cases, synchrotron radiation seems to be more important than nonthermal bremsstrahlung (for a discussion in the case of RCW 86, see Rho et al., 2002).

Sophisticated spectral models exist for both the spatially integrated and spatially resolved X-ray synchrotron emission from SNRs, which can be constrained by the flux and spectral index of the object at radio wavelengths (see Reynolds, 1998, Dyer, 2001, for details on the models; also Dyer et al., 2001; Dyer et al., 2004, for an application to the *ASCA* observations of SN1006). In contrast to the thermal emission from the shocked AM, there is no way to estimate the contribution of synchrotron emission to the total spectrum of a SNR from within the simulation scheme described in chapter 3, which relies on the assumption of adiabaticity. In that sense, the amount of synchrotron emission is independent of the modeling of the thermal X-ray emission of each individual object, and will have to be estimated in an independent way. Sometimes this can be done from the spectral index or the morphology of the emission at high energies, but not in all cases (see Dyer, 2001).

4.4   Considerations on the spectral fitting of thermal X-ray spectra

In a recent paper on the analysis of a *Chandra* observation of SN1006 it is said: 'thermal fitting in general of (...) X-ray SNR spectra is a treacherous and uncertain business; in the face of calibration uncertainties, oversimplified models and less-than-ideal atomic data, it is difficult to make unassailable assertions' (Long et al., 2003). This section will be devoted to review and discuss the complexities of this 'treacherous and uncertain business', with an emphasis on the situations and circumstances that might pose specific difficulties for the spectral analysis of the ejecta emission.

The limitations of X-ray detectors

The data obtained by the CCD detectors of modern X-ray observatories like *Chandra* and *XMM-Newton* are subject to many uncertainties. Even though their spectral and spatial resolutions represent a spectacular improvement over past missions, they are still not capable of exploiting the full richness of information contained in the spectra of young SNRs (for an example, see Fig. C.1).

Calibration is complicated, specially at low photon energies, to the point that it can effectively reduce the energy range available for spectral analysis. In addition, it is precisely at low energies that the spectral resolution of CCD detectors is worse and the effects of interstellar absorption are strongest. This could be critical for those ejecta models which are rich in C and O, whose distinctive spectral features are at low energies.

Depending on the location of the source and the duration of the observation, poor counting statistics may also be a concern, specially at high energies, where both the emitted flux and the effective area of the detectors drop steeply. A weak Fe Kα line, for instance, might be difficult to detect with a reasonable statistical significance in a poor data set, thus compromising the ability of the data set to discriminate between an ejecta model or evolutionary stage with weak Fe Kα and one without any Fe Kα at all.

These issues are sometimes dismissed or played down in theoretical discussions as being mere 'technicalities', but they are of capital importance for X-ray spectroscopy. An understanding of the operation of the available instruments is required for a careful, quantitative analysis of X-ray spectra. For more information, see Fraser, 1998; Paerels, 1998.

The role of spatially resolved spectroscopy

The simulation scheme that has been described in this work has the potential to go beyond the spatially integrated spectra of SNRs. The hydrodynamic, ionization and spectral calculations are all Lagrangian (fluid-element oriented), and therefore it is possible to focus on a region of the SNR instead of on the whole structure, and compute spectra to compare with spatially resolved X-ray CCD data. In order to do this, it would be necessary to calculate the projection from the 3D SNR structure onto the 2D plane of the sky, as the spectra of the outer layers are superposed to those of the inner layers, and there are limb brightening effects. The spatial resolution of the instrument that is used to make the observations would also have to be taken into account.

This technique would allow, for instance, to sample ejecta and AM separately, fit the shocked AM spectra with a suitable combination of thermal and nonthermal models and then use this knowledge to facilitate the spectral analysis of the shocked ejecta spectrum. Within the shocked ejecta, differences in chemical composition between the regions could be probed to provide further constraints on the spatial distribution of the nucleosynthesis in Type Ia SN models. An implementation of these and other spatially resolved spectral techniques is one of the future lines of work that will be discussed in chapter 7.

Model fitting and component separation

The models for the ejecta emission that have been presented in this chapter can be used in many ways. The simplest by far is to treat them as just another parametrized spectral model and incorporate them to a spectral package like XSPEC. In this scenario, the parameters for each explosion model would be the SNR age t, the AM density ρ_{AM}, the amount of collisionless electron heating at the reverse shock β, and a normalization factor. An integrated SNR spectrum such as that of Tycho (Fig. 3.1) could be fitted

with one of these shocked ejecta models, plus a shocked AM model (such as the Sedov model, for instance) and a synchrotron model, all of them multiplied by an interstellar absorption model. The power of the data set to discriminate between different SN explosion mechanisms would depend on the relative importance of the components for the explosion model that offers the best fit.

In practice, each particular object will offer special constraints. In Tycho and SN1006, for instance, the age is known, so t is not a free parameter, and the available data sets are good enough to allow for spatially resolved spectroscopy. In some of the SNRs in the LMC, on the other hand, spatially resolved techniques might or might not provide strong constraints, but the distance to the objects is well determined, so ρ_{AM} could be related to the explosion energy E_K through the apparent radius of the SNR (this might not be so easy, however; see Ellison et al., 2004). Depending on the information available, different ways to apply the models will suggest themselves.

Some reflections on fitting procedures and the χ^2 method

As was mentioned in section 3.2, the standard procedure for data analysis in X-ray spectroscopy is the maximum likelihood fitting of parametrized spectral models, which is done by minimizing the χ^2 statistic. The outcome of the fitting process is an estimate of the model parameters, a confidence range on those parameter values and a statistical measure of the goodness-of-fit. This goodness-of-fit measure is usually the χ^2 statistic divided by the number of degrees of freedom (the number of data bins minus the number of free parameters in the model), also called 'reduced χ^2' (see Press et al., 1994, chapter 15, pp. 659-660 for details). Despite being used in virtually all the published papers on the spectral analysis of X-ray astronomical data, this technique has several serious drawbacks. An in-depth analysis of the applicability of χ^2 fitting to the spectral analysis of SNRs in general, and to the SN-SNR connection in particular would be an interesting topic for an extensive monograph, but is clearly outside the scope of this work. Nevertheless, a few important points seem worth raising:

The χ^2 fitting procedure assumes that the fitted model is the *true model*, because it compares the data with all the possible outcomes of the model within the parameter range. In other words, if the model used to fit the data is not a reasonable description of the physical processes involved in the emission, the derived parameters and the goodness-of-fit measure *have no physical meaning*. The spectra of young SNRs are complex enough that simple models, such as single temperature and/or single ionization timescale generally provide very poor fits to the observations. Indeed, just a glance at the emission measure averaged plots of different elements for the ejecta models presented in section 4.1 should discard the use of these simple models to fit shocked ejecta spectra right away. The fits might be improved by using more sophisticated models, such as plane parallel shock models with adjustable abundances, but doing so is not exempt of risks. Given a complex enough model, any data set can be fitted, but the validity of the results thus obtained will be questionable. In this scenario, what should be the role played by the spectral models for the shocked ejecta that have been introduced in this chapter?

The fact is that it would be very surprising for any of the models presented here to provide a perfect statistical fit to the spectrum of a particular ejecta dominated Type Ia SNR. In a conventional spectral model with adjustable abundances, a deficit in the flux of a given line, for example, might be compensated by increasing the abundance of the required element. In the explosion models reviewed in chapter 2, on the other hand, the elemental abundances and composition profiles are not adjustable, they are the product of nucleosynthetic calculations which have their own uncertainties. Given the quality of the

atomic data available and the limitations of the simulation scheme, a perfect agreement between model and data is not to be expected, even under the most favorable conditions. Rather, a general description of the spectral properties of the elements in the ejecta is a more reasonable goal.

To provide a specific example, one might consider the implications of the χ^2 procedure putting more statistical weight in the energy bins with higher flux. This penalizes the high energy line emission, which carries vital information concerning the ionization state of the elements in the ejecta, in favor of the low energy emission. Thus, one of the ejecta models presented here might provide a good approximation to the high energy line emission with a relatively poor fit at low energies, resulting in a high value of χ^2. For the same data set, a conventional spectral model might have severe shortcomings in the high energy line emission, but a better adjustment to the low energy spectrum would yield a lower χ^2. Despite the fact that neither model provides an ideal result, one might be inclined to prefer the first to the second, despite the worse χ^2. But then, how does one *quantify* the preference for one model over another in a systematic way?

These are clearly complex matters, best discussed in the context of a specific SNR with specific constraints. That will be the subject of chapter 5, where the spectrum of Tycho will be examined with more detail. As a final remark, it is important to mention that the problem of comparing several possible models for a given data set while taking into account different types of constraints *can* be solved quantitatively in a consistent way. The solution lies beyond the frequentist approach to statistics and the χ^2 fitting procedure, in the realm of Bayesian probability theory (for an introduction to this fascinating topic, see Loredo, 1990; Bretthorst, 1990).

Chapter 5

The remnant of Tycho's supernova (SN 1572)

'I was led into such perplexity by this unbelievable appearance that I began to doubt the faith of my own eyes...'
    Tycho Brahe (1546-1601) , *Astronomiae Instauratae Progymnasmata.*

5.1   Introduction

5.1.1   A supernova in the Renaissance

The supernova of 1572 is the first one for which we have data that are accurate and comprehensive enough to reconstruct the light curve and color evolution. This is largely the merit of Tycho Brahe, who not only made a series of careful observations of the supernova himself, but also compiled the results of other contemporary astronomers, including those of the Spanish mathematician Jerónimo Muñoz. From his first observation of the *stella nova* in the constellation of Cassiopeia on November 11, 1572, until March 1574, when it finally became invisible, Tycho followed its evolution regularly for 17 months, keeping track of its apparent brightness and color.

In 1945, Walter Baade used Tycho's observations to derive a light curve that enabled him to classify the *stella nova* of 1572 as a Type I supernova (Baade, 1945), scarcely four years after Minkowski had proposed the division of SNe in two classes (Minkowski, 1941). Since then, Tycho's data have been revisited by many authors, and controversy has arisen regarding the spectral classification of the supernova and whether it was subluminous or not (see van den Bergh, 1993; Schaefer, 1996, and references therein). More recently, a study of the stars close to the location of SN 1572 (Ruiz-Lapuente, 2004) yielded an extinction of $A_V = 1.86 \pm 0.12$ mag and an average reddening of $E(B-V) = 0.6 \pm 0.04$ in that direction of the sky. Taking these values into account, the author of this study concluded that the light curve and color evolution as recorded by Tycho and others in the sixteenth century would correspond to those of a normal Type Ia SN, at least within the uncertainties associated with the data. Moreover, the absolute peak visual magnitude for SN 1572 was found to be $\mathcal{M}_V = -19.58 - 5log(D/3.5\,\mathrm{kpc}) \pm 0.42$ mag, a value which compares well with the corrected mean for Type Ia SNe (eqn. 2.1), provided that the distance to the supernova D is around or slightly less than 3.5 kpc. As we shall see in the following section, however, the value of D is not as well constrained as one might wish.
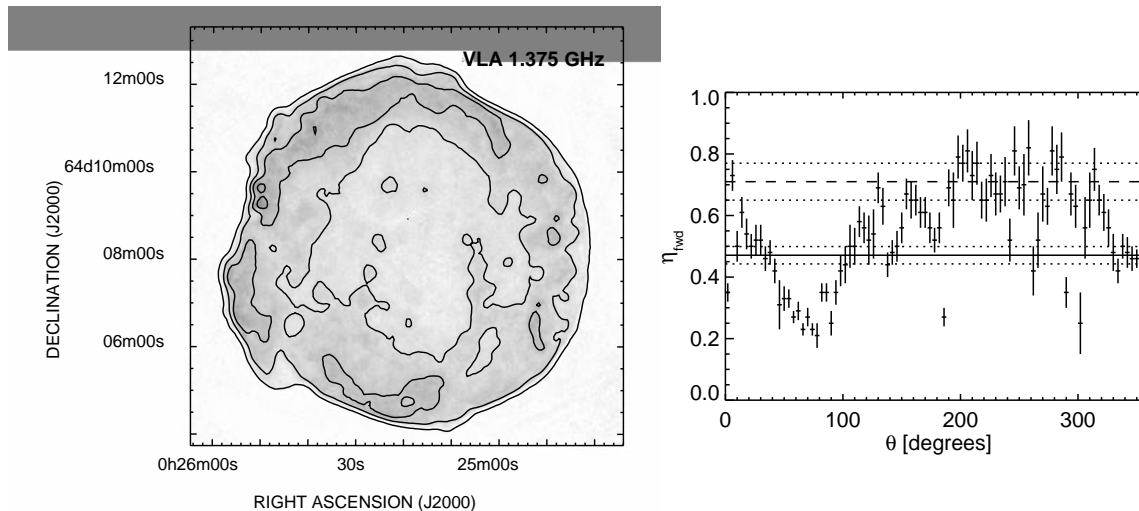
Figure 5.1: Left: Radio image of the Tycho SNR, taken with the VLA at 21 cm (1.375 GHz) in 1994. Contours are approximately at 0.02, 0.5, 1.0 and 1.5 mJy/beam. Data from the *Chandra* SNR Catalog (Seward et al., 2004). Right: Expansion parameter along the forward shock in the Tycho SNR from VLA measurements, as published in Reynoso et al., 1997. The solid line corresponds to the average expansion parameter, 0.47 ± 0.03. The dashed line corresponds to the forward shock expansion parameter measured at X-ray wavelengths, 0.71 ± 0.06 (Hughes, 2000). The measurement errors given by the authors are represented with dotted lines.

5.1.2   A supernova remnant in modern times

After many unsuccessful searches for an optical remnant of SN1572 in the region specified by Tycho Brahe, the discovery of the SNR in 1952 constituted one of the first successes of radioastronomy (Hanbury-Brown and Hazard, 1952). This was the second identification of a SNR with a historical supernova after that of the Crab Nebula with SN 1054. Even though our primary interest shall be the X-ray spectrum of Tycho, we give a brief summary of the observations at other wavelengths, with the aim of gathering information that might help to the analysis of the X-ray data.

Radio measurements and the expansion parameter of the forward shock

In the line of neutral H at 1375 MHz ($\lambda = 21$ cm), the Tycho SNR appears as a clearly defined shell with an approximate angular diameter of 8' (see Fig. 5.1). The shell is very smooth and nearly spherical from the northwest to the southeast, with an irregular outbreak and a slight brightening to the north, northeast and east.

In Reynoso et al., 1997, VLA observations at two different epochs were used to study the expansion parameter of the forward shock with a baseline of 10 yr along the rim of the SNR shell. This is an important measurement, because the value of the expansion parameter does not depend on the distance to the object, and allows to put important constraints on its evolutionary stage. These results are plotted in Fig. 5.1, following the convention adopted by the authors for the azimuthal angle along the shell (counterclockwise starting from the north). The average expansion parameter was found to be $\eta_{fwd} = 0.47 \pm 0.03$, with distinctly lower values towards the north and east, where the shell departs from its nearly spherical shape. The authors suggested that this could be due to an interaction with dense material, which would be slowing down the parts of the SNR that extended

further away from the geometric center in the past. The high scatter of the measurements in the west was attributed to a difficulty in defining the rim of the shell in this region due to a less abrupt rise in the radio flux across the edge (apparent in the contour plot in Fig. 5.1). In a later work, a high density HI region was detected close to the SNR, in a direction coincident with that of the slower expanding section of the shell (Reynoso et al., 1999; see also Lee et al., 2004).

The radio measurements, however, do not allow to determine the expansion parameter of Tycho's forward shock unambiguously. In Hughes, 2000, two X-ray images taken by the *ROSAT* satellite with a difference of five years were used to derive an average value of $\eta_{fwd} = 0.71 \pm 0.06$. The author of this work suggested that the results of Reynoso et al., 1997, might be contaminated by a sinusoidal component as a result of the misplacement of the geometric center of the SNR, but remarked that this should not affect the average value, because any such sinusoidal term would have zero mean over the entire rim. This puzzling disagreement between radio and X-ray measurements of η_{fwd} has also been observed in other SNRs like Cas A and Kepler. It is worth noting that the expansion parameter of some interior features of the Tycho SNR, measured using the same technique, is consistent in radio ($\eta \simeq 0.44$, Reynoso et al., 1997) and X-rays ($\eta \simeq 0.45$, Hughes, 2000).

Optical measurements and the distance to Tycho

Very faint 'gaseous filaments' were associated with the SNR by Minkowski in 1957 (private communication cited in Baldwin and Edge, 1957). Later studies determined that the filaments consisted almost exclusively of Balmer line emission from H, and that this emission was produced at the nonradiative forward shock (see the discussion in section 3.4.1 for more details on the optical emission from nonradiative shocks). No evidence of any lines other than the Balmer H lines was found in the interior of the SNR (Kirshner and Chevalier, 1978; Ghavamian et al., 2000), implying that optical emission from radiatively cooled plasma, if present, should be very faint. In Ghavamian et al., 2001, the spectrum of the brightest knot in the eastern rim (knot g) was examined with detail, yielding a velocity between 1940 and 2300 $\mathrm{km \cdot s^{-1}}$ and a small amount of collisionless heating ($\beta \leq 0.1$) for the forward shock. It is worth emphasizing that, in the light of the radio results discussed in the previous section, the properties of this bright knot in the eastern rim might not be representative of the overall dynamics of the blast wave.

In any case, the value for the forward shock velocity is an important measurement, because it can be combined with the proper motion of knot g to obtain an estimate for the distance to Tycho's SNR. This proper motion was measured in Kamper and van den Bergh, 1978, over a temporal baseline of 28 years, and found to be $0.20 \pm 0.01 \, \mathrm{arcsec \cdot yr^{-1}}$, which results in a distance estimate of $1.9 \, \mathrm{kpc} \leq \mathrm{D} \leq 2.3 \, \mathrm{kpc}$ for the range of forward shock velocities cited above [1]. This is perhaps the best constrained distance estimate, but it is by no means unique: other techniques yield different, and even contradictory, results, ranging between 1.5 and 4.5 kpc (see compilation in Schaefer, 1996).

---

[1] These optical proper motion measurements, of course, yielded estimates for the expansion parameters of the brightest features as well. The optical results were in reasonable agreement with those of Reynoso et al., 1997 (see discussion in section 4.2 of that paper).
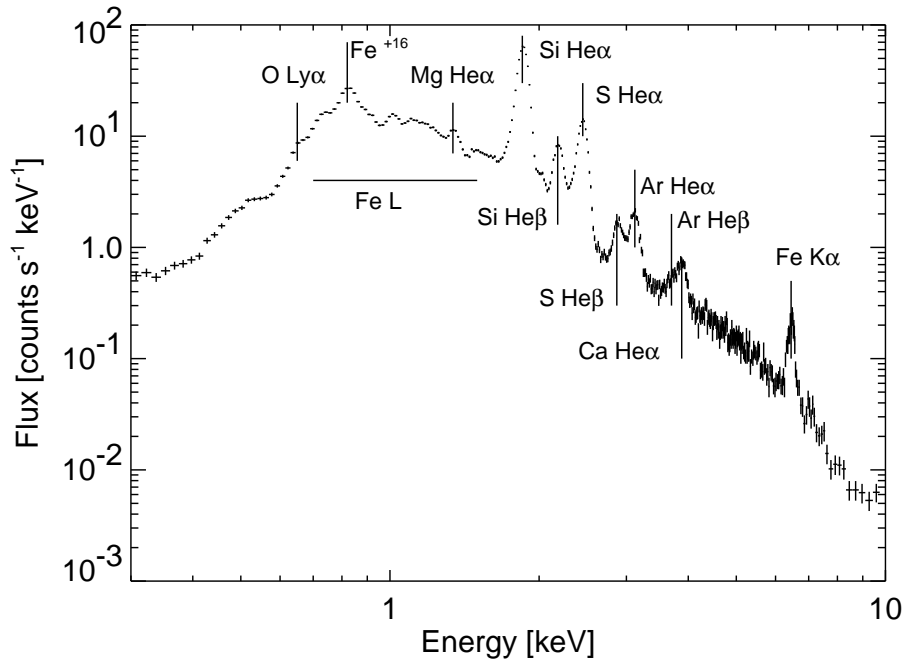
Figure 5.2: Integrated spectrum from the EPIC MOS1 camera onboard the *XMM-Newton* satellite. The data are from an extraction region in the western sector (see discussion in section 5.3.1; this is the same as Figure 3.1).

5.2 The X-ray remnant of Tycho

5.2.1 Observations

The first X-rays from the Tycho SNR were detected with a rocket-borne proportional counter in 1967 (Friedman et al., 1967). Since then, the performance of the available instruments has been improving steadily. Spatially resolved spectroscopy of extended targets first became a reality in 1993 with the launch of the *ASCA* satellite, and was taken to an unprecedented level of detail with the advent of *Chandra* and *XMM-Newton* in 1999. These two satellites complement each other nicely, with the *Chandra* CCD cameras providing better spatial resolution and those of *XMM-Newton* having better spectral resolution.

To illustrate the quality of the data that are produced by these modern observatories in the case of the Tycho SNR, the spatially integrated spectrum from a region of Tycho collected by the EPIC MOS1 camera onboard *XMM-Newton* and the 'true color' image from the *Chandra* ACIS instrument are displayed in Figures 5.2 and 5.3. The spectrum has an excellent signal to noise ratio at all energies, and is dominated by prominent emission lines from Si, S, Ar, Ca and Fe. The true color X-ray image shows a rich and intricate structure, which is well resolved by the instrument. The present section is devoted to review the most important works that have analyzed X-ray observations of the Tycho SNR to this date.

Breaking the ground: *ASCA*

In Hwang and Gotthelf, 1997, a detailed study of the Tycho SNR was made using *ASCA* data, and images in the spectral bands corresponding to the most prominent emission lines were produced. All the lines showed a shell-like spatial distribution, with the Fe Kα
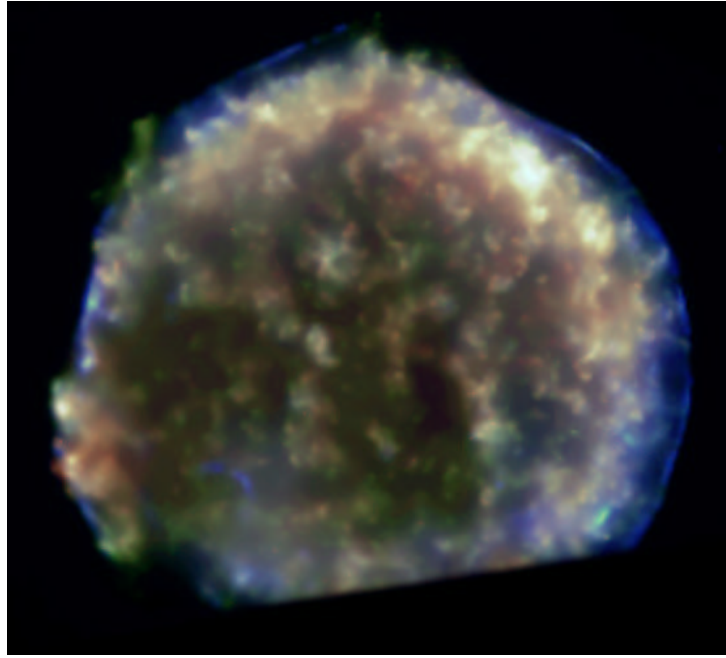
Figure 5.3: 'True color' image of the Tycho SNR from the *Chandra* ACIS camera. The color code used for the energies is: red from 0.3 to 0.95 keV (mostly Fe L emission); green from 0.95 to 2.65 keV (most of the Si and S lines); blue from 2.65 to 7.0 keV (continuum, Ca and Fe Kα emission). The southernmost portion of the SNR fell outside the area of the CCD chips and was not imaged. Image from the *Chandra* SNR Catalog (Seward et al., 2004).

line image appearing more diffuse and peaking at a smaller radius than the others. The apparent symmetry of the X-ray line emission and the absence of significant Doppler shifts suggested an overall spherical geometry, but local inhomogeneities in the line emission were manifest. The X-ray continuum was found to be brightest at the rim, but uncorrelated with the radio continuum. Spectral analysis yielded $0.72 \leq kT_e \leq 0.99$ keV and $10.9 \leq log(n_e t) \leq 11.1$ for Si and S, with consistent values for Ar and Ca. The Fe Kα emission was found to arise from conditions different to those of the other elements, with a higher value of T_e and a lower value of $n_e t$. Spatial overlap of the Si-S and Fe Kα emitting regions was considered evidence for some degree of mixing within the ejecta by comparison with stratified Type Ia SN models like W7. An important conclusion of this study was that accurate X-ray spectral analysis of the Tycho SNR would require the use of models that contemplate a distribution of T_e and $n_e t$ in the shocked ejecta.

The relationship between the Fe Kα and Fe L emission was explored in a later study using the same data (Hwang et al., 1998). In this work, it was shown that the Fe Kα line could not be originated at the forward shock, even if most of the continuum was, and hence must come from the ejecta. The properties of the Fe L emission were found to be different from those of the Fe Kα line, probably due to the distribution of T_e and $n_e t$ inside the Fe-rich ejecta. The integrated spectrum was fitted using three NEI components corresponding to blast wave, ejecta, and Fe ejecta, yielding $kT_{blast} = 4$ keV, $kT_{ejecta} = 0.86$ keV, $kT_{Fe\,ejecta} = 1.6$ keV; $log(n_e t)_{blast} = 10.2$, $log(n_e t)_{ejecta} = 11$, $log(n_e t)_{Fe\,ejecta} = 2$. This three component model failed to account for approximately 10% of the Fe Kα flux, and also had problems with the high energy continuum, where hints of nonthermal emission were found. The possibility of a contribution to the Fe Kα flux from fluorescence in Fe-rich dust grains (after Borkowski and Szymkowiak, 1997) was ruled out by the authors. The

result that the contribution of dust to the ejecta emission was small in Tycho was later strengthened by the work of Douvion et al., 2001, which found that the IR emission was well correlated with the optical emission, and therefore associated with the shocked AM rather than the ejecta.

Going beyond: *XMM-Newton* and *Chandra*

Tycho was first observed by the *XMM-Newton* satellite in June 2000, and an analysis of this observation was published in Decourchelle et al., 2001. The *XMM* data set was in agreement with the results obtained by Hwang and Gotthelf, 1997, and Hwang et al., 1998, with *ASCA*, but the improved spectral resolution allowed to identify some weak lines like O Lyα, Ne Heα and Mg Heα. Radial profiles of line emission confirmed that, while Si Heα and Fe L are spatially coincident, Fe Kα has a broader peak at a smaller radius. The Si image was found to have irregular boundaries that reached out towards the outer edge of X-ray emission in a way strongly suggestive of Rayleigh-Taylor fingers, an hypothesis that had been put forward based on radio images by Velázquez et al., 1998. Some particularly bright knots were identified and analyzed in the eastern and western edges. The hard $(4.5 \leq E \leq 5.8\,\mathrm{keV})$ continuum image revealed a slightly bipolar structure, similar to that found in SN1006, which suggested the presence of a nonthermal component in this band (see Dyer et al., 2001; and references therein).

A work that is specially relevant to understand the ejecta emission in Tycho is the analysis of a *Chandra* observation presented in Hwang et al., 2002. The excellent spatial resolution of the *Chandra* ACIS CCD cameras allowed to identify and separate the thin, smooth rim that traced the outer edge of X-ray emission to the W and NE (see Fig. 5.3; the rim appears blue in the true color image). This X-ray rim was identified with the forward shock. Analysis of the featureless spectra from several extraction regions along the rim showed remarkably uniform characteristics. The spectra were fitted with NEI models with $kT \simeq 2\,\mathrm{keV}$ and very low $n_e t$ (of the order of a few times $10^8\,\mathrm{cm^{-3} \cdot s}$), but a simple thermal bremsstrahlung at $kT \simeq 2\,\mathrm{keV}$ was found to provide a satisfactory fit in most cases. The addition of a nonthermal component did not improve the fits significantly, but this was not interpreted as evidence against the presence of such a component. The fitted temperatures behind the forward shock appeared consistent with low amounts of collisionless electron heating, in agreement with the optical results of Ghavamian et al., 2001. Line emission from Si and S was detected in extraction regions just behind the external rim, suggesting that the ejecta extended almost to the forward shock (this can be seen in the true color image of Fig. 5.3: the mixing of Si and S emission (green) with Fe L emission (red) appears as yellow). This Si and S emission consisted of clumps, approximately 5" in size, distributed uniformly in azimuth over the entire SNR, with a smoother component beneath the clumps that contributed approximately 25% of the flux. Fe L and Fe Kα emission appeared less clumpy and more sparse, with the distribution of Fe Kα interior to that of Fe L and Si.

5.2.2 Previous models

Observed spectrum vs. explosion models

The first detailed models for the X-ray spectrum of Tycho that included a realistic treatment of the ejecta emission, with hydrodynamic simulations coupled with nonequilibrium ionization and a spectral code, were published by Hamilton et al., 1986b (some techniques for their analysis were presented in a companion paper on the X-ray spectrum of SN1006, Hamilton et al., 1986a). The X-ray spectrum was reconstructed with observations from

four different missions, and had very poor spectral resolution. The authors assumed a constant density profile for both ejecta and AM, and used a three fluid plasma model to account for the collisionless heating of electrons at the shocks (see section 3.4.1). The ejecta composition profile was modeled with an onion shell structure loosely resembling that obtained by the carbon deflagration models which had then just begun to appear in the literature: Fe and Ni in the innermost shell; Si, S, Mg, Al, and O in the middle; and C and O in the outermost shell. This was clearly a simplified model, but the uniform density profile produced higher densities and ionization states for the elements in the outermost shocked ejecta, close to the CD, which seemed to agree with the observed spectrum. Such a model allowed to 'hide' a large amount of Fe in the innermost ejecta, either unshocked or at a low density, and made the observations compatible with a mass of ejecta low enough for a Type Ia SN. In order to reproduce the high Fe K to Fe L ratio, the authors were forced to assume partial mixing of Fe into the Si-rich layer. The onion shell structure was further modified by removing O from the outer shell to avoid an excess of O Lyα flux. Runaway radiative cooling was found to take place in this outermost pure C shell of ejecta, but no observational evidence was found to support this prediction.

In Itoh et al., 1988, full 1D hydrodynamic-ionization models, very similar to the ones presented in chapter 3 of this dissertation, were coupled to spectral calculations and compared to observations by the *TENMA* satellite. The goal of this work was to ascertain whether model W7 (Nomoto et al., 1984; see Fig. 2.4), which was then becoming very popular, could be used to explain the X-ray spectrum of Tycho's SNR. Therefore, even though the authors included the full density and chemical composition profile of model W7 in their calculations, no other SN explosion models were discussed. The authors came to the conclusion that it was impossible to explain the X-ray spectrum of Tycho, and specially the high Fe K to Fe L ratio, with model W7 without introducing substantial modifications to its structure. Satisfactory results were obtained by artificially mixing some of the Fe from the inner layers of model W7 into the Si-rich layers, arriving at a configuration similar to that inferred by Hamilton et al., 1986b. It was pointed out that such mixing was likely to occur in the phases of the SN explosion following maximum light, because the NSE region is convectively stable during this stage. Absence of collisionless electron heating at the shocks was assumed in all their models except one, which was discarded on the grounds that it resulted in a continuum too hard to be compatible with the observations.

A similar study was conducted by Brinkmann et al., 1989, also based exclusively on the W7 model, but using data from *EXOSAT*. In contrast to Itoh et al., 1988, the authors assumed full temperature equilibration between ions and electrons at the reverse shock, and yet claimed that the hard energy spectrum was compatible with the *EXOSAT* observations. Despite this, their main conclusion was the same: some mixing of Fe-rich material into the Si-rich layers of W7 was required in order to explain the high Fe K to Fe L emission ratio. Most line centroids in their model spectra were found to be at higher energies than in the observed spectrum, suggesting that they overestimated the electron temperature, and that the assumption of full temperature equilibration at the reverse shock might have been unjustified.

Summarizing, these works were successful in strengthening the case for a Type Ia origin of the Tycho SNR, but could not establish a clear connection between the W7 model and the observed X-ray spectrum of Tycho. All their results seemed to imply that Fe extends further outwards in Lagrangian mass coordinate in the ejecta of the Tycho SNR than it does in the W7 model.

Observed dynamics vs. explosion models

However, none of these models for the X-ray spectrum was able to explain the dynamics of the shocked AM in the Tycho SNR. The process of adjusting the shape of the spectrum and normalizing the detected flux yielded estimates for the AM density ρ_{AM} and the distance to the object D. These estimates were $\rho_{AM} \simeq 0.6 \cdot 10^{-24} \, \text{g} \cdot \text{cm}^{-3}$ and $D \simeq 3 \, \text{kpc}$ for Hamilton et al., 1986b; $\rho_{AM} \simeq 2.0 \cdot 10^{-24} \, \text{g} \cdot \text{cm}^{-3}$ and $D \lesssim 2.5 \, \text{kpc}$ for Itoh et al., 1988; and $1.0 \cdot 10^{-24} \lesssim \rho_{AM} \lesssim 2.0 \cdot 10^{-24} \, \text{g} \cdot \text{cm}^{-3}$ and $D \simeq 3 \, \text{kpc}$ for Brinkmann et al., 1989. The hydrodynamic simulations performed using these values of ρ_{AM} gave forward shock radii and speeds at the corresponding values of D that were systematically larger than the values inferred from the optical and radio observations reviewed in section 5.1.2. Even the forward shock expansion parameter η, which is independent of D, was always overestimated. There was clearly a contradiction between the X-ray spectrum, which required AM densities lower than $2.0 \cdot 10^{-24} \, \text{g} \cdot \text{cm}^{-3}$ to reproduce the ionization state of the elements in the shocked ejecta, and the forward shock dynamics, which required values of ρ_{AM} at least twice as high.

The situation was aggravated when high resolution X-ray observations became available. The fact that the ejecta reach out almost to the forward shock, which is plain to see in the *Chandra* true color image (Fig. 5.3), cannot be explained by simple hydrodynamic models. In 1D simulations the thickness of the shocked AM is always too large (Dwarkadas and Chevalier, 1998), and even 2D simulations that include the effect of Rayleigh-Taylor instabilities at the CD fail to bring the shocked ejecta close enough to the forward shock (Chevalier et al., 1992; Dwarkadas, 2000; Wang and Chevalier, 2001).

A partial answer to this puzzle was proposed by Wang and Chevalier, 2001, who performed 2D hydrodynamical simulations to study the effect of instabilities and clumping in the dynamics of Type Ia SNRs. They found that clumps in the ejecta with a density contrast above 100 could pierce through the CD as bullet-like projectiles and bring the ejecta almost to the forward shock. The authors proposed the Ni bubble effect as the mechanism responsible for the formation of these clumps (see discussion in section 3.5.1), and identified them with two fast X-ray knots in the southeast region of Tycho. However, these knots are known to be rich in Fe, a circumstance that precludes their formation due to the Ni-bubble effect. The explanation offered by the authors, that the clumps were synthesized as ^{54}Fe in the explosion, is difficult to reconcile with current models for Type Ia SNe, but this remains an open question. Another issue is whether the observed knots and clumps in the X-ray image of Tycho actually have the necessary density contrast of 100. Similar structures in Cas A are suspected to have densities only a factor 3 larger than the surrounding medium (Laming and Hwang, 2003). It is important to note that the presence of clumps in the ejecta cannot explain why the X-ray spectrum and forward shock dynamics require mutually exclusive values of ρ_{AM}.

A factor that might help to understand globally the dynamics of Tycho, at the cost of an even more complicated theoretical picture, is CR acceleration at the shocks. According to Decourchelle et al., 2000, this could modify substantially the dynamics of the forward shock, while having relatively minor effects in the dynamics of the reverse shock, and hence on the X-ray spectrum of the shocked ejecta (see discussion in section 3.5.2). Indeed, a realistic model for the dynamics of Tycho should include the effects of instabilities, ejecta clumping and CR acceleration in a self-consistent way. Such a model does not exist yet, but given the present knowledge of these processes and the level of sophistication of the available hydrocodes, it might become a reality in the near future (for a discussion, see Ellison et al., 2004).

5.3 Modeling the thermal X-rays from the ejecta in Tycho

5.3.1 Goals and strategy

In the last section, we have seen that the X-ray emission from the Tycho SNR is dominated by the shocked ejecta, and therefore bears a close relation to the explosion that originated the remnant in 1572. We have also seen that Tycho is a very complex object, whose spectrum and dynamics are affected by many different physical processes, some of which are not well known. In this context, and before we attempt to establish any kind of connection between SNR and SN, it is important to identify what the goals of this study shall be, and to outline a strategy for establishing that connection. As has been pointed out several times before, great care must be taken to consider the limitations of the models, the observations, and the spectral analysis techniques, and how these limitations restrict the methods that can be applied and the conclusions that can be drawn.

The most severe limitation of the models arises from the fact that they are based on one dimensional adiabatic hydrodynamics. The structure of the ejecta in Tycho is clumpy and there is evidence for nonlinear particle acceleration at the shocks, so any description of this SNR based on adiabatic 1D hydrodynamics is necessarily incomplete. Yet, the use of these models as a first approach for the shocked ejecta is encouraged by the results of Laming and Hwang, 2003, which found a low density contrast of the X-ray knots in Cas A, and Decourchelle et al., 2000, which found that CR acceleration had no impact on the X-ray ejecta emission in the Kepler SNR (see also the discussion in section 3.5). Without attempting to reproduce the intricate structure of the clumpy ejecta in Tycho, the models might provide a reasonable approximation to the distribution of T_e and $n_e t$, which was considered so important to understand the X-ray spectrum by the works reviewed in section 5.2.1.

The situation is more complex in the shocked AM, since in this case the dynamics will be severely affected by CR acceleration at the forward shock. Without detailed knowledge of the dynamics, it is difficult to build a theoretical model for the X-ray emission from the shocked AM. Fortunately, this emission was characterized by Hwang et al., 2002, who showed that it could be approximated by a thermal bremsstrahlung with $kT \simeq 2 \, \mathrm{keV}$ over the western and northeastern rims.

In view of this, a simple strategy suggests itself: to use the synthetic X-ray spectra presented in chapter 4 to model the ejecta emission and add a bremsstrahlung component to model the AM emission, effectively ignoring the hydrodynamic calculations for the shocked AM. This seems justified because, as we have seen, the 1D adiabatic calculations would fail to reproduce the observed dynamics of the shocked AM in Tycho anyway. However, this strategy can only be applied in the regions of Tycho where the shocked AM has been characterized, i.e., the western and northeastern sectors of the SNR. Since the forward shock seems to be interacting with a dense molecular cloud to the NE (Reynoso et al., 1997; see section 5.1.2), caution advises to discard this region and concentrate on the western sector. In addition to this, an inspection of Fig. 5.3 reveals that this is the part of the SNR that departs less significantly from spherical symmetry, and is therefore better suited for comparison with the 1D ejecta models than the rest of the SNR.

Application of this method requires an integrated spectrum in the appropriate region of Tycho with the best possible spectral resolution, in order to constrain the properties of the ejecta emission. Since spatial resolution is not an issue, the capabilities of *XMM-Newton* are better suited for this than those of *Chandra*. Within *XMM-Newton*, the EPIC MOS cameras offer the best possible performance of all the available X-ray CCD instruments. In the observation analyzed by Decourchelle et al., 2001, and whose
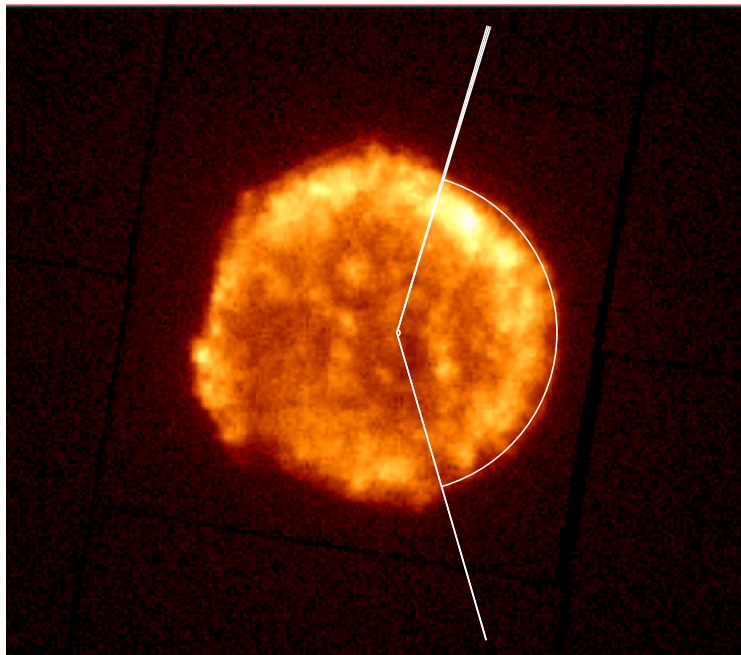
Figure 5.4: Extraction region plotted over the *XMM-Newton* EPIC MOS1 image. The extracted sector corresponds to what Reynoso et al., 1997, defined as region V, with an azimuth range of $200 \leq \theta \leq 345°$ (see Fig. 5.1).

results were summarized in section 5.2, the total exposure time for each EPIC MOS camera was about 12 ks, more than adequate for our needs. These data, which are now in the public domain, were downloaded from the *XMM-Newton* science archive web site (http://xmm.vilspa.esa.es/external/xmm_data_acc/xsa/index.shtml). An appropriate extraction region in the western sector was selected (see Figure 5.4[2]), and matrix response files and ancillary response files were generated using the standard *XMM-Newton* science analysis system (this was done by U. Hwang, private communication, July 2003). The resulting spectrum was presented in Figure 5.2, and will be the subject of all the analysis procedures detailed in the remainder of this chapter.

Once the data set is extracted, the only thing that remains to be specified is the technique for the comparison between models and observations. In the spirit of the discussion of section 4.4, we insist that the standard χ^2 spectral fitting procedure is not adequate for the problem at hand. An acceptable statistical fit to the data is not to be expected, given the limitations of the models and the available atomic data. One possibility is to focus first on the line emission, which should be contributed almost exclusively by the ejecta. This line emission can be characterized in a model independent way by determining line ratios and centroids, and these diagnostic quantities can then be used to discriminate which among the ejecta models in the grid offer a good approximation to the observed values. For those ejecta models that reproduce the line emission in a satisfactory way, the bremsstrahlung representative of the shocked AM emission can be added in order to compare with the whole spectrum. This is clearly a simplified approach, but it is robust

---

[2] It is interesting to compare the performance of *Chandra* and *XMM-Newton* through the level of detail in Figures 5.4 and 5.3. Note that, while we will focus the *XMM-Newton* data for the reasons detailed above, the characterization of the shocked AM spectrum was possible thanks to the superior spatial resolution of *Chandra*. Our analysis strategy, therefore, relies on the capabilities of both observatories.

enough to allow for a preliminary exploration of the SN-SNR connection in the Tycho SNR.

5.3.2 Line emission: observations

Despite the excellent spectral resolution of the *XMM-Newton* EPIC MOS1 camera, many of the lines that appear in the extracted spectrum in Figure 5.2 are blended. In order to determine line fluxes and centroids unambiguously, we have followed the analysis technique proposed in section 3.1 of Hwang and Gotthelf, 1997. These authors fitted the *ASCA* spectrum of Tycho above an energy of 1.5 keV with a model consisting of two bremsstrahlung components plus fourteen Gaussian lines, affected by an interstellar absorption fixed at $N_H = 0.45 \cdot 10^{22}$ cm^{-2} (from the measurements of Albinson et al., 1986). The two bremsstrahlung components were necessary due to a change of behavior in the continuum at ~ 3 keV (apparent in Fig. 5.2); one of them was fixed at a temperature of 10.0 keV to account for the high energy continuum, the other was fitted freely and yielded $kT = 0.99$ keV.

For the *XMM-Newton* data, we have chosen to divide the spectral region dominated by line emission in two windows, one at low energies ($1.6 \leq E \leq 2.75$ keV), and one at high energies ($2.75 \leq E \leq 8.0$ keV). In this way, the continuum can be modeled by using one single bremsstrahlung component in each window. Other than this, the Gaussian lines and interstellar absorption were the same as in Hwang and Gotthelf, 1997. The lines included in the model, and their fitted centroids and fluxes are given in Table 5.1, where the common notation of α, β, and γ has been used to label the lines corresponding to transitions from levels 2, 3, and 4. The quality of the data set does not allow the centroids of the weakest lines to be fitted independently, so these parameters have been fixed. The Heβ/Heγ line flux ratios of Si, S and Ar, and the Si Lyα/ Si Lyβ ratio, have also been fixed in the fit; the values listed in Table 5.1 correspond to the values at $T = 10^7$ K. This allows for an adequate (if simple) treatment of these blended lines, and is justified because the flux ratios vary by only 10%-20% over a decade in temperature (for details, see Hwang and Gotthelf, 1997). The most important line ratios have been listed in Table 5.2.

The complex interplay of line blends and the large number of free parameters in the model, even after fixating some of the centroids and fluxes, made the fitting process somewhat difficult, but acceptable fits were eventually achieved with XSPEC in both energy windows (see Figure 5.5). In the low energy window, the fitted temperature for the bremsstrahlung component was $kT = 1.67$ keV and the χ^2 was 289 for 60 DOF. In the high energy window, the fit yielded $kT = 3.93$ keV with a χ^2 of 239 for 224 DOF. The value of kT in the high energy window is in agreement with the results of Hwang et al., 1998, which found that the continuum was dominated by a component with $kT = 4$ keV in this energy range (see their Figure 4). The poorer quality of the low energy fit might be related to the difficulty in constraining the flux of the Si Lyα line, which is only barely noticeable above the continuum, and to the fact that the Si Heα line is not well approximated by a Gaussian. This is expected, since Si Heα is actually a blend of four lines, but the centroid and flux of this blend showed only very slight variations through the fitting process, so the values listed in Table 5.1 can be considered reliable enough for our goals. The same comments can be applied to the Fe Kα line, which is an even more complex blend.

It is interesting to compare these results with the ones obtained by Hwang and Gotthelf, 1997, for the *ASCA* observation of the entire SNR. The line centroids are constrained much better by the superior spectral resolution of *XMM-Newton*, but the values all fall within the *ASCA* error bars, with the notable exception of Ca Heα. The fit to the *XMM-Newton*

Line	Ion and transition	Expected energy [keV]	Fitted energy (XMM) [keV]	Fitted flux (XMM) [$10^{-3}\,\mathrm{phot}\cdot\mathrm{cm}^{-2}{\cdot}\mathrm{s}^{-1}$]
Si Heα	Si^{+12}, $n=2 \to n=1$	~ 1.86	1.8579 ± 0.0002	28.16 ± 0.13
Si Heβ	Si^{+12}, $1s3p \to 1s^2$	2.182	2.1821 ± 0.0001	2.22 ± 0.11
Si Heγ	Si^{+12}, $1s4p \to 1s^2$	2.294	...	$0.55 \times$ Si He$3p$
Si Lyα	Si^{+13}, $2p \to 1s$	2.006	...	0.82 ± 0.20
Si Lyβ	Si^{+13}, $3p \to 1s$	2.377	...	$0.14 \times$ Si Lyα
S Heα	S^{+14}, $n=2 \to n=1$	~ 2.45	2.4482 ± 0.0005	7.51 ± 0.08
S Heβ	S^{+14}, $1s3p \to 1s^2$	2.884	...	0.58 ± 0.04
S Heγ	S^{+14}, $1s4p \to 1s^2$	3.033	...	$0.56 \times$ S He$3p$
S Lyα	S^{+15}, $2p \to 1s$	2.623	...	< 0.046
Ar Heα	Ar^{+16}, $n=2 \to n=1$	~ 3.1	3.139 ± 0.002	0.65 ± 0.05
Ar Heβ	Ar^{+16}, $1s3p \to 1s^2$	3.685	...	0.09 ± 0.04
Ar Heγ	Ar^{+16}, $1s4p \to 1s^2$	3.875	...	$0.57 \times$ Ar He$3p$
Ca Heα	Ca^{+18}, $n=2 \to n=1$	~ 3.88	3.886 ± 0.007	0.21 ± 0.05
Fe Kα	Several, $n=2 \to n=1$	~ 6.45	6.463 ± 0.006	0.26 ± 0.03

Line	Fitted energy ($ASCA$) [keV]	Fitted flux ($ASCA$) [$10^{-3}\,\mathrm{phot}\cdot\mathrm{cm}^{-2}{\cdot}\mathrm{s}^{-1}$]
Si Heα	1.859 ± 0.002	52.7 ± 0.6
Si Heβ	2.185 ± 0.005	4.38 ± 0.13
Si Heγ	...	$0.55 \times$ Si He$3p$
Si Lyα	...	1.49 ± 0.18
Si Lyβ	...	$0.14 \times$ Si Lyα
S Heα	2.448 ± 0.003	13.6 ± 0.3
S Heβ	...	0.89 ± 0.08
S Heγ	...	$0.56 \times$ S He$3p$
S Lyα	...	< 0.13
Ar Heα	3.135 ± 0.015	1.07 ± 0.08
Ar Heβ	...	< 0.060
Ar Heγ	...	$0.57 \times$ Ar He$3p$
Ca Heα	3.818 ± 0.028	0.53 ± 0.07
Fe Kα	6.458 ± 0.026	0.44 ± 0.06

Table 5.1: Line fluxes and centroids for the extracted *XMM-Newton* EPIC MOS1 spectrum of the western sector of Tycho (top). Centroids marked as ... were not fitted. The *ASCA* results of Hwang and Gotthelf, 1997, are provided for comparison (bottom).

Line Ratio	Fitted Value (XMM)	Fitted Value (ASCA)
SiHe$(\beta + \gamma)$/SiHeα	0.122 ± 0.006	0.129 ± 0.005
SiLyα/SiHeα	0.029 ± 0.004	0.028 ± 0.003
SHe$(\beta + \gamma)$/SHeα	0.12 ± 0.01	0.102 ± 0.007
SLyα/SHeα	< 0.006	< 0.010
SHeα/SiHeα	0.267 ± 0.004	0.26 ± 0.01
ArHeα/SiHeα	0.023 ± 0.002	0.020 ± 0.002
CaHeα/SiHeα	0.007 ± 0.002	0.010 ± 0.002
FeKα/SiHeα	0.009 ± 0.001	0.008 ± 0.002

Table 5.2: Diagnostic line ratios for the extracted *XMM-Newton* EPIC MOS1 spectrum of the western sector of Tycho. The *ASCA* results of Hwang and Gotthelf, 1997, which are provided for comparison, have been adapted to represent the same line ratios.
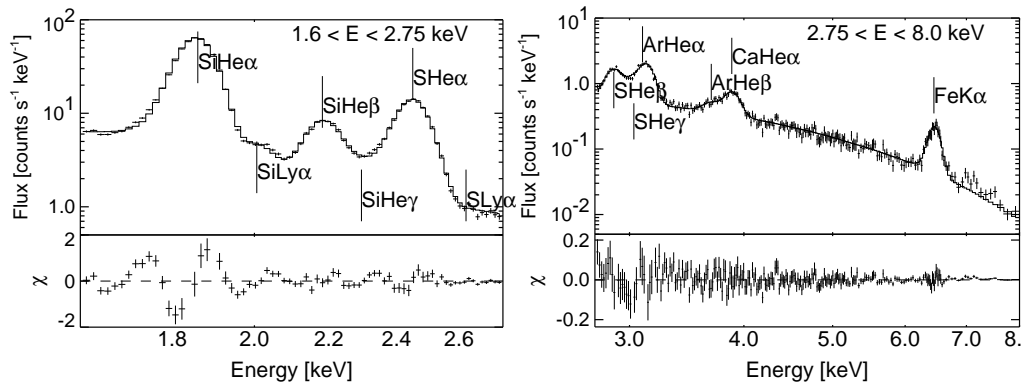

Figure 5.5: Fits to the line emission in the extracted *XMM-Newton* EPIC MOS1 spectrum of Tycho in the low energy (left) and high energy (right) windows. The most important lines and line blends have been labeled for clarity. See text for details.

data set in this region gives more importance to the contribution from the neighboring Ar Heβ and Ar Heγ lines, and places the centroid of the Ca Heα at a more reasonable energy, close to the expected value. Since the *XMM-Newton* data set corresponds to only $\sim 40\%$ of the SNR surface, the fit yields line fluxes that are lower by approximately a factor 2 with respect to the *ASCA* fit. The values themselves, however, are not better constrained, because the signal to noise ratio was similar in both observations. The differences in the line ratios are small, and the error bars overlap, except in the case of S He$(\beta + \gamma)$/S Heα. This might be attributed to a spatial extraction effect, but a more detailed analysis of the data would be necessary to draw a conclusion.

5.3.3 Line emission: models

Preliminary considerations

For the comparison with Tycho, the ρ_{AM}, β parameter space has been explored extensively for both the grid and the off-grid supernova ejecta models at an age of 430 years after the explosion. The parameter space has been sampled with five points in ρ_{AM} ($2 \cdot 10^{-25}$, $5 \cdot 10^{-25}$, 10^{-24}, $2 \cdot 10^{-24}$, and $5 \cdot 10^{-24} \, \mathrm{g \cdot cm^{-3}}$) and three points in β (β_{min}, 0.01, and 0.1); these ranges have been selected to encompass the highest and lowest estimates for

Line	Energy Window [keV]
Si Heα	$1.80 - 1.90$
Si He($\beta + \gamma$)	$2.10 - 2.31$
Si Lyα	$1.95 - 2.05$
S Heα	$2.35 - 2.50$
S He($\beta + \gamma$)	$2.80 - 3.05$
S Lyα	$2.60 - 2.70$
Ca He$\alpha^\dagger$	$3.60 - 4.00$
Fe K$\alpha^\dagger$	$6.20 - 6.90$

Table 5.3: Extraction energy windows for the unconvolved model spectra. †: see text.

the values of ρ_{AM} and β in the Tycho SNR (see sections 3.4.1, 5.1.2, and 5.2.2). That is 15 synthetic spectra for each SN explosion model, a total of 285 spectra for the 12 models of the sample subgrid plus the 7 off-grid ejecta models presented in chapter 2.

Due to the number of synthetic spectra produced, it is impractical to repeat the complex fitting procedure described in last section for every one of them. However, the calculation of the line centroids and fluxes in the synthetic spectra is straightforward if it is performed before convolution with an instrumental response (see Figure C.1 for an example of unconvolved synthetic spectrum). In this format, all the lines that contribute to a given blend can be singled out and selected without the risk of contamination from neighboring lines, and the continuum can be subtracted easily. The selection energy windows for each of the lines in the unconvolved model spectra are listed in Table 5.3. The Ca and Fe line blends have been labeled Ca Heα and Fe Kα because these are the most important contributions in the observed spectrum, but this need not be the case for the models. As the ionization and temperature of the plasma change with varying ρ_{AM} and β, contributions from the neighboring Ca Kα and Fe Heα blends will sometimes dominate the emitted flux in the synthetic spectra. This has to be taken into account in the extraction windows, which also include these neighboring line blends. Whenever there is a shift in the dominant component within the Ca or Fe line blends, it will become evident by the position of the centroid (see Table 3.2 for the line energies and an explanation of the Kα and Heα nomenclature). For consistency with the fitted values, a fiducial interstellar absorption with $N_H = 0.45 \cdot 10^{22}\,\mathrm{cm}^{-2}$ has been applied to the synthetic spectra as well. Before any kind of comparison with the observed values is attempted, however, two issues need to be discussed in some detail.

One is the quality of the atomic data included in the Hamilton & Sarazin code. Due to the limitations of this spectral code, which are discussed in appendix C, it is not advisable to compare directly some parameters of the line emission in the synthetic spectra with the observations. The predictions of the HS code are not reliable for the centroids of the Si Heα and S Heα blends, and since no data are included for Ar, any comparison with Ar emission is obviously impossible. Taking this into account, a set of nine representative quantities has been selected: the line ratios Si He($\beta+\gamma$)/Si Heα, Si Lyα/Si Heα, S He($\beta+\gamma$)/S Heα, S Lyα/S Heα, S Heα/Si Heα, Ca Heα/Si Heα and Fe Kα/Si Heα; and the centroids of the Ca Heα and Fe Kα line blends. These nine parameters provide an adequate diagnostic of the properties of the emitting plasma in the shocked ejecta, and they will be used for the comparison between the line emission from the models and the observations.

Another is the effect of Doppler shifts, which has not been taken into account, either in the generation of synthetic spectra or in the fit with Gaussian lines to the *XMM-Newton*

data. In the spherically symmetric hydrodynamic models, of course, the Doppler effect would produce no actual shifts in the line centroids, but would certainly broaden the lines to some extent. The most affected models would be those with high E_k and low ρ_{AM}, where the shocked ejecta move at high velocity. The highest E_k of the grid models corresponds to DET, but we have seen in chapter 2 that the spectrum emitted by this model has virtually no line emission from any elements except Fe, so we will consider the next highest by E_k, which is model PDDa. The shocked ejecta of PDDa interacting with a ρ_{AM} of $2 \cdot 10^{-25}\,\mathrm{g} \cdot \mathrm{cm}^{-3}$ have a velocity of $\sim 6 \cdot 10^8\,\mathrm{cm} \cdot \mathrm{s}^{-1}$ at the age of Tycho, about 2% of c, so the maximum possible Doppler broadenings would be of $\sim \pm 30\,\mathrm{eV}$ at the energy of Si Heα and $\sim \pm 120\,\mathrm{eV}$ at that of Fe Kα. An interaction with ambient medium densities of 10^{-24} and $5 \cdot 10^{-24}\,\mathrm{g} \cdot \mathrm{cm}^{-3}$ results in velocities of $\sim 3 \cdot 10^8$ and $\sim 1.5 \cdot 10^8\,\mathrm{cm} \cdot \mathrm{s}^{-1}$ for the shocked ejecta, and Doppler broadenings of $\sim \pm 15$ and $\sim \pm 7$ eV for Si Heα, and $\sim \pm 60$ and $\sim \pm 30$ eV for Fe Kα. In addition to the possible Doppler broadenings, these blends are intrinsically broad due to the separation of the contributing lines: for the Si Heα blend this separation is approximately 25 eV; the Fe Kα blend is more complex, but 80 eV is a rough estimate for its maximum expected intrinsic broadness. The fitted values of σ for the Gaussian lines in the *XMM-Newton* data set are 21 eV for Si Heα and 59 eV for Fe Kα, implying that the lines are broadened by ~ 15 and ~ 40 eV, respectively. These values seem to favor AM densities larger than $10^{-24}\,\mathrm{g} \cdot \mathrm{cm}^{-3}$, but more precise conclusions would require a more detailed analysis. A final possibility is that there are actual shifts, not broadenings, in the centroids of the *XMM-Newton* spectrum due to a net positive or negative velocity, either affecting the entire SNR or some of the ejecta lines in the extraction region. While a net nonzero velocity for some of the elements in the ejecta cannot be discarded, the apparent symmetry of the images reviewed in section 5.2 and the fact that all fitted centroids have been found close to the expected values (see Table 5.1) do not support the existence of such shifts. Regarding the bulk motion of the entire SNR, Lee et al., 2004, give a range of $-7 \cdot 10^6$ to $-5 \cdot 10^6\,\mathrm{cm} \cdot \mathrm{s}^{-1}$ for the receding velocity in the environment of Tycho. Assuming that these figures can be applied to the SNR as well, the maximum possible Doppler shifts would be of $\sim -1.5\,\mathrm{eV}$ for the Fe Kα line and $\sim -0.4\,\mathrm{eV}$ for Si Heα, which can be safely ignored.

Discussion: grid models

The values of the diagnostic quantities as a function of ρ_{AM} and β are presented in Figures 5.6 to 5.17 for the sample subgrid models SCH, DET, DEFa, DEFc, DEFf, DDTa, DDTbb, DDTc, DDTe, PDDa, PDDc, and PDDe. Wherever a point is not represented, it is because the line involved is either altogether absent or has a flux below twice the level of the continuum at that energy in the unconvolved model spectrum. The values derived from the *XMM-Newton* spectrum, taken directly from Tables 5.1 and 5.2, are represented in the plots as well. Tolerance boundaries have been set on the observed values, to a factor two up and down for the line ratios, to 0.5% of the observed value for the Fe Kα centroid, and to 1% of the observed value for the Ca Heα centroid. These ranges are in all cases much larger than the estimated parameter errors obtained in the fits. For the S Lyα/S Heα ratio, the data only provide an upper limit, so no lower tolerance boundary has been set. In the case of the Si Lyα/Si Heα ratio, even though the fit to the observed spectrum does provide a flux for the Si Lyα line which implies a lower tolerance boundary on the ratio, the data do not constrain this lower limit strongly, and values below it can be accepted. Needless to say, these tolerance ranges are arbitrary and so is, ultimately, the decision to accept or discard a model that falls inside or outside of them. They should

only be regarded as reasonable quantitative criteria that help to assess the performance of candidate models.

Before each model is discussed in detail, it is worth to make a few general comments. First, it is evident that no model matches all nine diagnostic quantities at once within the tolerance ranges. This is largely due to the fact that Ca line emission is dominated by Ca Kα in almost all the models, in clear contradiction with the observed spectrum from Tycho, which is dominated by Ca Heα. No grid model comes even close to matching the Ca line centroid energy and Ca Heα/Si Heα line ratio at the same time. This behavior of the Ca emission in the models is very puzzling, and will be revisited later. For the time being, the characteristics of Ca line blend will not be taken into account in the comparison between models and observations.

Second, the behavior of the grid models with varying ρ_{AM} and β follows some common trends. These trends were outlined in section 4.2, but here they can be quantified and examined with detail thanks to the fineness of the simulation grid. The choice of values for ρ_{AM} seems adequate in that reasonable results are obtained in the middle range, if at all, while the extrema can be discarded in most cases. This is particularly clear for Si and S line emission. In the high density limit, the more advanced ionization state of the plasma leads to significant amounts of H-like ions being produced, and therefore to strong Si Lyα and S Lyα lines, which are either absent or very weak in the spectrum of Tycho. In the low density limit, Si Heβ and S Heβ usually disappear or become too weak when compared to Si Heα and S Heα, but there are exceptions to this (most notably the PDD models). The Fe Kα line also shows clear trends, but they are complicated by the effect of collisionless electron heating. Values of β above β_{min} affect Fe more than the other elements because the location of the Fe-rich layers in the innermost ejecta exposes them directly to the higher temperatures towards the reverse shock. The Fe Kα/Si Heα ratio, for instance, always increases with increasing ρ_{AM} if $\beta = \beta_{min}$, but this tendency can be reversed for larger values of β. A greater amount of collisionless electron heating always results in a higher value for the Fe Kα/Si Heα ratio, because the emissivity of this line is very sensitive to T_e, but this effect is somewhat assuaged at large AM densities. The energy of the Fe Kα centroid, on the other hand, is always lower for larger values of β, and also increases with increasing ρ_{AM}, specially above $10^{-24}\,\mathrm{g} \cdot \mathrm{cm}^{-3}$. In any case, values of β larger than 0.1 do not seem compatible with the Fe Kα line emission from Tycho, in agreement with the indirect arguments presented in section 3.4.1.

The SCH model does not give results within the tolerance ranges for any combination of β and ρ_{AM}. The spectrum corresponding to $\rho_{AM} = 5 \cdot 10^{-25}\,\mathrm{g} \cdot \mathrm{cm}^{-3}$ and $\beta = 0.01$ comes close, but the S Lyα/S Heα ratio is somewhat high. Larger values of ρ_{AM} are discarded by the swift rise of Si and S Lyα in this model, which is prompted by the presence of a secondary density peak in this region of the ejecta (see section 3.3.2).

As expected, the DET model fails to reproduce most of the features of the line emission from Tycho. Besides the overwhelmingly strong Fe Kα blend and the Si Heα line, the only other major line that appears is S Heα, and even that requires the highest values of ρ_{AM}.

The DEF models do not perform too well in general, since many of the important lines are absent throughout most of the simulation space. DEFa can be discarded right away, because S Heβ only appears at $\rho_{AM} = 5 \cdot 10^{-24}\,\mathrm{g} \cdot \mathrm{cm}^{-3}$, and the model has strong Si and S Lyα emission at that AM density. DEFc shows a similar behavior, with the values of ρ_{AM} required by the Si Heβ/Si Heα and S Heβ/S He α ratios being ruled out by the high Si Lyα flux. Surprisingly, model DEFf comes close to producing an acceptable result for $\rho_{AM} = 10^{-24}\,\mathrm{g} \cdot \mathrm{cm}^{-3}$ and $\beta = 0.01$, but the energy of the Fe Kα centroid falls below the tolerance boundary.
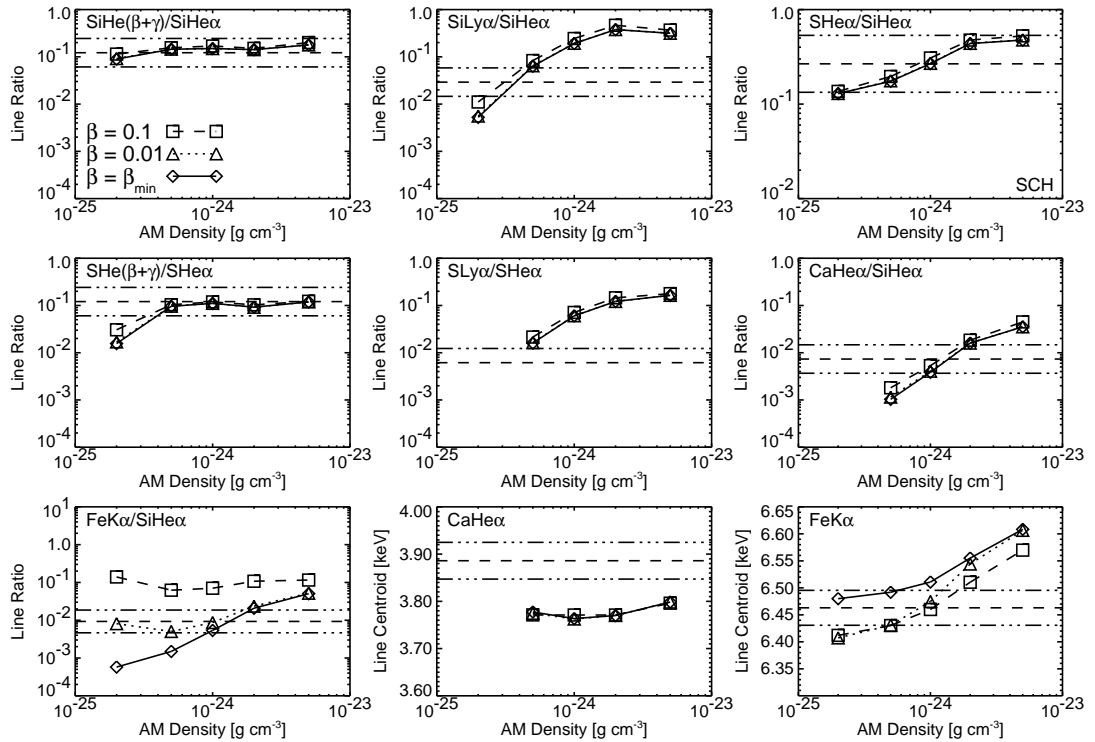
Figure 5.6: Diagnostic line ratios and centroids at the age of Tycho for model SCH represented as a function of ρ_{AM}. The observed values from Table 5.1 are plotted as horizontal dashed lines; tolerance ranges are plotted as dash-triple-dotted lines. For the model spectra, the different values of β at the reverse shock are represented by diamonds joined by a solid line ($\beta = \beta_{min}$), triangles joined by a dotted line ($\beta = 0.01$), and squares joined by a dashed line ($\beta = 0.1$).

The DDT models are more promising as a class, with diagnostic quantities close to or within the tolerance ranges in the upper ρ_{AM} region of the simulation grid. For all these models, the Si Lyα/Si Heα, S Lyα/S Heα and S Heα/Si Heα ratios rule out values of ρ_{AM} higher than $2 \cdot 10^{-24}\,\mathrm{g} \cdot \mathrm{cm}^{-3}$, while the S He($\beta + \gamma$)/S He$\alpha$ ratio is incompatible with lower AM densities, so the Si and S line emission can only be reproduced for $\rho_{AM} = 2 \cdot 10^{-24}\,\mathrm{g} \cdot \mathrm{cm}^{-3}$, if at all. Model DDTa gives a result within the tolerance ranges at this AM density for $\beta \leq 0.01$, with the Fe Kα flux and centroid closer to the observed values for $\beta = \beta_{min}$. The Fe line emission of model DDTbb also looks promising in this region, but the Si Lyα and S Lyα fluxes are slightly above the tolerance threshold. For model DDTc, the Fe Kα/Si Heα ratio requires a value of β larger than 0.01, but not too close to 0.1, if the Fe Kα line centroid and Si and S Lyα fluxes are to be reproduced as well. Finally, model DDTe gives mutually exclusive results for the Fe Kα centroid energy and line flux at $\rho_{AM} = 2 \cdot 10^{-24}\,\mathrm{g} \cdot \mathrm{cm}^{-3}$.

While the DDT models work better at high values of the AM density, the more advanced ionization state of the plasma in the PDD models demands lower AM densities in order to prevent an excess Si Lyα and S Lyα flux (see section 3.4.3 for the physical cause of this). PDDa provides marginally acceptable results at $\rho_{AM} = 2 \cdot 10^{-25}\,\mathrm{g} \cdot \mathrm{cm}^{-3}$ and $\beta = \beta_{min}$, which could be improved with a slight increase of β. For this AM density, PDDc might reproduce the Fe Kα flux for a value of β between β_{min} and 0.01, but the Fe Kα centroid energy would be too low. PDDe, the model with the highest content of Si and S in the ejecta, shows strong Lyα emission from these elements throughout the simulation space and is therefore incompatible with the observations. This problem might be solved
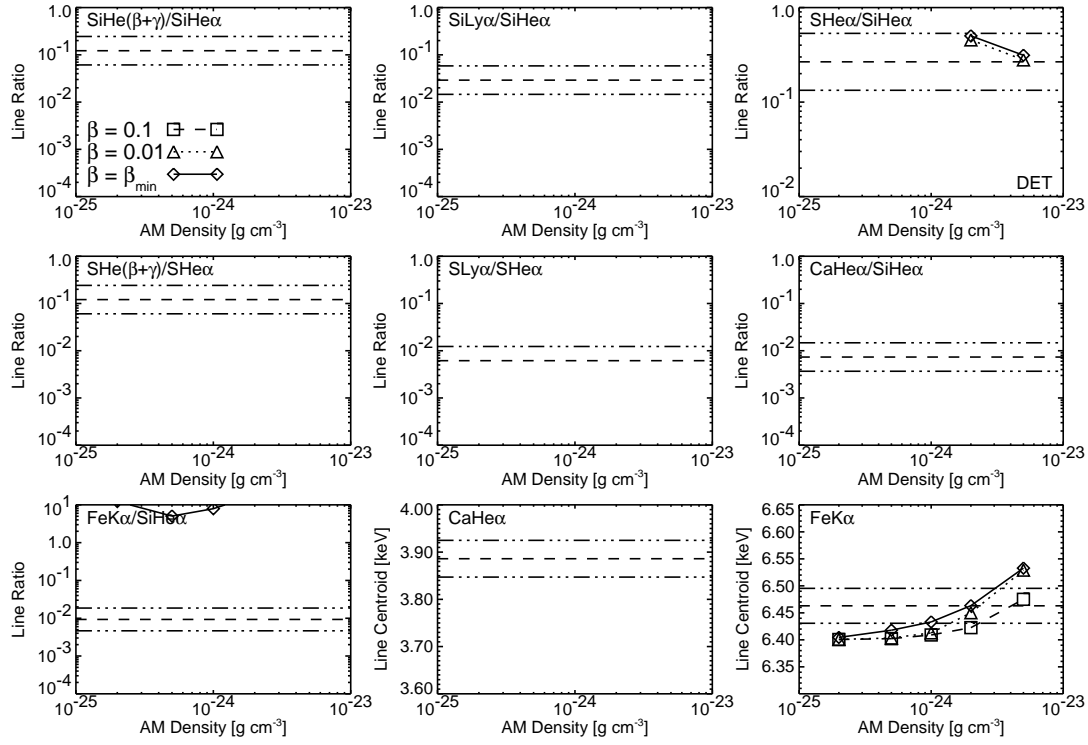
Figure 5.7: Diagnostic line ratios and centroids for model DET. All plots labeled as in Figure 5.6.

by adopting a value of ρ_{AM} lower than $2 \cdot 10^{-25}\,\mathrm{g} \cdot \mathrm{cm}^{-3}$, but that would probably drive the S Heβ flux below the tolerance threshold. It is worth noting that the PDD models are capable of reproducing the centroid of the Ca Heα line, but the high AM density values required by this put all the other diagnostic quantities well outside the tolerance ranges.

Discussion: off-grid models

The diagnostic quantities for the off-grid models W7, 5p0z22.25, DEF3D30b, DDT3DA, SCH3DOP, SCH3DMP, and b30_3d_768 are presented in Figures 5.18 to 5.24, with the same conventions and tolerance ranges that were used for the grid model plots. The structure of the one dimensional W7 and 5p0z22.25 models is similar to that of the grid models, so the results obtained for the line emission are similar as well. In the case of W7, it is worth noting that the Fe Kα/Si Heα ratio of Tycho can be reproduced by a moderate amount of collisionless electron heating at the reverse shock, with no need for the layer mixing proposed by the works reviewed in section 5.2. The model has to be discarded, however, because it is not possible to reconcile this ratio with the energy of the Fe Kα centroid and the Si and S emission. Model 5p0z22.25 cannot provide a good approximation to the S line emission for any combination of ρ_{AM} and β due to the swift drop in S Heβ emission below $\rho_{AM} = 5 \cdot 10^{-24}\,\mathrm{g} \cdot \mathrm{cm}^{-3}$. It is remarkable that these 1D off-grid models, whose nucleosynthesis is calculated with codes different from those used in the grid models, are also incapable of reproducing the characteristics of the line emission from Ca.
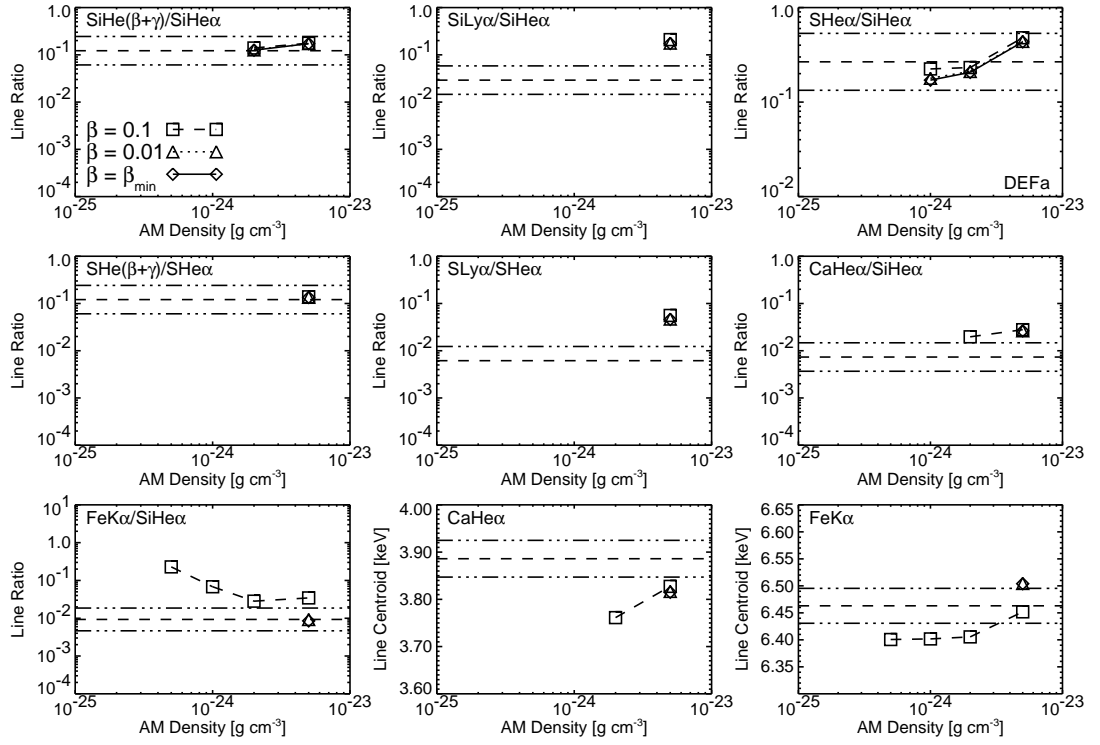
Figure 5.8: Diagnostic line ratios and centroids for model DEFa. All plots labeled as in Figure 5.6.

The 1D averages of 3D explosion calculations behave in a somewhat different way. The most remarkable feature of these models is that they overpredict the Fe Kα/Si Heα line ratio for all the values of ρ_{AM} and β, in most cases by an order of magnitude or more. As was pointed out in section 4.2.2, this is due to the mixing of large quantities of Fe into the outer ejecta layers in 3D Type Ia explosion calculations. It seems clear that this kind of models is not capable of reproducing the characteristics of the X-ray line emission from Tycho, at least within the simulation scheme that is being used here. It is interesting to note that in the more thoroughly mixed models DDT3DA and b30_3d_768, the impact of the collisionless electron heating on the Fe Kα emission is greatly reduced when compared to standard 1D models. Once again, the characteristics of the Ca line are systematically mispredicted in all cases.

Survival of the fittest

As has been mentioned before, a decision to accept or discard a model based exclusively on the arbitrary tolerance ranges that have been set on the observed values would be arbitrary itself. Strictly speaking, only the DDTa model has complied with the quantitative criteria defined in this section. In order to select a group of candidate spectral models that is representative of the explosion model grid, it seems reasonable to include some models that are marginally acceptable, or even slightly outside the tolerance ranges. In a few special cases, such as DDTc, the properties of the line emission justify the need to generate new synthetic spectra at intermediate values of β. With these considerations in mind, the group of seven candidate models listed in table 5.4 has been selected. The next section will be devoted to test these seven models against the entire spectrum of Tycho.
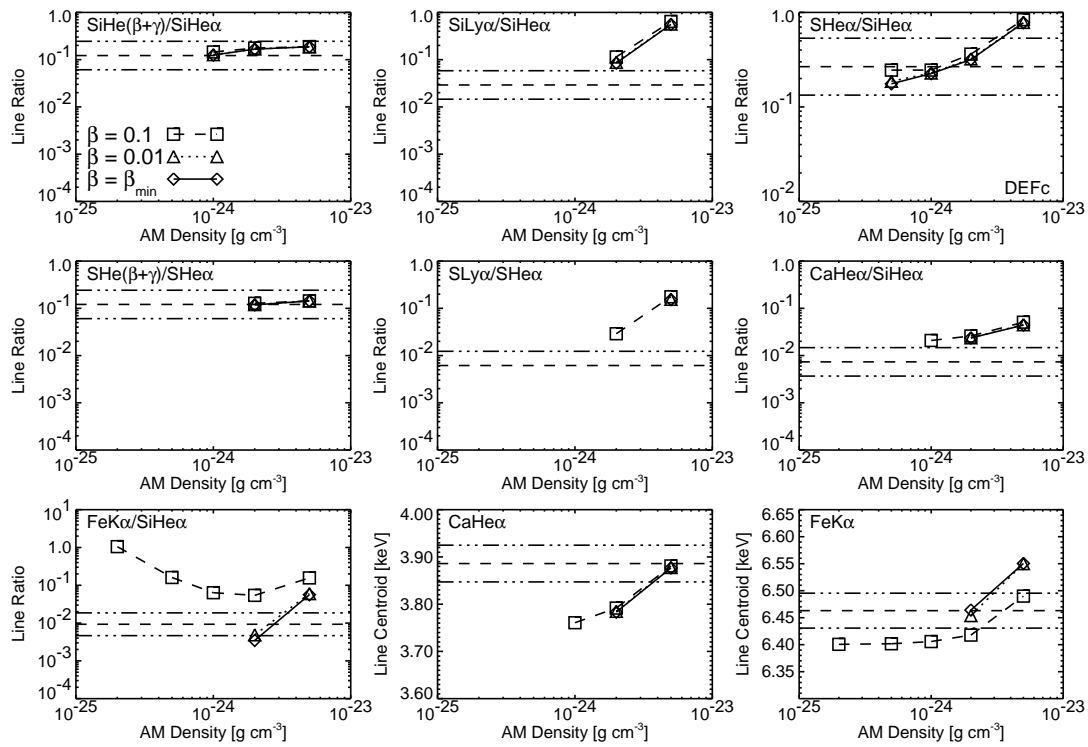
Figure 5.9: Diagnostic line ratios and centroids for model DEFc . All plots labeled as in Figure 5.6.

Figure 5.10: Diagnostic line ratios and centroids for model DEFf. All plots labeled as in figure 5.6.

Figure 5.11: Diagnostic line ratios and centroids for model DDTa. All plots labeled as in figure 5.6.

Figure 5.12: Diagnostic line ratios and centroids for model DDTbb. All plots labeled as in figure 5.6.

Figure 5.13: Diagnostic line ratios and centroids for model DDTc. All plots labeled as in figure 5.6.
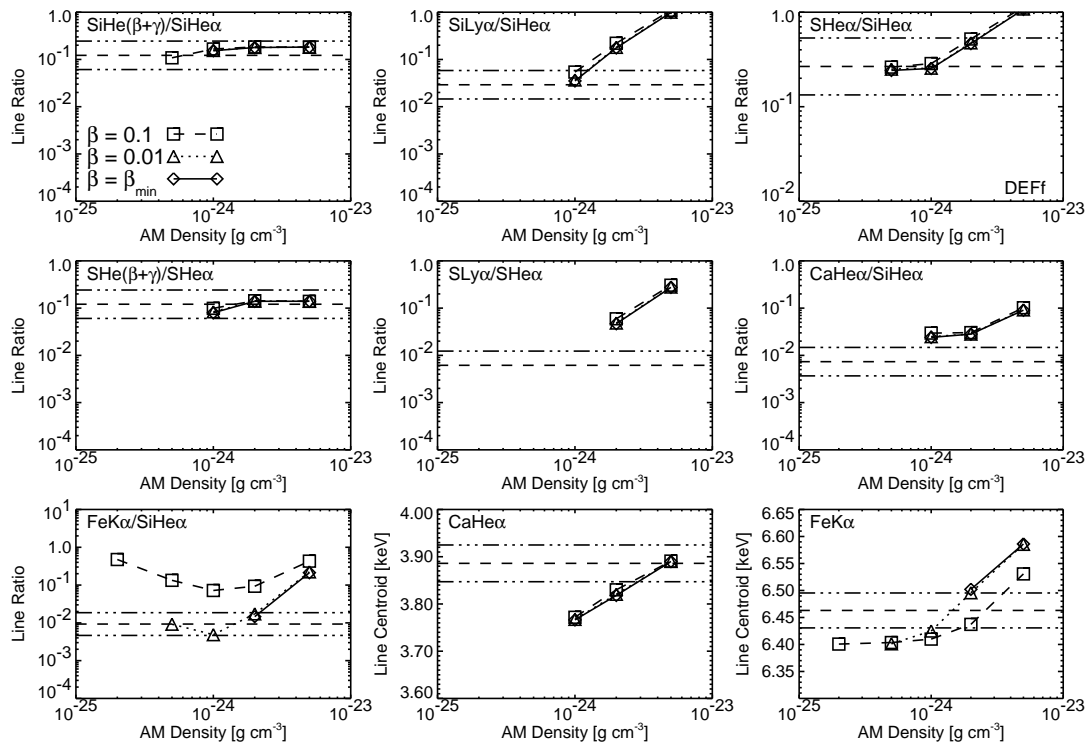

Figure 5.14: Diagnostic line ratios and centroids for model DDTe. All plots labeled as in figure 5.6.

Figure 5.15: Diagnostic line ratios and centroids for model PDDa. All plots labeled as in figure 5.6.

Figure 5.16: Diagnostic line ratios and centroids for model PDDc. All plots labeled as in figure 5.6.
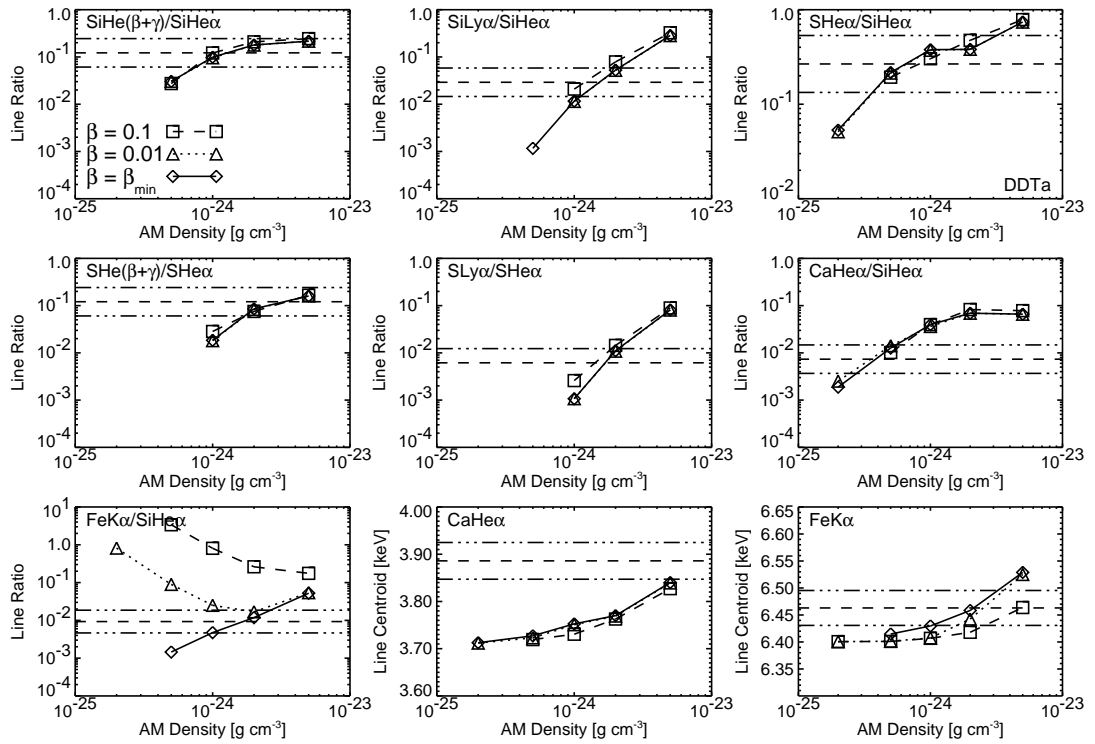
Figure 5.17: Diagnostic line ratios and centroids for model PDDe. All plots labeled as in figure 5.6.
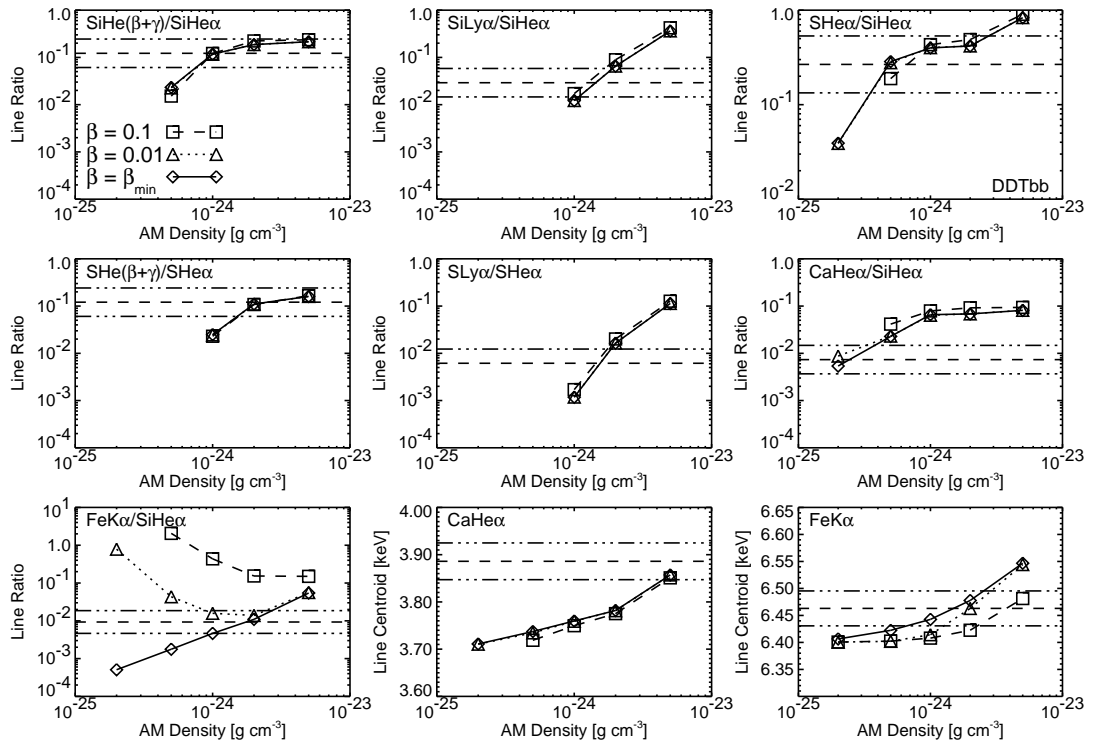

Figure 5.18: Diagnostic line ratios and centroids for model W7. All plots labeled as in figure 5.6.

Figure 5.19: Diagnostic line ratios and centroids for model 5p0z22.25. All plots labeled as in figure 5.6.

Figure 5.20: Diagnostic line ratios and centroids for model DEF3D30b. All plots labeled as in figure 5.6.

Figure 5.21: Diagnostic line ratios and centroids for model DDT3DA. All plots labeled as in figure 5.6.

Figure 5.22: Diagnostic line ratios and centroids for model SCH3DOP. All plots labeled as in figure 5.6.
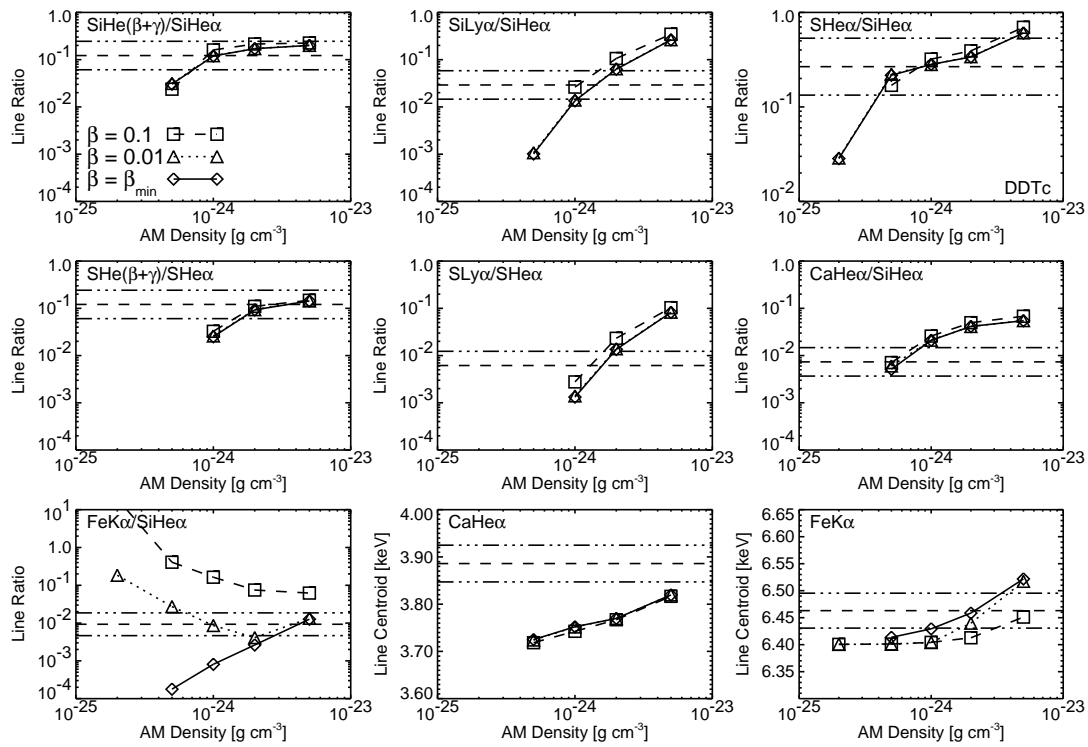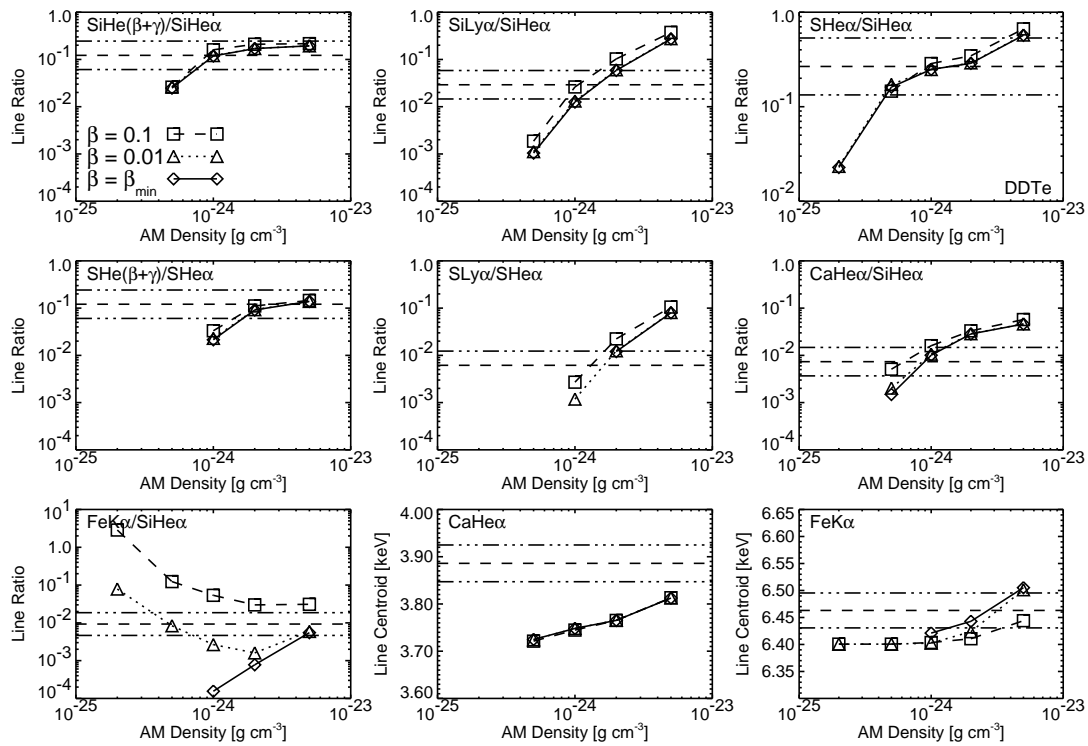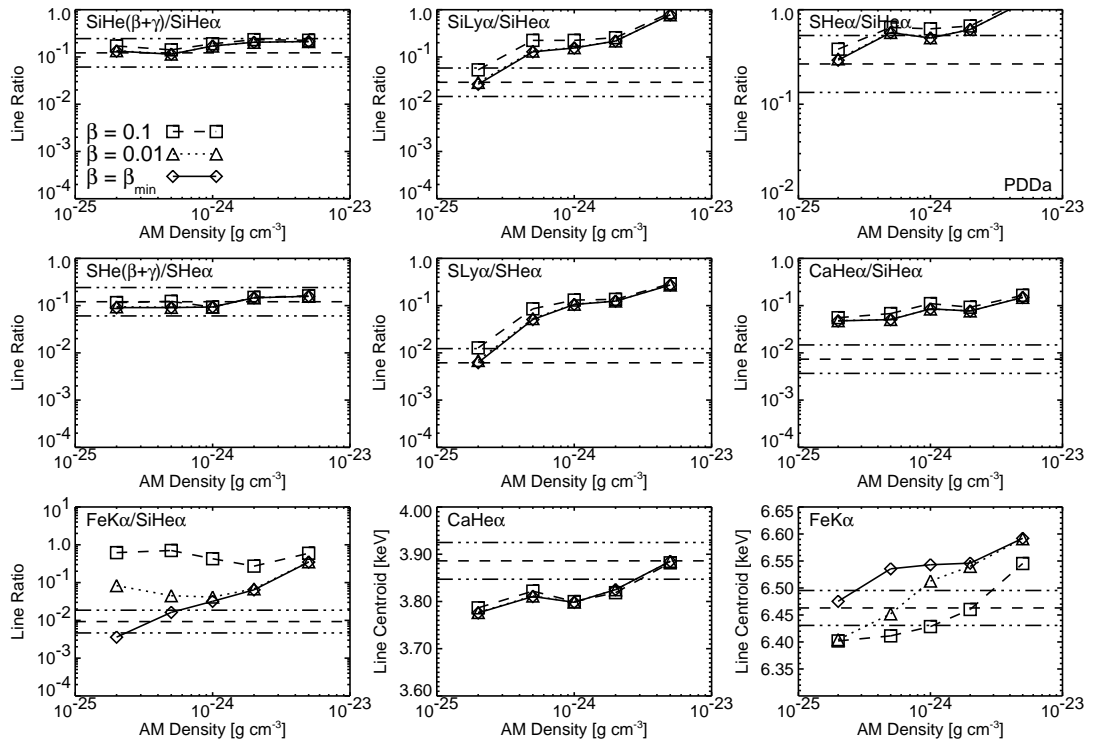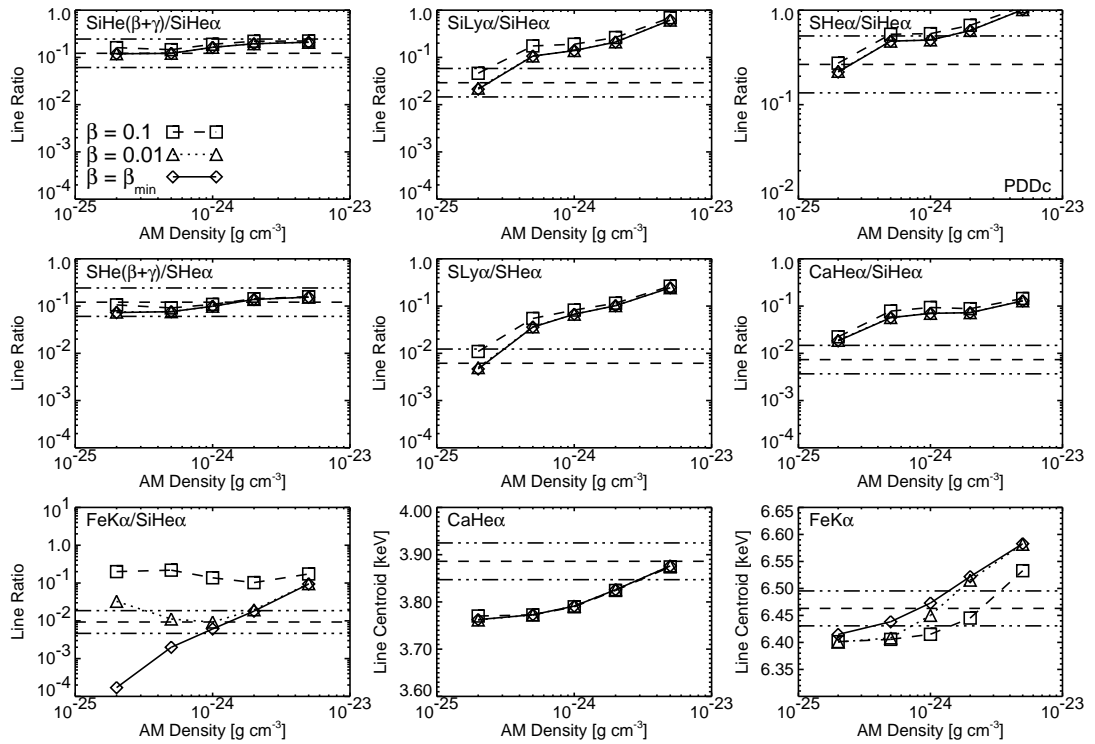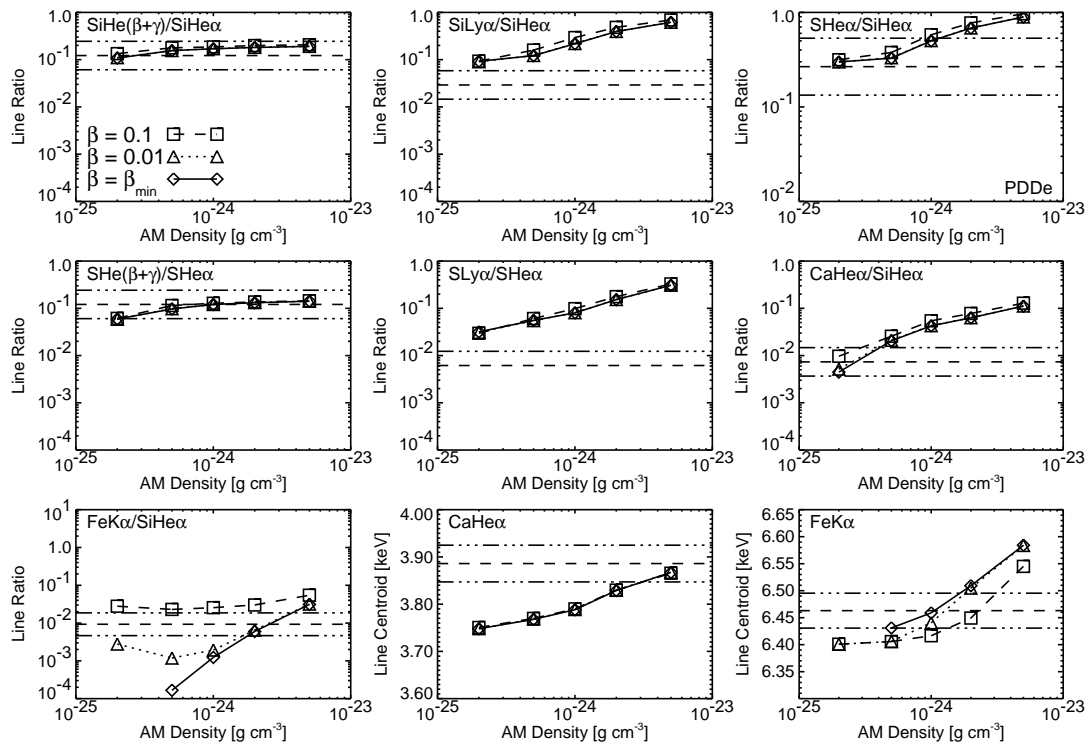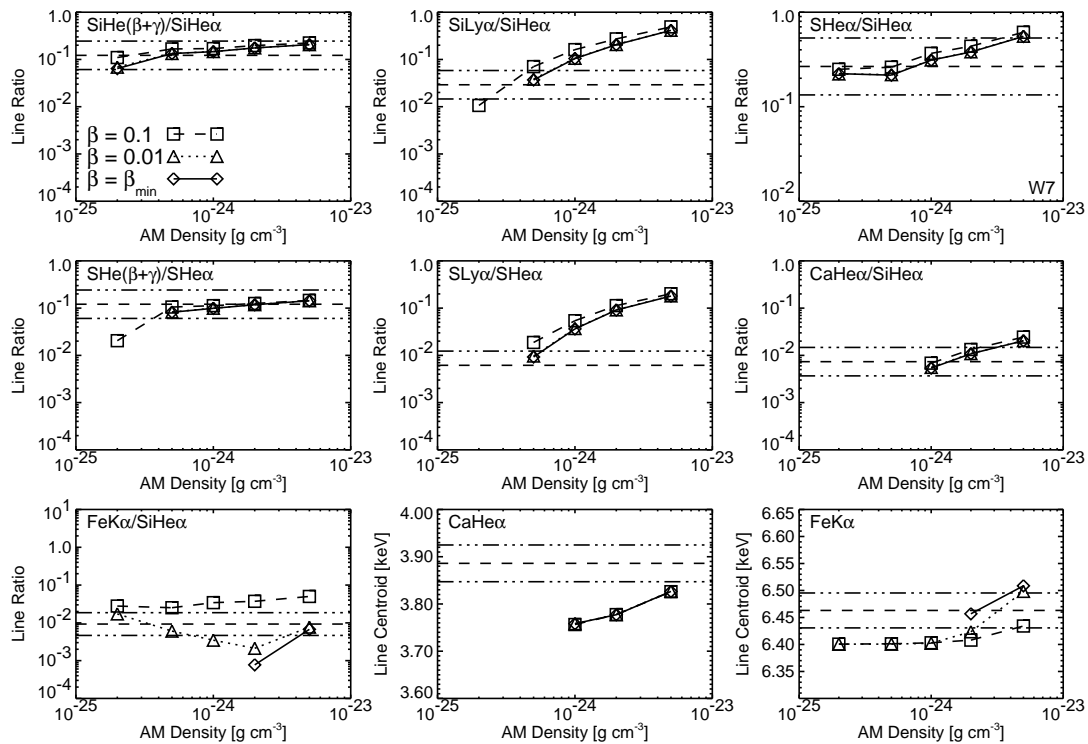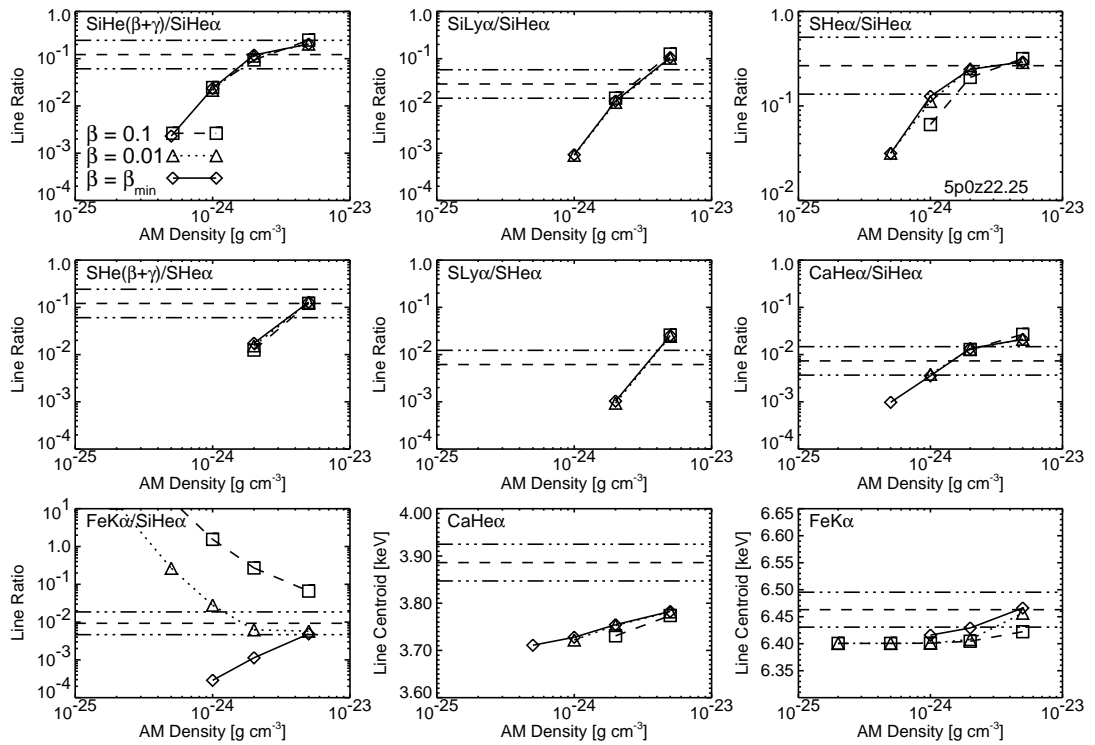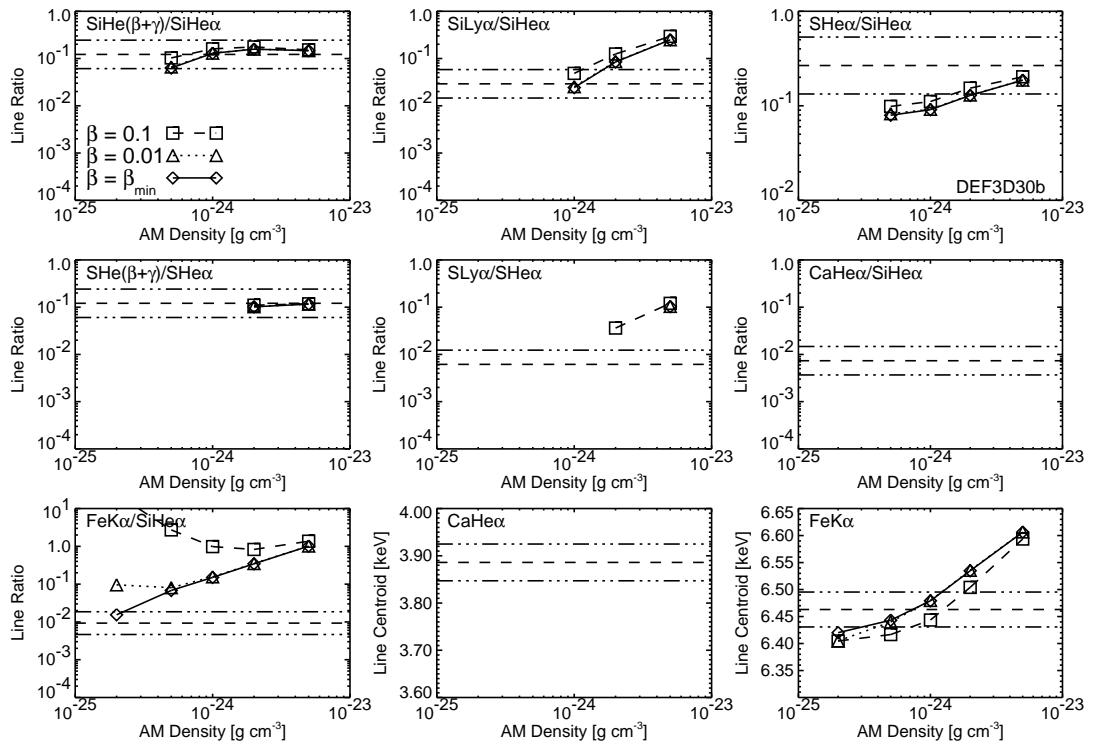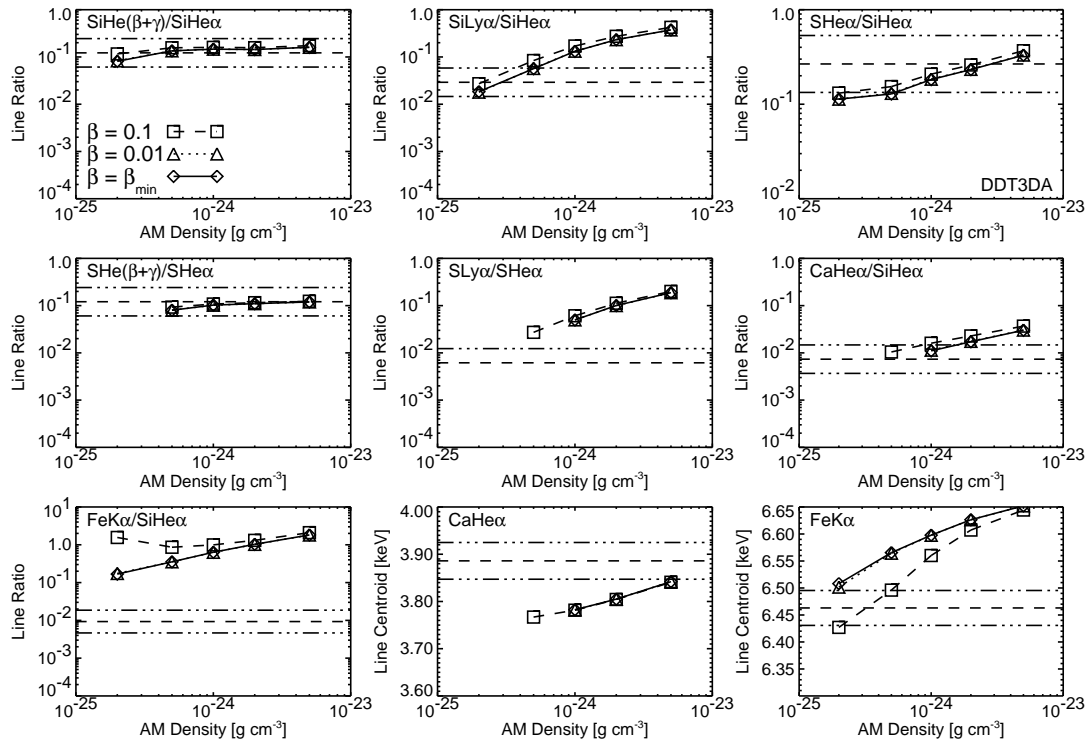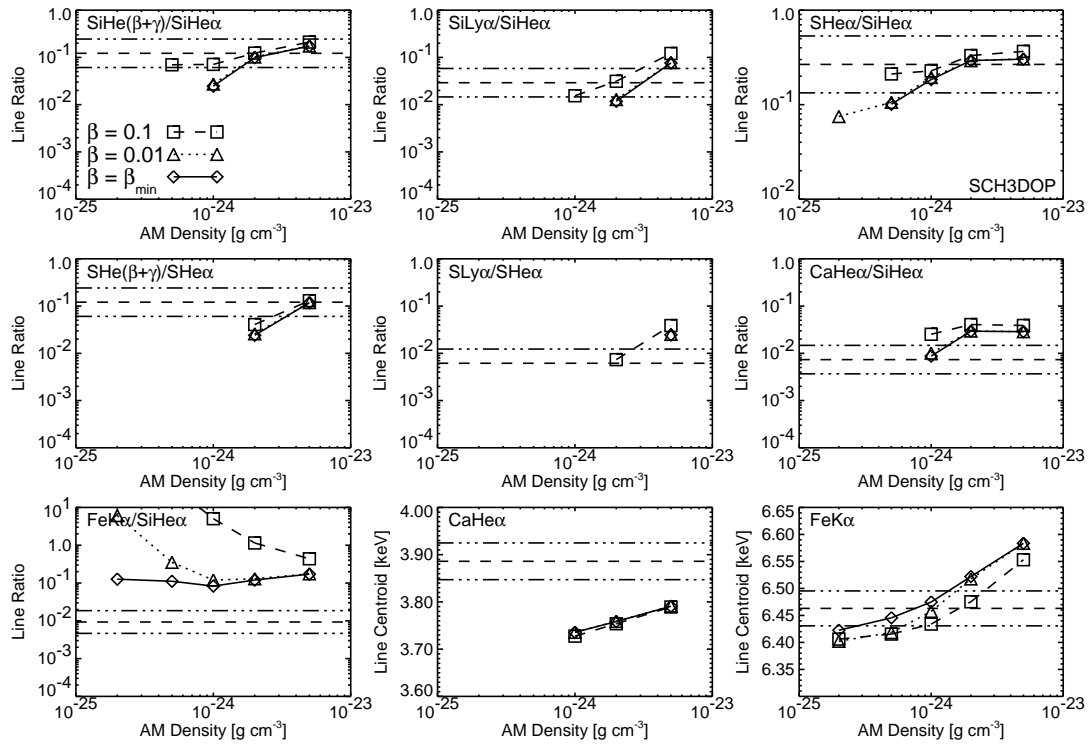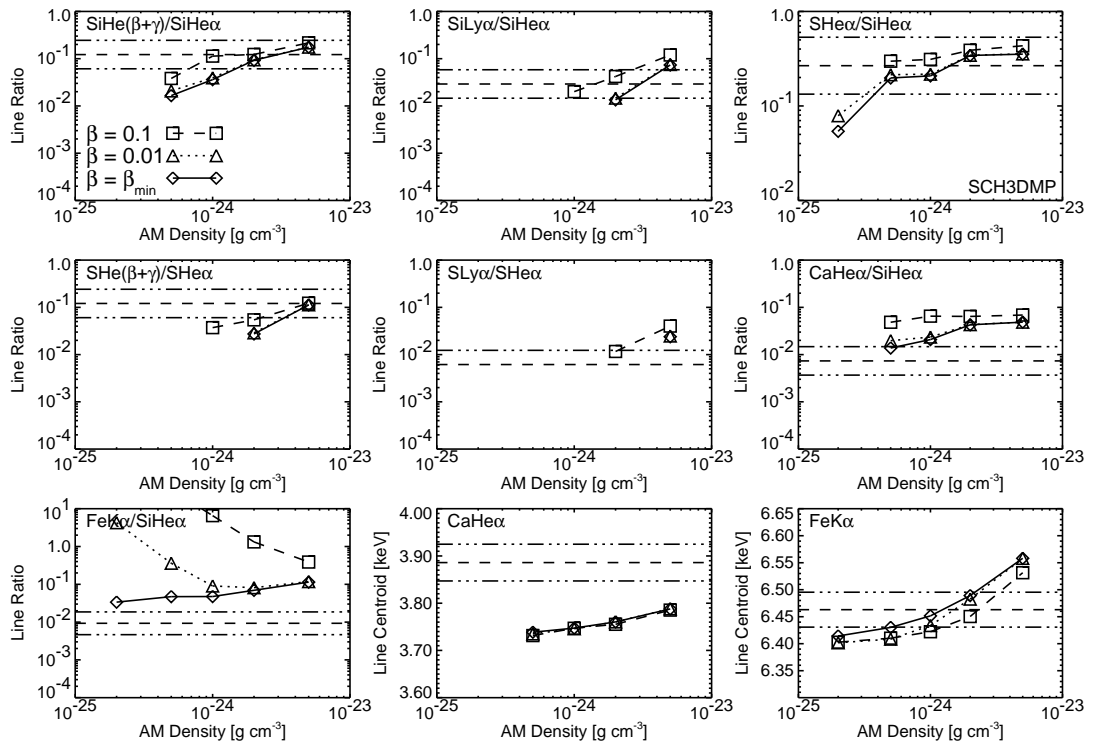
Figure 5.23: Diagnostic line ratios and centroids for model SCH3DMP. All plots labeled as in figure 5.6.
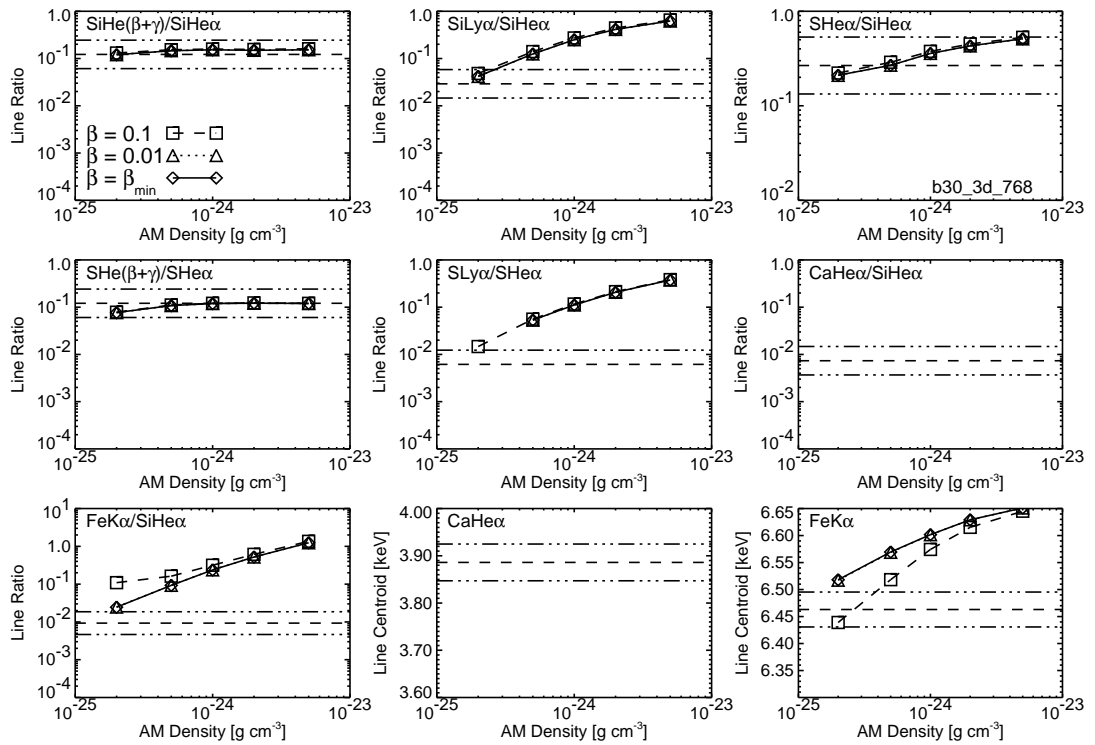

Figure 5.24: Diagnostic line ratios and centroids for model b30_3d_768. All plots labeled as in figure 5.6.

5.3.4 Global approximations to the X-ray spectrum of Tycho

Even if an ejecta model succeeds in reproducing the most important features of the line emission from Tycho, there is no guarantee that it can provide a reasonable global approximation to the X-ray spectrum. In fact, given that an acceptable statistical fit to the observed spectrum is not to be expected, one should find an alternative way to define what constitutes a 'reasonable approximation' and what does not.

The following method has been devised to produce these spectral 'approximations' (as opposed to fits). First, a global spectral model is defined within XSPEC consisting of the ejecta model that is being tested plus a thermal bremsstrahlung, affected by an interstellar absorption which is initially set to $N_H = 0.45 \cdot 10^{22}\,\mathrm{cm}^{-2}$. The temperature of the bremsstrahlung and the normalization of the two additive components is adjusted by fitting the global model to the *XMM-Newton* spectrum in two energy windows simultaneously, the Si Heα line at $1.6 < E < 2.0\,\mathrm{keV}$ and the continuum between the Ca and Fe lines at $4.1 < E < 6.0\,\mathrm{keV}$. With this procedure, the spectrum above 1.6 keV will be approximated as closely as the limitations of the ejecta and the AM models allow. Even though a bremsstrahlung with $kT \simeq 2\,\mathrm{keV}$ was found by Hwang et al., 2002, to be an adequate model for the AM emission in fits to *Chandra* data, a free fit of kT seems more reasonable in view of the result obtained in section 5.3.2. It is important to normalize the ejecta with respect to the Si Heα line, because this is the reference for most of the line ratios that have been used; if the model provided a good approximation to the diagnostic quantities as required in the previous section, the rest of the line fluxes will fall into place. Next, the component normalizations and the bremsstrahlung temperature are fixed (or 'frozen' in the XSPEC jargon), and the interstellar absorption is fitted freely using the data above an energy of 0.8 keV, which corresponds to the peak in Fe L emission associated with Fe^{+16}. The goal of this final fit is to assess the ability of the ejecta model to reproduce at once the Fe L and Fe Kα emission of Tycho, which has proved a difficult challenge in the past (see section 5.2.2). Photon energies below 0.8 keV are not included in the fit, in part because the presence of bright O Lyα and Ca L emission in some models might lead to overestimate the value of N_H, in part because of the complexity of adjusting CCD spectra at such low energies. These low energies can be used as an *a posteriori* test for those models that manage to reproduce reasonably well the high energy line emission and the Fe L emission.

Before going back to the selected ejecta models, we will insist, once again, that these approximations to the spectrum of Tycho should neither be regarded as nor compared with conventional spectral fits. The method that has just been described is obviously not unique, and several alternatives with varying degrees of sophistication could be easily conceived. We only intend to provide a reasonable procedure to gauge the capabilities of the ejecta models and arrive at preliminary conclusions. More detailed analysis techniques are not justified at this point, in view of the limitations that affect the models and the atomic data used for the generation of the synthetic spectra.

The normalization for the ejecta and AM components, the temperature for the AM bremsstrahlung kT_{AM} and the hydrogen column density N_H are listed in Table 5.4 for the seven candidate models. Even though the standard 90% confidence ranges are provided for the fitted quantities, no statistical significance should be attached to these errors, since the parameters have not been 'fitted' in the usual sense.

The normalization of the ejecta component provides an estimate of the distance to Tycho, D_{norm}, that is required for each model to match the observed flux. The value of D_{norm} can be readily calculated knowing that the synthetic ejecta spectra are generated assuming a fiducial distance to the source of 10 kpc:

Model	ρ_{AM} [g $\cdot$ cm^{-3}]	β	$norm_{ej}$	D_{norm} [kpc]	$norm_{AM}$ [10^{-2}]	kT_{AM} [keV]	N_H [10^{22} cm^{-2}]
SCH	$5 \cdot 10^{-25}$	0.01	30.6 ± 0.1	1.367 ± 0.002	$0.6^\dagger$	$99.9^\dagger$	1.112 ± 0.001
DEFf	10^{-24}	0.01	8.70 ± 0.02	2.563 ± 0.003	†	†	0.868 ± 0.001
DDTa	$2 \cdot 10^{-24}$	β_{min}	11.73 ± 0.04	2.207 ± 0.004	3.4 ± 0.1	2.01 ± 0.04	1.275 ± 0.001
DDTa	$2 \cdot 10^{-24}$	0.01	11.94 ± 0.04	2.188 ± 0.004	3.4 ± 0.1	1.99 ± 0.04	1.286 ± 0.001
DDTc	$2 \cdot 10^{-24}$	0.02	6.86 ± 0.02	2.886 ± 0.004	2.1 ± 0.8	2.71 ± 0.01	0.710 ± 0.001
DDTe	$2 \cdot 10^{-24}$	0.03	5.76 ± 0.02	3.150 ± 0.005	1.6 ± 0.1	3.27 ± 0.13	0.510 ± 0.001
PDDa	$2 \cdot 10^{-25}$	β_{min}	117.6 ± 0.6	0.697 ± 0.002	2.9 ± 0.1	2.57 ± 0.06	0.694 ± 0.001

Table 5.4: Parameters for the approximations to the global spectra of the ejecta models selected in section 5.3.3. In the models marked with †, the bremsstrahlung model for the AM emission is not well constrained.

$$D_{norm} = \frac{10\,\text{kpc}}{\sqrt{\xi \cdot norm_{ej}}} \tag{5.1}$$

In this expression, ξ is a correction factor to allow for the fact that the spectrum only contains photons from $\sim 40\%$ of the SNR surface, or $1/\xi$ of the flux. If the brightness of Tycho was uniform all over its surface, ξ would be equal to $1/0.4 = 2.5$, but this is clearly not the case (see Figs. 5.3 and 5.4). A better estimate of ξ can be obtained by comparing the line fluxes in the *XMM-Newton* and *ASCA* spectra listed in Table 5.1. The correction factor varies between 1.9 and 1.6 for the most important lines, so $\xi = 1.75$ has been adopted in order to calculate the values of D_{norm}.

The fitted interstellar absorption can also be used to test the consistency of the models. At radio wavelengths, Albinson et al., 1986, obtained the hydrogen column density of $0.45 \cdot 10^{22}\,\text{cm}^{-2}$ that has been used in the previous sections. The fits to several extraction regions along the western rim performed by Hwang et al., 2002, yielded values between $0.24 \cdot 10^{22}$ and $0.95 \cdot 10^{22}\,\text{cm}^{-2}$, but this spatial variation of the interstellar absorption was difficult to interpret, and the authors suggested that it might be related to spectral complexities that were not properly modeled. In any case, values of N_H larger than their upper limit of $0.95 \cdot 10^{22}\,\text{cm}^{-2}$ do not seem reasonable, and might affect the Si Heα blend flux to the point of distorting the line ratios presented in Figures 5.6 to 5.24. Models that require higher hydrogen column densities are probably overpredicting the flux in the Fe L complex.

The spectral approximations are plotted in Figure 5.25. They are clearly unacceptable as statistical fits, but it must be kept in mind that, once the ejecta models are selected, the only free parameters are the normalization of the components, the bremsstrahlung temperature, and the hydrogen column density. Most models cannot reproduce the continuum at the highest energies, probably due to a nonthermal contribution to the X-ray spectrum of Tycho (see section 5.2.1). The larger effective area at high energies of the *XMM-Newton* EPIC CCDs reveals this component, that did not appear clearly in the *Chandra* spectra fitted by Hwang et al., 2002. Since this does not affect the ejecta emission, however, we shall not concern ourselves with it.

Model SCH has several problems. The thermal continuum emission from the ejecta is rather high, coming mostly from O in the secondary density peak of this model, and matches well that of the observed spectrum. As a consequence, XSPEC uses the AM bremsstrahlung component to adjust the high energy continuum, resulting in the inordi-
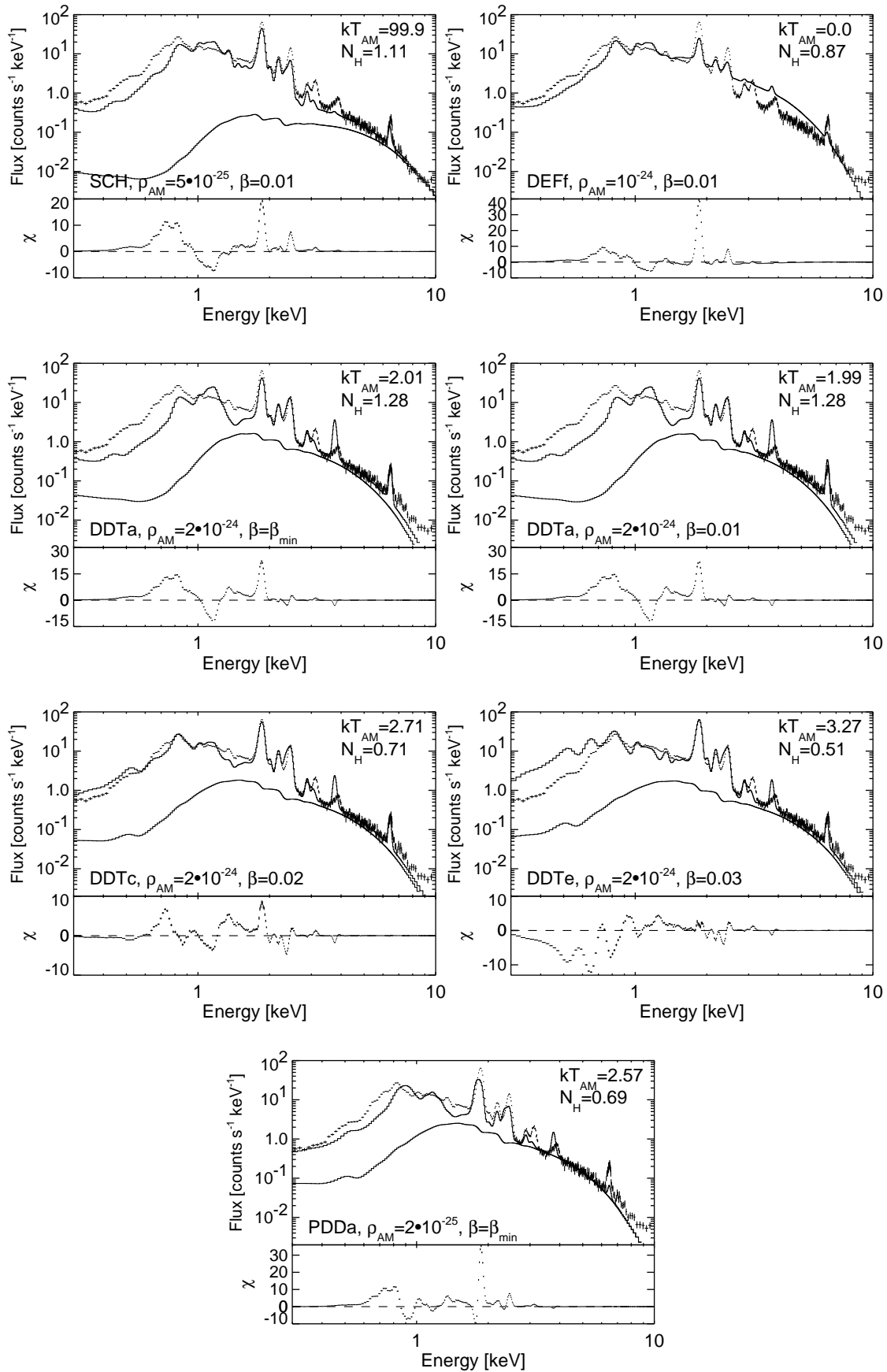
Figure 5.25: Global approximations to the X-ray spectrum of Tycho using the ejecta models whose line emission conformed to the criteria exposed in section 5.3.3. The contribution of the AM model has been plotted alongside the total spectral model. See text for details.

nately high fitted value for kT_{AM}. The Fe L emission is overpredicted and forces an excess of interstellar absorption that affects the Si Heα line. The S Heα flux, and the Fe Kα flux and centroid energy, which were in the limit of the tolerance regions in Figure 5.6 are all underpredicted. Finally, the low value of ρ_{AM} for this model requires a high normalization constant for the ejecta emission, making the value of D_{norm} incompatible with previous estimates ($1.9 \leq D \leq 2.3$ kpc from optical measurements; $1.5 \leq D \leq 4.5$ kpc including all methods, see section 5.1.2).

Model DEFf does better in terms of fitted N_H and estimated D_{norm}, but the continuum from the unburned C and O in the outer ejecta is so high that the bremsstrahlung is suppressed in the fit. In fact, it is impossible to find a convenient normalization for the ejecta model, so the values listed in Table 5.4 should be regarded with extreme caution.

The DDT models produce the most interesting results. The estimated values of D_{norm} are compatible with the observations, and the temperature of the AM bremsstrahlung component is in all cases between the ~ 2.0 keV found by Hwang et al., 2002 and the 3.9 keV of the fit in the high energy window in section 5.3.2. The line emission is also well reproduced, with a few minor caveats. As seen in Figures 5.11, 5.13 and 5.14, there is an excess of S Heα flux in all DDT models, and the centroid of this line is underestimated, but this deviation could be due to problems in the spectral code. Some excess Si Lyα can also be appreciated in models DDTc and DDTe. Since Si Heα is not overpredicted, this comes probably from the outermost ejecta, not from the large Si-rich region that extends to the inner ejecta in these models (see Figure 2.2). The emission at energies below 1.5 keV poses crucial constraints on the DDT models. The energetic, Fe-rich DDTa model clearly overpredicts the flux in the Fe L complex, resulting in a high N_H and too much absorption in the Si Heα line. Model DDTe, on the other hand, matches the Fe L emission pretty well, and even the Mg Heα line at 1.34 keV, but overpredicts the O Lyα line at 0.65 keV due to the large amount of O that it has in the outer ejecta. Model DDTc provides a good intermediate point between these two extrema, being the best model reviewed so far. It is worth noting that the less energetic DDT models, which reproduce the Fe L/Fe K ratio successfully, yield an energy for the Fe Kα line centroid that is slightly low, while DDTa, which overpredicts Fe L, matches the Fe Kα centroid very well, specially with $\beta = \beta_{min}$.

Finally, the PDDa model is clearly unsatisfactory. The line emission has obvious flaws, with strange shapes of the Si Heα and S Heα lines that do not allow to find the correct balance between ejecta and AM. In addition to this, the value of ρ_{AM} in this model is very low, and the normalization required to match the observed flux yields a D_{norm} that cannot be reconciled with any of the estimates presented in section 5.1.2.

5.4   Conclusions

The supernova of 1572: post mortem

The models and analysis procedures that have been applied to the Tycho SNR have several limitations and shortcomings, but they have allowed us to improve our understanding of the X-ray spectrum of this object and its relationship with the supernova that originated it in 1572. Within the unavoidable uncertainties, we conclude that the ejecta of Tycho's supernova are well matched by 1D DDT models of moderate energy that are interacting with an AM whose density is larger than 10^{-24} g $\cdot$ cm^{-3} but lower than $5 \cdot 10^{-24}$ g $\cdot$ cm^{-3}, and that undergo some amount of collisionless electron heating at the reverse shock. Other supernova explosion models have been able to reproduce the line emission, but the delayed detonations provide much more consistent approximations to the global spectrum. Delayed detonations have been the preferred paradigm of theorists for some time, mostly based on

the results obtained from the modeling of light curves (see Fisher et al., 1997; Höflich et al., 1998; and Wheeler et al., 1998). The preliminary result that we have obtained constitutes an important and completely independent confirmation that the overall ejecta composition and structure in delayed detonation models seem to agree with the observations. It is interesting to note that the highly mixed 3D SN models are not nearly as successful as the layered 1D models.

From the supernova explosion models that we have examined, the best results are provided by DDTc interacting with an AM of $\rho_{AM} = 2 \cdot 10^{-24}\,\mathrm{g} \cdot \mathrm{cm}^{-3}$, and with a small, but noticeable, amount of collisionless heating at the reverse shock ($\beta = 0.02$). The model cannot be used to fit the X-ray spectrum of Tycho in a conventional way, but it is capable of approximating the emission at all wavelengths from all the elements in the ejecta, with the exception of Ca. This suggests that the underlying temperature, ionization timescale and chemical composition profiles are basically correct, and that effects such as ejecta clumping, instabilities and radiative cooling, which were ignored in the model, don't seem to have a major impact on the emitted spectrum.

Not only does this model approximate the X-ray spectrum of Tycho reasonably well, it is also capable of explaining a number of important characteristics of the SNR. The presence of collisionless heating at the reverse shock, for instance, leads to higher temperatures at the low density ejecta just behind the reverse shock (see Figure 3.12), which could explain why the Fe Kα line emission peaks at a smaller radius than that of the Fe L complex. This explanation is more simple than that proposed by Dwarkadas and Chevalier, 1998, which required a relic CSM interaction in Tycho to yield the correct temperature profile in the shocked ejecta. Another interesting point is the fact that Fe L and Si emission are spatially coincident in Tycho, which was interpreted in previous works as evidence for mixing in the ejecta by comparison with the composition profile of model W7. While this does not discard the presence of such mixing, we note that Fe and Si are indeed spatially coincident in the ejecta of DDTc for $0.7 \lesssim M \lesssim 1.2\,\mathrm{M_\odot}$ (compare Figures 2.2 and 2.4).

Other details contribute to strengthening the case for this model. The required value of ρ_{AM} is fully compatible with the previous estimates of Itoh et al., 1988, and Brinkmann et al., 1989, (see section 5.2.2), and with the maximum Doppler broadenings found in section 5.3.3. The inferred value of 2.88 kpc for D is in agreement with some of the observational results reviewed in section 5.1.2, and not too far from the upper limit given by the more restrictive optical measurements. At this value of D, the angular radius of the contact discontinuity would be $\alpha = r_{CD}/D_{norm} = 3.3'$, for $r_{CD} = 2.75\,\mathrm{pc}$ (given by model DDTc interacting with $\rho_{AM} = 2 \cdot 10^{-24}\,\mathrm{g} \cdot \mathrm{cm}^{-3}$ at $t = 430\,\mathrm{yr}$). The observed radius of the ejecta emission in Tycho is $\sim 3.6'$ (Decourchelle et al., 2001), which can be reconciled with the former value if some allowance is made for the effect of Rayleigh-Taylor instabilities on the CD. Finally the results of Ruiz-Lapuente, 2004, imply an absolute peak visual magnitude of -19.16 ± 0.42 for SN1572 at $D = 2.88\,\mathrm{kpc}$, which is also compatible with the listed value of -19.51 for model DDTc in Table 2.1.

Future improvements and the mystery of Ca

There is clearly much work left to do on the subject of the SN-SNR connection in the Tycho SNR. Specifically, multi-D hydrodynamic simulations need to be coupled to ionization and spectral codes in order to establish clearly the effect of ejecta clumping and hydrodynamic instabilities on the X-ray spectrum of Type Ia SNRs. Without this important verification, our 1D results can only be regarded as preliminary, and it is difficult to know whether the models that we have used constitute an acceptable approximation. If the Tycho SNR is to be understood globally, the effect of CR acceleration should be included as well. The

unprecedented level of detail in the *XMM-Newton* and *Chandra* observations of this object requires that a significant effort be done to improve the theoretical models that can help to analyze them.

Before we think of improving the present models, however, the puzzling problems with the Ca line emission should be solved. It is specially unfortunate that the spectral code has no atomic data for Ar, because Ca and Ar are synthesized under similar conditions in Type Ia explosions, and a comparison of their line emission would be very useful. Since all the examined Type Ia explosion models have mispredicted the characteristics of Ca line emission, the problem is probably either in the ionization code or in the spectral code. The fact that the temperature and ionization state of Si and Fe, which are respectively exterior and interior to Ca in most models, are well reproduced by the ionization code suggests that the spectral code might be at the heart of this issue. In order to establish this firmly, and to circumvent the other limitations of the Hamilton & Sarazin code, we will have to wait for the new generation of spectral codes to implement full NEI capabilities suitable for the analysis of X-ray CCD spectra of SNRs.

Chapter 6

The imprint of presupernova evolution on SNRs

Always look on the bright side of death,

Just before you draw your terminal breath.

Monty Python (1979), *Life of Brian.*

6.1 Type Ia SN progenitors

The problem of identifying the progenitor systems of thermonuclear SNe was introduced at the beginning of chapter 2. Several observational and theoretical arguments point at the the single degenerate Chandrasekhar scenario as the most promising route to Type Ia SNe (Branch et al., 1995), but there are still many uncertainties associated with this model. The main problem is related to the necessity of bringing the CO WDs, which are created with a mean mass of $0.7\,M_\odot$, and never larger than $1.1\,M_\odot$ (Domínguez et al., 1993; but see Domínguez et al., 1996), to the Chandrasekhar mass through accretion of matter from a binary companion. Theoretical modeling of these systems is complicated, because in order to transform the accreted H first into He and then into C and O, it is necessary to burn it steadily and quietly in a shell on top of the WD in near-degenerate conditions, a process that is very unstable. It seems that a Type Ia SN is only produced for a narrow range of values of $\dot{M}_{acc}$, the accretion rate on top of the WD. Above $\sim 10^{-6}\,M_\odot\mathrm{yr}^{-1}$, off center ignition results in accretion induced collapse and the formation of a neutron star (Nomoto and Kondo, 1991); below $\sim 5\cdot 10^{-8}\,M_\odot\mathrm{yr}^{-1}$, the material is ignited in degenerate conditions, leading to a nova-like explosion (Nomoto, 1982). It has to be kept in mind, however, that these limits on the accretion rate depend on the composition of the accreted material.

Detailed simulations have been used to explore the potential of the SD-Ch scenario to produce viable Type Ia SNe at a rate comparable to the rate inferred in our Galaxy ($4 \cdot 10^{-3}\,\mathrm{yr}^{-1}$, Tammann et al., 1993). For a long time, it was assumed that in most cases the mass transfer was destabilized and a common envelope was formed, but in Hachisu et al., 1996, it was found that a peak in the Fe opacity allows the mass that cannot be steadily burnt by the WD to be blown away in an 'accretion wind'. Thus a new possibility was opened for SD systems to evolve to Type Ia SNe, a possibility that has been explored extensively in Li and van den Heuvel, 1997, King and van Teeseling, 1998, Hachisu et al., 1999a, Hachisu et al., 1999b, Langer et al., 2000, and Han and Podsiadlowski, 2004, among other works. A transient supersoft X-ray source in the LMC, RX J0513.9-6915, has long-

term light curve variations that can be explained by the accretion wind evolution model, thus becoming the first known example of this mechanism (Hachisu and Kato, 2003). Accretion winds, however, have not put an end to the controversy surrounding the SD-Ch scenario: some authors still claim that shell He burning on top of a WD is unstable and a H-accreting CO WD cannot grow to the Chandrasekhar mass (Cassisi et al., 1998; Piersanti et al., 1999; Piersanti et al., 2000; Piersanti et al., 2001). In addition, the double degenerate scenario, which was discarded some time ago as leading to accretion induced collapse (Segretain et al., 1997) is being revisited, as more detailed simulations including the effects of rotation prevent the merging white dwarfs from collapsing, and might produce healthy Type Ia SNe (Piersanti et al., 2003a; Piersanti et al., 2003b).

Several means to discriminate between the candidate progenitor systems through observations of Type Ia SNe have been proposed. In SD systems, weak features of H or He stripped from the companion envelope could appear in the early optical spectra, as proposed by Cumming et al., 1996, and Lentz et al., 2002. The recent detection of an Hα signature in the spectrum of the Type Ia SN2002ic (Hamuy et al., 2003) was taken to be the first clear evidence for the presence of an AGB star in the progenitor system of a Type Ia supernova, but this conclusion could be premature: in Livio and Riess, 2003, it is argued that the signature could even come from a DD progenitor with a residual common envelope. The systematic searches that have been undertaken recently should clarify this issue in the near future (Lundqvist et al., 2003). Alternatively, evidence for the interaction of the Type Ia SN ejecta with some kind of CSM modified by the progenitor could be found in the 'prompt' emission from the SN in the first few weeks or months after the explosion. Attempts to detect this emission have been made in the radio (Eck et al., 1995) and X-rays (Schlegel and Petre, 1993), but these studies have just constrained the presupernova mass loss in the progenitors to be lower than a few $10^{-6}\,\mathrm{M}_\odot \cdot \mathrm{yr}^{-1}$.

The search for clues of the progenitor systems in the supernova remnants of Type Ia SNe has not been so extensive. One interesting possibility is the identification of the companion star to the WD in SD systems, which should survive the explosion (Marietta et al., 2000) and would be seen as a bright star with peculiar abundances and high proper motion near the center of young Type Ia SNRs (Canal et al., 2001). These searches have been unsuccessful so far for Tycho and SN1006 (Ruiz-Lapuente et al., 2003). In this chapter, we shall follow another line of work, exploring the observational imprint that the accretion wind mechanism in Type Ia SN progenitor systems could have on their SNRs, and comparing the results with the appearance of the Tycho SNR.

6.2 Presupernova evolution of accretion wind systems

In Hachisu et al., 1999a, and Hachisu et al., 1999b, the evolution of the binary systems leading to Type Ia SNe was explored for the two channels supported by the accretion wind mechanism: symbiotic systems (the WD companion is a red giant) and supersoft systems (the WD companion is a main sequence or subgiant star). For the two channels, and for all the cases explored, a significant mass loss rate from the progenitor system due to the accretion wind was found. This mass loss rate decreases with time, and there might be a conservative phase before the explosion. In Langer et al., 2000, an extensive exploration of the parameter space (component masses and orbital period) was made, and in some cases (about 50%), the WDs were found to reach the Chandrasekhar mass without a significant amount of mass lost by the progenitor system. In Han and Podsiadlowski, 2004, however, the accretion on top of the WD was treated with more detail, and all the Type Ia progenitor systems in their grid of 2298 models were found to lose some mass in
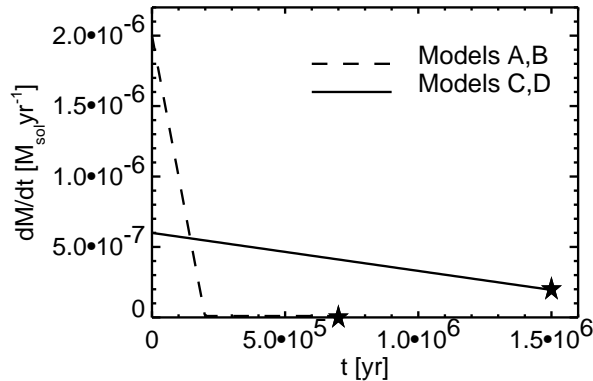
Figure 6.1: Time evolution of the wind mass loss rate for models A and B (dashed line) and models C and D (solid line). The time at which the SN explodes is identified by a star.

Model	a $[\mathrm{M_\odot yr^{-1}}]$	b $[\mathrm{M_\odot yr^{-2}}]$	t_{end} [Myr]	t_{SN} [Myr]	v_w $[\mathrm{km\,s^{-1}}]$	M_w $[\mathrm{M_\odot}]$	E_{51} $[10^{51}\mathrm{erg}]$
A	$2 \cdot 10^{-6}$	10^{-11}	0.2	0.7	200	0.2	$8 \cdot 10^{-5}$
B	$2 \cdot 10^{-6}$	10^{-11}	0.2	0.7	20	0.2	$8 \cdot 10^{-7}$
C	$6 \cdot 10^{-5}$	$2.7 \cdot 10^{-13}$	1.5	1.5	200	0.6	$2.4 \cdot 10^{-4}$
D	$6 \cdot 10^{-5}$	$2.7 \cdot 10^{-13}$	1.5	1.5	20	0.6	$2.4 \cdot 10^{-6}$

Table 6.1: Parameters for the wind models. The listed quantities are the mass loss function parameters a and b, the duration of the wind phase t_{end}, the time of the SN explosion t_{SN}, the wind velocity v_w, the total mass ejected by the wind M_w and the total energy deposited in the ISM in units of 10^{51}erg, E_{51}.

their presupernova evolution (see section 3 and Figures 1 and 4 in Han and Podsiadlowski, 2004).

In order to investigate the impact that this mass loss would have on the structure of the CSM around the progenitor system, hydrodynamic simulations have been carried out with an adapted version of the 1D code that was used to follow the evolution of SNRs in chapter 3. The code was modified to include a source of mass and momentum at the center to reproduce the effects of the optically thick wind (see appendix A for details on these modifications). For the time-dependent mass loss rate, simple analytical approximations were built to the plots presented in Figures 8, 9 and 10 of Hachisu et al., 1999a, and Figure 7 of Hachisu et al., 1999b. Two kinds of mass loss rates are suggested by these plots, one with a conservative phase prior to the supernova explosion and one with an active wind up to the explosion. In either case, the mass loss rate of the progenitor system can be approximated by a linear function:

$$\dot{M} = \frac{dM}{dt} = a - bt \tag{6.1}$$

with a and b arbitrary parameters that are set to reproduce the basic features and magnitudes that appear in the plots of Hachisu et al., 1999b, and Hachisu et al., 1999a. The two types of analytic mass loss rates are plotted in Figure 6.1. Since no reference to the velocity of the ejected material is made in the works cited above, a 'fast' ($v_w = 200\,\mathrm{km \cdot s^{-1}}$) and 'slow' ($v_w = 20\,\mathrm{km \cdot s^{-1}}$) wind were contemplated for each mass loss function, resulting in the four wind models A, B, C and D listed in Table 6.1.
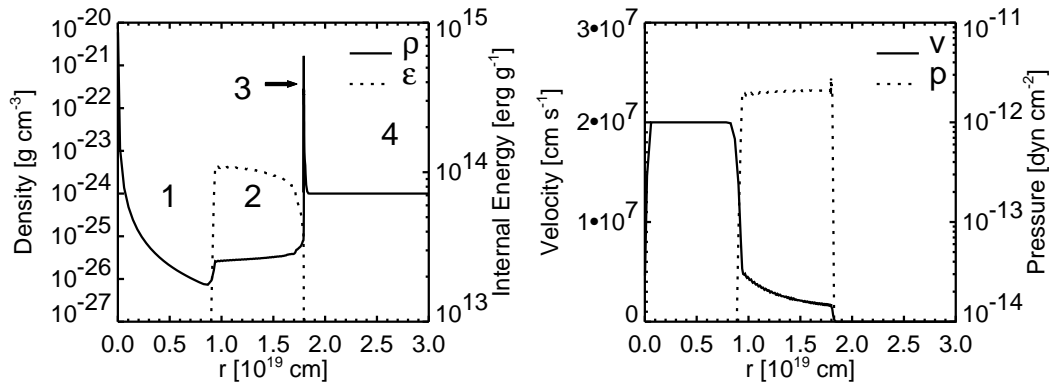
Figure 6.2: Standard structure of a wind-blown bubble around a massive star in the last stages of its evolution.

The hydrodynamic simulations followed the interaction of the four wind models with a uniform ISM, whose density was set to $\rho_{ISM} = 10^{-24} \text{g} \cdot \text{cm}^{-3}$. This interaction is similar to the process of formation of a SNR, the main differences being that the kinetic energies involved are four to seven orders of magnitude lower than those of a typical SN explosion, and that this energy is released over a long period of time, rather than instantaneously. A forward shock wave propagates into the uniform ISM, heating, compressing and accelerating it, while a reverse shock wave propagates into the wind, heating, compressing and decelerating it. Due to the low kinetic energies, however, the shock waves are much slower, and the forward shock stays radiative throughout its lifetime. As a consequence, radiative losses have to be taken into account in order to calculate the interaction of the winds with the ISM. For the wind-ISM interaction, this problem is easy to solve, because all the material involved has solar composition and, given the time scales of the interaction, can be assumed to be in collisional ionization equilibrium (see appendix A for details).

The interaction of optically thick winds with the ISM is usually studied in the context of the stellar evolution of early-type stars. These massive stars experience heavy mass loss in the last stages of their lifetime, going through different phases with different wind parameters $\dot{M}$ and v_w. As a result of the interaction of these winds with the surrounding ISM, regions with low density and high pressure known as wind-blown bubbles are excavated around the stars, which lose most of their initial mass through this mechanism. The formation of wind-blown bubbles was studied extensively using analytic methods in Castor et al., 1975, and Weaver et al., 1977, which have become the classic references on this subject. The bubble generated by a wind with $\dot{M} = 2 \cdot 10^{-6} \, \text{M}_\odot \cdot \text{yr}^{-1}$ and $v_w = 2 \cdot 10^2 \, \text{km} \cdot \text{s}^{-1}$ has been calculated, and is shown as an illustrative example in Figure 6.2. These parameters are not adequate to characterize the winds of massive stars, which usually have values of $\dot{M}$ and v_w an order of magnitude higher, but the CSM configuration will be useful for comparison with the accretion wind models. The structure obtained, from the center outwards, is identical to that of the wind-blown bubbles around massive stars: a freely moving wind with a $\rho \propto r^2$ density profile (region 1), an inner or wind termination shock, a low density region of hot, shocked wind (the bubble itself, region 2), a contact discontinuity between shocked wind and shocked ISM, a thin, dense shell of shocked ISM that has cooled radiatively (region 3), and a forward shock that propagates into the undisturbed ISM (region 4). This example is very similar to those shown in Figure 3 of Tenorio-Tagle et al., 1990, and Figure 1 of Dwarkadas, 2001.
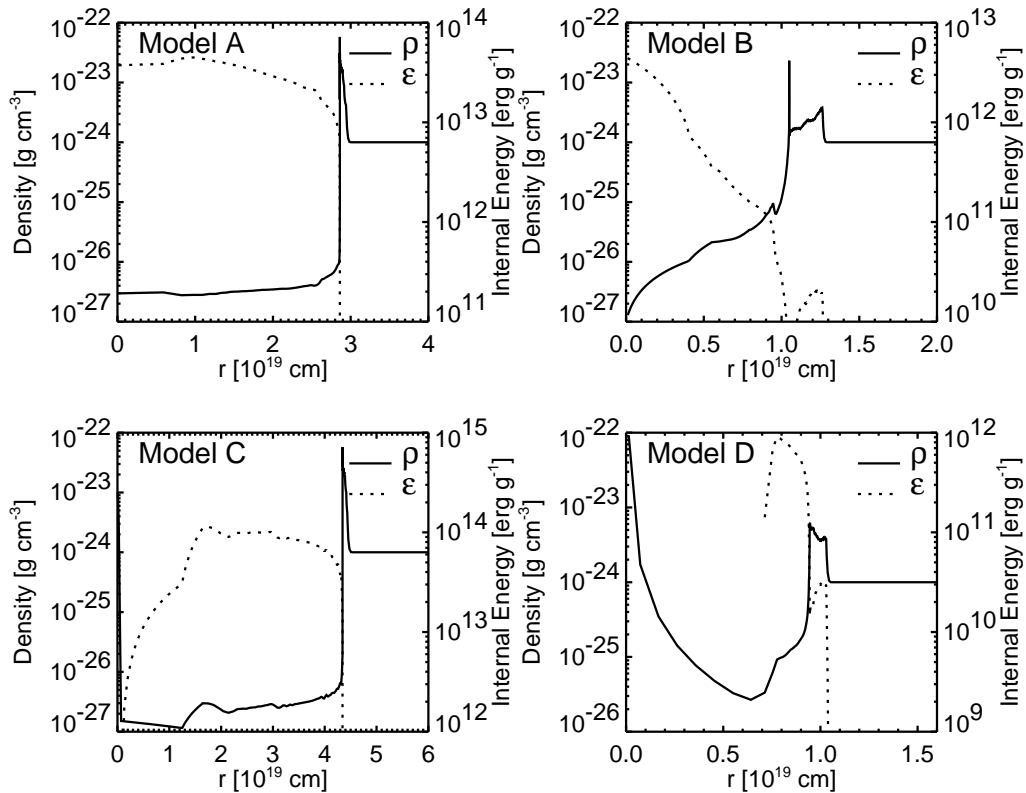
Figure 6.3: Structure of the CSM around the Type Ia progenitor system at the time of the SN explosion for the four accretion wind models A, B, C and D. Note that the scales are different for each figure.

The structure of the CSM of the progenitor system at the moment of the supernova explosion for the four accretion wind models A, B , C and D can be seen in Figure 6.3[1]. Although the mass loss rates of the accretion wind systems are on average two orders of magnitude lower than those found in massive stars, conspicuous bubbles are formed in all cases. The fast wind models A and C produce cavities with a radius larger than 10 pc., while the slow wind models B and D form smaller bubbles. Another difference between slow and fast wind models is the structure behind the forward shock, which is related to the amount of radiative cooling that takes place in each case. For the fast winds, the postshock temperatures are near the peak of the cooling curve and result in very efficient cooling, while the material behind the shock in the slower winds is cooler and does not radiate so efficiently (see appendix A, Fig. A.1). In the models with a mass conservative phase prior to the SN explosion (A and B), the wind termination shock has reached the center of the simulation space, and there is no freely expanding wind. In the models with active winds at the moment of the explosion, on the other hand, the region of freely expanding wind still survives. This region is quite small for the fast accretion wind model C, and it is not well resolved by the Lagrangian code due to the fact that, at the time of the explosion, only two layers of freely expanding wind are left. Note that none of the four models produces a structure identical to a conventional wind-blown bubble.

---

[1] In Badenes and Bravo, 2001, these calculations were done without taking radiative losses into account. Even though the conclusions of that study are still valid, the present calculations supersede those found in that paper.

It is remarkable that the modest mass loss rates of accretion wind models should result in such substantial modifications of the CSM around the progenitor systems of Type Ia SNe. This is in disagreement with the usual assumption in hydrodynamic simulations of Type Ia SNRs, which is a uniform density AM (see Dwarkadas and Chevalier, 1998, for a discussion). A $\rho \propto r^{-2}$ profile, that has sometimes been proposed as an alternative to a uniform ISM for SNR simulations, also fails to provide a reasonable approximation to the structure of these 'accretion wind bubbles'. The impact of the accretion winds on the CSM is enhanced by the fact that the mass loss rates decrease with time. The layers that are ejected first carry more momentum and act as a snow-plow to excavate the bubble, while the cavity is being filled by less and less material as the mass loss rate decays up to the time of the explosion.

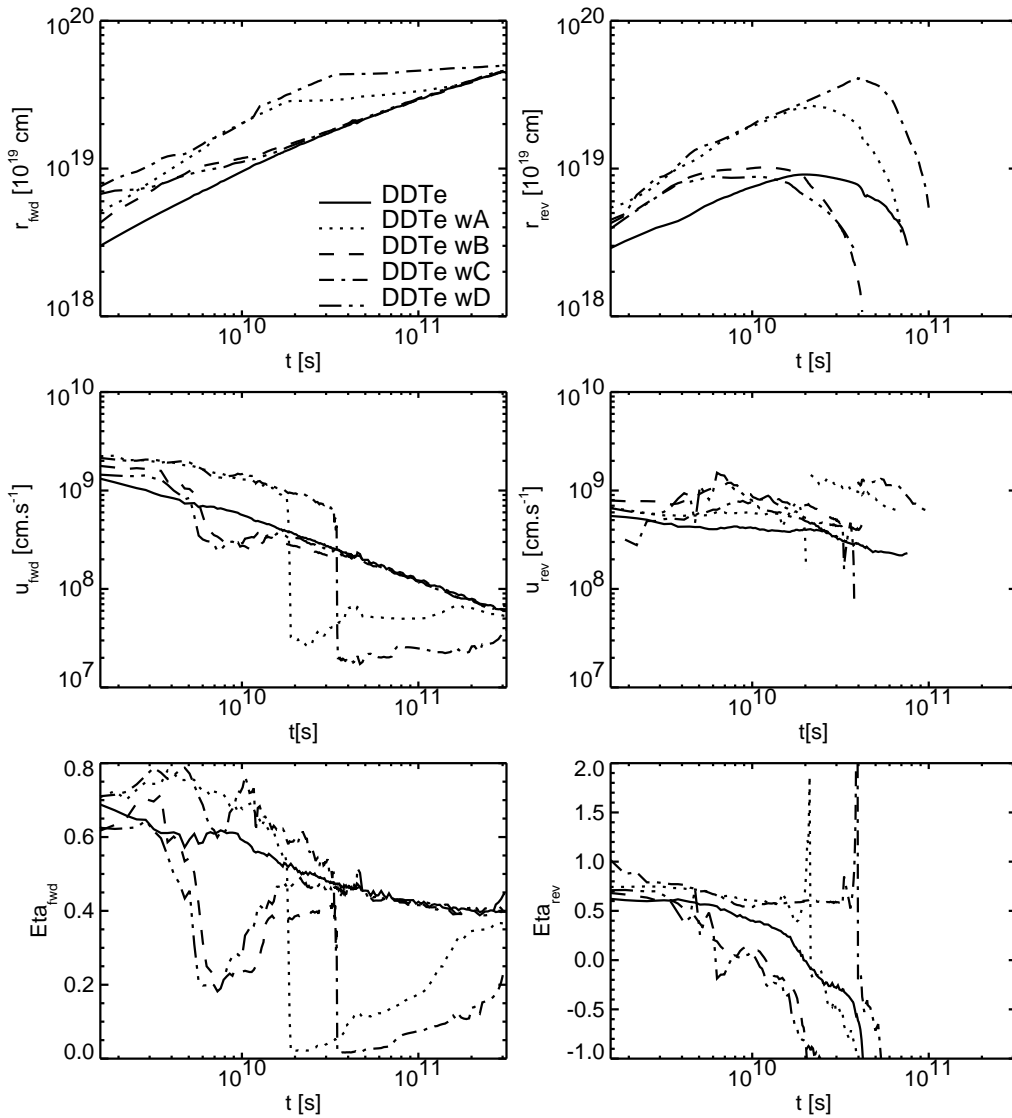Figure 6.4: Forward and reverse shock radii (r_{fwd}, r_{rev}), velocities (u_{fwd}, u_{rev}) and expansion parameters (η_{fwd}, η_{rev}) for the interaction of the ejecta model DDTe with the accretion wind bubbles from wind models A, B, C, and D. The interaction of the ejecta with a uniform AM of $\rho_{AM} = 10^{-24}\,\mathrm{g \cdot cm^{-3}}$ has also been included for comparison purposes.

6.3   Dynamic interaction of supernova ejecta with the CSM

The interaction of supernova ejecta with wind-blown bubbles has been studied extensively in the frame of core collapse SNe, both analytically (Chevalier and Liang, 1989, and references therein) and numerically (see Tenorio-Tagle et al., 1990, for 1D simulations and Tenorio-Tagle et al., 1991, for 2D simulations). A review of these studies can be found in Franco et al., 1991. The evolution of the SNR is severely affected by the preexisting CSM, and its appearance at X-ray and optical wavelengths is also expected to change radically. The details, however, are complex, and will be different in each particular case (see, for instance, Dwarkadas, 2001, for the whole pre-SN and SNR evolution of a 35 $M_\odot$ star in 2D).

The gross features of the evolution of a SNR inside a conventional wind-blown cavity like the one shown in Fig. 6.2 can be sketched as follows. The supernova ejecta will interact first with the freely expanding wind. The reverse shock will develop during this stage, and the forward shock will be accelerated due to the negative density gradient of the CSM in this region. When the bubble itself is reached, the double shock structure will expand rapidly inside the low density cavity, up to the time when the forward shock reaches the radiatively cooled shell. What happens then depends on how large the mass of the shell M_{sh} is compared to the mass of the SN ejecta M_{ej}. If $M_{sh}/M_{ej} \lesssim 1$, the forward shock overcomes the shell with little or no radiative losses, experiencing first a sudden deceleration and then a re-acceleration. The shell becomes embedded in the SNR and after a while it is first distorted and then destroyed by the action of the Rayleigh-Taylor instability (Tenorio-Tagle et al., 1991). Eventually, the SNR 'loses memory' of the interaction with the shell. On the other hand, if $M_{sh}/M_{ej} > 1$, the forward shock becomes radiative as it crosses the shell, and the reverse shock is dramatically strengthened, resulting in a rapid thermalization of the ejecta. In extreme cases, the forward shock might lose an important fraction of its energy before it emerges from the shell, leaving the SNR in the radiative snow-plow phase until its final merging with the ISM (Dwarkadas, 2001).

For the accretion wind bubbles that were presented in the previous section, only in the case of wind model D is a significant interaction with the freely expanding wind expected. In all other cases, the ejecta will expand almost freely until the shells are encountered. The effects of the ejecta-shell interaction can be gauged from the values of M_{sh}, which are 58, 7, 190, and 3 $M_\odot$ for models A, B, C, and D, respectively. Comparing these values with $M_{ej} \simeq 1.4\,M_\odot$ for a standard Chandrasekhar Type Ia SN model, the impact of the shell interaction on the forward and reverse shocks is expected to be important in all cases, specially for the fast accretion wind models A and C.

In order to explore these effects, the hydrodynamic evolution of several SNR models was calculated following the procedure detailed in chapter 3, but using the CSM profiles of Figure 6.3 instead of a uniform AM. It has to be stressed that a 1D adiabatic hydrocode is inadequate to simulate the interaction of the SN ejecta with the accretion wind bubbles as a whole, because radiative losses and dynamic instabilities will be important at the shocked shell. While the radiative losses in the formation of the wind-blown bubbles affect material in CIE, in the SNR most of the shocked ejecta and CSM is in NEI, and radiative losses are not straightforward to calculate. They can be estimated *a posteriori* using the technique described in section 3.5, but if they are to be included in a self-consistent way, a fully integrated hydrodynamic-ionization code is needed.

The evolution of the forward and reverse shocks of the ejecta model DDTe interacting with the bubbles excavated by winds A, B, C and D is plotted in figure 6.4 as an illustrative example. Note how the velocity and expansion parameter of the forward shock drops dramatically when the shells of the 'fast' wind models A and C are reached at $t \simeq 1.6 \cdot 10^{10}$ s
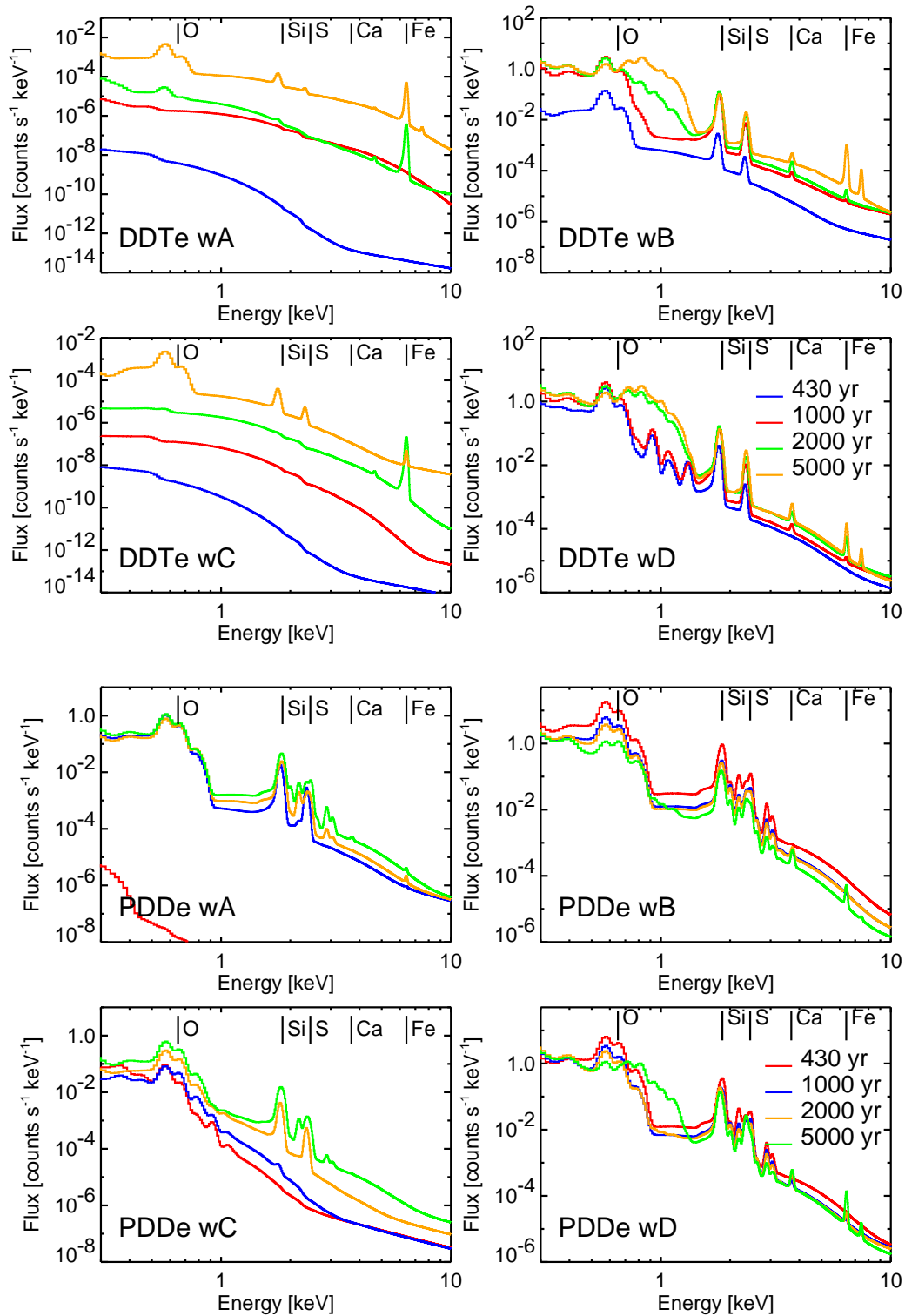
Figure 6.5: Spectra for the shocked ejecta of models DDTe (top four panels) and PDDe (bottom four panels) interacting with the accretion wind bubbles from wind models A, B, C and D. The spectra are plotted 430, 1000, 2000 and 5000 yr after the SN explosion. Note the different scales in flux for each panel, and compare with the scales of Figures 4.11 to 4.14.

and $t \simeq 3.2 \cdot 10^{10}$ s, respectively. The forward shock is expected to become radiative then, and the evolution beyond that point should be disregarded, particularly the apparent relaxation towards a Sedov regime at $t \gtrsim 10^{11}$ s. The sudden deceleration of the forward shock is followed by a sudden acceleration of the reverse shock, marked by a discontinuity in the u_{rev} plots and a sudden rise of η_{rev}, which results in the rapid thermalization of the ejecta. In the 'slow' wind models B and D the interaction with the shell is not so dramatic. The deceleration of the forward shock, which happens at $t \simeq 5 \cdot 10^9$ s for both wind models does not seem strong enough to drive it into a radiative regime, but this is hard to say without including self-consistent radiative losses. The subsequent acceleration imparted upon the reverse shock is smaller than in the case of the fast wind bubbles, and the thermalization of the ejecta happens over longer timescales. For the PDD, DEF and SCH explosion models, the details of the dynamic interaction between ejecta and CSM are different, but the overall behavior of the shocks is very similar.

Even if it is not possible to follow in detail the evolution of the SNR inside the wind blown bubble, the emitted thermal spectrum from the shocked ejecta can be calculated using the techniques presented in chapters 3 and 4, because the reverse shock does not become radiative at any time. The results of these calculations are shown in Figure 6.5 for the interaction of models DDTe and PDDe with the four accretion wind bubbles, 430, 1000, 2000 and 5000 yr after the SN explosion.

In the spectra produced by model DDTe, the differences between the fast and slow accretion wind models are plain to see. For the interaction with the wind bubbles A and C, the ejecta expand to a low density before the reverse shock thermalizes the material, resulting in low emitted fluxes, emission measures and ionization timescales. The only line emission that appears is Fe Kα, but just at late times, after the rapid thermalization of the ejecta. In the interaction of DDTe with the slow accretion wind bubbles B and D, the forward shock has already arrived to the cool shell at $t = 430$ yr, and the ejecta do not expand to such low densities before the reverse shock is accelerated. As a result, higher fluxes, higher ionization timescales, and more line emission are seen in these spectra. The Heα lines of Si and S are present at all times, accompanied by O lines, and later by some Fe L and Fe Kα, as the reverse shock proceeds further inwards. In the interaction with bubble D, the reverse shock manages to bring out some Ne and Mg emission as well. The early spectra of model DDTe interacting with bubble D are qualitatively similar to the ones obtained with a uniform ambient medium of $\rho_{AM} = 2 \cdot 10^{-25}$ g $\cdot$ cm^{-3} (see Figure 4.13).

In the case of PDDe, the slightly larger kinetic energy and more compact ejecta density profile tend to assuage the effects of the initial expansion inside the low density bubbles. In the interaction with bubbles A and C, some Si and S line emission can be seen after the rapid thermalization of the ejecta. Note that, for bubble A, the reverse shock makes little progress before the cool shell is reached, and then the emitted flux has an abrupt increase. In the interaction with bubble C , the initial flux is not so low because the reverse shock goes through the outermost layers of ejecta early on, as the ejecta sweep the small region of freely expanding wind. The interaction of PDDe with the slow accretion wind models B and D yields more line emission than that of DDTe. The ionization timescales are low, but the temperatures are high enough to produce some flux in the Si and S Lyα lines from H-like ions. Little or no flux is emitted in the Fe L and Fe Kα lines, except at very late times.

6.4   Accretion winds in the Tycho SNR?

In principle, more detailed simulations of the interaction of the supernova ejecta with the accretion wind models would be needed to make a detailed quantitative comparison with the dynamics and X-ray spectra of Type Ia SNRs. This is clearly a complex problem, which requires an adequate treatment of issues that have not been taken into account in our calculations, like radiative cooling and dynamic instabilities. However, it is instructive to compare our preliminary results with the characteristics of the Tycho SNR reviewed in sections 5.1.2 and 5.2.1.

The wind bubbles A and C are immediately ruled out because the blast wave of the SNR is very fast ($v \simeq 2 \cdot 10^4 \, \text{km} \cdot \text{s}^{-1}$) before it encounters the shell and then becomes strongly radiative, in clear contradiction with the nonradiative shock with a velocity of a few thousand $\text{km} \cdot \text{s}^{-1}$ observed in Tycho (Ghavamian et al., 2001). This does not depend on the model that is assumed for the ejecta, and would not be different in more detailed simulations. Even if the morphology of the forward shock is ignored, the synthetic X-ray spectra of the ejecta models DDTe and PDDe interacting with bubbles A and C lack some of the fundamental lines listed in Table 5.1, and seem inadequate as models for the *XMM-Newton* observation of Tycho. From a general point of view, it can be argued that any ejecta model which is allowed to expand into such low density cavities and then is suddenly thermalized will not provide a reasonable approach to the spectrum of Tycho.

The bubbles produced by the slow accretion wind models are less extreme cases, and it is harder to draw conclusions. It is worth noting that, while the forward shock is overcoming the radiatively cooled shells of models B and D, its expansion parameter is well below the observed value at radio wavelengths ($\eta = 0.47$, Reynoso et al., 1997) for a period of at least one hundred years in all the ejecta models that have been considered. If this sort of interaction has happened earlier in the history of Tycho, then the remnant has lost memory of it by now, and the process did not leave behind any radiatively cooled material inside the remnant (Ghavamian et al., 2001), nor did it distort the shape of the forward shock, at least in the western rim (see Figures 5.1 and 5.3). This seems unlikely, but cannot be discarded completely without a more detailed analysis. Regarding the spectrum of the shocked ejecta, the ionization timescales are quite low when compared with those obtained from Tycho. For model PDDe interacting with wind bubble D, which has the highest ionization states in the shocked ejecta of all the examples that have been reviewed in this chapter, the emission measure averaged ionization timescales of the principal elements are plotted in Figure 6.6. The values of $\langle \tau \rangle_X$ are about an order of magnitude lower than those obtained from an interaction with $\rho_{AM} = 10^{-24} \, \text{g} \cdot \text{cm}^{-3}$ (see Figure 4.6), and, in the case of Si and S, they are incompatible with the fitted τ of $\sim 10^{11} \, \text{s} \cdot \text{cm}^{-3}$ obtained by Hwang et al., 1998. This problem persists in other PDD models with higher kinetic energies.

Needless to say, all these arguments do not imply that the progenitor system of SN 1572 did not undergo an accretion wind phase before its explosion. They do suggest, however, that if such an episode existed, it did not modify the CSM in the substantial way predicted by the accretion wind bubbles that have been presented in this chapter. One possibility is that the impact of the accretion wind phase on the CSM has been overestimated in our simulations. The only free parameters (i.e., those not determined by the accretion wind models themselves) are the wind velocity v_w and the ISM density ρ_{ISM}. In order to have a CSM with a structure more compatible with the present morphology of Tycho, the wind velocity would have to be much lower than the $20 \, \text{km} \cdot \text{s}^{-1}$ assumed for models B and D, since higher velocities are discarded by models A and C. Such a low velocity does not seem likely for an optically thick wind, but this cannot be properly calculated without
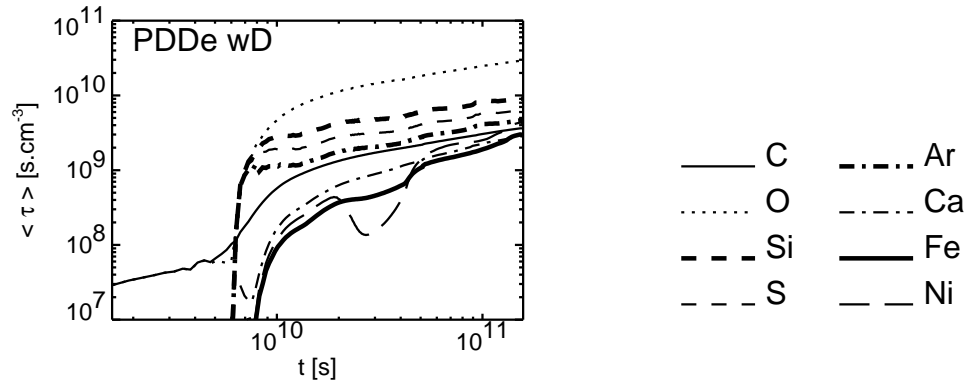
Figure 6.6: Emission measure averaged ionization timescale as a function of time in the shocked ejecta of model PDDe interacting with bubble D.

a detailed study of the momentum deposited by the SN progenitor system in the ISM. Variations in the value of ρ_{ISM}, which was arbitrarily set to $10^{-24}\,\mathrm{g}\cdot\mathrm{cm}^{-3}$, can also be considered. Lower ISM densities would lead to larger bubbles and even lower ionization timescales for the ejecta. Higher ISM densities would lead to smaller bubbles, which would be easier to overcome by the forward shock and could be better 'hidden' in the past history of the Tycho SNR. However, the value of ρ_{ISM} cannot be much larger than $10^{-24}\,\mathrm{g}\cdot\mathrm{cm}^{-3}$ if the present velocity and expansion parameter of the forward shock in Tycho are to be reproduced.

In conclusion, and within the limitations of our simplified analysis, we find no evidence for an interaction of the Tycho SNR with a CSM modified by a progenitor system which evolved to a Type Ia SN through the accretion wind mechanism proposed by Hachisu et al., 1996. In order for this kind of mechanism to be compatible with the present morphology of the Tycho SNR, the mass loss rates would have to be significantly lower than the values given by Hachisu et al., 1999a and Hachisu et al., 1999b. As a final remark, we would like to point out that SNRs can be a valuable diagnostic for the Type Ia SN progenitor models. A self consistent picture of the events that lead to the thermonuclear explosion of a white dwarf in a binary system should not only explain the supernova itself, but also account for the possible modifications to the CSM that will influence the early evolution of the SNR.

Chapter 7

Conclusions

Sois satisfait des fleurs, des fruits, même des feuilles,

Si c'est dans ton jardin à toi que tu les cueilles!

Edmond Rostand (1868-1918). *Cyrano de Bergerac, acte II, scène VIII.*

7.1 The SN - SNR connection challenge for thermonuclear SNe, revisited

The main goal of this dissertation was to establish a connection between the current theoretical models for Type Ia supernovae and the thermal X-ray spectrum of the supernova remnants that they originate. The utility of this connection is twofold: on one side, to use SNRs as constraints for theoretical Type Ia SN models, and on the other, to facilitate the analysis of the X-ray emission from the ejecta in young SNRs.

Given the diversity in the structure of the ejecta among the Type Ia explosion models and the complexity of the interactions with the AM, it was not possible to use analytic solutions to follow the evolution of the SNRs. Instead, we based our approach on 1D numerical hydrodynamic simulations coupled to NEI ionization and electron heating calculations. In this way, we were able to build detailed models for the physical state of the plasma throughout the shocked ejecta as a function of time. Once the composition, density, electron temperature and ionization state for each fluid element were known, a spectral code was used to produce synthetic X-ray spectra that could then be compared with the excellent observations obtained by modern satellites like *XMM-Newton* and *Chandra*.

This technique, while conceptually simple, is rather more sophisticated than the conventional spectral models used to analyze the X-ray spectra of SNRs. The comparison of the synthetic model spectra with observations is complicated, in part because of the underlying physical complexity of the situation, in part because of the limitations in the models and the observations themselves. Since acceptable statistical fits are not expected, it is not possible to apply the standard χ^2 procedure, and new ways to quantify the performance of the models have to be found and adapted to each particular case. Yet, the technique has a significant potential, and it can help to understand the distribution of chemical compositions, temperatures and ionization timescales that contribute to the spectra emitted by the shocked ejecta in SNRs. In principle, it can also be extended and adapted to study core collapse supernova remnants (originated by SN Types II, Ib and Ic).

7.2   Results

7.2.1   Hydrodynamics and ionizations

In order to explore the parameter space for Type Ia supernova explosions, a grid of one dimensional models was contrived, including examples of all the explosion mechanisms currently under debate: pure detonations (DET), pure deflagrations (DEF), delayed detonations (DDT), pulsating delayed detonations (PDD) and sub-Chandrasekhar models (SCH). This grid was complemented with models calculated by other groups: the popular model W7, a high resolution 1D delayed detonation, and five 1D averages of very recent 3D simulations of Type Ia SN explosions.

For each of these models, the interaction with an AM of uniform density was followed using a 1D Lagrangian hydrocode. We found that the density profiles of the ejecta models, which are intimately related to the explosion mechanism and the nucleosynthetic output of the supernova, produce a complex dynamic evolution before the onset of the Sedov stage. This complexity affects both the behavior of the forward and reverse shocks (velocities and expansion parameters) and the structure of the interaction region between them. In general, the conclusions of Dwarkadas and Chevalier, 1998, were reproduced: the density profile of the shocked ejecta peaks at the contact discontinuity between ejecta and AM, while the mean plasma temperature has a drop in this region. We confirmed that the SNR dynamics are better approximated by an exponential ejecta profile than by a power law, as suggested by these authors, but the structure of the shocked ejecta is too rich to be represented by simple analytic models in most cases. We also noticed that explosion models with steeper density profiles in the outer ejecta, such as pure deflagrations and pulsating delayed detonations, have a more violent interaction with the AM, leading to more pronounced density peaks towards the contact discontinuity and larger forward shock expansion parameters. We verified that these 1D hydrodynamic calculations follow a scaling law for the AM density ρ_{AM}, as pointed out by Gull, 1973.

In our calculations, the structure of the shocked ejecta is determinant for the nonequilibrium ionization and electron heating that take place after the passage of the reverse shock. In the outer layers of ejecta, where these collisional processes act for a longer time and in a denser medium than elsewhere, we found high ionization timescales and electron temperatures. By contrast, in the inner layers of the shocked ejecta the ionization timescale is always low, but the behavior of the electron temperature profile depends on the efficiency of the collisionless electron heating process at the reverse shock. We represented this efficiency by the parameter β, the ratio of postshock electron to ion temperature. Values of β close to 1 are ruled out by the observations, but even a comparatively small value of β has a dramatic impact on the electron temperature, increasing it by orders of magnitude in this region. All these effects are modulated by the density of the AM that is interacting with the ejecta. Higher values of ρ_{AM} lead to higher densities in the whole SNR, and an acceleration of the dynamic evolution and the collisional processes inside the shocked ejecta. In the models where collisionless electron heating at the reverse shock is important, we found that its effect wears off faster for increasing AM densities due to this acceleration.

The chemical composition profile of the explosion models acquires new relevance when it is examined under the light of the distribution of densities, electron temperatures and ionization timescales in the shocked ejecta. We noticed that the mean ionization timescale and electron temperature corresponding to each element depend on the range of Lagrangian coordinates where the element was synthesized during the explosion. Moreover, the density profile in the shocked ejecta tends to enhance the emission measures of the

elements in the outermost layers. As a result of this, the relative contribution of each element to the emitted X-ray spectrum of the ejecta deviates by orders of magnitude from the ratio of masses synthesized in the explosion. We derived approximate scaling laws with ρ_{AM} for the temporal evolution of the element emission measures and ionization timescales. These laws are only approximate, because the hydrodynamic scaling does not apply to the ionization processes in the plasma, but we have found them to be valid within a factor 2. Unfortunately, the scaling laws cannot be applied to the electron temperatures, nor can they be easily used as a tool to support spectral calculations.

7.2.2 Spectra

All these circumstances result in strikingly different synthetic spectra for the different ejecta models. For an interaction with $\rho_{AM} = 10^{-24}\,\mathrm{g \cdot cm^{-3}}$, we found that the DEF models have a high continuum flux, mostly contributed by the C and O in the dense outer ejecta, and show little line emission from Fe, even though this element is more abundant in the ejecta than C or O. Lines from the small amount of Si, S and Ca synthesized in these models only show weakly at late stages, when the continuum flux from C and O goes down. These features would be common to all SN Ia explosion models whose composition in the outer ejecta is clearly dominated by C and O. By contrast, the Heα and Heβ lines from Si and S, and the Ca Kα blend, are prominent in the DDT and PDD models, and the level of continuum is much lower. The steeper density profiles of the PDD ejecta lead to higher densities towards the CD when compared to DDT models, which result in a more advanced ionization state of Si and S and prominent Lyα lines from the H-like ions of these elements. Within the DDT and PDD mechanisms, we found that models with high kinetic energies are characterized by strong emission in the Fe Kα and Fe L line complexes, while those with low kinetic energies have weaker Fe emission but show distinct features from O and other low mass elements in the outer ejecta. Model DET, as expected, has a spectrum completely dominated by Fe Kα and Fe L, with no line emission from other elements. Finally, model SCH was found to have a complex evolution, with the spectra being influenced by a double peak structure in the shocked ejecta. In this model, the ionization states of Si and S are advanced, and the continuum flux and emission measures of O and Ni are rather high. The two 1D models outside the grid are not essentially different from the grid models, and their spectra are similar to those of low energy DDT and PDD, except for a few details.

Variations of ρ_{AM} and β affect the spectra in a complex way. We found that higher values of the AM density lead to more advanced ionization states of the elements and higher temperatures in the shocked ejecta. This shows in the spectra as enhanced Lyα emission from Si and S, enhanced Fe L emission, more continuum flux, and a displacement of the centroids of the Ca and Fe Kα line blends to higher energies. Lower values of ρ_{AM} result in less Heβ emission from Si and S and less Fe L, with enhanced O Lyα emission being favored by the less advanced ionization state and lower electron temperatures. The element whose emission is more distinctly affected by collisionless electron heating at the reverse shock is Fe, due to its location interior to the other elements in most 1D models. Higher values of β lead to a significant increase in the Fe Kα flux for all AM densities.

The SNR models obtained from the 3D explosion calculations produce synthetic spectra that are quite different from any of the 1D models. We found that their spectra are characterized by very strong Fe L and Fe Kα emission, and comparatively weak Si, S and Ca lines. This is a direct consequence of the high degree of mixing between nuclear fuel and ashes that takes place in all 3D calculations, which disrupts the layered structure found in 1D models. The presence of a large amount of Fe in the outer ejecta, where the

density, electron temperature and ionization timescale are high, results in an enhanced Fe emission. A prominent Ni Kα line is also seen in the synthetic spectra of most 3D ejecta models.

7.2.3 A test case: the Tycho SNR

We tested the capabilities of the synthetic spectra as tools for the analysis of X-ray observations using the ejecta emission from the Tycho SNR as a test case. Two important issues were raised in the attempt to compare the theoretical predictions with the spectrum of Tycho observed by *XMM-Newton*. First, even though the synthetic spectra are significantly more sophisticated than other available spectral models, they cannot match the level of complexity of an object like Tycho. Important features, like the clumps observed in the X-ray CCD images or the dynamics of the forward shock, which are probably modified by CR pressure, must remain unexplained. Second, the limitations of the spectral code are an important factor in the comparison between the synthetic spectra and the observations, and they determine which spectral features can be used safely to discard candidate models.

With these restrictions in mind, and since we found the usual χ^2 procedure to be inadequate for the problem at hand, we devised an alternative strategy to find the best model for the Tycho SNR. A grid of synthetic spectra for the ejecta emission at $t = 430\,\mathrm{yr}$ was produced by taking a representative sample of the explosion models and varying β and ρ_{AM} to cover the range of possible values. A first comparison between the observations and the synthetic spectra was based on a set of carefully selected line flux ratios and centroids. The models that were found to provide a good approximation to the line emission as determined by these diagnostic quantities were then compared to the global spectrum of the Tycho SNR. This global comparison required the addition of a simple model for the AM emission and the effect of interstellar absorption. Even though a number of models were capable of reproducing the diagnostic quantities for the line emission, only the DDT models provided a satisfactory approach to the overall spectrum. Other candidates, like PDD or SCH models, required low values of ρ_{AM} , and the normalization of the X-ray spectrum implied distances to Tycho that were outside the estimated ranges. Within the DDT models, those with high kinetic energies overestimated the Fe L emission, while those with low kinetic energies overestimated the O Lyα emission.

The best candidate turned out to be the intermediate model DDTc, interacting with $\rho_{AM} = 2 \cdot 10^{-24}\,\mathrm{g} \cdot \mathrm{cm}^{-3}$ and with a small, but important, amount of collisionless electron heating at the reverse shock ($\beta = 0.02$). For this model, the amount of ^{56}Ni synthesized in the explosion is $0.8\,\mathrm{M}_\odot$, and the kinetic energy in the ejecta is $1.16 \cdot 10^{51}$ erg. Not only did the model provide a good approximation to the X-ray spectrum of Tycho, but it also explained a number of important characteristics of the SNR. These included the apparent size and distance to the object, and the observed peak magnitude of the supernova reconstructed from the observations of Tycho Brahe in 1572. Despite all its virtues, however, the synthetic spectrum of model DDTc could not be used to fit the observations in the usual way. Even if the model reproduced accurately the distribution of densities, electron temperatures and ionization timescales for all the elements, the atomic data used in the ionization and spectral codes have uncertainties that can be as large as 50% in some cases, and this would preclude a statistically acceptable fit to the observed spectrum.

The only serious drawback that we found in the synthetic spectra is that they systematically mispredicted the characteristics of the Ca line emission. This happened for all the grid and off-grid models at all values of β and ρ_{AM}, which suggests that the problem might be related to the spectral or ionization codes. In addition to this, the unfortunate

circumstance that the spectral code has no atomic data for Ar made it impossible to check the model predictions for this element. However, we believe that the success of model DDTc in approximating the emission of all other elements from O to Fe is a significant achievement, and a new argument in favor of the delayed detonation mechanism for Type Ia SNe. It is worth pointing out that none of the 3D models was capable of providing a reasonable approximation to the spectrum of the Tycho SNR.

7.2.4 Presupernova evolution models

One of the simplifying assumptions in our simulation scheme, the fact that Type Ia SN ejecta interact with a uniform AM, was revised in the context of the models for thermonuclear supernova progenitors. In the most popular scenario for Type Ia progenitor systems, known as single degenerate Chandrasekhar or SD-Ch systems, the white dwarf explodes because it is destabilized due to accretion from its binary companion. This can only happen if it reaches the Chandrasekhar mass in a quiet way, avoiding accretion induced collapse and nova-like explosions. The only mechanism that has been able to explain this phase of the presupernova evolution is the so called accretion wind mechanism, where the white dwarf only accretes part of the material lost by the companion and the rest is blown away by an optically thick wind. There is currently an open debate about the validity of this mechanism to produce viable Type Ia SNe.

We have computed the structure of the CSM around the SN progenitor at the time of the explosion predicted by these accretion wind models. Even though the mass loss rates associated with accretion winds are quite low, conspicuous low density regions surrounded by a dense radiatively cooled shell were found in all cases. If the supernova exploded inside one of these 'accretion wind bubbles', it would have a noticeable imprint on the evolution of the SNR, affecting the dynamics of the forward shock and the X-ray emission from the shocked ejecta. A comparison with the morphology of the Tycho SNR reveals no trace of such an imprint. This suggests that, if an accretion wind mechanism operated in the progenitor system of SN1572, it did not modify the CSM in a substantial way, and therefore the mass loss rates currently predicted in the literature are probably overestimated.

7.3 The future

Even though much remains to be done before the SN-SNR connection for Type Ia SNe is properly understood, we believe that the present dissertation represents a step in the right direction. In that sense, future lines of work should include both the improvement of our modeling technique based on hydrodynamic, ionization and spectral simulations, and its application, either in its present form or in a more refined version, to a selected group of targets.

7.3.1 Improvements

The most necessary improvements at the present stage are clearly those related to the spectral code. Specifically, the atomic data for Ar have to be incorporated, and the problems with Ca emission have to be fixed before the technique can be used to its full potential. Much of the required atomic data are already published, but to incorporate them to one of the existing spectral codes implies a considerable effort. In the near future, the best strategy might be to adopt a temporary solution, at least until the ATOMDB project finally produces a tool compatible with NEI plasmas that depart significantly from

ionization equilibrium. One possibility is to patch the HS code to fix the problems with Ca and Ar, but the use of other NEI codes should also be considered.

Another issue that needs to be addressed is the efficient use of the synthetic spectra for the analysis of observations. Unless a quantum leap in the quality of the atomic data changes the situation, statistically acceptable fits to the observations will remain a chimera for a long time, no matter how sophisticated the underlying simulations become. In this context, it might be necessary to change the standard procedures used in the spectral analysis of the X-ray SNR observations. Ideally, one would like to find a method that is more flexible than the χ^2 procedure, but still provides a quantitative measure of the performance of the models. Bayesian techniques offer a promising alternative, but this is clearly a complex matter that needs to be discussed openly in the community. The need for better ways to model the X-ray CCD spectra of SNRs will become even more acute in 2005 with the launch of *Astro-E2*, whose superior spectral resolution is bound to open a plethora of new possibilities in SNR research.

While these fundamental issues are settled, it is important to keep refining and improving the simulations. The first step should be the use of a multi-D hydrodynamic code that enables to study clumping and dynamic instabilities in the shocked ejecta. An accurate understanding of the impact that these effects have on the formation of the X-ray spectra of SNRs will be necessary to ascertain the validity of our 1D simulations as a first approximation to the problem. If this impact is found to be important, our conclusions about the Tycho SNR might have to be revised. The coupling of a multi-D hydrocode with an ionization and a spectral code could help to understand the formation of the rich structures that we observe in the *Chandra* images of most SNRs. Another important effect that should be incorporated at some point is the modification of the SNR dynamics due to cosmic ray acceleration. This would be necessary for a global study of the dynamics and X-ray spectrum of objects like Tycho, whose forward shock is probably affected by CR pressure. In the more distant future, other improvements like the inclusion of radiative losses and thermal conduction might be considered, but only if it is deemed that they play a sufficiently important role in the overall dynamics and spectral properties of young SNRs to justify the effort.

While this process of improvement is taking place, the developments in SN explosion models will have to be followed closely. It is important to keep in mind that one of our basic goals is to provide constraints for these models, and this cannot be done effectively unless there is a substantial rapport with the community of SN theorists.

7.3.2   Application to other objects

In order to fully exploit the potential of this technique, it is of capital importance to apply it to the largest possible number of candidates. In this sense, it will be necessary to approach each object with an open mind and adapt the analysis strategy to each particular case without renouncing to a global understanding of Type Ia SNRs as a class. In this context, it is our intention to make the tools and synthetic spectra that we develop available to the community, so that other researchers can apply them to their own projects if they choose to do so.

Among the Galactic candidate Type Ia SNRs, SN1006 is perhaps the most interesting target. This young object is evolving in an AM less dense than that of Tycho, and even though its spectrum is dominated by synchrotron emission, it has prominent lines from the shocked ejecta in its central region (Long et al., 2003). If both Tycho and SN1006, which have quite different dynamic ages, could be explained with the same (or even a similar) SN explosion model, that would represent a significant achievement in both SN and SNR

research. Other possible targets are the Kepler SNR, whose origin is still unknown, but seems to be undergoing a complex CSM interaction (Cassam-Chenai et al., 2004), and G337.2-0.7, on which work has already begun (private communication by C. Rakowski, April 2004).

A number of interesting Type Ia SNR candidates can also be found in the Magellanic Clouds, including DEM L71 (Hughes et al., 2003), N103B (Lewis et al., 2003), 0509-67.5 (Warren et al., 2004), 0548-70.4, and 0534-69.9 (Hendrick et al., 2003). The ages of these SNRs are somewhat uncertain, but the known distance to the Magellanic Clouds makes them specially attractive targets for testing spectral models.

An aspect of the problem that we have not addressed yet, but that is well within the capabilities of the simulation technique without the need of further improvements, is its application to spatially resolved spectroscopy. The Tycho SNR constitutes an ideal benchmark for this, so work on this object should continue in the future.

Finally, there is no reason to restrict the application of this technique to the remnants of thermonuclear SN explosions. Core collapse SNe produce somewhat more complex SNRs, but the interaction of the ejecta with the AM follows basically the same laws. An object like Cas A, for instance, would pose a fascinating challenge, demanding a significant degree of sophistication in any attempts to understand the spatially resolved emission from its shocked ejecta.

Appendix A

The Hydrodynamic Code

A.1   Introduction

The hydrodynamic code computes the dynamic interaction of the SN ejecta with the AM that surrounds the progenitor system at the time of the explosion. It integrates a finite difference discretization of the Euler equations of hydrodynamics in a one dimensional Lagrangian grid, using an explicit scheme and assuming an ideal gas equation of state. The code is implemented in C++, and it relies on Blitz++, a C++ class library for scientific computing which provides performance on par with Fortran 77/90 by using template techniques (Veldhuzien, 2001).

The code has been built under the following simplifying assumptions (see also section 3.3.1):

- One-dimensional dynamics with spherical symmetry .

- No thermal conduction.

- Adiabatic dynamics. In particular, no radiative losses or cosmic ray pressure are included.

These assumptions are the same that were considered in Truelove and McKee, 1999, and the treatment of the problem we propose here follows that paper, unless indicated.

A.2   Description of the hydrodynamic code

A.2.1   Conservation laws

Under the assumptions detailed in the introduction, the conservation laws for momentum, energy and mass for an ideal gas ($\gamma = 5/3$) can be written as:

$$\frac{\partial^2 r}{\partial t^2} = \frac{\partial v}{\partial t} = -4\pi r^2 \frac{\partial p}{\partial M} \tag{A.2.1}$$

$$\frac{\partial}{\partial t}\left(\frac{p}{\rho^{5/3}}\right) = 0 \tag{A.2.2}$$

$$\frac{\partial}{\partial M}\left(\frac{4}{3}\pi r^3\right) = \frac{1}{\rho} \tag{A.2.3}$$

where M is the Lagrangian mass coordinate, defined as

$$M(r,t) \equiv \int_0^r 4\pi r'^2 \rho(r',t)dr' \tag{A.2.4}$$

A.2.2   The finite difference equations

The hydrodynamic code is no more than a way to discretize and integrate equations A.2.1 and A.2.2. In a Lagrangian scheme without advection of material between layers, the mass is always conserved, and it is not necessary to integrate equation A.2.3. The numerical treatment of the shocks is done with the standard artificial viscosity formulation (Richtmyer and Morton, 1967). The artificial viscosity coefficient c_0 is set to 2, which spreads the shocks over approximately 5 zones.

Let i be the discrete space (radial) coordinate and n be the discrete time coordinate. The spherical computational space is a grid of N Lagrangian zones with constant mass, whose interfaces are labeled from 0 at the origin to N at the outer surface of the last layer. In order to achieve second order accuracy in space and time, some quantities are defined at half-integral space and time points. Velocity and radius are defined at the interfaces (v_i, r_i), but density, specific internal energy, pressure and artificial viscosity pressure are defined at the layers ($\rho_{i+1/2}$, $\varepsilon_{i+1/2}$, $p_{i+1/2}$, $q_{i+1/2}$). Following this notation, the mass of each layer is defined as $\Delta M_{i+1/2}$.

The difference equations, in order of evaluation for $i \in \{1, N-1\}$ are

$$v_i^{n+1/2} = v_i^{n-1/2} + \Delta t^n \left[\frac{4\pi (r_i^n)^2 (p_{i-1/2}^n + q_{i-1/2}^{n-1/2} - p_{i+1/2}^n - q_{i+1/2}^{n-1/2})}{\frac{1}{2}(\Delta M_{i-1/2} + \Delta M_{i+1/2})} \right] \tag{A.2.5}$$

$$r_i^{n+1} = r_i^n + \Delta t^{n+1/2} v_i^{n+1/2} \tag{A.2.6}$$

$$\rho_{i-1/2}^{n+1} = \frac{\Delta M_{i-1/2}}{(4/3)\pi[(r_i^{n+1})^3 - (r_{i-1}^{n+1})^3]} \tag{A.2.7}$$

$$q_{i-1/2}^{n+1/2} = \begin{cases} \frac{c_0^2}{2}(\rho_{i-1/2}^n + \rho_{i-1/2}^{n+1})(v_i^{n+1/2} - v_{i-1}^{n+1/2})^2 & \text{if } \rho_{i-1/2}^{n+1} > \rho_{i-1/2}^n \\ 0 & \text{if } \rho_{i-1/2}^{n+1} \le \rho_{i-1/2}^n \end{cases} \tag{A.2.8}$$

$$\varepsilon_{i-1/2}^{n+1} = \frac{\varepsilon_{i-1/2}^n - [(1/2)P_{i-1/2}^n + q_{i-1/2}^{n+1/2}](1/\rho_{i-1/2}^{n+1} - 1/\rho_{i-1/2}^n)}{1 + \frac{\gamma-1}{2}\rho_{i-1/2}^{n+1}(1/\rho_{i-1/2}^{n+1} - 1/\rho_{i-1/2}^n)} \tag{A.2.9}$$

$$p_{i-1/2}^{n+1} = (\gamma - 1)\rho_{i-1/2}^{n+1} \varepsilon_{i-1/2}^{n+1} \tag{A.2.10}$$

Note the semi-implicit calculation of the specific internal energy in eq. A.2.9. The artificial viscosity pressure, as indicated in eq. A.2.8, exists only in the layers that are being compressed. The two different time steps are related by $\Delta t^n = (1/2)(\Delta t^{n-1/2} + \Delta t^{n+1/2})$, with $\Delta t^{n+1/2} \equiv t^{n+1} - t^n$. The inner and outer boundary conditions are $v_0 = 0$, $r_0 = 0$ and $p_{N+1/2} = q_{N+1/2} = 0$, respectively. For more details on the finite difference equations, see Truelove and McKee, 1999.

A.2.3   Code structure

The hydrodynamic code follows the standard structure for explicit codes:

1. The initial conditions are set.

2. The finite difference equations are integrated over time. Each time step has to be validated in order to verify the criteria of numerical stability and convergence. For the integration, the utilities of the Blitz++ library allow to operate on the arrays as a whole, with no need for loops in the spatial coordinate. Thus, a reasonable degree of performance is achieved with little numerical sophistication.

3. When a specific condition is met (usually, when the simulation time t reaches a given value), the simulation is terminated.

Initial conditions

The initial conditions are determined by the SN explosion model up to the Lagrangian mass coordinate M_{ej} and by whatever AM configuration is used for $M > M_{ej}$. The output of the ejecta models is homologously expanded from $t = 10^6$ s (or whatever initial time corresponds to the off-grid SN models) to $t_0 = 10^7$ s after the explosion before the SNR simulation is started. The final results are not sensitive to the value of t_0, which can be increased or decreased by a factor of a few without noticeable consequences. For the simulations of SN ejecta interacting with a uniform AM, all layers above M_{ej} are set to $v_i = 0$, $\rho_{i+1/2} = \rho_{AM}$, $e_{i+1/2} = 0$, $p_{i+1/2} = 0$, $q_{i+1/2} = 0$.

Time step validation procedure

In explicit hydrodynamic schemes, the maximum time step in a given layer is limited by the Courant-Friedrichs-Lewy (CFL) condition (Richtmyer and Morton, 1967, pp. 262 and 323). For the calculated solution at t^{n+1} to be stable, all layer interfaces must verify that

$$\Delta t^{n+1/2} \leq \xi_{CFL} \frac{r_{i+1}^n - r_i^n}{\left| v_i^{n-1/2} + c_{s\,i+1/2}^n \right|} \tag{A.2.11}$$

where $c_{s\,i+1/2}$ is the local speed of sound at the layer $i + 1/2$, defined as

$$c_{s\,i+1/2}^n \equiv \sqrt{\frac{\gamma p_{i+1/2}^n}{\rho_{i+1/2}^n}} \tag{A.2.12}$$

and ξ_{CFL} is a tolerance on the CFL condition that has been set to 0.1. The inaccuracy in the estimate of the CFL condition that is produced in expression A.2.11 by mixing magnitudes defined at indexes i and n with magnitudes defined at indexes $i + 1/2$ and $n + 1/2$ is compensated by the restrictive value of ξ_{CFL}.

   In addition to the CFL condition, the following conditions are imposed:

$$\frac{\left| v_i^{n+1/2} - v_i^{n-1/2} \right|}{\max(\left| v_i^{n-1/2} \right|, c_{s\,i+1/2}^{n-1/2}, v_{min})} \leq \zeta \tag{A.2.13}$$

$$\frac{\left| \rho_{i+1/2}^{n+1} - \rho_{i+1/2}^n \right|}{\max(\rho_{i+1/2}^n, \rho_{min})} \leq \zeta \tag{A.2.14}$$

$$\frac{\left|\varepsilon_{i+1/2}^{n+1} - \varepsilon_{i+1/2}^{n}\right|}{\max(\varepsilon_{i+1/2}^{n}, \ \varepsilon_{min})} \leq \zeta \tag{A.2.15}$$

Expressions A.2.13, A.2.14 and A.2.15 effectively limit the relative variation of v, ρ, and ε over a single time step to a numerical tolerance ζ whose value has been set to 0.05. In order to avoid exceedingly large relative variations when the monitored magnitudes are very small, the minimum values for the denominators have been set to $v_{min} = 10^4 \, \mathrm{cm \cdot s^{-1}}$, $\rho_{min} = 10^{-30} \, \mathrm{g \cdot cm^{-3}}$ and $\varepsilon_{min} = 10^{10} \, \mathrm{erg \cdot g^{-1}}$.

If any of the conditions A.2.13, A.2.14 or A.2.15 is not verified, the values calculated at $t^{n+1/2}$ and t^{n+1} are considered invalid, the time step $\Delta t^{n+1/2}$ is halved, and the iteration is repeated. If all conditions are verified, $\Delta t^{n+1/2}$ is increased, the new values are considered valid and a new iteration is calculated. In either case, the value of $\Delta t^{n+1/2}$ is always limited by eq. A.2.11. For standard initial conditions (i.e., the interaction of one of the grid SN models with a uniform AM), the number of invalid iterations is around 1% in the first years of simulation time, and then becomes very small as the shocks get weaker. In general, the SNR model can be followed to $t = 10,000 \, \mathrm{yr}$ after the explosion in a few minutes of computer time, running the hydrodynamic code in an AMD 6 desk computer at 1100 MHz.

A.2.4   Modifications

In order to simulate the interaction of the accretion winds with the ISM (chapter 6), some modifications have been made to the finite difference equations:

First, a source of mass and momentum has been incorporated at the central layer, which is considered to be outside the computational space for all time step validation purposes. Every time the mass of this layer grows to a certain value (typically 1/100 of the total mass of wind to be ejected in the simulation run), it enters the computational space and a new central layer is created that continues to produce mass and momentum. The capabilities of Blitz ++ allow for this growth of the computational space without any memory allocation problems.

Second, radiative losses have been taken into account. In order to do this, a cooling term has been introduced in the finite difference equation A.2.9 with a second order formalism:

$$\varepsilon_{i-1/2}^{n+1} = \frac{\varepsilon_{i-1/2}^{n} - [(1/2)P_{i-1/2}^{n} + q_{i-1/2}^{n+1/2}](1/\rho_{i-1/2}^{n+1} - 1/\rho_{i-1/2}^{n}) - (\Gamma_{i-1/2}^{n} - \varepsilon_{i-1/2}^{n}\overline{\Gamma}_{i-1/2}^{n})}{1 + \frac{\gamma-1}{2}\rho_{i-1/2}^{n+1}(1/\rho_{i-1/2}^{n+1} - 1/\rho_{i-1/2}^{n}) + \overline{\Gamma}_{i-1/2}^{n}} \tag{A.2.16}$$

where the term $\Gamma_{i-1/2}^{n}$ represents the specific internal energy lost due to radiative processes in layer $i-1/2$ between t^n and t^{n+1}, and the term $\overline{\Gamma}_{i-1/2}^{n}$ represents the derivative of $\Gamma_{i-1/2}^{n}$ with respect to ε. These terms are calculated as follows:

$$\Gamma_{i-1/2}^{n} = \Delta t^{n+1/2}\rho_{i-1/2}^{n+1}\Lambda_{rad}[\varepsilon_{i-1/2}^{n}] \tag{A.2.17}$$

$$\overline{\Gamma}_{i-1/2}^{n} = \Delta t^{n+1/2}\rho_{i-1/2}^{n+1}\frac{\partial \Lambda_{rad}}{\partial \varepsilon}[\varepsilon_{i-1/2}^{n}] \tag{A.2.18}$$

Here, Λ_{rad} and $\partial \Lambda_{rad}/\partial \varepsilon$ are tabulated functions of ε that are evaluated at the value closest to $\varepsilon_{i-1/2}^{n}$. The function Λ_{rad} is known as cooling curve, and it generally depends on the composition and ionization state of the material. In the case of the accretion wind bubbles, the material has solar composition and, given the time scales involved, can be assumed to be in collisional ionization equilibrium (see section B.3 for an easy way to prove
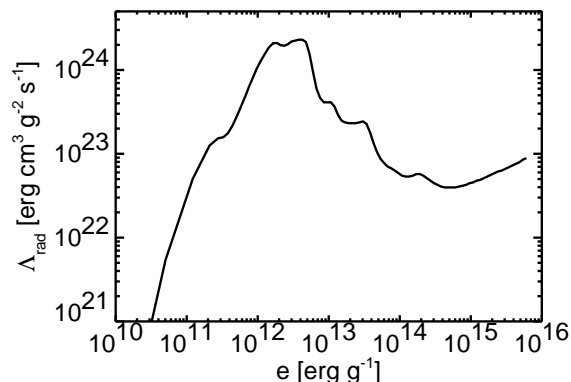
Figure A.1: Cooling curve as a function of specific internal energy for a solar plasma in collisional ionization equilibrium. Data from Sutherland and Dopita, 1993.
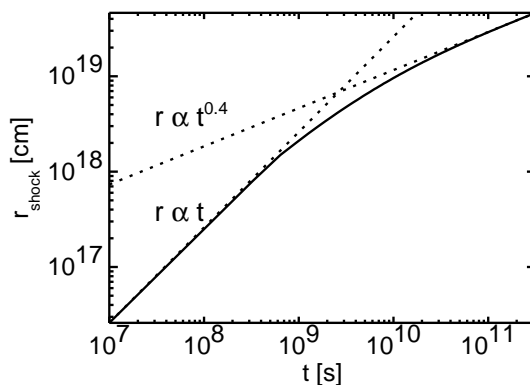

Figure A.2: Transition from the freely expanding regime to the Sedov stage in the forward shock of a SNR generated with an exponential ejecta profile. The solid line correspond to the forward shock trajectory, the dotted lines to the limiting regimes.

this). Most of the cooling curves that have been published in the literature are calculated under these conditions, so they can be applied directly to the problem at hand; in this case, the data of Sutherland and Dopita, 1993, have been used (see Figure A.1).

A.3 Benchmarking

There are a number of more or less sophisticated tests that are used to verify the performance of hydrodynamic codes. In this particular case, since the applicability of the code is restricted to the simulation of SNRs and wind-blown bubbles, the verification has been done directly on the results, which were at all times consistent with those of previous works and analytic calculations. As an example, Figure A.2 shows the transition of the forward shock from the freely expanding $r \propto t$ stage to the Sedov regime $r \propto t^{2/5}$ for a SNR simulated with an exponential ejecta profile ($M_{ej} = 1.4\,\mathrm{M_\odot}$, $E_k = 10^{51}\,\mathrm{erg}$) interacting with a uniform AM ($\rho_{AM} = 10^{-24}\,\mathrm{g\cdot cm^{-3}}$). The transition between the two regimes should happen around the characteristic time T', which has a value of $\sim 10^{10}\,\mathrm{s}$ for these parameters (eq. 3.3). The behavior of the code across three decades in radius and almost five decades in time is in accordance with the expectations. In the interaction region between the forward and reverse shocks, the calculated density profiles are also very

similar to those obtained by Dwarkadas and Chevalier, 1998 (compare Figure 6 of that work with Figures 3.7 to 3.11 of this dissertation).

Benchmarking of the modified version of the code that has been used to simulate the wind-blown bubbles is more complicated, because of the introduction of the cooling curve in the radiative cooling scheme. The structures obtained, however, are very similar to those calculated in other works, so no further verification has been deemed necessary (see chapter 6).

Appendix B

The Ionization Code

B.1   Introduction

The ionization code computes the temporal evolution of the temperature and charge state distribution (CSD) of a given fluid element by integrating the ionization and electron heating equations under the varying conditions characterized by the hydrodynamic history of the fluid element. The hydrodynamics are decoupled from the temperature and CSD of the fluid element at all times. The code is implemented in IDL, and it is built using object-oriented programming concepts. In this appendix, a review of the most important aspects of the code is presented, including the data structures used, the most relevant numerical techniques and the benchmarking procedures that have been performed on the code.

B.2   Description of the ionization code

From a numerical point of view, keeping track of the temperature and CSD of a fluid element can be assimilated to the constant updating of a data structure that has internal consistency rules. The total of the normalized ion abundances, for instance, must add to one ($\sum_i f_{X^i} = 1$), etc. The best way to deal with this situation is to use the concept of 'class' in object oriented programming. Formally, a class is a data structure that can only be accessed by programs and routines through a well defined interface, so that there is no risk of any operation performed on the data structure of violating its internal consistency rules. Also, since all the initialization and cleanup procedures, as well as the data access routines, are written into the class definition, the risk of memory leakage and segmentation errors is minimized. For a short introduction to the concepts of object oriented programming in IDL, see Fanning, 2000, chapter 13. A number of classes have been developed for the ionization code, but here we will only present the most important one, `ionStruct`, since the numeric performance of the code is based on its characteristics.

B.2.1   The `ionStruct` class

The `ionStruct` class has been designed to manage all the relevant information concerning the temperature and CSD of the fluid element. Each time the evolution of a new fluid element has to be followed, a new object of the `ionStruct` class is created.

Data structure

The class has the following data fields (IDL data type is given in brackets):

- `nElems [int]`: An integer specifying the number of chemical elements present in the fluid element.

- `atomicNumbers [ptr->IntArr(nElems)]`: A pointer to an array of `nElems` integers with the atomic numbers of the chemical elements. This variable has to be a pointer because `nElems` varies for each fluid element, and the size of the array cannot be fixed. The IDL routines `Ptr_New()` and `Ptr_Free` are used for memory management wherever pointers are involved.

- `abundances [ptr->DblArr(nElems)]`: A pointer to an array of `nElems` double precision floating point numbers (doubles) with the normalized number abundances of the chemical elements.

- `fEelectrons [Dbl]`: A double that specifies the fraction of the specific internal energy of the fluid element that is carried by the electrons ($\varepsilon_e/\varepsilon$, see eq. 3.6). By definition, `fEions = 1.0-feElectrons`.

- `ionFractions [ptr->PtrArr(nElems)]`: The ion fractions themselves. Since `nElems` can vary and the number of ions of each element depends on its atomic number Z, the ion fractions have to be coded via a double indirection, and `ionFractions` is a pointer to an array of pointers. The ith pointer in the array points to an array of $Z_X + 1$ doubles, the normalized abundances for the $Z_X + 1$ ions of the ith element, X. The indexes correspond to the ion charge, so that index 0 represents the neutral ion and index $Z_X + 1$ the bare ion.

Of these data fields, `nElems`, `atomicNumbers` and `abundances` are defined constant, i.e., they may only be manipulated by the initialization function `IonStruct::Init,` which is invoked by IDL every time a new object of this class is created. The inputs to this procedure are the arrays `atomicNumbers` and `abundances`, which must have the same number of elements (`nElems`) and no negative values. In addition to this, the atomic numbers must be physically meaningful and the normalized abundances must add up to one. It also allocates the memory for the `ionFractions` structure, initializes all elements to the neutral state and `fEelectrons` to 0.0[1]. The corresponding cleanup routine, `IonStruct::Cleanup`, is automatically invoked by IDL every time an object of the class is deleted and takes care of the memory deallocation.

Interface and internal consistency rules

None of the data fields of the class is directly accessible to the programs that have to manipulate the `ionStruct` object; all the necessary operations are performed through the class interface. The most important interface routines are:

- `ionStruct::Get_State, ionFractions, Z, fEelectrons, fEions`: output procedure. When called, the variables `ionFractions` and `fEelectrons` are set to the values currently held by the `ionStruct` object; Z (the mean charge per ion, $\overline{Z}$) and `fEions` are calculated from the same values.

- `[int]=ionStruct::Set_State(fEelectrons,ionFractions)`: input function. This function verifies the format of the input variables and returns 1 if they are valid and -1 if they are not. Deviation from 'valid' values might come as a result of numerical

---

[1] Note that this is just an initialization procedure, ionization cannot proceed in this state!

noise or code malfunction, and the interface acts as a safeguard against both. To be accepted, the new values have to fulfill ALL the following conditions:

> ▷ $0.0 < (\varepsilon_e/\varepsilon) < 1.0$. The fraction of internal energy in electrons (and ions) has to be a positive number below 1.0.

> ▷ $f_{X^i} \geq 0.0$ for all i, X. All ion fractions have to be positive. An exception is allowed to this condition: if one negative ion fraction with a small absolute value is detected ($0 \geq f_{X^i} \geq -\xi_n$ for one X, i), it is set to zero and the new values are not rejected because of this. The value of the tolerance ξ_n is set to 10^{-8}. If $f_{X^i} < -\xi_n$ or there is more than one negative ion fraction, the new values are rejected.

> ▷ $|1.0 - \sum_i f_{X^i}| \leq \xi_l$ for all elements X. The ion fractions have to be normalized. The tolerance ξ_l represents the maximum deviation from normalization that is accepted, and it is set to 10^{-4}. If a small deviation from normalization is detected, $\xi_s \leq |1.0 - \sum_i f_{X^i}| \leq \xi_l$, the new values are not rejected, but the ion fractions for the element X are renormalized. The value of ξ_s is set to 10^{-6}. No action is taken for deviations smaller than ξ_s.

The interface has other more specific routines to retrieve information that might be required by the code, like the value of $\overline{Z}$ or $\overline{A}$, or the dominant ion fractions of a given element, but the details of their implementation are not discussed here.

B.2.2 Code outline

Flowchart

To calculate the evolution of the ionization and thermal state evolution for each fluid element, the following information is needed:

- Hydrodynamic history, i.e., $\rho(t)$ and $\varepsilon(t)$ in vector form, extracted from the output file of the HD code.

- Chemical composition: atomic numbers and abundances

- Initial (preshock) ionization state (see sec. 3.4.1)

- β parameter for the shock (see sec. 3.4.2)

With these inputs, an `ionStruct` object is created and initialized, and the code starts to iterate through the HD evolution of the fluid element, calculating at each time step the new state of the fluid element from the ionization and electron heating equations, which are solved using an implicit scheme. A flowchart of the ionization code is presented in Figure B.1. The implicit scheme, which constitutes the core of the ionization code, is discussed in section B.2.3.

Time step interpolation and shock passage

Since the code always proceeds in time steps that are shorter than the sampling intervals of the HD evolution, a linear interpolation scheme is used to calculate the appropriate values of ρ and ε at the beginning of each ionization time step. The values of T_e, T_i, n_e and n_i, which are needed to solve the ionization and electron heating equations, are calculated by combining the present state of the fluid element (that is, f_{X^i} and $\varepsilon_e/\varepsilon$, obtained with the
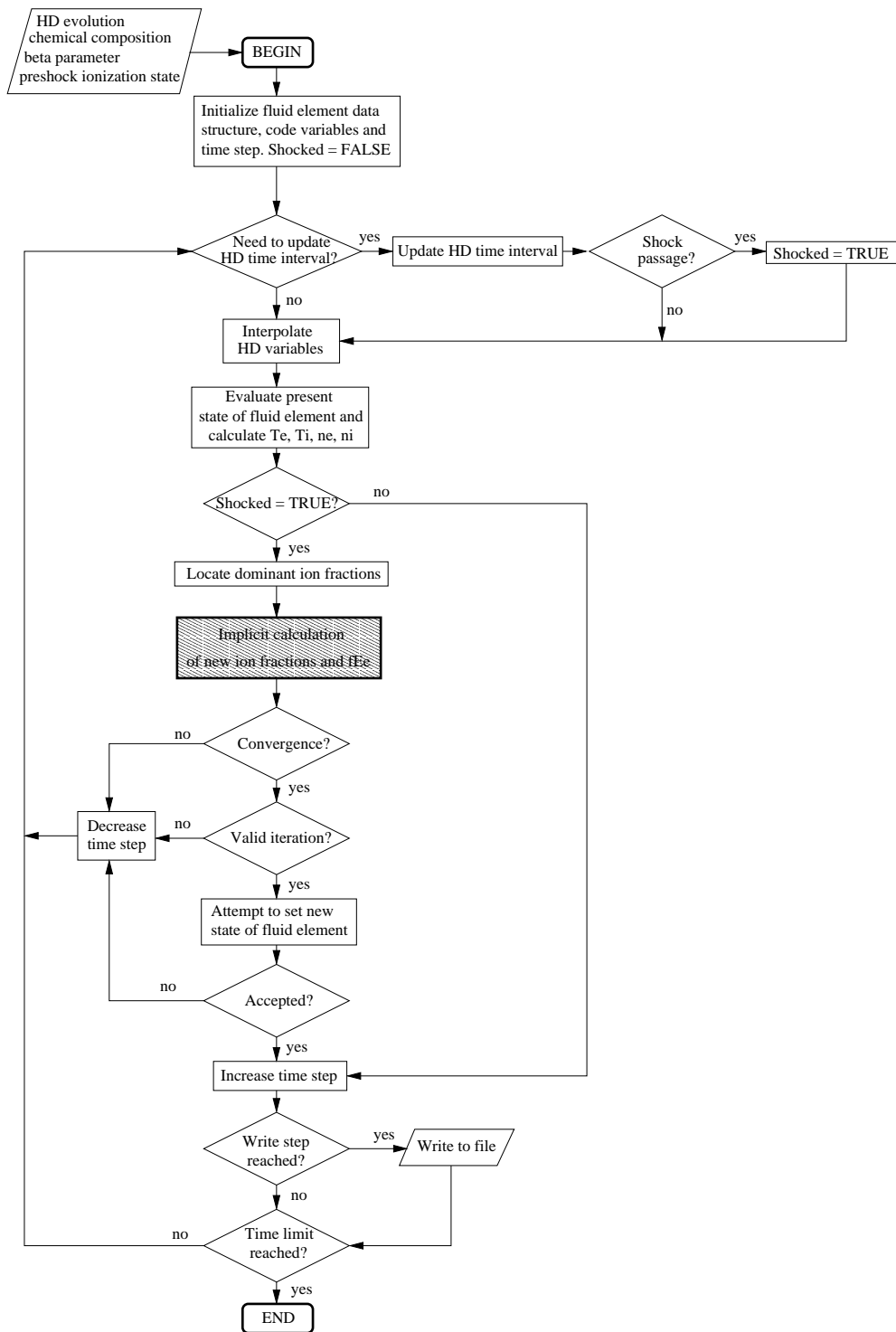
Figure B.1: Flowchart for the ionization code

routine `ionStruct::Get_State`) with the interpolated values of ρ and ε. The ionization and thermal states are not modified until the fluid element is shocked, a condition that is detected by a sudden rise of ε above a certain threshold ε_{th}, triggering the change of a flag from FALSE to TRUE.

Time step validation

Four conditions have to be met for an iteration to be considered considered valid:

- The implicit scheme has to converge (see section B.2.3).

- The variation of the ion fractions in the time step must not exceed a certain threshold:

$$\frac{|f_{X^i}(t + \Delta t) - f_{X^i}(t)|}{f_{X^i}(t)} \leq \zeta_f \tag{B.2.1}$$

  This condition is verified only if $f_{X^i} \geq 10^{-4}$, that is, only for the dominant ion fractions of each element. The use of the implicit scheme described in the following section allows for a high threshold value, so ζ_f is set to 0.1.

- The variation of the fraction of specific internal energy in the electrons must not exceed a certain threshold:

$$\frac{\left|\frac{\varepsilon_e}{\varepsilon}(t + \Delta t) - \frac{\varepsilon_e}{\varepsilon}(t)\right|}{\frac{\varepsilon_e}{\varepsilon}(t)} \leq \zeta_\varepsilon \tag{B.2.2}$$

  ζ_ε is set to 0.1.

- The `ionStruct::Set_State` function must accept the new state (see section B.2.1).

If any of these four conditions is not met, the iteration is considered invalid, the ionization time step is halved, the simulation time is not incremented, and the fluid element state is not updated. The code loops back and the calculation is repeated with the reduced time step. If the iteration is considered valid, the simulation time is incremented and the time step is multiplied by 1.5.

Results file and output write step

A complete description of the state of the fluid element is written periodically to an output file: T_e, T_i, n_e, n_i, $\varepsilon_e/\varepsilon$, $\varepsilon_i/\varepsilon$, the HD variables and all the ion fractions. The interval of file writing can be selected by the user, but its default value is equal to the HD sampling interval.

B.2.3 Integrating the equations: the implicit scheme

Rewriting the ionization equations

For each fluid element, we have `nElems` sets of $Z_X + 1$ equations (one for each ion), plus the electron heating equation. If we write the ion fractions for each element in vector form, $\overrightarrow{f}_X = [f_{X^0}, f_{X^1}, ..., f_{X^{Z_X}}]$, the ionization equations 3.9 can be reduced to a matrix equation for each element:

$$\frac{d}{dt}\overrightarrow{f_X} = \frac{\overline{Z}\rho}{\overline{A}m_u}\mathbb{M}_X(T_e)\overrightarrow{f_X} \tag{B.2.3}$$

where

$$
\mathbb{M}_X = \begin{bmatrix}
-I_{X^0} & R_{X^1} & 0 & \cdots & 0 \\
I_{X^0} & -(I_{X^1} + R_{X^1}) & R_{X^2} & \cdots & 0 \\
0 & I_{X^1} & -(I_{X^2} + R_{X^2}) & \cdots & 0 \\
\vdots & \vdots & \vdots & \ddots & \vdots \\
0 & 0 & 0 & \cdots & -R_{X^{Z_X}}
\end{bmatrix}
\tag{B.2.4}
$$

is the ionization matrix for element X. The coefficients I_{X^q} and R_{X^q} are tabulated functions of T_e, taken from Mazzotta et al., 1998[2]. These functions are given at discrete values of T_e, from 10^4 to 10^9 K with a spacing of 0.1 in $logT_e$. The ionization matrices for all the chemical elements present in the fluid element at the discrete values of T_e are stored in an IDL variable, and the code performs a linear interpolation between adjacent discrete values to calculate $\mathbb{M}_X$ at the present value of T_e every time the ionization equations are evaluated.

The ionization code takes advantage of the sparse character of $\mathbb{M}_X$ by using the storage format proposed in Press et al., 1994, (chapter 2, section 8, pp. 78-83), so that each matrix is reduced to a vector of indexes and a vector of data. This format is fully supported by IDL, and all the necessary routines are provided (like `SprsAX`, for instance, to perform the product $\mathbb{M}_X \cdot \overrightarrow{f_X}$). This also facilitates the linear interpolation mentioned in the preceding paragraph, since only the data vectors need to be interpolated.

Solving the stiff set

The ionization equations in matrix form and the electron heating equation form what is called a stiff set, mainly due to the very rapid ionization of low-charge stages. Stiff sets of differential equations are discussed in Press et al., 1994, (chapter 16, section 5, pp. 734-747), and two techniques based on implicit schemes are proposed for dealing with them: Rosenbrock methods and semi-implicit extrapolation methods. An alternative explicit method, tailored specifically to the problem of NEI ionization in SNRs and based on a set of precalculated eigenvalues for the ionization matrices was first proposed in Hughes and Helfand, 1985, and later improved in Borkowski et al., 1994.

The ionization code adopts a simplified version of the semi-implicit extrapolation. Initially, an explicit form of the equations is used to calculate tentative values of $\overrightarrow{f_X}$ and $\varepsilon_e/\varepsilon$ at $t + \Delta t$:

$$
\left[\frac{\varepsilon_e}{\varepsilon}(t + \Delta t) \right]^{(0)} = \frac{\varepsilon_e}{\varepsilon}(t) + \Delta t \cdot \frac{C \ln \Lambda \left[\overline{Z}(t) \right]^3 \rho(t) \cdot [T_i(t) - T_e(t)]}{\overline{A}^3 \varepsilon(t) \left[\frac{T_i(t)}{\overline{A} m_u} + \frac{T_e(t)}{m_e} \right]^{3/2}}
\tag{B.2.5}
$$

$$
\left[\overrightarrow{f}_X(t + \Delta t) \right]^{(0)} = \overrightarrow{f_X}(t) + \Delta t \cdot \frac{\rho(t) \overline{Z}(t)}{\overline{A} m_u} \mathbb{M}_X(t) \cdot \overrightarrow{f_X}(t)
\tag{B.2.6}
$$

Equations B.2.6 and B.2.5 are a straightforward rendering of eqns. 3.10 and 3.9 in finite differences. In equation B.2.5, n_e and n_i have been written in terms of ρ (from eq. 3.5), and all constants have been grouped under C. Once the first tentative values are known, the implicit loop is started and at each iteration the increment of $\overrightarrow{f_X}$ and $\varepsilon_e/\varepsilon$ over Δt is evaluated using the tentative values from the previous iteration:

---

[2] Dr. P.Mazzotta kindly provided his FORTRAN routines to calculate the ionization and recombination rates and the necessary tabulated atomic data.

$$\left[\Delta\frac{\varepsilon_e}{\varepsilon}(t+\Delta t)\right]^{(i)} = \left[\frac{\varepsilon_e}{\varepsilon}(t+\Delta t)\right]^{(i)} - \frac{\varepsilon_e}{\varepsilon}(t) =$$

$$= \Delta t \cdot \frac{C\ln\Lambda\left[\overline{Z}^{(i-1)}(t+\Delta t)\right]^3 \rho(t+\Delta t)\cdot\left[T_i^{(i-1)}(t+\Delta t) - T_e^{(i-1)}(t+\Delta t)\right]}{\overline{A}^3\varepsilon(t+\Delta t)\left[\frac{T_i^{(i-1)}(t+\Delta t)}{\overline{A}m_u} + \frac{T_e^{(i-1)}(t+\Delta t)}{m_e}\right]^{3/2}} \qquad \text{(B.2.7)}$$

$$\left[\Delta\overrightarrow{f_X}(t+\Delta t)\right]^{(i)} = \left[\overrightarrow{f}_X(t+\Delta t)\right]^{(i)} - \overrightarrow{f_X}(t) =$$

$$= \Delta t \cdot \frac{\rho(t+\Delta t)\overline{Z}^{(i-1)}(t+\Delta t)}{\overline{A}m_u}\mathbb{M}_X^{(i)}(t+\Delta t)\cdot\overrightarrow{f_X}^{(i-1)}(t+\Delta t) \qquad \text{(B.2.8)}$$

Note that in equation B.2.8 the ionization matrices are taken at the temperature corresponding to the present (i-th) iteration, which is known from equation B.2.7 and expression 3.7.

Convergence criteria and code performance

At the end of each iteration of the implicit loop, three convergence criteria are checked:

- For the fraction of specific internal energy in the electrons:

$$\left|\left[\Delta\frac{\varepsilon_e}{\varepsilon}(t+\Delta t)\right]^{(i)} - \left[\Delta\frac{\varepsilon_e}{\varepsilon}(t+\Delta t)\right]^{(i-1)}\right| \leq \epsilon_{\varepsilon_e} \qquad \text{(B.2.9)}$$

- For the average ion charge:

$$\left|\left[\Delta\overline{Z}(t+\Delta t)\right]^{(i)} - \left[\Delta\overline{Z}(t+\Delta t)\right]^{(i-1)}\right| \leq \epsilon_{\overline{Z}} \qquad \text{(B.2.10)}$$

- For the ion fractions:

$$\max_{X,j}\left|[\Delta f_{X^j}(t+\Delta t)]^{(i)} - [\Delta f_{X^j}(t+\Delta t)]^{(i-1)}\right| \leq \epsilon_{f_X} \qquad \text{(B.2.11)}$$

As mentioned in section B.2.2, condition B.2.11 is only applied to the dominant ion fractions of each element ($f_{X^i} \geq 10^{-4}$). If all three conditions are met before seven iterations are completed, the calculation is considered valid and the implicit scheme is considered to have converged. All the convergence thresholds are set to 10^{-6}.

For implicit schemes, it is always possible to improve the performance of the code by relaxing the convergence criteria. In the absence of a straightforward method to verify the solutions obtained (see following section), this relaxation is not exempt of risks, and it might be very time consuming to search for the optimal criteria. A conservative approach has been adopted, settling for the conditions detailed above after verifying that a set of more restrictive conditions produces the same results. The performance of the code under these conditions is probably suboptimal, but nevertheless adequate: the complete ionization evolution for the ejecta of one of the SN models from the grid in chapter 2 can be followed up to $t = 5,000\,\text{yr}$ after the explosion in less than an hour of computer time, with IDL running on an AMD 6 desk computer at 1100 MHz.

B.3   Benchmarking

The performance of the ionization code is difficult to test, mainly due to the lack of an analytical solution for the evolution of the electron temperature and CSD in NEI plasmas. As expressed in Liedahl, 1998, 'the tedium involved in obtaining closed-form solutions of the time-dependent equations for systems with more [than two] charge stages begins to test the limits of human patience'. Without straining the limits of anybody's humanity, the output of the code can be examined qualitatively for overall consistency in any particular case. In Figure B.2, the evolution of a fluid element composed of pure O is shown over the $10,000\,\mathrm{yr}\,(3.16\cdot10^{11}\,\mathrm{s})$ following the passage of the shock wave. The preshock ionization state was set to O^{+1}, and the postshock ρ and ε were kept constant at $4\cdot10^{-24}\,\mathrm{g}\cdot\mathrm{cm}^{-3}$ and $10^{15}\,\mathrm{erg}\cdot\mathrm{g}^{-1}$ respectively, with $\beta=0$. The temperatures, internal energy fractions and ion fractions evolved rapidly at first, as expected for a stiff set of differential equations. Around $t=5\cdot10^9\,\mathrm{s}$ He-like O becomes the dominant ion, and the evolution is slowed somehow due to the higher ionization potential in this ion (notice the change of slope in Fig.B.2b). As T_e keeps increasing, however, He-like O is eventually destroyed and H-like O takes over at $t\simeq3\cdot10^{10}\,\mathrm{s}$, followed by bare O at $t\simeq6\cdot10^{10}\,\mathrm{s}$. Temperature equilibration finally sets in at $t\simeq2.5\cdot10^{11}\,\mathrm{s}$, and the evolution of the CSD comes to a halt at the equilibrium fractions corresponding to the final electron temperature, $T_e=1.41\cdot10^7\mathrm{K}$. The equilibrium fractions corresponding to the varying T_e are also shown for the last stages of the evolution. As expected, the plasma is always underionized compared to the CIE for as long as T_e continues to evolve. It is instructive to compare this example with the one presented in section 4.5 of Liedahl, 1998, (pp. 258-260, Figs. 18 and 19), that follows the temporal evolution of the CSD of O in a fluid element whose electron pool is dominated by H and He. In that case, the lower number of electrons available makes the temperature evolution slower, but the CSD evolution is very similar.

A simple quantitative test that can be performed on the code is to verify whether the CIE state is attained within the expected time scale. According to Mewe, 1998, for astrophysical plasmas the transient (NEI) conditions cease to apply and CIE equilibrium sets in at $t_{rel}\simeq\min(t_{ion},t_{rec})$, with t_{ion} and t_{rec} the approximate ionization and recombination timescales for a given ion:

$$t_{ion}\approx\frac{10^{10}}{n_e}(z+1)^4n_z^{-4}\zeta_z^{-1}T_e^{-1/2}e^y\,[s] \tag{B.3.12}$$

$$t_{rec}\approx\frac{10^{11}}{n_e}(z+1)^{-2}n_z^{5/2}\xi_z^{-1}T_e^{1/2}\,[s] \tag{B.3.13}$$

Here, z is the charge of the relevant ion, ζ_z (or ξ_z) the number of valence electrons (or empty spaces) in the outer shell with principal quantum number n_z and $y=1.58\cdot10^5(z+1)^2n_z^{-2}T_e^{-1}$. In the previous test case, the value of T_e keeps changing due to the effect of electron heating. To follow the relaxation to CIE, however, the collisional heating processes have to be be deactivated so that the temperature remains constant, as shown in Fig.B.3. Here, the fluid element is kept at $T_e=5\cdot10^6\,\mathrm{K}$ and at a density of $\rho=4\cdot10^{-23}\,\mathrm{g}\cdot\mathrm{cm}^{-3}$, and the preshock ionization state is O^{+7}. With these parameters, the relevant time scales are t_{ion} for O^{+7} and t_{rec} for O^{+8}, which can be found by substitution in eqns. B.3.12 and B.3.13 to be $t_{ion,O^{+7}}\sim1.3\cdot10^{10}\,\mathrm{s}$ and $t_{rec,O^{+8}}\sim1.3\cdot10^{11}\,\mathrm{s}$. In the test case, the relaxation to the CIE fractions happens over a timescale of a few times $10^{10}\mathrm{s}$, confirming that the the code evolves within the approximate time scales predicted by the analytic expressions.
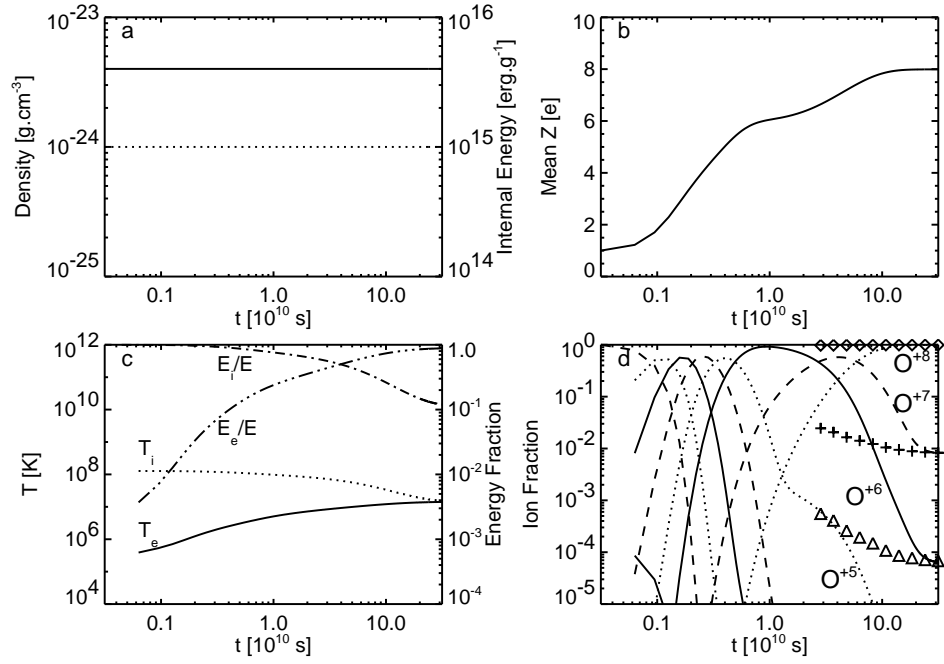
Figure B.2: Evolution of a fluid element composed of pure O. Top left (a): ρ (solid line) and ε (dotted line). Top right (b): $\overline{Z}$. Bottom left (c): T_e and T_i (solid and dotted lines), and $\varepsilon_e/\varepsilon$ and $\varepsilon_i/\varepsilon$ (dash-triple dotted and dash dotted lines). Bottom right (d): f_{O^i} (alternating solid, dashed and dotted lines from i=0 to i=8) and the equilibrium fractions corresponding to $O^{+6,+7,+8}$ for the varying values of T_e during the final evolution towards CIE (diamonds, crosses and triangles, respectively).

Figure B.3: Relaxation to CIE for a fluid element composed of pure O. Panels labeled as in figure B.2.

Appendix C

The spectral code

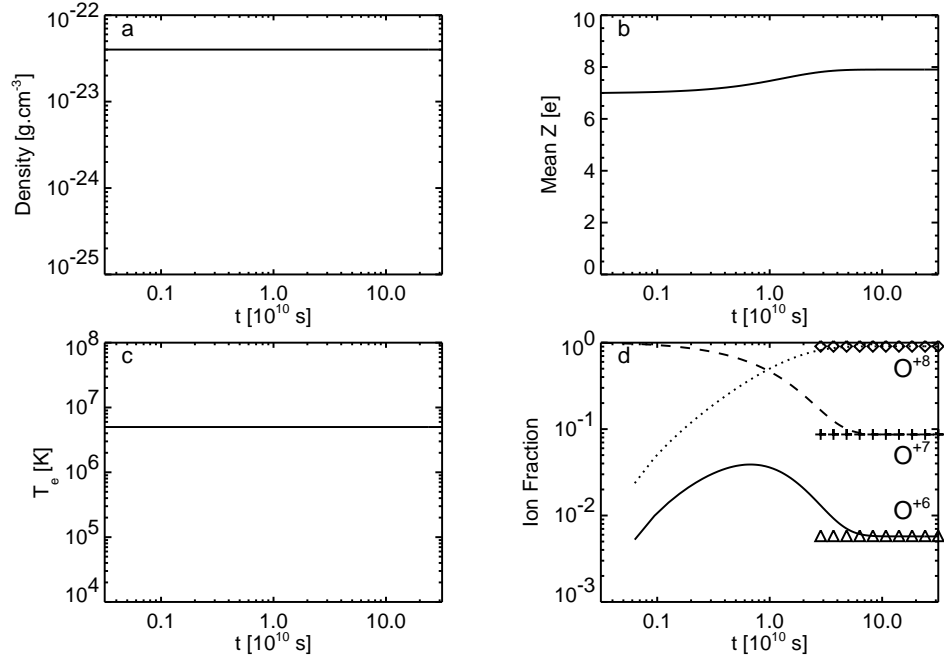## C.1   The Hamilton and Sarazin spectral code

The Hamilton and Sarazin (HS) spectral code was developed specifically to produce model X-ray spectra of SNRs, but it has also been applied to the study of galaxy clusters and other astrophysical problems. In recent times, the HS code has been incorporated to the XSPEC analysis package, and it plays a central role in many of the NEI models that are now part of XSPEC (see Borkowski et al., 2001; Arnaud and Dorman, 2004). A short overview of the code is provided here for reference purposes.

Overview

In order to calculate a spatially integrated model spectrum from one of the hydrodynamic + ionization simulations presented in chapter 3, the HS code is run once for every fluid element in the simulation space. The inputs to the HS code are the electron temperature in the fluid element T_e and the emission integral for each of the ions included in the code. In the present version of the code, these ions are H^{+1}, He^{+2} and all the ions, from neutral to bare, of C, N, O, Ne, Mg, Si, S, Ca, Fe, and Ni (a total of 159 ions). The emission integral of ion X^q is defined as

$$EI_{X^q} = V \cdot n_e \cdot n_i \cdot f_X \cdot f_{X^q} \qquad \text{(C.1.1)}$$

where V is the volume of gas in the fluid element and the rest of the quantities are defined in section 3.4.2. This calculation is straightforward if the abundances f_X, the charge state distribution f_{X^q}, and the hydrodynamic variables ρ and r in the fluid element are known.

In the terminology used to characterize solar and stellar plasmas, this 'emission integral' is in fact a 'differential emission measure'. This lexical *tour de force* comes from a change in the point of view: while the emission measure is the result of an integral in the volume of the fluid element, it is in fact differential with respect to the electron temperature, since each fluid element has a unique value of T_e. Note that the spectra produced by the HS code for the fluid elements are already normalized with respect to each other, and can be added together directly, without further changes. The fact that the fluid elements have different volumes and densities is taken into account by using the emission integrals as an input. In order to facilitate spectral analysis, the HS code calculates the line and continuum emission separately for each element.

Included processes

Line emission is calculated including the contribution of collisional excitation of valence electrons, collisional excitation of inner shell electrons, radiative recombination, dielectronic recombination, and radiative cascades from higher levels following any of these processes. The rates for collisional excitation of each line are derived from effective collision strengths which include the branching ratio for that line and a correction factor for cascades. More than 2000 emission lines are included in the current version of the code.

The emission processes that contribute to the continuum are thermal bremsstrahlung (free-free emission), radiative recombination and two-photon decays of metastable levels. For the two-photon decays, only the n=2 singlet and doublet s states for the H- and He-like ions of each element are included. The continuum is evaluated at 70 points in photon energy across the X-ray spectrum, between 0.0544 and 85.8 keV.

Atomic data and caveats

A complete review of all the atomic data that are included in the HS code is beyond the scope of this appendix. The original data are listed in Hamilton et al., 1983, but there have been a number of updates since then. Some significant changes are related to Fe Kα and Fe L emission. The contribution to Fe Kα from fluorescent emission has been taken into account, both from inner shell ionization followed by fluorescent decay and from collisional excitation of energy levels above the ionization threshold or (at lower temperatures) dielectronic recombination. Also, the energies, transition probabilities, and excitation rates by electrons for the Fe L-shell transitions in Ne- to Li-like Fe have been updated (Liedahl et al., 1995). A detailed list of the most important updates to the original atomic data is given in section 2.4. of Borkowski et al., 2001.

The HS code has been used in the present work because it is the most complete and updated spectral code that is fully compatible with NEI plasmas, but it should be stressed that the quality of the included atomic data is far from being ideal. In the future, all relevant atomic data for X-ray spectral modeling should be collected in the ATOMDB data base and spectral code (previously APEC/APED; Smith et al., 2001; Smith, 2003), but the current versions of these tools are not adequate for modeling NEI plasmas. Until a better, more powerful spectral code becomes available, the HS code provides a useful first approach to the calculation of model spectra, but there are many pitfalls to avoid. In this sense, it is crucial to know where the limitations of the HS code lie, and to make a distinction between those properties of the calculated spectra that are derived from well established data and those that are not. The most important caveats to the current version of the HS code are:

- No data are included for Ar. Besides the obvious fact that this makes the modeling of Ar emission impossible, care must be taken when drawing conclusions about the models for lines that are blended with those of Ar. Specifically, the Ca Kα and Ca Heα line complexes at 3.69 and 3.88 keV will be difficult to separate from Ar Heβ and Ar Heγ in real data, so model predictions concerning these lines might not be easy to verify.

- There are deficiencies in the data for Ne-like Fe. Inner shell collisional ionization, radiative and dielectronic recombination, and resonance excitation have been shown to be important in enhancing the $3s$ to $2p$ transitions in the Ne-like ion of Fe (Gu, 2003), and atomic resonances were also found to be important in the collisional excitation of Ne-like Fe (Chen et al., 2003). Since none of these processes are included

in the HS code, the emission in the Fe L complex between 0.7 and 0.9 keV might be affected. For a discussion, see Dyer et al., 2004.

- Discrepancies have been reported in the emission rates for the lines of some ions between the HS code and preliminary versions of ATOMDB adapted for NEI plasmas (K. Borkowski, 2004 , private communication). In general, inner shell processes for all ionization stages below He-like are inaccurate by factors that range from a few to an order of magnitude. This might introduce deviations in the centroids of the Kα blends of Si and S under specific combinations of T_e and charge state distribution.

- The contribution to the continuum from the two-photon decay of metastable n=2 triplet s state in He-like ions (which is produced by inner shell collisional excitation of Li-like ions in 75% of the cases) is not included, so the continuum might be underestimated in those elements with abundant Li-like ions (K. Borkowski, 2004 , private communication).

- The energy grid for the calculation of continuum emission is rather coarse when compared with the spectral resolution of modern instruments. In particular, there might be problems in the model spectra at or around sharp recombination edges.

C.2   Interface with XSPEC

Once the synthetic spectrum is calculated, it is important to ensure that it can be used as a tool for spectral analysis in an efficient way. This is done by reading the synthetic spectra into a spectral model in the XSPEC package, which is called SRHYDRO. This makes it possible to apply the many capabilities of XSPEC to the synthetic spectra, such as convolution with instrumental responses, χ^2 fitting of observations, etc (see Arnaud and Dorman, 2004 for details). The spectra presented in chapters 4, 5 and 6 were generated with XSPEC by producing 'fake data' based on the SRHYDRO model and an appropriate instrumental response.

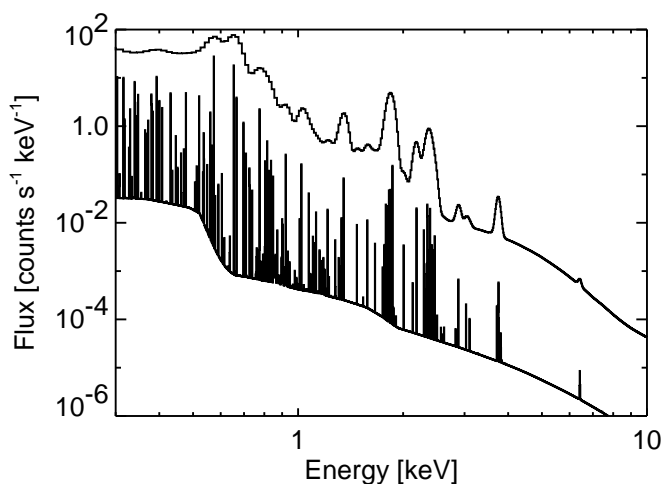Figure C.1: Synthetic spectrum of the ejecta from model DDTe at the age of the Tycho SNR, with nominal values of β and ρ_{AM}, compared with the same spectrum convolved with the response matrix of the EPIC MOS1 camera of *XMM-Newton*.

An example of this is given in Figure C.1, where the synthetic ejecta spectrum of model DDTe at the age of Tycho is compared to the same spectrum convolved with a

nominal response matrix for the EPIC MOS1 camera onboard *XMM-Newton*. Note that, even though this instrument has the highest spectral resolution currently available in an astronomical X-ray CCD camera, most of the fine structure in the line emission is lost in the convolution[1]. The instrumental variation of effective area and spectral resolution with photon energy is also plain to see in the convolved spectrum.

The SRHYDRO model, and its interface with the output of the HS code, were kindly provided by K. Borkowski (private communication, October 2002).

---

[1] Some of the details of this fine structure in the line emission are probably not to be trusted in the first place, due to the limitations of the model and the HS code, but that is another issue.

Bibliography

J.S. Albinson, R.J. Tuffs, E. Swinbank, and S.F. Gull (1986). Neutral hydrogen towards 3C 10, the remnant of Tycho's supernova. *MNRAS*, (219):427.

R. Arendt (2001). Young SNRs: IR Observations. In Holt and Hwang, 2001, page 163.

K.A. Arnaud (1996). XSPEC: The First Ten Years. In G. Jacoby and J. Barnes, editors, *ASP Conf. Ser. 101, Astronomical Data Analysis Software and Systems V*, San Francisco. ASP.

K. Arnaud and B. Dorman (2004). XSPEC: An X-Ray Spectral Fitting Package. User's Guide for version 11.3.x. HEASARC, Laboratory for High Energy Astrophysics, NASA/GSFC, available on the World Wide Web at http://xspec.gsfc.nasa.gov/docs/xanadu/xspec/manual/manual.html.

M. Arnaud and R. Rothenflug (1985). An updated evaluation of recombination and ionization rates. *A&AS*, (60):425.

D.W. Arnett (1969). A Possible Model of Supernovae: Detonation of 12C. *Ap&SS*, (5):180.

D. Arnett (1996). *Supernovae and Nucleosynthesis*. Princeton University Press.

W. Baade (1945). B Cassiopeiae as a Supernova of Type I. *ApJ*, (102):309.

C. Badenes and E. Bravo (2001). The imprint of presupernova evolution on supernova remnants. *ApJ*, 556:L41.

C. Badenes, E. Bravo, K.J. Borkowski, and I. Domínguez (2003). Thermal X-ray emission from shocked ejecta in Type Ia supernova remnants: Prospects for explosion mechanism identification. *ApJ*, (593):358.

J.E. Baldwin and D.O. Edge (1957). Radio emission from the remnants of the supernovae of 1572 and 1604. *Observatory*, (77):139.

J. Ballet and A. Decourchelle (2002). X-ray Spectroscopy of Supernova Remnants. *NewAR*, (46):507.

R. Barbon, F. Ciatti, and L. Rosino (1973). On the light curve and properties of type I supernovae. *A&A*, (25):241.

E. Baron, E.J. Lentz, and P.H. Hauschildt (2003). Detectability of Mixed Unburnt C+O in Type Ia Supernova Spectra. *ApJ*, (588):L29.

M. Basko (1994). Nickel bubble instability and mixing in SN 1987A. *ApJ*, (425):264.

R. Bedogni and A. D'Ercole (1988). The electron thermal conduction in young supernova remnants. *A&A*, (190):320.

W.P Blair (2001). UV/Optical Observations of Young Supernova Remnants. In Holt and Hwang, 2001.

J.M. Blondin, K.J. Borkowski, and S.P. Reynolds (2001). Dynamics of Fe Bubbles in Young Supernova Remnants. *ApJ*, (557):782.

J.M. Blondin and D.C. Ellison (2001). Rayleigh-Taylor Instabilities in Young Supernova Remnants Undergoing Efficient Particle Acceleration. *ApJ*, (560):244.

K.J. Borkowski, W.J. Lyerly, and S.P. Reynolds (2001). Supernova Remnants in the Sedov Expansion Phase: Thermal X-ray Emission. *ApJ*, (548):820.

K.J. Borkowski, C.L. Sarazin, and J.M. Blondin (1994). On the X-ray spectrum of Kepler's supernova remnant. *ApJ*, (429):710.

K.J. Borkowski and A.E. Szymkowiak (1997). X-Ray Emission from Dust in Hot Plasmas. *ApJ*, (477):L49.

D. Branch (1981). Some statistical properties of type I supernovae. *ApJ*, (248):1076.

D. Branch (1982). The Hubble diagram for type I supernovae. *ApJ*, (258):35.

D. Branch (1986). On the relative frequencies of the kinds of Type I supernovae. *ApJ*, (300):L51.

D. Branch (1998). Type Ia supernovae and the Hubble Constant. *ARA&A*, (36):17.

D. Branch (2001). Spectroscopically Peculiar Type Ia Supernovae and Implications for Progenitors. *PASP*, (113):169.

D. Branch and A. Khokhlov (1995). Type Ia supernovae: observations, modeling, distances. *Phys. Rep.*, (256):53.

D. Branch, M. Livio, L.R. Yungelson, F.R. Boffi, and E. Baron (1995). In search of the progenitors of Type Ia supernovae. *PASP*, (717):1019.

E. Bravo, I. Domínguez, J. Isern, R. Canal, P. Höflich, and J. Labay (1993). On the photometric homogeneity of Type IA supernovae. *ApJ*, (269):187.

E. Bravo and D. García-Senz (1999). Coulomb corrections to the equation of state of nuclear statistical equilibrium matter: implications for SNIa nucleosynthesis and the accretion-induced collapse of white dwarfs. *MNRAS*, (307):984.

E. Bravo, A. Tornambé, I. Domínguez, and J. Isern (1996). Clues to Type Ia SN progenitors from degenerate carbon ignition models. *A&A*, (306):811.

G.L. Bretthorst (1990). An Introduction to Parameter Estimation Using Bayesian Probability Theory. In P.F. Fougère, editor, *Maximum Entropy and Bayesian Methods, Dartmouth 1989*, page 53. Kluwer Academic Publishers.

W. Brinkmann (1992). Nonequilibrium Non-LTE Ionization in Supernova Remnants. *A&A*, (254):460.

W. Brinkmann, H.H. Fink, A. Smith, and F. Haberl (1989). Non-equilibrium ionisation in supernova remnants - The case of Tycho. *A&A*, (221):385.

R. Canal, J. Méndez, and P. Ruiz-Lapuente (2001). Identification of the companion stars of Type Ia supernovae. *ApJ*, (550):L53.

P.J. Cargill and K. Papadopoulos (1988). A mechanism for strong shock electron heating in supernova remnants. *ApJ*, (329):L29.

G. Cassam-Chenai, A. Decourchelle, J. Ballet, U. Hwang, J.P. Hughes, and R.Petre (2004). XMM-Newton observation of Kepler's supernova remnant. *A&A*, (414):545.

S. Cassisi, I. Iben Jr., and A. Tornambé (1998). Hydrogen-accreting Carbon-Oxygen White Dwarfs. *ApJ*, (496):376.

J. Castor, R. McCray, and R. Weaver (1975). Interstellar bubbles. *ApJ*, (200):L107.

G.X. Chen, A.K. Pradhan, and W. Eissner (2003). Breit-Pauli R-matrix calculations for electron impact excitation of Fe XVII: a benchmark study. *J. Phys. B*, (36):453.

R.A. Chevalier (1982). Self-similar solutions for the interaction of stellar ejecta with an external medium. *ApJ*, (258):790.

R.A. Chevalier, J.M. Blondin, and R.T. Emmering (1992). Hydrodynamic Instabilities in Supernova Remnants: Self-Similar Driven Waves. *ApJ*, (392):118.

R.A. Chevalier and E.P. Liang (1989). The Interaction of Supernovae with Circumstellar Bubbles. *ApJ*, (344):332.

R.A. Chevalier and J.C. Raymond (1978). Optical emission from a fast shock wave - The remnants of Tycho's supernova and SN 1006. *ApJ*, (225):L27.

D.H. Clark and F.R. Stephenson (1977). *The Historical Supernovae*. Pergamon Press.

W. Cui and D.P Cox (1992). Two-temperature models of old supernova remnants with ion and electron thermal conduction. *ApJ*, (401):206.

R.J. Cumming, P.Lundqvist, L.J. Smith, M. Pettini, and D.L. King (1996). Circumstellar H alpha from SN 1994D and Future Type Ia Supernovae: An Observational Test of Progenitor Models. *MNRAS*, (283):1355.

A. Decourchelle, D.C. Ellison, and J. Ballet (2000). Thermal X-Ray Emission and Cosmic-Ray Production in Young Supernova Remnants. *ApJ*, (543):L57.

A. Decourchelle, J.L. Sauvageot, M. Audard, B. Aschenbach, S. Sembay, B. Rothenflug, J. Ballet, T. Stadlbauer, and R.G. West (2001). XMM-Newton observation of the Tycho supernova remnant. *A&A*, (365):L218.

I. Domínguez, O. Straniero, A. Tornambé, and J. Isern (1996). On the Formation of Massive C-O White Dwarfs: The Lifting Effect of Rotation. *ApJ*, (472):783.

I. Domínguez, A. Tornambé, and J. Isern (1993). On the Formation of O-Ne White Dwarfs in Metal-rich Close Binary Systems. *ApJ*, (419):268.

T. Douvion, P.O. Lagage, C.J. Cesarsky, and E. Dwek (2001). Dust in the Tycho, Kepler and Crab supernova remnants. *A&A*, (373):281.

V.V. Dwarkadas (2000). Interaction of Type IA Supernovae with Their Surroundings: The Exponential Profile in Two Dimensions. *ApJ*, (541):418.

V.V. Dwarkadas (2001). Interaction of Supernova Remnants With the Ambient medium. *JKAS*, (34):243.

V.V. Dwarkadas and R.A. Chevalier (1998). Interaction of Type Ia Supernovae With Their Surroundings. *ApJ*, (497):807.

K.K. Dyer (2001). *Thermal and Non-Thermal Emission in Supernova Remnants*. PhD thesis, North Carolina State University.

K.K. Dyer, S.P. Reynolds, and K.J. Borkowski (2004). Separating Thermal and Nonthermal X-Rays in Supernova Remnants. II. Spatially Resolved Fits to SN 1006 AD. *ApJ*, (600):752.

K.K. Dyer, S.P Reynolds, K.J. Borkowski, G. E. Allen, and R. Petre (2001). Separating Thermal and Nonthermal X-rays in Supernova Remnants I. Total Fits to SN 1006 AD. *ApJ*, (551):439.

C.R. Eck, J.J. Cowan, D.A. Roberts, F.A. Boffi, and D. Branch (1995). Radio observations of the Type Ia supernova 1986G as a test of a symbiotic star progenitor. *ApJ*, (451):L53.

J. H. Elias, K. Matthews, G. Neugebauer, and S. E. Persson (1985). Type I supernovae in the infrared and their use as distance indicators. *ApJ*, (296):379.

D.C. Ellison, A. Decourchelle, and J. Ballet (2004). Hydrodynamic Simulation of Supernova Remnants Including Efficient Particle Acceleration. *A&A*, (413):189.

D.W. Fanning (2000). *IDL Programming Techniques*. Fanning Software Consulting, second edition.

R.A. Fesen, J.A. Morse, R.A. Chevalier, K.J. Borkowski, C.L. Gerardy, S.S. Lawrence, and S. van den Bergh (2001). Hubble Space Telescope WFPC2 Imaging of Cassiopeia A. *AJ*, (122):2644.

R.A. Fesen, J.M. Saken, and A.J.S. Hamilton (1989). Discovery of the remnant of S Andromedae (SN 1885) in M31. *ApJ*, (341):L55.

A. Fisher, D. Branch, P. Nugent, and E. Baron (1997). Evidence for a High-velocity Carbon-rich Layer in the Type IA SN 1990N. *ApJ*, (481):89.

J. Franco, G. Tenorio-Tagle, P. Bodenheimer, and M. Rózyczka (1991). Evolution of supernova remnants inside preexisting wind-driven cavities. *PASP*, (103):803.

G.W. Fraser (1998). Instrumentation for X-ray Spectroscopy. In van Paradijs and Bleeker, 1998, page 477.

H. Friedman, E.T. Byram, and T.A. Chubb (1967). Distribution and Variability of Cosmic X-Ray Sources. *Science*, (156):374.

V.N. Gamezo, A.M. Khokhlov, E.S. Oran, A.Y. Chtchelkanova, and R.O. Rosenberg (2003). Thermonuclear Supernovae: Simulations of the Deflagration Stage and Their Implications. *Science*, (299):77.

D. García-Senz and E. Bravo (2004). The Boiling-pot Model for Type Ia Supernovae. *A&A*. in preparation.

D. García-Senz, E. Bravo, and N. Serichol (1998). A Particle Code for Deflagrations in White Dwarfs I. Numerical Techniques. *ApJS*, (115):119.

D. García-Senz, E. Bravo, and S.E. Woosley (1999). Single and multiple detonations in white dwarfs. *A&A*, (349):177.

P. Ghavamian (1999). *Optical Spectroscopy and Numerical Modeling of Nonradiative Shocks in Supernova Remnants*. PhD thesis, Rice University.

P. Ghavamian, J. Raymond, P. Hartigan, and W.P. Blair (2000). Evidence for Shock Precursors in Tycho's Supernova Remnant. *ApJ*, (535):266.

P. Ghavamian, J. Raymond, R.C. Smith, and P. Hartigan (2001). Balmer-dominated Spectra of Nonradiative Shocks in the Cygnus Loop, RCW 86, and Tycho Supernova Remnants. *ApJ*, (547):995.

D.A. Green (2004). A Catalogue of Galactic Supernova Remnants (January 2004 version). Mullard Radio Astronomy Observatory, Cavendish Laboratory, Cambridge, available on the World Wide Web at http://www.mrao.cam.ac.uk/surveys/snrs/.

M.F. Gu (2003). Indirect X-Ray Line-Formation Processes in Iron L-Shell Ions. *ApJ*, (582):1241.

J. Guerrero (2001). *Col.lisió d'objectes compactes amb SPH*. PhD thesis, Universitat de Barcelona.

S.F. Gull (1973). A numerical model of the structure and evolution of young supernova remnants. *MNRAS*, (161):47.

I. Hachisu and M. Kato (2003). RX J0513.9-6951: The First Example of Accretion Wind Evolution, a Key Evolutionary Process to Type Ia Supernovae. *ApJ*, (590):445.

I. Hachisu, M. Kato, and K. Nomoto (1996). A New Model for Progenitor Systems of Type IA Supernovae. *ApJ*, (470):L97.

I. Hachisu, M. Kato, and K. Nomoto (1999a). A Wide Symbiotic Channel to Type IA Supernovae. *ApJ*, (522):487.

I. Hachisu, M. Kato, K. Nomoto, and H. Umeda (1999b). A New Evolutionary Path to Type IA Supernovae: A Helium-rich Supersoft X-Ray Source Channel. *ApJ*, (519):314.

A.J.S. Hamilton, R.A. Fesen, C.C. Wu, D.M. Crenshaw, and C. L. Sarazin (1997). Interpretation of Ultraviolet Absorption Lines in SN 1006. *ApJ*, (481):838.

A.J.S. Hamilton and C.L. Sarazin (1984). Heating and cooling in reverse shocks into pure heavy-element supernova ejecta. *ApJ*, (287):282.

A.J.S. Hamilton, C.L. Sarazin, and R.A. Chevalier (1983). X-ray line emission from supernova remnants. I - Models for adiabatic remnants. *ApJS*, (51):115.

A.J.S. Hamilton, C.L. Sarazin, and A.E. Szymkowiak (1986a). The X-ray spectrum of SN 1006. *ApJ*, (300):698.

A.J.S. Hamilton, C.L. Sarazin, and A.E. Szymkowiak (1986b). The X-ray spectrum of Tycho. *ApJ*, (300):713.

M. Hamuy, M.M. Phillips, N.B. Suntzeff, J. Maza, L.E. González, M. Roth, K.Krisciunas, N. Morrell, E.M. Green, S.E. Persson, and P.J. McCarthy (2003). An asymptotic-giant-branch star in the progenitor system of a Type Ia supernova. *Nature*, (424):651.

M. Hamuy, M.M. Phillips, N.B. Suntzeff, R.A. Schommer, J. Maza, and R. Aviles (1996). The Absolute Luminosities of the Calan/Tololo Type IA Supernovae. *AJ*, (112):2391.

Z. Han and P. Podsiadlowski (2004). The single degenerate channel for the progenitors of Type Ia supernovae. *MNRAS*. accepted, [astro-ph/0309218].

R. Hanbury-Brown and C. Hazard (1952). Radio-frequency Radiation from Tycho Brahe's Supernova (A.D.1572). *Nature*, (170):364.

S.P. Hendrick, K.J. Borkowski, and S. P. Reynolds (2003). Ejecta Detection in Middle-Aged Large Magellanic Cloud Supernova Remnants 0548-70.4 and 0534-69.9. *ApJ*, (593):370.

W. Hillebrandt and J.C. Niemeyer (2000). Type Ia Supernova Explosion Models. *ARA&A*, (38):191.

P. Höflich, C.L. Gerardy, R.A. Fesen, and S. Sakai (2002). Infrared Spectra of the Subluminous Type Ia Supernova SN 1999by. *ApJ*, (568):791.

P. Höflich and A. Khokhlov (1996). Explosion Models for Type IA Supernovae: A Comparison with Observed Light Curves, Distances, H 0, and Q 0. *ApJ*, (457):500.

P. Höflich and J. Stein (2002). On the Thermonuclear Runaway in Type Ia Supernovae: How to Run Away? *ApJ*, (568):779.

P. Höflich, J.C. Wheeler, and F.K. Thielemann (1998). Type IA Supernovae: Influence of the Initial Composition on the Nucleosynthesis, Light Curves, and Spectra and Consequences for the Determination of Omega M and Lambda. *ApJ*, (495):617.

S.S. Holt and U. Hwang, editors (2001). *Young Supernova Remnants: Eleventh Astrophysics Conference. College Park, Maryland, 2000*, volume 565 of *AIP Conference Proceedings*. American Institute of Physics.

D.A. Howell, P. Höflich, L. Wang, and J.C. Wheeler (2001). Evidence for Asphericity in a Subluminous Type Ia Supernova: Spectropolarimetry of SN 1999by. *ApJ*, 556(302).

F. Hoyle and W.A. Fowler (1960). Nucleosynthesis in Supernovae. *ApJ*, (132):565.

J.P. Hughes (2000). The Expansion of the X-ray Remnant of Tycho's Supernova (SN 1572). *ApJ*, (545):L53.

J.P. Hughes, P. Ghavamian, C.E. Rakowski, and P.O. Slane (2003). Iron-rich Ejecta in the Supernova Remnant DEM L71. *ApJ*, (582):L95.

J.P. Hughes, I. Hayashi, D. Helfand, U. Hwang, M. Itoh, R. Kirshner, K. Koyama, T. Markert, H. Tsunemi, and J. Woo (1995). ASCA observations of the Large Magellanic Cloud supernova remnant sample: Typing supernovae from their remnants. *ApJ*, (444):L81.

J.P. Hughes and D.J. Helfand (1985). Self-consistent models for the X-ray emission from supernova remnants: An application to Kepler's remnant. *ApJ*, (291):544.

U. Hwang (2001). X-ray Observations of Young Supernova Remnants. In Holt and Hwang, 2001.

U. Hwang, A. Decourchelle, S.S. Holt, and R. Petre (2002). Thermal and Nonthermal X-Ray Emission from the Forward Shock in Tycho's Supernova Remnant. *ApJ*, (581):1101.

U. Hwang and E.V. Gotthelf (1997). X-Ray Emission-Line Imaging and Spectroscopy of Tycho's Supernova Remnant . *ApJ*, (475):665.

U. Hwang, J.P. Hughes, and R. Petre (1998). The X-Ray Iron Emission from Tycho's Supernova Remnant. *ApJ*, (497):833.

I. Iben and A.V. Tutukov (1984). Supernovae of type I as end products of the evolution of binaries with components of moderate initial mass (M not greater than about 9 solar masses). *ApJS*, (54):335.

H. Itoh (1978). Two-fluid blast-wave model for SNR. *PASJ*, (30):489.

H. Itoh (1984). Temperature relaxation in supernova remnants, revisited. *ApJ*, (285):601.

H. Itoh, K. Masai, and K. Nomoto (1988). X-ray emission from the remnant of a carbon deflagration supernova - SN 1572 (Tycho). *ApJ*, (334):279.

K. Iwamoto, F. Brachwitz, K. Nomoto, N. Kishimoto, H. Umeda, W.R. Hix, and F-K. Thielemann (1999). Nucleosynthesis in Chandrasekhar Mass Models for Type IA Supernovae and Constraints on Progenitor Systems and Burning-Front Propagation. *ApJS*, (125):439.

T.W. Jones, L. Rudnick, B.-I. Jun, K.J. Borkowski, G. Dubner, D.A. Frail, H. Kang, N.E. Kassim, and R. McCray (1998). 1E51 Ergs: The Evolution of Shell Supernova Remnants. *PASP*, (110):125.

J.S. Kaastra (1998). X-ray Spectroscopic Observations with ASCA and BeppoSAX. In van Paradijs and Bleeker, 1998, page 269.

K. W. Kamper and S. van den Bergh (1978). Expansion of the optical remnant of Tycho's supernova. *ApJ*, (224):851.

D. Kasen, P. Nugent, R.C. Thomas, and L. Wang (2004). Could There Be A Hole In Type Ia Supernovae? *ApJ*. submitted, [astro-ph/0311009].

D. Kasen, P. Nugent, L. Wang, D.A. Howell, J.C. Wheeler, P. Höflich, D. Baade, E. Baron, and P.H. Hauschildt (2003). Analysis of the Flux and Polarization Spectra of the Type Ia Supernova SN 2001el: Exploring the Geometry of the High-Velocity Ejecta. *ApJ*, (593):788.

A. M. Khokhlov (1991). Delayed detonation model for Type Ia supernovae. *A&A*, (245):114.

A.R. King and A. van Teeseling (1998). Wind-driven evolution of accreting binaries and the progenitors of SNe Ia. *A&A*, (338):965.

R.P. Kirshner and R.A. Chevalier (1978). The spectrum of Tycho's supernova remnant. *A&A*, (67):267.

K. Koyama, R. Petre, E.V. Gotthelf, U. Hwang, M. Matsuura, M. Ozaki, and S.S. Holt (1995). Evidence for Shock Acceleration of High-Energy Electrons in the Supernova Remnant SN1006. *Nature*, (378):255.

M.J. Kuchner, R.P. Kirshner, P.A. Pinto, and B. Leibundgut (1994). Evidence for 56Ni -> 56Co -> 56Fe decay in type IA supernovae. *ApJ*, (426):L89.

J.M. Laming (2001a). Accelerated Electrons in Cassiopeia A: An Explanation for the Hard X-Ray Tail. *ApJ*, (546):1149.

J.M. Laming (2001b). Accelerated Electrons in Cassiopeia A: Thermal and Electromagnetic Effects. *ApJ*, (563):828.

J.M. Laming and U. Hwang (2003). On the Determination of Ejecta Structure and Explosion Asymmetry from the X-Ray Knots of Cassiopeia A . *ApJ*, (597):347.

J. M. Laming (2000). Electron Heating at SNR Collisionless Shocks. *ApJS*, (127):409.

N. Langer, A. Deutschmann, S. Wellstein, and P. Höflich (2000). The evolution of main sequence star + white dwarf binary systems towards Type Ia supernovae. *A&A*, (362):1046.

J. Lee, B. Koo, and K. Tatematsu (2004). The Environment of Tycho: Possible Interaction with the Molecular Cloud. *ApJ*, (605):L113.

B. Leibundgut (2000). Type Ia Supernovae. *A&AR*, (10):179.

E.J. Lentz, E. Baron, D. Branch, and P.H. Hauschildt (2001). Non-LTE Synthetic Spectral Fits to the Type Ia Supernova 1994D in NGC 4526. *ApJ*, (557):266.

E.J. Lentz, E. Baron, P.N. Hauschildt, and D. Branch (2002). Detectability of Hydrogen Mixing in Type Ia Supernova Premaximum Spectra. *ApJ*, (580):374.

K.T. Lewis, D.N. Burrows, J.P. Hughes, P.O. Slane, G.P. Garmire, and J.A. Nousek (2003). The Radial Structure of Supernova Remnant N103B. *ApJ*, (582):770.

W. Li, A.V. Filippenko, R.R. Treffers, A.G. Riess, J. Hu, and Y. Qiu (2001). A High Intrinsic Peculiarity Rate among Type Ia Supernovae. *ApJ*, (546):734.

X.D. Li and E.P.J. van den Heuvel (1997). Evolution of white dwarf binaries: supersoft x-ray sources and progenitors of type ia supernovae. *A&A*, (322):L9.

D.A. Liedahl (1998). Spectral Properties of PIE and NIE Plasmas. In van Paradijs and Bleeker, 1998, page 189.

D.A. Liedahl, A.L. Osterheld, and W.H. Goldstein (1995). New calculations of Fe L-shell X-ray spectra in high-temperature plasmas. *ApJ*, (438):L115.

M. Livio and A.G. Riess (2003). Have the Elusive Progenitors of Type Ia Supernovae Been Discovered? *ApJ*, (594):L93.

K.S. Long, S.P. Reynolds, J.C. Raymond, F.P. Winkler, K.K. Dyer, and R. Petre (2003). Chandra CCD Imagery of the Northeast and Northwest Limbs of SN 1006. *ApJ*, (586):1162.

M.S. Longair (1998). Continuum Processes in X-ray and Gamma-ray Astronomy. In van Paradijs and Bleeker, 1998, page 1.

T.J. Loredo (1990). From Laplace to Supernova SN 1987A: Bayesian Inference in Astrophysics. In P.F. Fougère, editor, *Maximum Entropy and Bayesian Methods, Dartmouth 1989*, page 81. Kluwer Academic Publishers.

P. Lundqvist, S. Mattila, J. Sollerman, E. Baron, P. Ehrenfreund, C. Fransson, B. Leibundgut, and K. Nomoto (2003). High-resolution optical studies of nearby Type Ia supernovae. In J.M. Marcaide and K.W. Weiler, editors, *Supernovae (10 years of SN1993J), IAU Colloquium 192*. Springer Verlag. in press, astro-ph/0309006.

E. Marietta, A. Burrows, and B. Fryxell (2000). Type Ia Supernova Explosions in Binary Systems: The Impact on the Secondary Star and its Consequences. *ApJS*, (128):615.

K. Masai (1997). Effect of iron ionization balance on X-ray spectral analysis. *A&A*, (324):410.

P.A. Mazzali, K. Nomoto, E. Cappellaro, T. Nakamura, H. Umeda, and K. Iwamoto (2001). Can Differences in the Nickel Abundance in Chandrasekhar-Mass Models Explain the Relation between the Brightness and Decline Rate of Normal Type Ia Supernovae? *ApJ*, (547):988.

P. Mazzotta, G. Mazzitelli, S. Colafrancesco, and N. Vittorio (1998). Ionization balance for optically thin plasmas: Rate coefficients for all atoms and ions of the elements H to Ni. *A&AS*, (133):403.

C. F. McKee (1974). X-Ray Emission from an Inward-Propagating Shock in Young Supernova Remnants. *ApJ*, (188):335.

R. Mewe (1990). Ionization of Hot Plasmas. In W. Brinkmann, A.C. Fabian, and F.Giovannelli, editors, *Physical Processes in Hot Cosmic Plasmas*, NATO Advanced Research, page 39. Kluwer Academic Publishers, Dordrecht, The Netherlands.

R. Mewe (1998). Atomic Physics of Hot Plasmas. In van Paradijs and Bleeker, 1998, page 109.

P.A. Milne (2001). Gamma-Ray Line Emission from Supernova Remnants. In Holt and Hwang, 2001.

R. Minkowski (1941). Spectra of supernovae. *PASP*, (53):224.

K. Nomoto (1982). Accreting White Dwarf Models for Type Ia Supernovae. I. Presupernova Evolution and Triggering Mechanisms. *ApJ*, (253):798.

K. Nomoto and Y. Kondo (1991). Conditions for accretion-induced collapse of white dwarfs. *ApJ*, (367):L19.

K. Nomoto, F.-K. Thielemann, and K. Yokoi (1984). Accreting white dwarf models of Type I supernovae. III - Carbon deflagration supernovae. *ApJ*, (286):644.

F. Paerels (1998). Future X-ray Spectroscopy Missions. In van Paradijs and Bleeker, 1998, page 345.

S. Perlmutter, G. Aldering, G. Goldhaber, R.A. Knop, P. Nugent, P.G. Castro, S. Deustua, S. Fabbro, A. Goobar, D.E. Groom, I.M. Hook, A.G. Kim, M.Y. Kim, J.C. Lee, N.J. Nunes, R. Pain, C.R. Pennypacker, R. Quimby, C. Lidman, R.S. Ellis, M. Irwin, R.G. McMahon, P. Ruiz-Lapuente, N. Walton, B. Schaefer, B.J. Boyle, A.V. Filippenko, T. Matheson, A.S. Fruchter, N. Panagia, H.J.M. Newberg, and W.J. Couch (1999). Measurements of Omega and Lambda from 42 High-Redshift Supernovae. *ApJ*, (517):565.

R. Petre (2001). Evidence for Cosmic Ray Acceleration in Supernova Remnants from X-ray Observations. In Holt and Hwang, 2001.

M.M. Phillips (1993). The absolute magnitudes of Type Ia supernovae. *ApJ*, (413):L105.

L. Piersanti, S. Cassisi, I. Iben Jr., and A. Tornambé (1999). On the Very Long Term Evolutionary Behavior of Hydrogen-accreting Low-Mass CO White Dwarfs. *ApJ*, (521):L59.

L. Piersanti, S. Cassisi, I. Iben Jr., and A. Tornambé (2000). Hydrogen-Accreting Carbon-Oxygen White Dwarfs of Low Mass: Thermal and Chemical Behavior of Burning Shells. *ApJ*, (535):932.

L. Piersanti, S. Cassisi, and A. Tornambé (2001). The Influence of 14N(e-, nu)14C(alpha, gamma)18O Reaction on He Ignition in Degenerate Physical Conditions. *ApJ*, (558):916.

L. Piersanti, S. Gagliardi, I. Iben Jr., and A. Tornambé (2003a). Carbon-Oxygen White Dwarf Accreting CO-Rich Matter. II. Self-Regulating Accretion Process up to the Explosive Stage. *ApJ*, (598):1229.

L. Piersanti, S. Gagliardi, I. Iben Jr., and A. Tornambé (2003b). Carbon-Oxygen White Dwarfs Accreting CO-rich Matter. I. A Comparison between Rotating and Nonrotating Models. *ApJ*, (583):885.

D. Porquet, M. Arnaud, and A. Decourchelle (2001). Impacts of a power-law non-thermal electron tail on the ionization and recombination rates. *A&A*, (373):1110.

W.H. Press, S.A. Teukolsky, W.T. Vetterling, and B.P. Flannery (1994). *Numerical Recipes in C*. Cambridge University Press, second edition.

I. P. Pskovskii (1977). Light curves, color curves, and expansion velocity of type I supernovae as functions of the rate of brightness decline. *SvA*, (21):675.

C.E. Rakowski, P. Ghavamian, and J.P. Hughes (2003). The Physics of Supernova Remnant Blast Waves. II. Electron-Ion Equilibration in DEM L71 in the Large Magellanic Cloud . *ApJ*, (590):846.

J.C. Raymond (2001). Emission Processes in Young SNRs. In Holt and Hwang, 2001, page 203.

M. Reinecke, W. Hillebrandt, and J.C. Niemeyer (2002). Three-dimensional simulations of Type Ia supernovae. *A&A*, (391):1167.

S.P. Reynolds (1998). Models of Synchrotron X-Rays from Shell Supernova Remnants. *ApJ*, (493):375.

E.M. Reynoso, D.A. Moffett, W.M. Goss, G.M. Dubner, J.R. Dickel, S.P. Reynolds, and E.B. Giacani (1997). A VLA Study of the Expansion of Tycho's Supernova Remnant. *ApJ*, (491):816.

E. M. Reynoso, P. F. Velázquez, G. M. Dubner, and W. M. Goss (1999). The Environs of Tycho's Supernova Remnant Explored through the H I 21 Centimeter Line. *AJ*, (117):1827.

J. Rho, K.K. Dyer, K.J. Borkowski, and S.P. Reynolds (2002). X-Ray Synchrotron-emitting Fe-rich Ejecta in Supernova Remnant RCW 86. *ApJ*, (581):1116.

J. Rho and R. Petre (1998). Mixed-Morphology Supernova Remnants. *ApJ*, (503):167.

R.D. Richtmyer and K.W. Morton (1967). *Difference Methods for Initial-Value Problems.* Interscience.

A.G. Riess, A.V. Filippenko, P. Challis, A. Clocchiatti, A. Diercks, P.M. Garnavich, R.L. Gilliland, C.J. Hogan, S. Jha, R.P. Kirshner, B. Leibundgut, M.M. Phillips, D. Reiss, B.P. Schmidt, R.A. Schommer, R.C. Smith, J. Spyromilio, C. Stubbs, N.B. Suntzeff, and J. Tonry (1998). Observational Evidence from Supernovae for an Accelerating Universe and a Cosmological Constant. *AJ*, (116):1009.

P. Ruiz-Lapuente (2004). Tycho Brahe's supernova: light from centuries past. *ApJ*. submitted [astro-ph/0309009].

P. Ruiz-Lapuente, R. Canal, and J. Isern, editors (1997). *NATO Advanced Study Institute on Thermonuclear Supernovae, Aiguablava, Spain, 1995*, volume 486 of *NATO ASI Series C*. Kluwer Academic Publishers.

P. Ruiz-Lapuente, F. Comerón, S. Smartt, R. Kurucz, J. Méndez, R. Canal, A. Filippenko, and R. Chornock (2003). Search for the companions of Galactic SNe Ia. In W. Hillebrandt and B. Leibundgut, editors, *From Twilight to Highlight: the Physics of Supernovae*, page 140. Springer.

G.B. Rybicki and A.P. Lightman (1985). *Radiative Processes in Astrophysics.* Wiley.

B.E. Schaefer (1996). Peak Brightnesses of Historical Supernovae and the Hubble Constant. *ApJ*, (459):438.

E. Schlegel and R. Petre (1993). A ROSAT Upper Limit on X-ray Emission from SN1992A. *ApJ*, (412):L29.

B.P. Schmidt, N.B. Suntzeff, M.M. Phillips, R.A. Schommer, A. Clocchiatti, R.P. Kirshner, P. Garnavich, P. Challis, B. Leibundgut, J. Spyromilio, A.G. Riess, A.V. Filippenko, M. Hamuy, R.C. Smith, C. Hogan, C. Stubbs, A. Diercks, D. Reiss, R. Gilliland, J. Tonry, J. Maza, A. Dressler, J. Walsh, and R Ciardullo (1998). The High-Z Supernova Search: Measuring Cosmic Deceleration and Global Curvature of the Universe Using Type IA Supernovae. *ApJ*, (507):46.

F. Schweizer and J. Middleditch (1980). A hot blue star near the center of the remnant of supernova A.D. 1006. *ApJ*, (241):1039.

L.I. Sedov (1959). *Similarity and Dimensional Methods in Mechanics.* Academic Press, New York.

L. Segretain, G. Chabrier, and R. Mochkovitch (1997). The Fate of Merging White Dwarfs. *ApJ*, (481):355.

F. Seward, P. Slane, R. Smith, T. Gaetz, B. Koo, and J. Lee (2004). Chandra supernova remnant catalog. Available on the World Wide Web at http://snrcat.cfa.harvard.edu//.

R.K. Smith (2003). The ATOMDB data base, version 1.3.1. Available on the World Wide Web at http://cxc.harvard.edu/atomdb/.

R.K. Smith, N.S. Brickhouse, D.A. Liedahl, and J.C. Raymond (2001). Standard Formats for Atomic Data: the APED. In G. Ferland and D.W. Savin, editors, *Spectroscopic Challenges of Photoionized Plasmas*, volume 247 of *ASP Conference Series*, page 159, San Francisco. Astronomical Society of the Pacific.

R.C. Smith, R.P. Kirshner, W.P. Blair, and P.F. Winkler (1991). Six Balmer-dominated Supernova Remnants. *ApJ*, (375):652.

L. Spitzer (1962). *Physics of Fully Ionized Gases*. Wiley.

H.P. Summers and R.W.P. McWhirter (1979). Radiative power loss from laboratory and astrophysical plasmas. I. Power loss from plasmas in steady-state ionisation balance. *J. Phys. B*, (12):2387.

R.S. Sutherland and M.A. Dopita (1993). Cooling functions for low-density astrophysical plasmas. *ApJS*, (88):253.

G.A. Tammann, W. Löffler, and A. Schröder (1993). The Galactic supernova rate. *ApJS*, (92):487.

G. Tenorio-Tagle, M.Rózyczka, J.Franco, and P.Bodenheimer (1991). On the evolution of supernova remnants - II. Two-dimensional calculations of explosions inside pre-existing wind-driven bubbles. *MNRAS*, (251):318.

G. Tenorio-Tagle, P.Bodenheimer, J.Franco, and M.Rózyczka (1990). On the evolution of supernova remnants - I. Explosions inside pre-existing wind-driven bubbles. *MNRAS*, (244):563.

F.X. Timmes and S.E. Woosley (1992). The conductive propagation of nuclear flames. I - Degenerate C + O and O + Ne + Mg white dwarfs. *ApJ*, (396):649.

J.K. Truelove and C.F. McKee (1999). Evolution of Nonradiative Supernova Remnants. *ApJS*, (120):299.

S. van den Bergh (1993). Was Tycho's supernova a subluminous supernova of type Ia? *ApJ*, (413):67.

K.J. van der Heyden, J.A.M. Bleeker, and J.S. Kaastra (2003). Synoptic Study of the SMC SNRs using XMM-Newton. *A&A*.

J. van Paradijs and J.A.M. Bleeker, editors (1998). *X-ray Spectroscopy in Astrophysics, EADN School X, Amsterdam, The Netherlands, 1997*. Lecture Notes in Physics. Springer Verlag.

P.F. Velázquez, D.O. Gomez, G.M. Dubner, G. Giménez de Castro, and A. Costa (1998). Study of the Rayleigh-Taylor instability in Tycho's supernova remnant. *A&A*, (334):1060.

P.F. Velázquez, J.J. Martinell, A.C. Raga, and E.B. Giacani (2004). Effects of Thermal Conduction on the X-Ray and Synchrotron Emission from Supernova Remnants. *ApJ*, (601):885.

T. Veldhuzien (2001). The blitz++ library. Available on the World Wide Web at http://www.oonumerics.org/blitz/.

J. Vink (2004). A Review of X-ray Observations of Supernova Remnants. *Nucl. Phys. B, Part. Phys.* in press [astro-ph/0311406].

J. Vink, M.J. Laming, M.F. Gu, A. Rasmussen, and J.S. Kaastra (2003). The Slow Temperature Equilibration behind the Shock Front of SN 1006. *ApJ*, (587):L31.

C.-Y. Wang and R.A. Chevalier (2001). Instabilities and Clumping in Type Ia Supernova Remnants. *ApJ*, (549):1119.

L. Wang, D. Baade, P. Höflich, A. Khokhlov, J.C. Wheeler, D. Kasen, P.E. Nugent, S. Perlmutter, C. Fransson, and P. Lundqvist (2003). Spectropolarimetry of SN 2001el in NGC 1448: Asphericity of a Normal Type Ia Supernova. *ApJ*, (591):1110.

J.S. Warren, J.P. Hughes, and P.O. Slane (2004). Raising the Dead: Clues to Type Ia Supernova Physics from the Remnant 0509-67.5. *ApJ*.

R. Weaver, R. McCray, J. Castor, P. Shapiro, and R. Moore (1977). Interstellar bubbles. II - Structure and evolution. *ApJ*, (218):377.

K.W. Weiler and R.A. Sramek (1988). Supernovae and supernova remnants. *ARA&A*, (26):295.

J.C. Wheeler, P. Höflich, R.P. Harkness, and J. Spyromilio (1998). Explosion Diagnostics of Type IA Supernovae from Early Infrared Spectra. *ApJ*, (496):908.

J.C. Wheeler, D. Swartz, Z. Li, and P.G. Sutherland (1987). Models for Type Ia supernovae with composition inversions. *ApJ*, (316):733.

R.N. Williams (1999). *Supernova Remnants in the Large Magellanic Cloud*. PhD thesis, University of Illinois at Urbana-Champaign.

L. Woltjer (1972). Supernova Remnants. *ARA&A*, (10):129.

Y.B. Zel'dovich and Y.P. Razier (1966). *Physics of Sock Waves and High-Temperature Hydrodynamic Phenomena*. Academic Press, first edition.